

TECHNISCHE UNIVERSITÄT MÜNCHEN

Lehrstuhl für Experimentelle Genetik

Discovery of new pathomechanisms in murine bone disease mutants
by systemic analysis

Christian Matthias Cohrs

Vollständiger Abdruck der von der Fakultät Wissenschaftszentrum Weihenstephan für Ernährung, Landnutzung und Umwelt der Technischen Universität München zur Erlangung des akademischen Grades eines

Doktors der Naturwissenschaften

genehmigten Dissertation.

Vorsitzender: Univ.-Prof. Dr. B. Küster

Prüfer der Dissertation:

1. Univ.-Prof. Dr. M. Hrabé de Angelis
2. Univ.-Prof. A. Schnieke, PhD

Die Dissertation wurde am 19.05.2011 bei der Technischen Universität München eingereicht und durch die Fakultät Wissenschaftszentrum Weihenstephan für Ernährung, Landnutzung und Umwelt am 05.10.2011 angenommen.

Für
Magdalena und Konrad,
Martina, Wilfried und Sabrina

I. Table of contents

I. TABLE OF CONTENTS	I
II. FIGURES AND TABLES	VI
III. ABBREVIATIONS	IX
IV. PUBLICATIONS	XIV
V. ACKNOWLEDGEMENTS	XV
VI. AFFIRMATION	XVII
1. SUMMARY/ZUSAMMENFASSUNG	1
2. INTRODUCTION	5
2.1 Skeletal development	5
2.1.1 Bone function.....	5
2.1.2 Bone structure.....	6
2.1.3 Bone development.....	7
2.1.4 Bone cells	11
2.1.5 Bone modelling and homeostasis	13
2.1.6 Bone diseases	14
2.1.6.1 Osteoarthritis and ankylosis.....	16
2.1.6.2 <i>Osteogenesis imperfecta</i> (OI)	17
2.2 Mouse models for human (bone) diseases	19
2.2.1 <i>Ali34</i>	20
2.2.2 <i>Aga2</i>	21
2.3 Systemic analysis of disease models	22
2.3.1 Systemic analysis	22
2.3.2 The German Mouse Clinic	22
2.3.3 Systemic effects on/of bone alterations	23
2.4 Thesis outline	25
3. MATERIALS AND METHODS	26
3.1 Materials	26
3.1.1 Chemicals	26

3.1.2 Standard buffers	26
3.1.3 Antibodies	28
3.1.4 Bacterial strains	29
3.1.5 Vectors.....	30
3.1.6 Cell lines	30
3.1.7 Inbred mouse strains	30
3.2 Methods.....	31
3.2.1 Isolation and purification methods.....	31
3.2.1.1 DNA isolation	31
3.2.1.2 RNA isolation	31
3.2.1.3 Protein isolation	32
3.2.1.4 Plasmid purification.....	32
3.2.2 Molecular methods.....	32
3.2.2.1 Polymerase chain reaction (PCR).....	32
3.2.2.2 Sequencing.....	33
3.2.2.3 Site-directed mutagenesis	34
3.2.2.4 Restriction digests.....	34
3.2.2.5 cDNA synthesis.....	36
3.2.2.6 qRT-PCR	36
3.2.2.7 TOPO cloning	37
3.2.2.8 Ligation	38
3.2.2.9 Gateway cloning	38
3.2.2.10 Transfection methods	39
3.2.2.11 Western Blot	39
3.2.3 Genotyping	40
3.2.2.1 <i>Ali34</i>	40
3.2.2.2 <i>Aga2</i>	40
3.2.4 Cell culture methods.....	40
3.2.4.1 Primary fibroblast cell culture.....	40
3.2.4.2 Primary osteoblast cell culture assay.....	42
3.2.4.3 Primary pancreatic islet culture.....	43
3.2.4.4 Cell line culture	44
3.2.5 Histological methods.....	45
3.2.5.1 Tissue preparation for paraffin sections.....	45

3.2.5.2 Tissue preparation for cryosections	45
3.2.5.3 H&E staining	46
3.2.5.4 Alcian blue staining	46
3.2.5.5 Safranin O staining	46
3.2.5.6 TRAP staining	46
3.2.5.7 Immunohistochemistry on paraffin sections	47
3.2.5.8 Immunohistochemistry on cryosections	47
3.2.5.9 Immunocytochemistry	48
3.2.5.10 SEM analysis	49
3.2.6 Skeletal stainings	49
3.2.7 Methods within the GMC	50
3.2.7.1 Animal housing and caretaking	50
3.2.7.2 Cardiovascular phenotyping	50
3.2.7.3 Dymorphological phenotyping	51
3.2.7.4 Behaviour screen	52
3.2.7.5 Neurology screen	52
3.2.7.6 Eye screen	52
3.2.7.7 Clinical chemical screening	53
3.2.7.8 Pathological phenotyping	53
3.2.7.9 Expression profiling	54
3.2.7.10 pO ₂ measurements	54
3.2.8 Alendronate treatment	55
3.2.9 Imaging techniques	55
3.2.10 Blood plasma collection	56
3.2.11 ELISA-measurements	56
3.2.11.1 Insulin ELISA	56
3.2.11.2 Osteocalcin ELISA	57
3.2.11.3 Adiponectin ELISA	57
3.2.12 Blood glucose evaluation	57
3.2.13 Statistical analysis	58
4. RESULTS	59
4.1 <i>Ali34</i>	59
4.1.1 Phenotypical characterisation of <i>Ali34</i> during embryogenesis	59
4.1.2 Characterisation of the bone phenotype in <i>Ali34</i> /+	62

4.1.2.1 Development and severity of the skeletal phenotype.....	62
4.1.2.2 C57BL/6J outcross analysis.....	68
4.1.2.3 Expression analysis	70
4.1.2.4 <i>In vitro</i> analysis of primary osteoblasts	71
4.1.3 Primary Screen of the GMC.....	72
4.1.3.1 Dysmorphology screen	72
4.1.3.2 Behaviour screen.....	76
4.1.3.3 Neurology screen.....	76
4.1.3.4 Eye screen.....	77
4.1.3.5 Clinical chemical screen	78
4.1.3.6 Molecular phenotyping.....	78
4.1.3.7 Pathology screen	79
4.1.4 Protein analysis.....	80
4.1.4.1 Overexpression of <i>Plxnd1</i> in L929 fibroblasts.....	81
4.1.4.2 <i>In vitro</i> analysis of mouse embryonic fibroblasts.....	83
4.1.5 Following steps	84
4.2 <i>Aga2</i>.....	86
4.2.1 Phenotypical classification of <i>Aga2</i> /+.....	86
4.2.2 Bisphosphonate treatment during neonatal development.....	86
4.2.3 Cardiovascular defects in OI.....	91
4.2.3.1 Cardiovascular phenotyping of <i>Aga2</i> /+.....	91
4.2.3.2 Comparison to human patient data.....	96
4.2.4 Pulmonary defects in OI.....	98
4.2.4.1 Pulmonary phenotyping of <i>Aga2</i> /+.....	98
4.2.4.2 Comparison to human patient data.....	99
4.2.5 Blood gas analysis in <i>Aga2</i>	102
4.2.6 <i>In vivo</i> imaging of the cardiopulmonary systems in <i>Aga2</i> /+	102
4.2.7 Expression profiling of heart and lung tissue of <i>Aga2</i> /+ ^{severe}	104
4.2.8 <i>Col1a1</i> expression analysis	105
4.2.8.1 <i>In vitro</i> analysis of primary cardiac and pulmonary fibroblasts.....	105
4.2.8.2 Onset of <i>Col1a1</i> downregulation and allele-specific <i>Col1a1</i> expression	107
4.2.9 Conditional gene targeting.....	110
4.2.10 Metabolic phenotypes in <i>Aga2</i>	111

4.2.10.1 General strategy	111
4.2.10.2 Experimental setup	114
4.2.10.3 Preliminary results	115
4.2.11 Following steps	118
5. DISCUSSION	120
5.1 <i>Ali34</i>.....	120
5.1.1 <i>Plxnd1</i> 's role during embryogenesis	120
5.1.2 <i>Plxnd1</i> signalling affects bone development and maintenance.....	123
5.1.3 Systemic phenotypes of <i>Ali34</i>	127
5.1.4 <i>Plxnd1</i> 's association to human diseases	128
5.1.5 Impact of <i>Plxnd1</i> 's cytoplasmic region on intracellular signalling.....	129
5.1.6 Conclusion and future perspective.....	131
5.2 <i>Aga2</i>.....	133
5.2.1 Bone phenotype improvement has no effect on perinatal lethality.....	133
5.2.2 Cardiac defects in <i>Aga2</i> /+.....	134
5.2.3 Pulmonary complications in <i>Aga2</i>	136
5.2.4 Functional linkage of cardiac and pulmonary defects in <i>Aga2</i> / ^{severe} ..	137
5.2.5 Human patients with type III and IV OI.....	138
5.2.6 Osteoporosis in <i>Aga2</i> – Connection to type 2 diabetes?	139
5.2.7 Conclusion and future perspective.....	141
5.3 Final remarks	143
6. APPENDIX	144
6.1 Supplemental figures.....	144
6.2 Supplemental tables.....	152
6.3 Primer sequences.....	157
6.4 Plasmid constructs	159
7. REFERENCES	163

II. Figures and tables

II.I Figures

Figure 1. Classification of bones.	6
Figure 2. Intramembranous and intermembranous ossification.	8
Figure 3. Cellular events and molecular markers of chondrogenesis.	10
Figure 4. Differentiation of mesenchymal progenitor cells.	11
Figure 5. Osteoclast differentiation.	13
Figure 6. Bone remodelling and achievement of homeostasis.	14
Figure 7. Classification of bone diseases.	15
Figure 8. Schematic representation of collagen processing.	19
Figure 9. GMC Timetable.	23
Figure 10. <i>Plxnd1</i> ^{Ali34/Ali34} phenotypes during embryogenesis.	60
Figure 11. Immunohistochemical stainings of 12.5 dpc embryos.	61
Figure 12. <i>Plxnd1</i> expression analysis in 11.5 dpc embryos.	62
Figure 13. Phenotypical hallmarks known from previous characterisations.	63
Figure 14. Cartilage canal misguidance results in ectopic bone formation.	64
Figure 15. Phenotypes in 2-weeks old <i>Ali34/+</i> mice.	65
Figure 16. Epiphyseal plate of the proximal humerus of 2-weeks old animals.	66
Figure 17. Histological analysis of 4-weeks old <i>Ali34/+</i> hindlimb bones.	67
Figure 18. Histological analysis of 8-weeks old <i>Ali34/+</i> hindlimb bones.	68
Figure 19. Ectopic bone formation in <i>Ali34/+</i> outcrossed to the <i>C57BL6/J</i> inbred strain.	69
Figure 20. qRT-PCR analysis of one week old hindlimb bone samples.	70
Figure 21. Data evaluation of the <i>in vitro</i> assays in primary osteoblasts of <i>Ali34/+</i> and controls.	72
Figure 22. Scout view of the pQCT measurement.	73
Figure 23. Results of the primary neurology screening in the GMC.	77
Figure 24. General <i>Plxnd1</i> protein analysis.	81
Figure 25. Overexpression of <i>Plxnd1</i> in L929 fibroblasts.	82
Figure 26. Cellular localisation of <i>Plxnd1</i> in mouse embryonic fibroblasts.	84
Figure 27. Alendronate treatment in <i>Aga2/+</i> newborn mice.	88
Figure 28. Evaluation of bone densitometric data obtained by μ CT measurements.	90
Figure 29. Ultrasound analysis at 10 dpp.	92
Figure 30. Histological analysis of cardiac phenotypes in <i>Aga2</i>	94
Figure 31. Myocardial ECM comparison between different murine OI models.	95

Figure 32. Immunohistochemical staining of PECAM-1 for morphological analysis of blood vessels.....	95
Figure 33. Histological analysis of lung tissue in <i>Aga2/+^{mild}</i> and <i>Aga2/+^{severe}</i>	99
Figure 34. Relationship of age to lung volume and function in type III and IV OI patients...	101
Figure 35. Relationship of scoliosis to lung volume and function in patients with types III and IV OI.....	101
Figure 36. Blood gas analysis of wild type, <i>Aga2/+^{mild}</i> and <i>Aga2/+^{severe}</i>	102
Figure 37. <i>Aga2/+</i> slicing images.....	104
Figure 38. <i>In vitro</i> culture of primary heart and lung fibroblasts and expression analysis by qRT-PCR.	107
Figure 39. <i>Col1a1</i> expression in hearts during perinatal development.	108
Figure 40. Emetine treatment of pulmonary fibroblasts.....	109
Figure 41. General strategy for gene targeting the <i>Col1a1^{Aga2}</i> locus.	111
Figure 42. General model for the interaction between bone and β -cells.....	112
Figure 43. Timetable for the systemic metabolic phenotyping of <i>Aga2</i>	113
Figure 44. ELISA and blood glucose analysis in 4-weeks old mice.	116
Figure 45. Immunohistochemical analysis of pancreata in 4-weeks old mice.	117
Figure 46. qRT-PCR analysis of isolated pancreatic islets of 4-weeks old mice.....	118
Figure 47. Schematic representation of the pathological processes provoked by the collagen mutation in <i>Aga2</i>	138
Supplemental Figure 1. Analysis of newborn <i>Ali34/+</i> mice.....	144
Supplemental Figure 2. Skeletal staining of 17-weeks old <i>Ali34/+</i> hindlimb bones.....	145
Supplemental Figure 3. Differentially expressed genes in heart tissue of <i>Ali34/+</i> animals..	145
Supplemental Figure 4. Differentially expressed genes in bone tissue of <i>Ali34/+</i> animals..	146
Supplemental Figure 5. μ CT pictures of alendronate treated animals.....	147
Supplemental Figure 6. Differentially expressed genes in heart tissue of <i>Aga2/+^{severe}</i>	148
Supplemental Figure 7. qRT-PCR data of <i>Col1a1</i> expression in heart and lung tissue of <i>Aga2/+^{severe}</i>	149
Supplemental Figure 8. Differentially expressed genes in lung tissue of <i>Aga2/+^{severe}</i>	150
Supplemental Figure 9. Schematic representation of known human mutations in <i>COL1A1</i> leading to types I, II and III OI.....	151

II.II Tables

Table 1. Current classification of osteogenesis imperfecta.....	18
Table 2. Primary antibodies	28
Table 3. Secondary antibodies.....	29
Table 4. Antibody dilution, incubation conditions and buffers used for IHC on paraffin sections.....	47
Table 5. Antibody dilution, incubation conditions and buffers used for IHC on cryosections.	48
Table 6. Antibody dilution, incubation conditions and buffers used for ICC.	49
Table 7. Summary of skeletal phenotypes observed during late embryogenesis	59
Table 8. Bone and weight-related quantitative parameters by DXA.....	74
Table 9. pQCT parameters	75
Table 10. Results of the behavioral observations in the Open Field test	76
Table 11. Clinical chemical paramters of the second blood sample.	78
Table 12. GO term analysis of regulated genes in <i>Ali34/+</i> bone tissue	79
Table 13. Results of the primary cardiovascular phenotyping	91
Table 14. Echochardigram and PFT findings in children with type III and IV OI.....	97
Supplemental Table 1. Gene expression analysis of <i>in vivo</i> cultured primary osteoblasts in <i>Ali34/+</i>	152
Supplemental Table 2. Spontaneous breathing pattern during rest and activity in <i>Aga2/+^{mild}</i>	153
Supplemental Table 3. GO-Term analysis of differentially expressed genes in hearts of <i>Aga2/+^{severe}</i> mice.....	154
Supplemental Table 4- GO-Term analysis of differrentially expressed genes in lungs of <i>Aga2/+^{severe}</i> mice.	154
Supplemental Table 5. Metabolic parameters of <i>Aga2/+^{mild}</i>	155
Supplemental Table 6. Gene expression analysis of <i>in vivo</i> cultured primary osteoblasts in <i>Aga2/+</i>	156

III. Abbreviations

μ CT	Micro computed tomography
3'UTR	3' untranslated region
A	Adenine
<i>Aga2</i>	Abnormal gait 2
<i>Aga2/+</i>	Heterozygous <i>Aga2</i> animals
<i>Aga2/+^{mild}</i>	Mildly affected <i>Aga2/+</i> animals
<i>Aga2/+^{severe}</i>	Severely affected <i>Aga2/+</i> animals (perinatal lethal)
<i>Ali34</i>	Abnormal limb 34
<i>Ali34/+</i>	Heterozygous <i>Ali34</i> animals
Alp	Alkaline phosphatase
α -MEM	Minimum essential medium alpha
ANOVA	Analysis of variants
ATP	Adenosine triphosphate
aVF	Lead augmented vector foot
aVL	Lead augmented vector left
aVR	Lead augmented vector right
BMC	Bone mineral content
BMD	Bone mineral density
bp	Base pair
BSA	Bovine serum albumin
C	Cytosine
CATK	Cathepsin K
CCD camera	Charged coupled device camera
cDNA	Complementary desoxyribonucleic acid
CHARGE	Coloboma of the eye, Heart defects, Atresia of the nasal choanae, Retardation of growth and/or development, Genital and/or urinary abnormalities, and Ear abnormalities and deafness.
ChIP	Chromatin immunoprecipitation
<i>ClCn7</i>	Chloride channel 7
cm	Centimetre
cm ²	Square centimetre
cm ³	Cubic centimetre
CO ₂	Carbon dioxide
<i>COL1A1</i>	α 1 chain of type I collagen
<i>Col1a1^{Aga2}</i>	<i>Aga2</i> allele of <i>Col1a1</i>
<i>COL1A2</i>	α 2 chain of type I collagen
<i>Col1a1^{WT}</i>	Wild-type allele of <i>Col1a1</i>
<i>CRTAP</i>	Cartilage associated protein

C _t	Crossing point (cycle threshold)
CT	Computed tomography
DAB	3,3'-Diaminobenzidine
DNA	Desoxyribonucleic acid
DAPI	4'6-diamidino-2'-phenylindole
dB	Decibel
DMEM	Dulbecco's modified eagle medium
dNTP	Dinucleotide triphosphate
dpc	Days post coitum
DPD	Deoxy pyridinoline
dpp	Days post partum
DXA	Dual energy X-ray absorptiometry
e.g.	For example (exempli gratia)
ECG	Echocardiography
ECM	Extracellular matrix
EDTA	Ethylene diamine tetraacetic acid
EF	Ejection fraction
ELISA	Enzyme-linked immunosorbant assay
ENU	N-ethyl-N-nitrosourea
ER	Endoplasmatic reticulum
etc	And so on (et cetera)
EtOH	Ethanol
EUCOMM	European conditional mouse mutagenesis program
EUMORPHIA	European union mouse research for public health and industrial application
f.c.	Final concentration
FACS	Fluorescence-activated cell sorter
FCS	Fetal calf serum
FDR	False discovery rate
FELASA	Federation of laboratory animal science association
FGF-23	Fibroblast growth factor 23
FMT	Fluorescence molecular tomography
FS	Fractional shortening
FVC	Forced vital capacity
g	Gram
G	Guanine
GEO	Gene expression omnibus
GFP	Green fluorescent protein
Gla-Ocn	Inactive osteocalcin
Glu-Ocn	Active osteocalcin
Gly	Glycine

GMC	German Mouse Clinic
GO	Gene ontology
GTT	Glucose tolerance test
H&E	Hematoxylin and Eosin
H ₂ O ₂	Hydrogenperoxide
HBSS	Hank's balanced salt solution
HPLC	High-performance liquid chromatography
HRP	Horseradish peroxidase
HTC	Hypertrophic chondrocyte
i.e.	That is (id est)
ICC	Immunocytochemistry
IHC	Immunohistochemistry
<i>Ihh</i>	Indian hedgehog
kDa	Kilodalton
KOH	Potassium hydroxide
<i>LEPRE1</i>	Leprecan
LVEDD	Left ventricular end-diastolic diameter
LVESD	Left ventricular end-systolic diameter
<i>M-CSF</i>	Macrophage colony-stimulating factor
MEF	Mouse embryonic fibroblast
MetOH	Methanol
mg	Milligram
min	Minute
mm ²	Square millimetre
<i>Mmp13</i>	Matrix metalloproteinase 13
<i>Mmp14</i>	Matrix metalloproteinase 14
<i>Mmp9</i>	matrix metalloproteinase 9
NaOH	Sodium hydroxide
Neo	Neomycine
NfκB	Nuclear factor kappa B
NMD	Nonsense-mediated decay
Nrp1	Neuropilin 1
Nrp2	Neuropilin 2
O ₂	Oxygen
OA	Osteoarthritis
<i>obd</i>	Out of bounds
OC	Osteocalcin
OF	<i>Open Field</i>
OI	Osteogenesis imperfecta
Opg	Osteoprotegerin
OsO ₄	Osmium tetroxide

pBMD	Partial bone mineral density (excluding the skull)
PBS	Phosphate buffered saline
PBST	Phosphate buffered saline with 0.05% Tween-20
pCO ₂	Carbon dioxide partial pressure
PCR	Polymerase chain reaction
pDEXA	Peripheral dual energy X-ray absorptiometry
PDZ	Post synaptic density protein (PSD95), Drosophila disc large tumor suppressor (DlgA), and zonula occludens-1 protein (zo-1)
PECAM-1	Platelet/endothelial cell adhesion molecule 1
PFA	Paraformaldehyde
PFT	Pulmonary function test
PINP	Amino-terminal propeptide of type I collagen
<i>Ptxnd1</i> ^{<i>Ali34</i>}	Protein harbouring the <i>Ali34</i> mutation
PNPP	4-nitrophenylphosphate
pO ₂	Oxygen partial pressure
PPI	Prepulse inhibition
PPIB	Peptidylprolyl isomerase B (cyclophilin B)
pQCT	Peripheral quantitative computed tomography
PTA	Persistent truncus arteriosus
PTHrP	Parathoid hormone related protein
PVDF	Polyvinylidene fluoride
qRT-PCR	Quantitative real-time PCR
RA	Rheumatoid arthritis
RANK	Receptor activator for nuclear factor kappa B
RANKL	Receptor activator for nuclear factor kappa B ligand
RNA	Ribonucleic acid
rpm	Rounds per minute
RPMI	Roswell Park Memorial Institute
RT	Room temperature
SAP	Shrimp alkaline phosphatase
sBMD	Specific bone mineral density (BMD related to body weight)
SEM	Scanning electron microscopy
SEM	Standard error of the mean
SHIRPA	SmithKline Beecham Pharmaceuticals, Harwell, MRC Mouse Genome Centre and Mammalian Genetics Unit, Imperial College School of Medicine at St Mary's, Royal London Hospital, St Bartholomew's and the Royal London School of Medicine, Phenotype, Assessment
SOC	Secondary ossification centre
SPF	Specific-pathogen-free
T	Thymine

TAE	Tris base, acetic acid and EDTA
TBS	Tris-buffered saline
TBST	Tris-buffered saline with 0.05% Tween-20
TEM	Transmission electron microscopy
TLC	Tidal lung capacity
TNAP	Tissue-nonspecific alkaline phosphatase
TRAP	Tartrate resistance acid phosphatase
VC	Vital capacity
VEGF	Vascular endothelial growth factor
VEGF ¹²⁰	Vascular endothelial growth factor 120 amino acid isoform
VEGF ¹⁶⁴	Vascular endothelial growth factor 164 amino acid isoform
VEGF ¹⁸⁸	Vascular endothelial growth factor 188 amino acid isoform
VEGFR1/2	Vascular endothelial growth factor receptor 1/2
WHO	World Health Organisation
XCT	X-ray computed tomography
Y	Tyrosine

1. Summary/Zusammenfassung

The complexity of the mammalian organism can lead to the development of diseases that affect multiple organ systems. These so called multifactorial diseases might be underestimated as long as only specific organ systems are investigated. For this reason, a systemic analysis of the whole model organism is an invaluable tool to discover novel pathomechanisms based on the underlying mutation.

Two ENU-induced mutant mouse lines (*Ali34*, *Aga2*), both with distinct bone dysmorphologies, were analysed systemically to further broaden the understanding of the underlying mutations in other organ systems and to identify novel pathomechanisms leading to multifactorial diseases.

The *Ali34* mouse mutant line harbours a point mutation in *Plxnd1* leading to a premature stop codon, generating a 48 amino acid shortened protein. Comparison to previously described *Plxnd1* knockout studies confirmed all known phenotypes in homozygous embryos. In this thesis, *Plxnd1* was shown to have an impact on proper bone formation during neonatal development of long bones due to its crucial function in angiogenic blood vessel guidance. These defects provoke previously unknown severe bone deformities including chondrodysplasia, non-inflammatory osteoarthritis and the development of osteophytes at the hindlimb bones resulting in a complete stiffening of the knee joints in a subgroup of heterozygous *Ali34* animals. In addition, systemic analysis within the primary screen of the German Mouse Clinic (GMC) provides evidence that angiogenic sprouting might affect more organ systems than previously expected. Biochemical analysis of *Plxnd1^{Ali34}* suggests that the truncation of the protein only affects its cytoplasmic region, although phenotypes described for knockouts were entirely confirmed for this ENU mutant. Taken together, the systemic analysis of *Ali34* provides new insight into pathological phenotypes caused by *Plxnd1*. In addition, it serves as a new model to investigate the function of the cytoplasmic domains of *Plxnd1*.

Aga2 was recently described as a new model for different types of *Osteogenesis imperfecta* (OI). OI is an inherited connective tissue disorder with skeletal dysplasia of varying severity, mainly caused by mutations in the collagen I genes (*COL1A1/COL1A2*). Although skeletal findings are predominant, OI is a

generalised connective tissue disorder as type I collagen also comprises about 80% of lung and cardiac collagen content. The non-skeletal manifestations of OI in the respiratory and cardiovascular systems are most frequently responsible for mortality and morbidity in severe and moderate types II-IV OI. However, these effects have not been directly linked to the underlying collagen mutation and have been considered secondary to skeletal changes. Based on systemic analysis of especially severely affected *Aga2/+* animals displaying perinatal lethality, a previously unknown bone-independent pathomechanism was identified. The *Col1a1^{Aga2}* mutation directly causes structural defects in both heart and lung tissue leading to hypertension, hypoxia and finally to *cor pulmonale*. Direct relevance of these findings was further demonstrated by a longitudinal study of type III and IV OI children at the NICHD, NIH. The patients exhibit collagen mutations causing severe and moderate non-lethal OI, corresponding more to mildly affected *Aga2/+* mice. Children both with and without scoliosis were shown to have clinically significant decline of pulmonary function during childhood, as well as primary cardiac valvular and chamber abnormalities. In addition, metabolic phenotyping was initiated to possibly identify currently undiscovered phenotypes with special focus on pancreatic function.

In conclusion, the systemic analysis of both mutant mouse lines identified novel pathomechanisms in different organ systems, which serve as a basis for a better understanding of gene function that can have an impact on new therapeutic approaches.

Die komplexe Struktur der Säugetiere bildet die Basis für Krankheiten die mehrerer Organsysteme betreffen können. Diese sogenannten multifaktoriellen Erkrankungen werden oftmals unterschätzt, da meist nur spezielle Teilbereiche untersucht werden. Es ist deshalb wichtig, den gesamten Organismus mittels systemischer Analysen zu beleuchten um bei genetisch bedingten Krankheiten mögliche neue Pathomechanismen zu identifizieren.

Die ENU-induzierten Mausmutantenlinien *Ali34* und *Aga2* wurden, ausgehend von ihren Knochendefekten, mittels systemischer Ansätze untersucht um mögliche multifaktorielle Erkrankungen in anderen Organsystemen zu identifizieren.

Die Mauslinie *Ali34* besitzt eine Punktmutation in *Plxnd1*, die zu einem um 48 Aminosäuren verkürzten Protein führt. Der Vergleich zu bereits bekannten Knockout-Linien konnte alle bisher bekannten Phänotypen in homozygoten Embryonen bestätigen. Darüber hinaus wurde in dieser Dissertation ein bisher unbekannter Einfluss auf die neonatale Knochenentwicklung nachgewiesen, der auf die wichtige Funktion von *Plxnd1* in der Blutgefäßeinwanderung zurückzuführen ist. Durch die frühe Störung in der Entwicklung der Längsknochen kommt es zu Chondrodysplasien, Osteoarthrose und der Bildung von Osteophyten, was bei vielen Tieren eine Versteifung der Kniegelenke zur Folge hat. Zusätzlich konnten durch den Primärscreen der German Mouse Clinic (GMC) bisher unentdeckte Defekte in anderen Organen heterozygoter Mäuse gezeigt werden. Die biochemische Analyse des Proteins deutet darauf hin, dass, obwohl alle bekannten Phänotypen von Knockout-Mäusen bestätigt wurden, nur die zytoplasmatische Region des mutanten Proteins betroffen ist.

Insgesamt konnten durch die systemische Analyse von *Ali34* neue Einblicke in die Pathogenese verschiedener Phänotypen aufgrund der Mutation in *Plxnd1* gewonnen werden. Darüber hinaus kann dieses Mausmodell eine wichtige Rolle für weiterführende Studien an den zytoplasmatischen Domänen von *Plxnd1* einnehmen.

Die Mauslinie *Aga2* wurde kürzlich als neues Modell für verschiedene Typen der Osteogenesis imperfecta (OI) beschrieben. OI ist eine erblich bedingte Bindegewebserkrankung mit unterschiedlich schweren Dysplasien des Skeletts die hauptsächlich auf Mutationen im Typ I Kollagen zurückzuführen (*COL1A1/COL1A2*) sind. Obwohl die Knochendefekte das Hauptmerkmal der OI sind, umfasst diese Krankheit auch die Bindegewebe in Herz und Lunge bei denen

das Typ I Kollagen nahezu 80% des Gesamtkollagens ausmacht. Obwohl die skeletale Veränderungen im respiratorischen und kardialen Bereich die häufigsten Ursachen für die Sterblichkeit und Erkrankungsrate in den schweren und moderaten Formen von OI (Typ II-IV) sind, wurden sie aber bisher nur als Begleiterscheinungen aufgrund der Knochendefekte angesehen. Durch die systemische Analyse mit besonderem Augenmerk auf neonatal letale *Aga2*⁺ Mäuse, konnten knochenunabhängige Defekte im kardiopulmonalen System entdeckt werden, die direkt auf die Mutation in *Col1a1* zurückzuführen sind. Die strukturellen Veränderungen bewirken eine Hypertonie, sowie eine Hypoxie, die letztendlich beide für die erhöhte Sterblichkeit in *Aga2* verantwortlich sind. Die neu gewonnen Erkenntnisse wurden durch die Analyse von Patienten mit Typ III und IV OI am NICHD, NIH zusätzlich bestätigt. Die Patientengruppe mit schwerer bis moderater nicht-letaler OI ist vergleichbar mit nicht perinatal letalen *Aga2* Mäusen, jedoch konnten auch hier knochenunabhängige Defekte im pulmonalen sowie kardialen System festgestellt werden.

Weiterführende Experimente an *Aga2* Mäusen befassen sich derzeit mit möglichen metabolischen Phänotypen in OI mit besonderem Augenmerk auf die Funktionen im Pankreas und eine damit verbundene Prädisposition für Typ 2 Diabetes.

Zusammenfassend konnte in dieser Dissertation gezeigt werden, dass durch die systemische Analyse beider Mausmutanten neue Pathomechanismen in verschiedenen Organsystemen gefunden werden konnten. Diese neuen Erkenntnisse dienen dem besseren Verständnis der einzelnen Genfunktionen und könnten zu neuen therapeutischen Ansätzen im medizinischen Bereich maßgeblich beitragen.

2. Introduction

2.1 Skeletal development

2.1.1 Bone function

Bone is a rigid but living organ, which together with cartilage forms parts of the vertebrate endoskeleton. It is a highly specialized form of connective tissue, consisting of 206 bones in adult humans, making up about 12% of the whole body weight¹. Tendons, ligaments and muscles support the bones and provide the movement of the body. Bone is composed of an organic matrix (~35%) consisting mainly of type I collagen and inorganic hydroxyapatite ($\text{Ca}_{10}(\text{PO}_4)\text{OH}_2$) elements (~65%) both providing rigidity. The structure of bone can be subdivided into an outer cortical part, accounting for approximately 80% of total bone mass and an inner cancellous part². While cortical (compact) bone is characterised by densely packed collagen fibrils forming concentric lamellae running in perpendicular planes, cancellous (spongy) bone has a more loosely and porous honeycomb structure. The differences in structures are related to their different functions for the organism³. Cortical bone is responsible for mechanical aspects like movement and shape of the body, support of breathing and sound transductions, as well as to protect inner organs (brain, spinal cord, heart, lung, pelvic viscera). The cancellous portion of bone supports blood cell production in the bone marrow, a process termed haematopoiesis. Furthermore, it fulfils metabolic functions like the storage of minerals (calcium and phosphorus) and the regulation of its homeostasis, the production and storage of growth factors (insulin-like growth factors, transforming growth factors, bone morphogenetic proteins, etc.), storage of fatty acids in the yellow bone marrow, detoxification of e.g. heavy metals, the regulation of the acid-base balance and the action as an endocrine organ by controlling phosphate metabolism (through FGF-23) and release of the hormone osteocalcin that regulates blood glucose levels through insulin secretion and sensitivity⁴.

2.1.2 Bone structure

Bone is a heterogeneous tissue not only in its composition; bones are classified into 5 groups according to their overall appearance (Figure 1). (1) Cylindrical long bones (femur, tibia) with two expanded ends surrounded by compact bone with a medulla cavity inside, (2) short bones (e. g. carpal and tarsal bones) with cancellous bone covered by a thin layer of compact bone, (3) sesamoid bones (e. g. patella) that are embedded in tendons and are a subgroup of short bones, (4) flat bones (e. g. scapula) with a thin layer of compact and cancellous bone and (5) irregular bones (e. g. vertebrae) varying in shape, with cancellous bone covered by a layer of compact bone⁵.

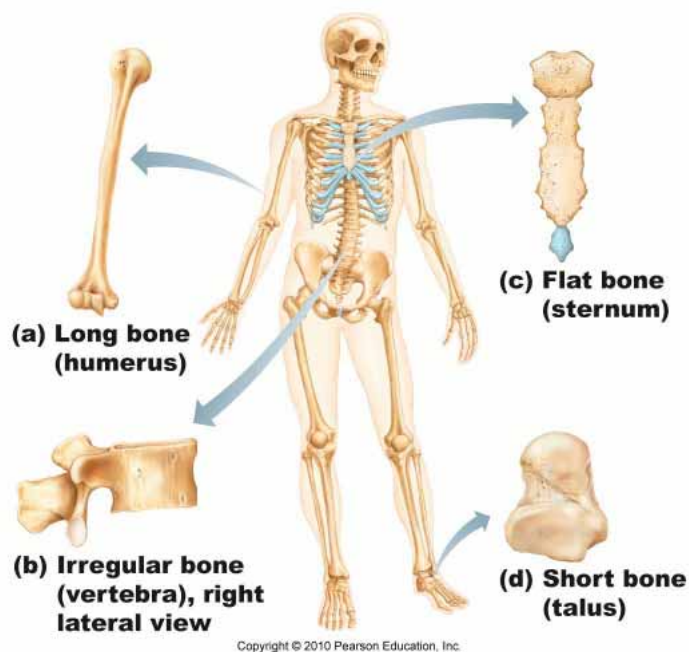


Figure 1. Classification of bones.

Illustration adopted from http://massasoit-bio.net/courses/201/201_content/topicdir/skeletal/skeletal_RG/skeletal_RG2/skeletal_RG2.html

Cortical bone is formed by multiple stacked layers, structurally arranged in osteons (Haversian system), small functional units composed of 4 to 20 concentric lamellae. Intermediate osteocytes reside in small lacunae in osteons and are connected by a network of narrow canals (canaliculi). Blood vessels and nerves interfuse the medial zone of the osteons to ensure nutrition and to transmit neurological stimuli. The vascular and neuronal network is arranged in horizontal (Haversian canals) and vertical (Volkmann canals) cavities and provide further communication between osteocytes in each osteon. The whole cortical bone is

enclosed by the periosteum (outside layer) and the endosteum (inner layer). The periosteum is composed of a dense irregular connective tissue divided into a fibrous and a cambium layer where osteoprogenitor cells reside. It is a highly vascularised tissue supporting the bone with nutrients. The endosteum forms the medullary cavity and is similar to the periosteal build-up. Cancellous bone is made up by a network of rod- and plate like elements with low density but high surface area. It serves as a scaffold for the development of the haematopoietic niche, blood vessels, nerves and the bone marrow in the medullary cavity.

2.1.3 Bone development

Bones evolve from three different cellular lineages. Neural crest cells give rise to most of the craniofacial skeleton, while the paraxial and lateral plate mesoderm develop the axial and appendicular skeleton respectively⁶⁻⁸. The development of the respective bones is initiated by mesenchymal condensation in either osteogenic or chondrogenic dissemination^{9,10}. The osteogenic lineage derives from epithelial-mesenchymal interaction that initiates preosteoblastic differentiation before condensation. Afterwards condensing preosteoblasts become functional osteoblasts that build up a mineralized bone matrix (Figure 2A). This process is called desmal or intramembranous bone formation and accounts for flat bones in the craniofacial region as well as the clavicle and the scapula¹¹. The major part of the skeleton is developing out of the chondrogenic lineage, building up a cartilage intermediate, which is subsequently mineralized and converted to bone tissue in a process called endochondral or intermembranous bone formation^{11,12} (Figure 2B). Both processes of bone formation occur in the formation of the long bones and are precisely controlled by the expression and interaction of specific genes in a spatial-temporal fashion¹³. Endochondral ossification is initiated by the migration and condensation of mesenchymal cells that differentiate into chondroblasts and chondrocytes, thus forming the cartilage anlagen, which serves as a framework building the epiphysis at either ends of the future bone^{13,14}. The anlagen are surrounded by the perichondrium, supplying the avascular template with nutrients. Chondrocytes in the anlagen can be distinguished on the basis of their spatial arrangement. Chondrocytes at the superficial layer will form the later articular cartilage, while the subjacent layer will form the epiphyseal cartilage later replaced

by the secondary ossification centre (see below). In the middle of the cartilage template the third portion of cartilage differentiates and forms the epiphyseal growth plate responsible for the later bone growth¹³.

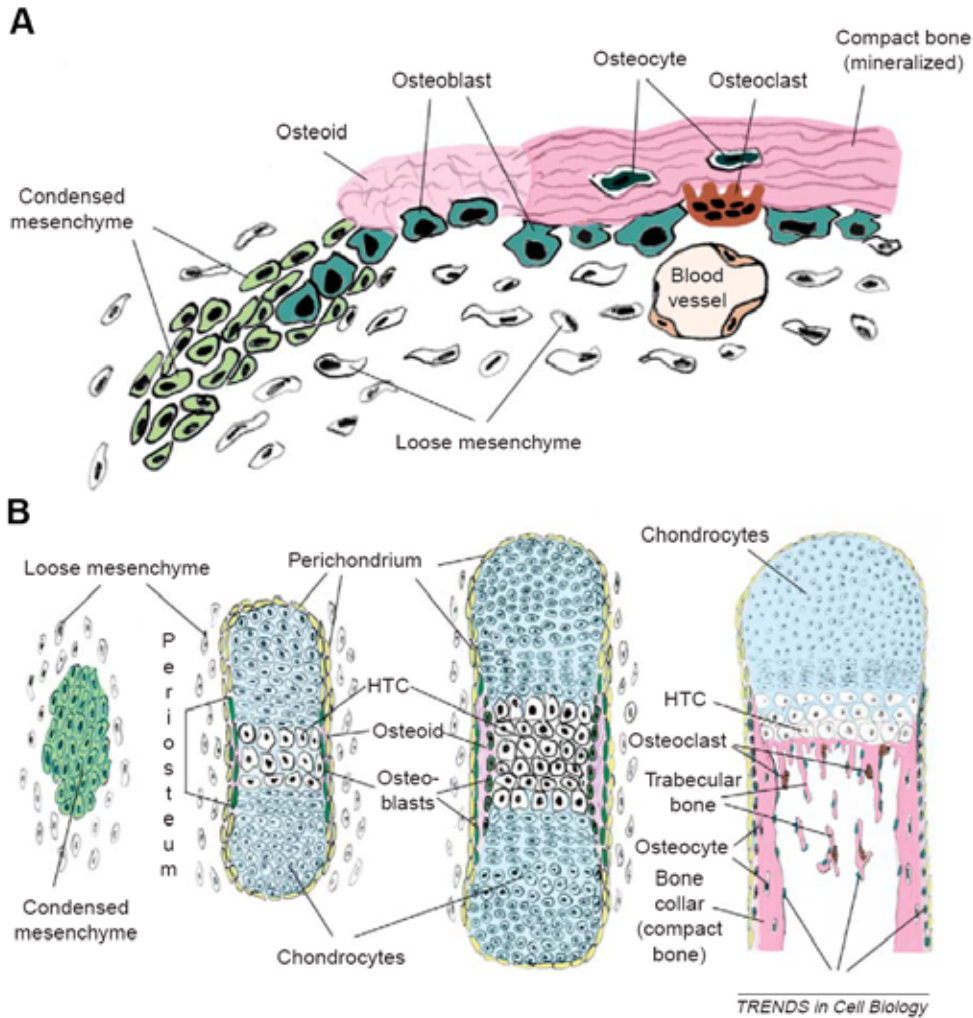


Figure 2. Intramembranous and intermembranous ossification.

A In the process of intramembranous bone formation, mesenchymal cells start to condense in the presence of blood vessels. Cells differentiate into osteoblasts that build up the extracellular matrix (ECM) termed osteoid. Osteoblasts enclosed by mineralized bone mature and become osteocytes. Further blood vessel support brings in bone resorbing osteoclasts. **B** During endochondral bone formation condensed mesenchymal cells differentiate into chondrocytes that proliferate and mature. While becoming hypertrophic chondrocytes (HTC) the periosteum forms and builds up bone in an intramembranous fashion. Hypertrophic chondrocytes become calcified and are replaced by bone tissue with osteoblasts and osteoclasts forming the trabecular bone. Illustration adopted from¹⁴.

In the epiphyseal growth plate, five distinct regions can be distinguished. In the first layer, resting chondroblasts serve as a repository for the future bone growth surrounded by a self-secreted ECM rich in type I collagen, hyaluronan, tenascin and fibronectin¹². Cells proliferate at a constant but relatively low rate. After chondroblasts become rounded they are referred to as chondrocytes that reside in

the second layer. The cells start to secrete a type II collagen rich ECM with a smaller amount of type IX and XI collagen under the control of the transcription factor *Sox9*, a key regulator of chondrogenesis¹¹⁻¹³. Together with the large proteoglycan aggrecan and glycosaminoglycans, the ECM acts as a framework for chondrocytes that reside in it by secreting growth factors, hormones and remodelling enzymes throughout the whole chondrogenic process (Figure 3A, C). Chondrocytes start to increase their proliferative rate, thus causing a flattened appearance and a columnar formation. After withdrawal of the cell cycle, cells initiate the process of hypertrophic differentiation in the third layer of the epiphyseal plate. This step includes the maturation of chondrocytes concomitantly with an enlargement of the cell size and the differentiation into hypertrophic chondrocytes. In comparison to resting and proliferating chondrocytes, the matrix composition in the hypertrophic zone of the growth plate switches to a higher amount of type X collagen, while type II collagen expression is diminished. Furthermore, hypertrophic chondrocytes start to secrete high levels of proangiogenic factors (e. g. VEGFs), runt-related transcription factor 2 (*Runx2*), Osterix (*Osx*), alkaline phosphatase (*Alp*) and matrix metalloproteinase 13 (*Mmp13*)^{15,16}. The changes in matrix composition and expression of these transcription factors and proteins, is a prerequisite for the fourth layer of terminal differentiation where hypertrophic chondrocytes undergo apoptosis, while invading blood vessels from the surrounding bone collar deliver osteoblasts and osteoclasts. This results in the calcification of the cartilage together with cartilage matrix degradation in the fifth layer where the primary spongiosa and the medullary cavity are created. Due to this highly controlled mechanism of endochondral bone formation, especially by gradients of *Sox9* and *Runx2* as well as *PTHrP* and *Ihh*^{15,16}, long bones grow in length over time, while the bone collar forms cortical bone mainly through intramembranous bone formation, and osteoblast at the chondro-osseous junction form the primary spongiosa, giving rise to trabecular bone.

The generation of a secondary ossification centre (SOC) between the articular cartilage and the epiphyseal growth plate appears during early postnatal development and separates both cartilaginous zones from each other. Cartilage canals invade from the surrounding perichondrium into the epiphysis and are thought to be the driving force of SOC development¹⁷. These canals contain

vascular and perivascular cells as well as resorbing mononuclear and multinuclear macrophages that disintegrate the epiphyseal chondrocytes¹⁸. These canals migrate into the middle portion of the epiphysis and prompt resting chondrocytes to undergo maturation. This event is similar to the chondrogenic differentiation process observable for the primary ossification centre (Figure 3B). The chondrocytes differentiate, hypertrophy, enter the apoptotic cycle and existing blood vessels guide osteoblasts and osteoclasts migration into the calcified cartilage template. Four distinct zones can be distinguished: The superficial zone that consists of up to two layers of flattened chondrocytes, the intermediate zone with round-shaped chondrocytes, the radial zone which shares high similarities to the hypertrophic zone of the growth plate and the zone of calcified cartilage. The speciality of the articular cartilage is its maintenance of appearance over life, while the potency of self-renewal is largely absent¹⁹.

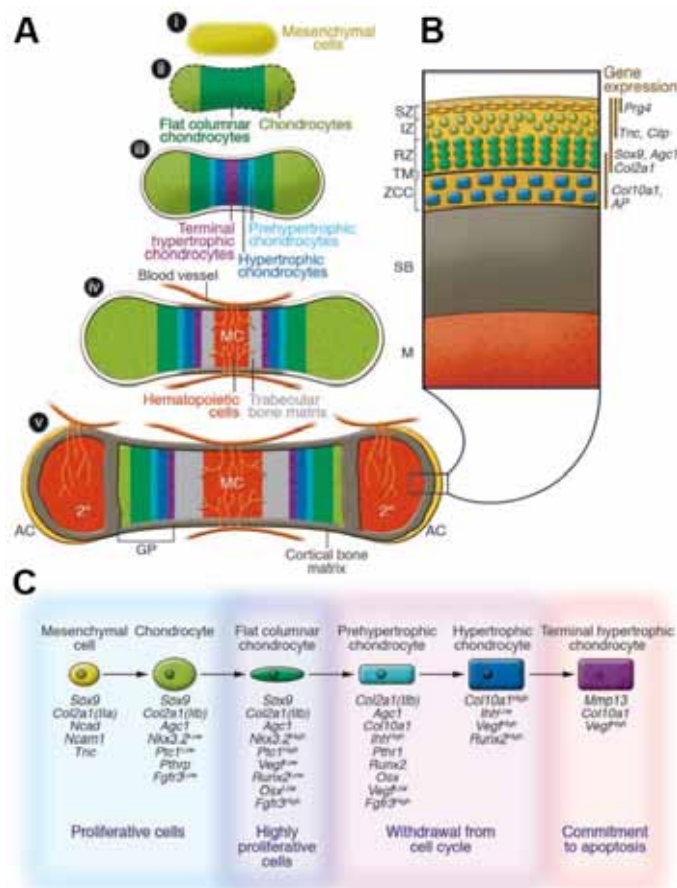


Figure 3. Cellular events and molecular markers of chondrogenesis.

A Model of endochondral bone development beginning with mesenchymal condensation (i); chondrocyte differentiation (ii), chondrocyte maturation and hypertrophy (iii), separation of cartilage growth regions, vascular invasion, and initiation of both cortical and trabecular bone (iv); generation of the secondary ossification centre (V). MC = marrow cavity; 2° = secondary ossification centre. **B** Cellular zones in the postnatal articular cartilage (AC). SZ = superficial zone; IZ = intermediate zone; RZ = radial zone; TM = tidal mark; ZCC = zone of calcified cartilage. **C** Model outlining the stages of chondrogenesis with its characteristic genes expressed. Illustration adopted from²⁰.

2.1.4 Bone cells

Four cell types constitute the bone: Osteoblasts, osteocytes and bone lining cells responsible for bone formation and bone resorbing osteoclasts.

Osteoblasts, osteocytes and bone lining cells originate from mesenchymal stem cells that are also capable to differentiate into chondrocytes, adipocytes, myocytes and stromal cells^{12,21} (Figure 4).

Differentiated preosteoblasts mature while migrating to the endosteal cortical surface and trabecular bone respectively. Once laid down, they secrete osteoid, a composition of approximately 90% type I collagen and a series of non-collagenous proteins²¹. An important non-collagenous protein is tissue-nonspecific alkaline phosphatase (TNAP) that initiates and regulates the mineralization process of osteoid to compact bone²².

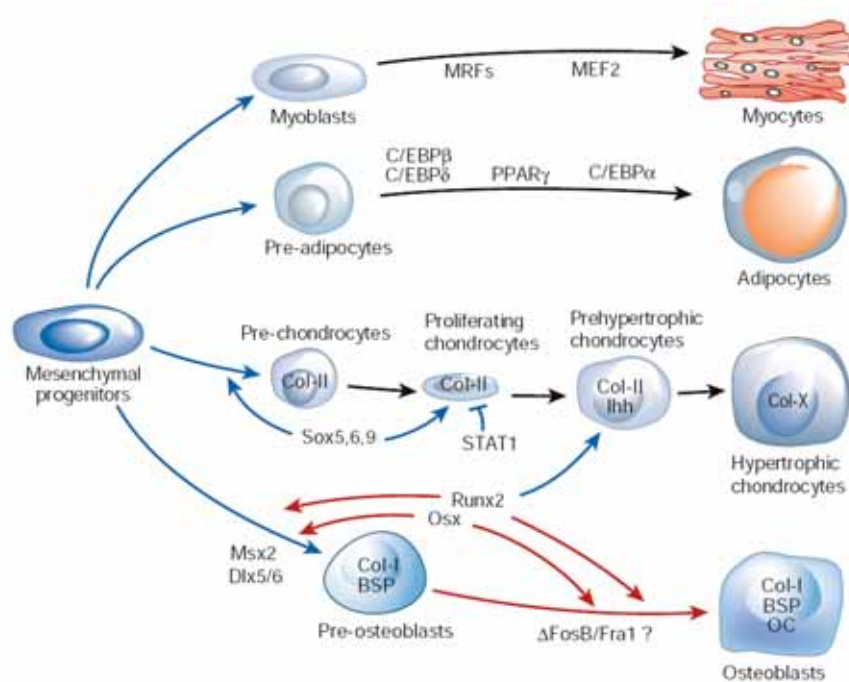


Figure 4. Differentiation of mesenchymal progenitor cells.

Mesenchymal cells can differentiate into the myogenic, adipogenic, chondrogenic or osteogenic lineage. Osteoblasts differentiate from mesenchymal progenitor cells that also give rise to myocytes, under the control of MRFs and *MEF2*, to adipocytes under the control of *C/EBP* α , β and δ and *PPAR* γ , and to chondrocytes under the control of *Sox5*, *-6* and *-9* and *STAT1*. *Runx2* is essential for osteoblast differentiation and is also involved in chondrocyte maturation. *Osterix* (*Osx*) acts downstream of *Runx2* by inducing osteoblasts maturation and subsequent expression of osteoblast markers, including osteocalcin. Abbreviations: MRFs, myogenic regulatory factors (including MyoD, myogenin, myogenic factor 5 and myogenic regulatory factor 4); *MEF2*, myocyte-enhancer factor 2; *C/EBP*, CCAAT-enhancer-binding protein; *PPAR* γ , peroxisome proliferator-activated receptor gamma; *STAT1*, signal transducers and activators of transcription-1; *Runx2*, runt-related transcription factor 2; *Col-I/II/X*, type I/II/X collagen; *Ihh*, Indian hedgehog; *BSP*, bone sialoprotein; *OC*, osteocalcin. Illustration adopted from²¹.

Due to osteoid secretion, osteoblasts at the bone surface get surrounded by their own matrix and terminally differentiate into osteocytes²³. These cells are characterised by a much lower bone formation activity than osteoblasts but are the most abundant cells (over 90%) of adult bone cells. They reside in the mineralized bone matrix in so called lacunae. Osteocytes are interconnected with each other by osteocyte processes similar to dendritic structures which run inside the canaliculi²⁴. Beside their function in matrix maintenance and the control of calcium homeostasis²⁵, osteocytes also regulate the response of stress and mechanical load by mechanosensing and mechanotransduction^{24,26}. This attributes osteocytes to direct bone formation and resorption upon mechanical signals^{27,28} by a proposed osteolytic fluid in the canaliculi network of bone²⁹. Key regulatory elements are the *Wnt/β-catenin* pathway that directs bone formation and its antagonist sclerostin (SOST)³⁰⁻³².

On inactive (non-remodelling) sites bone lining cells – the third cell type – cover the bone surface. Generally thought to be inactive osteoblasts, they separate bone and interstitial fluids and function as a barrier for ions³³. They are in direct contact with osteocytes and control bone remodelling. Additionally it was shown, that bone lining cells enter the resorption pits (Howship's lacunae) after osteoclast detachment, subsequently cleaning the bottom from bone matrix leftovers. This process is crucial for the deposition of newly formed osteoid in the resorption pits³⁴.

The fourth bone cell type is the bone resorbing multinucleated osteoclast. Osteoclasts originate from haematopoietic stem cells that give rise to all kinds of monocytes and macrophages as well as to blood cells²¹. Crucial factors for differentiation into osteoclast precursors out of the monocyte/macrophage lineage are transcription factors of the MITF family³⁵, *PU.1*³⁶ and *c-FOS*³⁷ as well as the cytokine macrophage stimulating factor (*M-CSF*)³⁸ (Figure 5). The commitment and polarisation (multinucleation) is driven by $\text{Nf}\kappa\text{B}$ ³⁹, the cytokine RANKL (secreted by osteoblasts and stromal and activated T-cells)^{40,41}, *c-Src*⁴² and $\alpha_v\beta_3$ -integrins⁴³ respectively. The polarized osteoclast subsequently attaches to the bone surface and develops a leak proof sealing zone with a ruffled border oriented to the bone surface. This specialised infolded membrane serves as a microenvironment that resorbs bone matrix resulting in resorption pits (Howships's lacunae). Mineralized matrix ablation is achieved by an acidic environment

($H^+ATPase$ ⁴⁴, $Clcn7$ ⁴⁵), while the organic elements are degraded by $TRAP$ ⁴⁶ and Cathepsin K⁴⁷ (Figure 5).

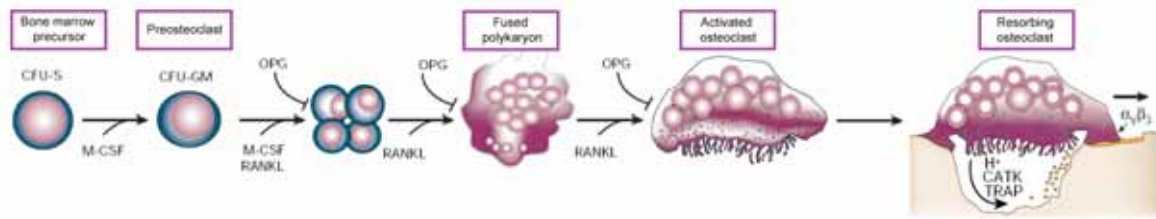


Figure 5. Osteoclast differentiation.

Developmental scheme of haematopoietic precursor cell differentiation into resorbing mature osteoclasts. *M-CSF* and *RANKL* are essential regulators for osteoclastogenesis during lineage allocation and maturation. *OPG*, the decoy receptor of *RANKL*, can bind and neutralize *RANKL*, thus inhibiting both osteoclastogenesis and activation of mature osteoclasts. After activation osteoclasts attach to bone with the help of $\alpha_v\beta_3$ -integrins and resorb bone matrix by secreting H^+ proton vesicles and matrix degrading enzymes (*TRAP*, *CATK*). Illustration adopted from³⁸

2.1.5 Bone modelling and homeostasis

After the initial ossification during embryogenesis, osteoblasts and osteoclasts start to rearrange the bone by modelling and remodelling. Modelling is referred to the shaping of bone, whereas remodelling is attributed to bone turnover⁴⁸. The rate of bone turnover approaches 100% in the first year of life and declines to about 10% in late childhood staying more or less constant throughout life⁴⁸. During childhood bone formation exceeds bone resorption resulting in new net bone formation until the achievement of peak bone mass. Afterwards, the process of bone maintenance is subjected only to bone remodelling or homeostasis, where ideally, bone resorption is equally balanced by bone formation⁴⁹. This continuous cycle is initiated by preosteoclasts that become activated and resorb bone. After osteoclast detachment, osteoblasts migrate to the resorption pits and replenish them with bone matrix (Figure 6A). This process is highly coordinated by anabolic and catabolic factors (Figure 6B) that steer homeostasis in bone⁵⁰. Two examples would be the release of calcium, requiring bone resorption, and the preservation of mechanical strength, achieved by bone formation. While some of the factors regulating homeostasis are of external origin (i.e. hormones or mechanical loading/ immobilisation) the crosstalk between osteoblasts and osteoclasts has emerged as an important feature for tackling this process in case of diseases. The *OPG/RANKL/RANK* system is one example for the reciprocal control of bone cells. Osteoclasts express *RANK*, a transmembrane receptor binding its ligand *RANKL*,

expressed by osteoblasts, stromal and T-cells^{51,52}. This interaction is necessary for the final differentiation step of osteoclasts to activate its resorptive ability. OPG is also expressed by osteoblasts and stromal cells and serves as the decoy receptor of RANKL, thus preventing osteoclasts recruitment⁵³. Hence, osteoblasts can therefore control osteoclasts resorption rate by expressing OPG and RANKL in a ratio dependent manner^{54,55}.

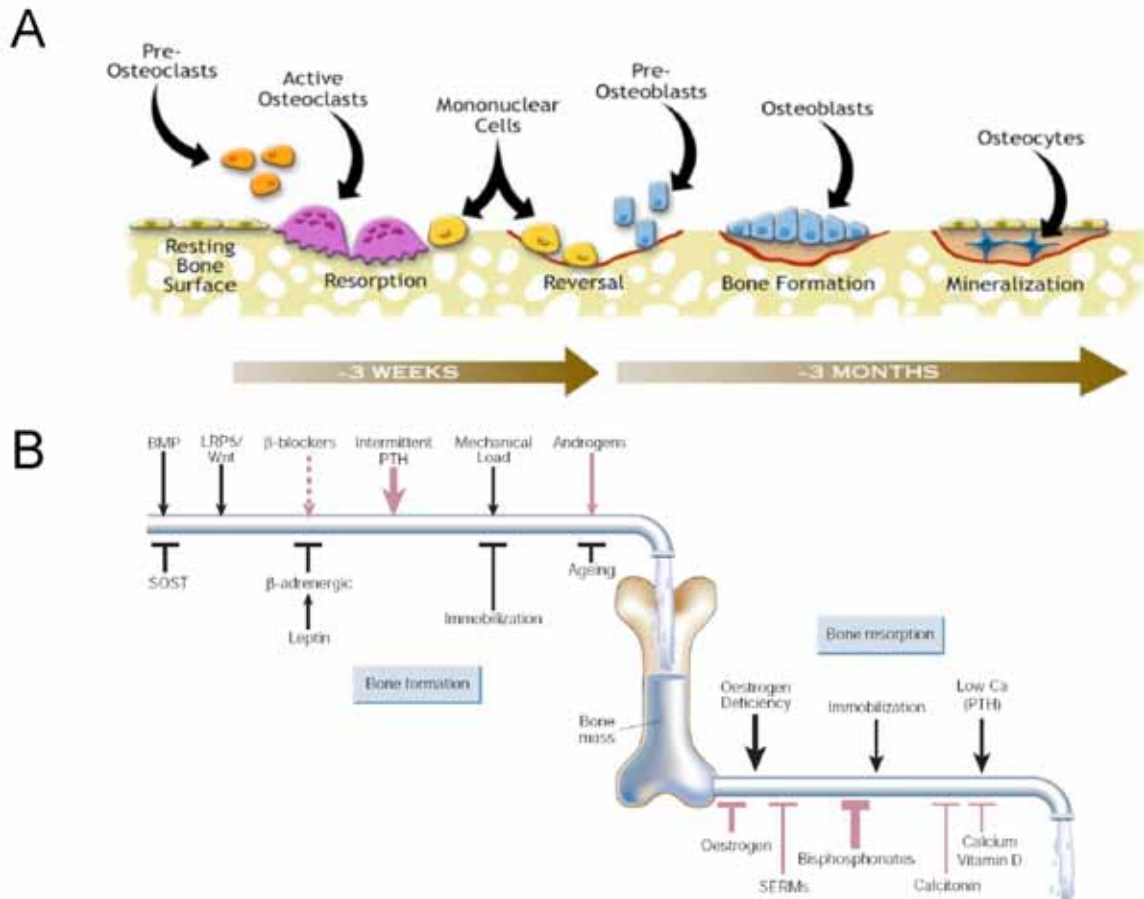


Figure 6. Bone remodelling and achievement of homeostasis.

A Process of bone remodelling is initiated by preosteoclasts attaching to bone. Active osteoclasts resorb the bone matrix. Subsequently after resorption, the Howship's lacunae are filled up by active bone formation of osteoblast. Finally, mineralization and differentiation into osteocytes complete the process. Illustration adopted from <http://ns.umich.edu/Releases/2005/Feb05/bone.html>. **B** Determinants of skeletal homeostasis and bone mass. Physiological (black) and pharmacological (pale pink) stimulators and inhibitors are shown. Thickness of arrows indicates their relative impact. Illustration adopted from⁵⁰

2.1.6 Bone diseases

Given the vast amount of genetic pathways and mechanisms developing, structuring and maintaining bone tissue, various skeletal disorders can emerge. These are noticeable by radiographic assessments, morphological alterations,

biochemical, metabolic or hormonal anomalies. For the classification of the diseases, Superti-Furga *et al.*⁵⁶ proposed to divide the disorders according to the structure and function of the causative genes and proteins, while Fuchs *et al.*⁵⁷ classified bone diseases in more generalized categories, namely (1) patterning, (2) metabolism and growth, (3) modelling and remodelling and (4) aging and immune system defects (Figure 7).

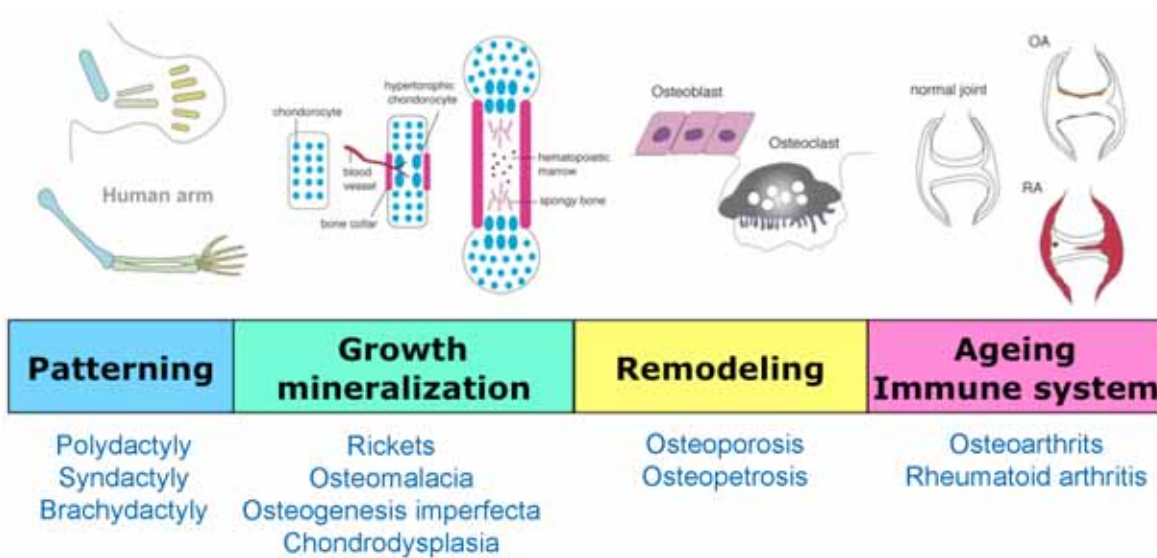


Figure 7. Classification of bone diseases.

Skeletal alterations and diseases are grouped into patterning, growth and mineralization, remodelling, and ageing and the immune system. At the bottom, examples for disorders in each category are shown. Illustration adopted from⁵⁷

(1) Patterning defects comprise malformations of the skeletal framework during embryogenesis. Examples for such diseases are polydactyly (supernumerary digits), syndactyly (fused digits), brachydactyly (shortened digits) or malformations of the vertebral column¹⁶. (2) Defects in bone metabolism and growth mostly result in growth retardation, bending or fractures of bone. Causative for these diseases are either a softening of bone tissue due to defective mineralisation processes, e.g. rickets (childhood)⁵⁸ and osteomalacia (adulthood)⁵⁹ or a hardening of the tissue caused by an increased ratio between mineralisation and non-mineralised elements in bone. Further examples for metabolic bone diseases are Osteogenesis imperfecta⁶⁰ or several forms of chondrodysplasias¹². (3) An imbalanced modelling or remodelling process leads to alterations in bone mass and bone mineral density (BMD) respectively. With the help of the T-score, a scaling unit comparing BMDs from patients with altered density with that of healthy adult individuals several, sub-classifications can be obtained. According to the

WHO, people with a T-score between -1.0 and -2.5 suffer from osteopenia, a relatively mild reduction in bone density, whereas values below -2.5 classify osteoporosis with moderate to severe reduction in BMD. Both osteopenia and osteoporosis are either caused by a decreased bone formation or increased bone resorption rate respectively. Pathophysiological increased T-scores are referred to as osteopetrosis, which is accompanied by defects in the resorption process. A common feature of all three diseases is an increase in fracture risk. (4) Osteoarthritis (OA) and rheumatoid arthritis (RA) are well-known diseases of the last group of skeletal disorders. While OA⁶¹ is characterised by a progressive erosion of the articular cartilage and subchondral bone, leading to destruction of the synovial joints. It appears mainly in the hip and knee, causing joint pain, tenderness, stiffness and inflammation amongst others. RA is, contrary to OA, a chronic and systemic inflammatory disorder, affecting many organs but primarily targets multiple joints⁶². Synovial membrane inflammation causes destruction of the articular surface of bones, bone erosions and joint deformities (e.g. ankylosis) that mostly result in a complete loss of joint function. For the purpose of this thesis, three diseases are explained in more detail.

2.1.6.1 Osteoarthritis and ankylosis

Osteoarthritis (OA) is the most common articular cartilage disorder in man and affects almost 85% of the population by the age of 75⁶¹. The German wording "Osteoarthritis" always implies inflammatory symptoms whereas the English term "osteoarthritis" describes the disease also as a non-inflammatory degenerative joint disease. It is characterised by a softening of the tissue, a decrease in proteoglycan content and an overall loss of matrix tensile strength and stiffness in the articular cartilage. This causes hypertrophy of bone at the margins, changes in the synovial membrane, leading to a progressive loss of joint function. Generally, OA can be classified into primary and secondary OA. Primary OA refers to the age-related cartilage degeneration affecting mainly older people. Secondary OA is caused by inactivity or injury of the joint as well as by obesity or by abnormalities in the joint structure at birth developing earlier in life⁶³. Recent studies also discovered several chromosomal loci associated with OA susceptibility of different joints⁶⁴⁻⁶⁸.

In conjunction with secondary OA, ankylosis is a common skeletal disorder characterised by immobility of joints. Ankylosis can be caused by injury, inflammation of the tendinous or muscular structures, altered bone structure or composition (e.g. caused by OA) or the complete fusion of the joint bones as reported for several genes^{69,70}.

2.1.6.2 Osteogenesis imperfecta (OI)

Osteogenesis imperfecta (OI) is a group of inherited connective tissue disorders, characterized by brittle bones, fractures and osteoporosis⁶⁰. Beside the skeletal manifestations of OI, corneal alterations with blue/white sclera, joint laxity, hearing loss and Dentinogenesis imperfecta (brittle teeth) are also attributed to the disease⁷¹⁻⁷⁴. The overall incidence of OI is approximately one in 10,000 and is mainly caused by autosomal dominant mutations in the two genes coding for type I collagen (*COL1A1/COL1A2*) the most prominent protein in the extracellular matrix of connective tissues⁷⁵. Recent studies reported that mutations in genes involved in collagens posttranslational modifications and fibrillation (*CRTAP*, *LEPRE1*, *PP1B*) accounting for autosomal recessive inheritance⁷⁶⁻⁷⁸. Depending on the clinical symptoms and the grade of severity, OI was classified into 4 subtypes according to Sillence *et al.*⁷⁴, ranging from mild to lethal forms. As recessive OI has emerged, this classification was further expanded and is now classified into nine distinct types (Table 1). Severity – based on clinical symptoms – increases in the order type I < types IV, V, VI, VII < types VIII, IX < type III < type II⁷⁵.

This classification can be partially related to the type of mutation in either genes of type I collagen. While N-terminal mutations and complete null-alleles lead to mild symptoms, C-terminal and core peptide alterations cause severe to lethal types. This can be explained by the fact, that the protein assembly of heterotrimeric type I collagen protein (consisting of two $\alpha 1$ and one $\alpha 2$ procollagen strains) starts at the C-terminal end of the propeptides. Thus, mutations at the C-terminal ends provoke early misfolding of the protein and its loss of function. The core peptide accounting for the mature collagen peptide consists of repetitive amino acid sequences of the amino acids glycine, proline and hydroxproline, where glycine is the most important residue located at every third position, creating a (Gly-X-Y)_n triplet (Figure 8). Substitutions of glycine residues dramatically change the triple helical

structure of mature collagen. This results in a reduced potential to provide tensile strength and to serve as a framework for interaction partners as well as for mineral deposition in bone in the ECM. As fibrillogenesis of type I collagen is crucial for its subsequent function in the organism, recessive types of OI also result in severe to lethal forms due to the lack of posttranslational modifications needed for proper protein folding and integration into the ECM.

Table 1. Current classification of osteogenesis imperfecta.

Adapted from ^{75,79}. AD (autosomal dominant), AR (autosomal recessive), * mainly premature stop codons resulting in null alleles, # associated with null mutations in *CRTAP* and *P3HI*.

Type	Clinical severity	Associated mutations	Inheritance
I	mild	<i>COL1A1</i> *	AD
II	perinatal lethal	<i>COL1A1/COL1A2</i>	AD (rarely AR#)
III	severe to lethal	<i>COL1A1/COL1A2</i>	AD
IV	mild to moderate	<i>COL1A1/COL1A2</i>	AD
V	mild to moderate	unknown	AD
VI	mild to moderate	unknown	AR
VII	severe to lethal	<i>CRTAP</i>	AR
VIII	severe to lethal	<i>LEPRE1</i>	AR
IX	moderate to severe	<i>PPIB</i>	AR

To present a general overview among the different mutations causing OI, the Leiden University Medical Centre (<https://oi.gene.le.ac.uk/home.php>) provides a database gathering all reported cases of OI and Ehlers-Danlos-Syndrom (another disease associated with collagen mutations). Currently, 1905 entries of which 1143 are unique variants mainly associated to the different types of OI are listed. Although skeletal findings are the most prominent feature in OI, the main causes of death especially in types III and IV OI have been linked to pulmonary and cardiac complications. Pulmonary compromise makes up 76.3% (29 of 38) of all deaths in type III OI and 44.9% in types I and IV OI. Lethality is caused by loss of lung capacity, acute and chronic respiratory failure, pneumonia, bronchitis and others⁸⁰. Although type I collagen makes up 80% of the lungs connective tissue, these disorders are generally thought to be secondary effects due to scoliosis and rib fractures^{60,80,81}. While one case report raised the possibility of an intrinsic defect as spine curvature was relatively small⁸¹, two further case reports even suggested abnormal collagen to be directly causal for lung hypoplasia^{82,83}.

Cardiovascular incidence also makes up a large percentage of death in OI (25% in type I, III, IV OI)⁸⁰. Pathological alterations like aortic root dilatation, atrial septal defects, valvular regurgitations as well as different types of haemorrhages have been described previously, but are exclusively attributed to skeletal manifestations like kyphoscoliosis⁸⁰.

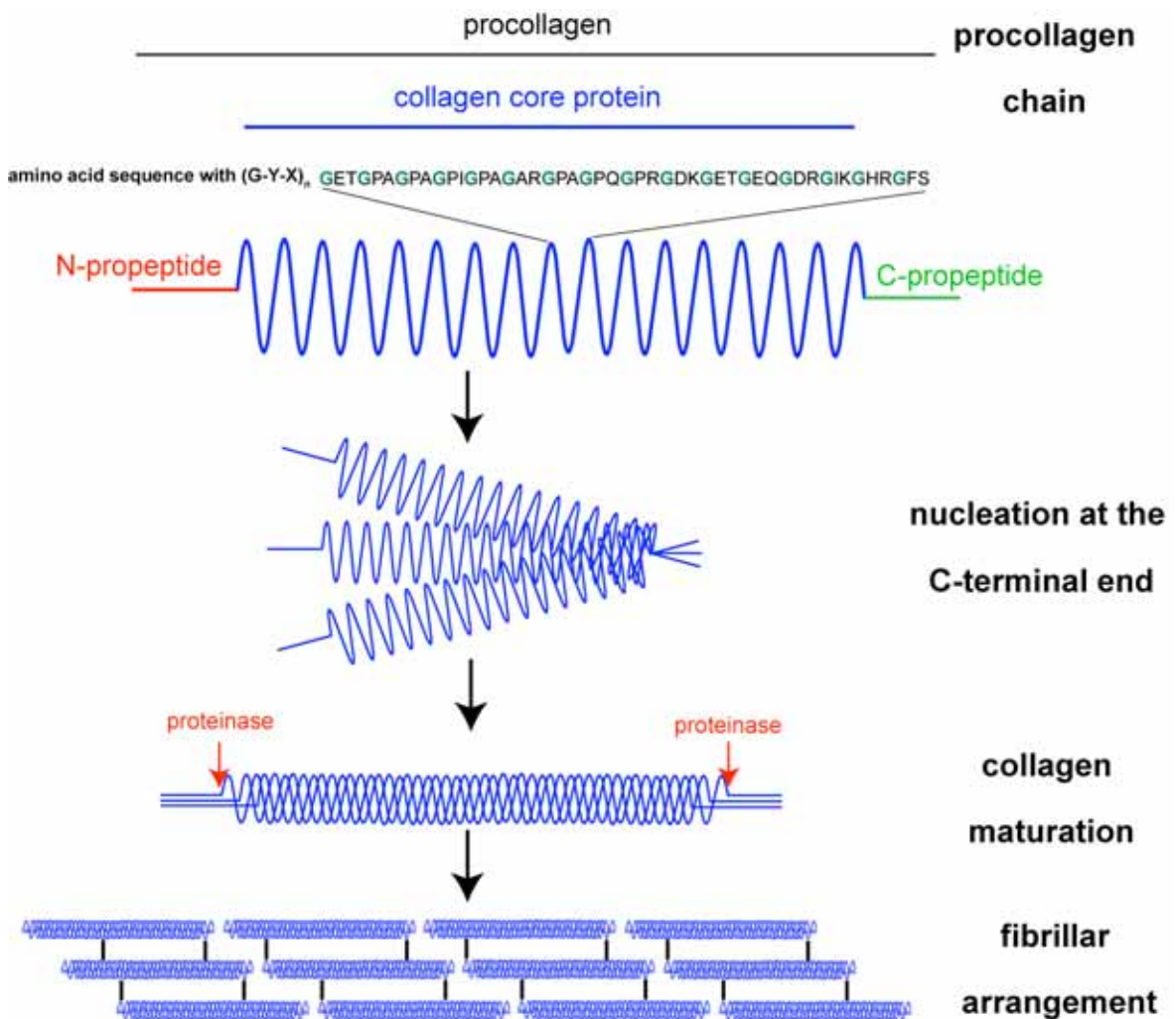


Figure 8. Schematic representation of collagen processing.

Procollagen chains consist of a core protein with N- and C-terminal propeptides. In the core protein a repetitive motif of (G-Y-X)_n is evident and crucial for heterotrimerisation and fibrillogenesis. Heterotrimerisation is initiated from the C-terminal end of the chains. Subsequently, maturation is performed by proteolytic cleavage of the propeptides and the fibrillation of mature collagen proteins.

2.2 Mouse models for human (bone) diseases

Model organisms are widely used to study human diseases and to gain novel insight into the molecular mechanisms of the phenotypical hallmarks⁵⁷. Despite the extensive studies of *D. melanogaster*, *C.elegans* and *D. rerio* in the field of

developmental disorders, *M. musculus* is the favoured model organism to study complex human diseases⁸⁴. Besides the short generation time and a large litter size, the mouse genome has been completely sequenced and shares approximately 95% homology to the human genome. Being nearly equivalent to the human genome size (3×10^9 bp), additionally large segments of synteny with similar intergenic distances could be described, thus providing an excellent basis for the characterisation of human diseases⁸⁵.

Large-scale mouse mutagenesis screens have been conducted to increase the number of mouse models for human diseases^{86,87}. While reverse genetic approaches generate transgenic or knockout alleles to study the functional role of genes, forward genetic approaches like ENU mutagenesis generate more nature-like mutations. In the Munich ENU mutagenesis screen, various mouse mutants have been isolated as models for human diseases, including mice with skeletal alterations⁸⁶. Among these, models for polydactyly, syndactyly, OI, achondrodysplasia, osteoporosis, RA and OA have been established (unpublished data).

2.2.1 *Ali34*

The *Ali34* (abnormal limb 34) autosomal dominant mouse line was isolated from the Munich ENU mutagenesis screen, exhibiting shorter limbs with stiffened knee joints. General morphological analysis of the mutants revealed indications for early-onset OA, chondrodysplasia and the formation of tibial osteophytes. Analysis of skeletal stainings exhibited shortening especially of the tibial bones with a stronger pronounced bending between tibia and fibula in 8-weeks old mice. Furthermore, the epiphyseal plate revealed a disorganization of the epiphyseal plate where resting chondrocytes seemed to be absent. Erosion of the tibial and femoral articular cartilage with an absent transitional zone was validated by histological methods. Linkage analysis of the *Ali34* locus revealed a 3 Mbp region on chromosome 6. Subsequent sequencing of candidate genes identified a point mutation in exon 35 of *Plxnd1* (T5793G) coding for a stop codon instead of a tyrosin (Y1878*) resulting in a 48 amino acid shortened protein. During embryogenesis, vascular mispatterning observable for *Plxnd1*^{*Ali34/Ali34*} embryos at 12.5 dpc were linked to vertebral malformation during later embryonic

development. Additionally, exencephaly was recorded for homozygous animals. (unpublished data obtained during my diploma thesis and the PhD thesis of Dr. Thomas Lisse). In contrast to recently described *Plxnd1* knockouts⁸⁸⁻⁹⁰, the *Ali34* mutation only shortens the protein by 48 amino acids, thus affecting only a small part of the cytoplasmic domain of the protein, while the extracellular portion might be still intact.

2.2.2 *Aga2*

A new mouse model for OI termed *Aga2* (abnormal gait 2) has recently been identified in the Munich ENU mutagenesis screen⁹¹. Positional cloning revealed a T→A transversion within intron 50 of *Col1a1*, generating a novel cryptic 3' splice acceptor site. The resulting alternative splicing possesses a 16bp elongated transcript with a frameshift of the endogenous stop, predicting 89 new amino acids beyond the original termination position leading to structural alterations of the mutated type I collagen protein. As *Col1a1* mutations generally result in dominant negative mutation, *Col1a1^{Aga2/Aga2}* animals are embryonic lethal at 9.5 dpc. *Col1a1^{Aga2/+}* animals display hallmarks of OI symptoms including multiple fractures in long bones, pelvis and the rib cage, scoliosis, reduced body size and an overall decrease in bone mass and density. Due to a high diversity in phenotypical severity ranging from moderate to perinatal lethal, *Aga2/+* mice reflect types II and III OI. Based on the severity of the disease, heterozygous animals were classified into two subgroups. Mildly affected *Aga2/+* mice possessing a moderate phenotype and survive to adulthood will be referred to as *Aga2/+^{mild}*. In contrast, *Aga2/+* animals that succumb to perinatal lethality within the first 2 weeks after birth, thus displaying a more severe aetiopathology, are referred to as *Aga2/+^{severe}*. Additionally, a new pathological mechanism involving ER stress related apoptosis in osteoblasts has been recently identified⁹¹. In contrast, the cause of perinatal lethality in *Aga2/+^{severe}* animals remains to be elucidated.

2.3 Systemic analysis of disease models

2.3.1 Systemic analysis

With the sequencing of the human and mouse genomes, the generation of murine disease models has emerged rapidly. Established mutant lines are analysed on the basis of their human counterparts in specific research fields. These analyses can nowadays provide more insight into the molecular mechanisms of several human diseases. However, the pleiotropic nature of gene functions raises the possibilities of mutational effects in other organs that are either not identified or simply neglected due to minor interest or expertise. In order to tease out the complete potential of an established murine disease model, a more generalized or systemic view has been recently proposed⁹². In the future, it should not be sufficient to only generate and analyse nature like or humanised murine disease models; it will also be indispensable to apply standardised all-embracing techniques to phenotype the mouse as an interconnecting whole system. To overcome and also model the impact of exogenous factors, with which humans are faced with every day, a consistent next step of mouse phenotyping will be the exposure of such factors.

2.3.2 The German Mouse Clinic

The German Mouse Clinic (GMC) has been established as the first facility combining the expertise of 14 different research fields to cover every organ system in mouse (Figure 9). The feasibility to measure over 320 parameters in mouse lines during an 8 weeks period under standardised conditions at one place rapidly advances the identification of novel phenotypes that are primarily undiscovered⁹³. If new phenotypes are found in distinct screens at the GMC, secondary and tertiary tests can be performed to further characterise the mutant line. In the dysmorphology screen analyses focus on bone and cartilage disorders^{94,95}. Primary screening includes macroscopical anatomical inspection as well as X-ray analysis and DXA measurements combined with a “Clickbox”-test to identify possible hearing defects. If distinct phenotypes are found during the primary screening, mutants can be analysed in secondary and tertiary tests in more detail.

Such tests include μ CT and pQCT analysis, three-point bending tests as well as analysis of different biochemical markers of bone remodelling (e.g. OC, ALP, TRAP, DPD, PINP, RANKL), fracture/stress parameters and skeletal stainings. Additionally, a comprehensive osteoblasts cell culture assay can provide insight whether a primary or a secondary (systemic) effect is causative for an observed bone alteration in mutant mouse lines (unpublished data).

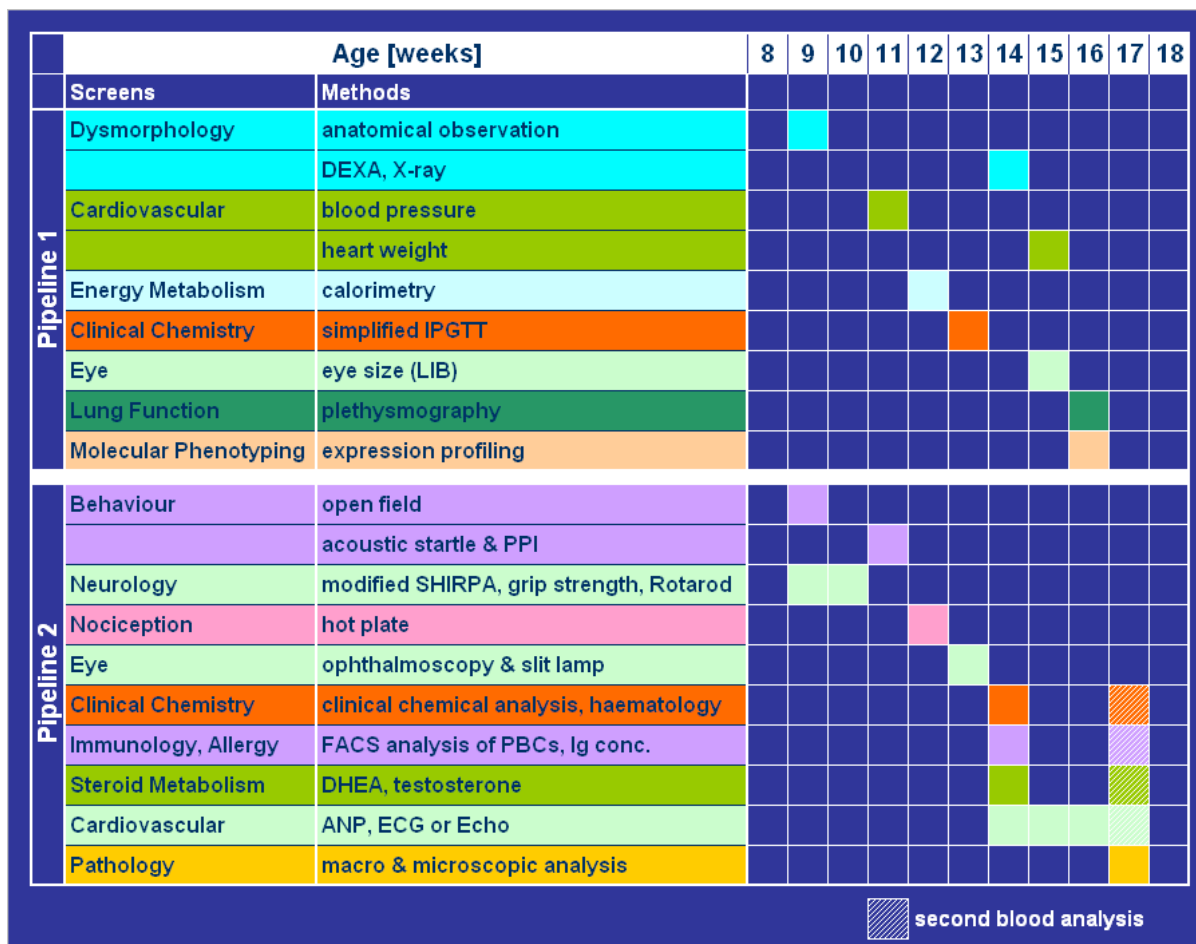


Figure 9. GMC Timetable.

Image adopted from the German Mouse Clinic Presentations

2.3.3 Systemic effects on/of bone alterations

Along with the multifaceted nature of bone as a result of the interplay between the bone cells and its general functions (mechanical, haematopoietic, metabolic) it is not surprising that alterations in bone metabolism can have an impact on other organs and vice versa, leading to multifactorial diseases.

To generally classify these factors with respect to bone, three main groups may be differed:

- (1) Intrinsic effects on bone and its metabolism affecting other organ systems.

(2) Extrinsic effects regulating bone metabolism

(3) Pleiotropic effects of genes do not exclusively act on bone but rather directly on other organ systems

(1) Skeletal mispatterning can cause defects in organs that are typically protected by bone. Kyphoscoliosis (abnormal curvature of the spine) can have an impact on breathing capacities, thus leading to an increase in cardiopulmonary distress⁹⁶.

It is also known that the regulatory functions of bone affect whole body homeostasis. Beside the regulation of calcium homeostasis, recent studies showed that bone can also act as an endocrine organ. Through its release of the hormone osteocalcin, bone controls glucose metabolism to an extent not expected before^{4,97-99}.

(2) Beside environmental factors, unlimited in their variety, individual systems or even hormones can trigger changes in bone. Blood vessel supply is one of the major requirements of the skeleton¹⁰⁰ as defects in vascularisation results in malnutrition of the bone. Mice deficient for different Vegfa isoforms – a key factor for the developing vasculature – showed impaired bone formation and maintenance^{101,102}. Furthermore, defects in vascular patterning also results in structural bone malformation^{101,102}.

Endocrinological studies substantiate that hormones have a major impact on bone. For example decreasing estrogen levels in postmenopausal women result in a higher susceptibility to suffer from osteoporosis¹⁰³. Additionally the hormone leptin was shown to control bone mass through serotonin mediated signalling¹⁰⁴.

(3) The pleiotropic effects of genes in different organ systems are also a major factor of multifactorial diseases. Gene variants leading to an impaired or even loss of protein function can have intrinsic effects in all tissues where the genes is expressed and should be taken into account for the characterisation of its function in a systemic way.

2.4 Thesis outline

Two ENU-induced mutant mouse lines (*Ali34*, *Aga2*) both with distinct bone dysmorphologies were analysed systemically, to further broaden the understanding of the underlying mutations not only in bone but also in other organ systems and to possibly identify novel pathomechanisms leading to multifactorial diseases.

Ali34, a potential new model for chondrodysplasia, osteoarthritis and ectopic bone formation harbours a mutation in *Plxnd1*. As *Plxnd1* expression was reported to be crucial for angiogenic pathfinding, and the gene was also reported to be expressed not exclusively in endothelial cells, first line phenotyping in the GMC and a continuative in depth analysis of the bone phenotype was conducted to reveal new phenotypical hallmarks in *Ali34*. Additionally, the mutational effect on the protein level is further assessed to delineate the molecular mechanism that controls proper pathfinding cues.

The *Aga2* mouse line, a novel murine model for human OI harbouring a *Col1a1* mutation was recently characterised by means of its bone phenotypes. Interestingly, two severity grades could be determined that display moderate to lethal types of OI. In humans, severe forms of OI are associated with increased mortality that can be traced back to cardiac or pulmonary complications that are considered secondary to the skeletal manifestation. As *Aga2/+^{mild}* mice displayed alterations in the cardiovascular as well as the pulmonary screen of the GMC, further analysis were intended to investigate a potential intrinsic effect of the underlying *Col1a1* mutation in hearts and lungs of perinatal lethal *Aga2/+* animals.

3. Materials and methods

3.1 Materials

3.1.1 Chemicals

If not specifically stated in the text, all chemicals were purchased from Sigma Aldrich, Merck, Invitrogen, AppliChem, Biozym, Qiagen and Roche.

3.1.2 Standard buffers

1M Tris-HCl

121.1 g Trizma Base
dissolved in ddH₂O and adjusted to pH 7.0, 7.5 and 8.0 with HCl
ddH₂O was added to receive 1 l

PBS (10x)

80 g	NaCl
2 g	KCl
17.8 g	Na ₂ HPO ₄ *2H ₂ O
2.72 g	KH ₂ PO ₄

dissolved in ddH₂O and adjusted to pH 7.3
ddH₂O was added to receive 1 l

PBST

100 ml	10x PBS
500 µl	Tween20 (f.c. 0.05%)
900 ml	ddH ₂ O

TBS (10x)

80 g	NaCl
2 g	KCl
30 g	Trizma Base

dissolved in ddH₂O and adjusted to pH 7.4
ddH₂O was added to receive 1 l

TBST

100 ml 10x TBS
500 µl Tween20 (f.c. 0.05%)
900 ml ddH₂O

RIPA buffer

15 ml 5M NaCl
5 ml NP40
25 ml 10% Natriumdeoxycholate
2.5 ml 10% SDS
25 ml 1 M Tris-HCl (pH 8.0)

pH was adjusted to pH 8.0 and added to 500 ml with ddH₂O

0.5 M Tris-HCl buffer (for Western Blot stacking gels)

6.05 g Trizma Base
adjust to pH 6.8
add to 100 ml with ddH₂O
add 0.4 g SDS
store at 4°C

Upper 1.5 M Tris-HCl buffer (for Western Blot resolving gels)

91 g Trizma Base
adjust to pH 8.8
add to 500 ml with ddH₂O
add 2 g SDS
store at 4°C

6x SDS loading buffer

3 ml Glycerol
7 ml Lower Tris buffer
3 mg Bromphenol blue
375 µl β-mercaptoethanol
1 g SDS

5x SDS running buffer

15.1 g Trizma base
 72.0 g Glycine
 5.0 g SDS
 add to 1l with ddH₂O
 store at 4°C

10x Transfer buffer

30.03 g Trizma base
 144.1 g Glycine
 add to 1l with ddH₂O
 store at 4°C

1x Transfer buffer

100 ml 10x Transfer buffer
 200 ml Methanol
 700 ml ddH₂O

3.1.3 Antibodies

Table 2. Primary antibodies

Primary antibody	Host	Customer	Reference number
α-tubulin	mouse	Abcam	ab7291
β-actin	mouse	Abcam	ab6276
type I collagen	rabbit	Abcam	ab292
PECAM-1	rabbit	Abcam	ab28364
PECAM-1	rat	BD Pharmingen	MCA 1364
Insulin	guinea pig	Abcam	ab7842
Glucagon	rabbit	Invitrogen	18-0064
Laminin	rabbit	Abcam	ab11575
Plxnd1	goat	Abcam	ab28762
His	rabbit	Abcam	ab9108
GFP	rabbit	Invitrogen	A6455
VEGF	rabbit	Abcam	ab46154

Table 3. Secondary antibodies

Secondary antibody	Host	Customer	Reference number
Alexa Fluor [®] anti-goat 488	donkey	Invitrogen	A-11055
Alexa Fluor [®] anti-rabbit 488	donkey	Invitrogen	21206
Alexa Fluor [®] anti-rabbit 594	donkey	Invitrogen	21207
anti-rabbit HRP-conjugated	goat	Invitrogen	656120
Alexa Fluor [®] anti-guinea pig 488	goat	Invitrogen	11073
Alexa Fluor [®] anti-guinea pig 594	goat	Invitrogen	11076
Alexa Fluor [®] anti-rat 488	donkey	Invitrogen	21208
Alexa Fluor [®] anti-mouse 488	donkey	Invitrogen	21202
Alexa Fluor [®] anti-mouse 594	donkey	Invitrogen	21203
Alexa Fluor [®] anti-goat 594	donkey	Invitrogen	11058
anti-goat HRP-conjugated	mouse	Dianova	205-035-108
anti-mouse HRP-conjugated	goat	Dianova	115-035-068

3.1.4 Bacterial strains

Strain	Customer	Reference number
<i>E.coli</i> DH5 α [™] chemically competent cells	Invitrogen	K4520-01
<i>E.coli</i> One Shot [®] TOP10 chemically competent cells	Invitrogen	K4500-01
<i>E.coli</i> ccdB Survival [™] 2 T1 ^R chemically competent cells	Invitrogen	A10460
<i>E.coli</i> 10-beta chemically competent cells	New England Biolabs	C3019H
SW106 electrocompetent cells	kind gift of Ingeborg Klymiuk	

3.1.5 Vectors

pCR [®] II-TOPO [®]	Invitrogen
pCR [®] 4-TOPO [®]	Invitrogen
pCR-XL-TOPO [®]	Invitrogen
pDONR [™] 201	Invitrogen
Vivid Colors [™] pcDNA [™] 6.2/N-EmGFP-DEST	Invitrogen
Gateway [®] pDEST [™] 26 Vector (N-terminal His tag)	Invitrogen
modified pSlo1.1K	Bio&Sell

3.1.6 Cell lines

The cell line L929 initially generated by W.R. Earle, was used from a previously purchased stock. The NIH3T3 fibroblast cell line was a kind gift of Dr. Heiko Lickert.

3.1.7 Inbred mouse strains

The used mouse inbred strains during the studies were *C3HFeB/FeJ* and *C57BL6/J*.

3.2 Methods

3.2.1 Isolation and purification methods

3.2.1.1 DNA isolation

DNA from yolk sacs and tail clips was isolated with the QIAamp[®] DNA purification kit (Qiagen, Germany) according to the manufacturer's manual. Briefly, tissue was digested in 180 μ l ATL-buffer containing 20 μ l Proteinase K at 56°C over night. After inactivation with 200 μ l AL-buffer and incubation at 70°C for 10 minutes, 200 μ l 100% EtOH was added and the lysates were transferred to a QIAGEN binding column. After centrifugation at 13,000 rpm for 1 min, bounded DNA was washed with 500 μ l AW1 and AW2-buffer with subsequent centrifugation for 1 min at 13,000 rpm respectively. To ensure that residual ethanol was removed, spin columns were again centrifuged for 2 minutes at 13,000 rpm. 50 μ l AMPUWA was used to elute DNA by centrifugation at 13,000 rpm for 1 min.

3.2.1.2 RNA isolation

RNA isolation of whole organ tissue was performed with the RNeasy Midi Kit (Qiagen, Germany). Sample preparation differs between the organs. Excised bone and pancreatic tissue was incubated in RNAlater[®] buffer (Qiagen, Germany) at 4°C over night before stored at -80°C. Heart and lung tissue was snap frozen and transferred to -80°C for storage purpose. Isolation was performed following the manufacturer's manual. The RNA was eluted with RNase free water and the concentrations were determined by OD_{260/280} readings with a NanoDrop ND-1000 Spectrophotometer (peqlab, Germany). Samples were stored at -80°C until used for expression profiling or qRT-PCR studies.

RNA extraction of *in vitro* cultivated cells was performed using the RNeasy Mini Kit (Qiagen, Germany). Briefly, cultures were washed in PBS twice. Cells were lysed in 350 μ l RLT buffer substituted with β -mercaptoethanol (10 μ l/ml) and subsequently applied to a QIAshredder spin-column (Qiagen, Germany) and centrifuged for 2 minutes at 13,000 rpm to remove cell compartments. All other steps were carried out as stated in the manufacturer's manual. RNA was eluted in

RNase free water, concentration was measured and samples were stored at -80°C.

3.2.1.3 Protein isolation

Snap frozen tissue was subjected to ice cold RIPA buffer containing cOmplete Mini EDTA-free Protease Inhibitor tablets (Roche, Germany) and homogenized for 1 minute using a Heidolph DIAX 900 homogenizer. Afterwards, samples were centrifuged at 13,000 rpm for 20 minutes at 4°C and subsequently stored at -80°C. *In vitro* cultivated cells were lysed in RIPA buffer containing cOmplete Mini EDTA-free Protease Inhibitor tablets (Roche, Germany) for 15 minutes on ice with gentle shaking. Samples were subsequently stored at -80°C.

3.2.1.4 Plasmid purification

Plasmid isolation was performed using the GenElute™ Plasmid Miniprep Kit (Sigma Aldrich, Germany). Briefly, overnight bacterial cultures were pelleted for 3 minutes at 13,000 rpm. Supernatant was removed and the pellet was resuspended in 200 µl resuspension solution. Subsequently, cells were lysed by adding 200 µl lysis buffer followed by incubation for 5 minutes. 350 µl neutralization buffer was added to the lysate and samples were centrifuged for 15 minutes at 13,000 rpm. The supernatant was applied to a spin-column, centrifuged for 1 minute at 13,000 rpm and washed in washing buffer by centrifugation for another minute at 13,000 rpm. Plasmid-DNA was eluted with 50 µl AMPUWA and the concentration was determined with a NanoDrop ND-1000 Spectrophotometer.

3.2.2 Molecular methods

3.2.2.1 Polymerase chain reaction (PCR)

General PCR was performed with *Taq* DNA polymerase (Qiagen, Germany) in a 25 µl reaction volume as follows:

Component	Final concentration	Volume
Q-Solution (5x)	1x	5.0 μ l
PCR Buffer (10x)	1x	2.5 μ l
dNTPs (10 mM)	200 μ M	0.5 μ l
Forward primer (10 μ M)	0.4 μ M	1.0 μ l
Reverse primer (10 μ M)	0.4 μ M	1.0 μ l
Taq Polymerase (5U/ μ l)	1.5 U/reaction	0.3 μ l
Water		13.7 μ l
DNA (10-100 ng/ μ l)		1.0 μ l
		Σ 25 μl

Thermal cycler conditions were performed on the basis of the manufacturer's protocol

94°C	4 min	} 35 cycles
94°C	30 seconds	
58°C	30 seconds	
72°C	40 seconds	
72°C	7 minutes	
12°C	until end	

PCR programs were adjusted for primer annealing temperature and elongation time.

PCR products were checked on a 2% TAE agarose gel.

3.2.2.2 Sequencing

PCR products were purified using the Agencourt® AMPure® PCR Purification Kit (Agencourt Bioscience Corporation, USA) according to the manual. For the fluorescence labelling of DNA, the BigDye v3.1 mastermix (Applied Biosystems, USA) was used. 1 μ l Primer (forward or reverse) and 2 μ l purified DNA were applied to a new PCR reaction plate and dried by using a speed-vac for 15 min. Afterwards 5 μ l HPLC graded water, 4 μ l 5x Sequencing buffer and 1 μ l BigDye v.3.1 were added to the lyophilised samples.

Thermal cycler condition for „BigDye-PCR“

95°C	1 min	
95°C	5 seconds] 39 cycles
50°C	10 seconds	
60°C	4 min	
12°C	until end	

To purify the products the Agencourt® CleanSEQ® Purification Kit (Agencourt Bioscience Corporation, USA) was used corresponding to the enclosed manual. Sequence detection was performed using the ABI-3730 (Applied Biosystems, Germany). Sequences were analysed using Sequencer 4.6 (Genecodes, USA)

3.2.2.3 Site-directed mutagenesis

Site-directed mutagenesis was performed to generate both the *Ali34* and *Aga2* mutation from the wild-type sequences using the Phusion® Site-Directed Mutagenesis Kit (Finnzymes, Germany) according to the manufacturer’s protocol. To generate the mutations, 5’ phosphorylated primer pairs were designed including a mismatch at the desired base pair to generate the mutated form of either *Plxnd1* or *Col1a1*. Primers used for the generation of the *Ali34* mutations were 5’- CATGGCTGAGATTTAGAAATATGCTAAGAGG-3’ for the forward and 5’-GCCACGTTTGTGTTGAACTCATTCT-3’ for the reverse primer. For the *Aga2* mutation, 5’-ACCCTCTCCCGCAGTCTTCATTACACCA-3’ as forward and 5’-CATTACCAAGGTAGGAATGAAGTGAGGCTCA-3’ as reverse primer were used. PCR products were checked on a 1% TAE agarose gel. Ligation of the phosphorylated ends was performed with the T4 Quick ligase and transformation was performed with 10-beta chemical competent cells.

3.2.2.4 Restriction digests

Restriction digests were performed with FastDigest® Enzymes (Fermentas, Germany) when applicable. All other enzymes were purchased from New England Biolabs, Germany according as stated below:

Enzyme	Customer	Reference number
Fast Digest [®] EcoRI	Fermentas	FD2074
Fast Digest [®] EcoRV	Fermentas	FD 0303
Fast Digest [®] HindIII	Fermentas	FD 0504
Fast Digest [®] BamHI	Fermentas	FD 0054
Fast Digest [®] PstI	Fermentas	FD 2064
Fast Digest [®] NotI	Fermentas	FD 0594
Fast Digest [®] XbaI	Fermentas	FD 0684
Fast Digest [®] XhoI	Fermentas	FD 0694
Fast Digest [®] SphI	Fermentas	FD 1253
MspA1I	New England Biolabs	R0577S
PstI	New England Biolabs	R0657S

Restriction digests were conducted in a 20 μ l reaction (see below) according to the purpose of the reaction with variable DNA amounts.

Single enzyme digest

Reaction buffer (10x)	2 μ l
Enzyme	1 μ l
DNA	x μ l
water	y μ l
	Σ 20 μl

Double enzyme digest

Reaction buffer (10x)	2 μ l
Enzyme 1	1 μ l
Enzyme 2	1 μ l
DNA	x μ l
water	y μ l
	Σ 20 μl

Digestion was performed at 37°C for 3 hours (FastDigest® Enzymes) or 8-16 hours (New England Biololabs Enzymes) and checked on a 2% TAE gel.

3.2.2.5 cDNA synthesis

RNA was reverse transcribed to cDNA using the Superscript II Kit (Invitrogen, Germany). A total of 2 µg RNA was preannealed with 2 µl Oligo dT Primer (Invitrogen, Germany) added up to 20 µl with RNase free water at 65°C for 10 minutes. Subsequently, a mix containing reverse transcriptase, reaction buffer, dNTPs and RNase inhibitor (Invitrogen, Germany) was added to the reaction (see below). Reverse transcription was performed for 60 minutes at 42°C. Enzyme inactivation was achieved by an additional incubation step at 70°C for 15 minutes. cDNA was stored at -20°C until use.

Mastermix for reverse transcription

Component	Volume
5x reaction buffer	10 µl
dNTPs (Fermentas)	2.5 µl
RNase Out (Invitrogen)	2.0 µl
Superscript II Reverse Transcriptase	2.0 µl
RNAase free water	13.5 µl
	Σ 30 µl

3.2.2.6 qRT-PCR

For qRT-PCR the following reaction mix was used:

Component	f.c.	Volume
gene-specific primers (forward and reverse)	10 µM each	2 µl
1:10 dilution of cDNA template		2 µl
Power SYBR Green (2x)	1x	10 µl
AMPUWA		6 µl
		Σ 20 µl

Power SYBR Green was purchased from Applied Biosystems (Germany) and primers were ordered from Metabion (Germany). To avoid amplification of genomic DNA, each primer was designed to prime in contiguous sequences of two adjacent exons, allowing binding of primers exclusively after splicing.

Reactions were pipetted on Thermo-Fast 384-well PCR plates (Thermo Scientific, Germany) and qRT-PCR was performed on the ABI Prism 7900HT Sequence Detection System (Applied Biosystems, Germany).

Cycling conditions

95°C	10 min	} 39 cycles
95°C	15 seconds	
60°C	1 min	
55°C-95°C	evaluation of dissociation curve	

For each probe, four technical replicates were performed to assure measurement quality. C_t values were obtained by automatic C_t analysis of the ABI Prism SDS 2.1 software (Applied Biosystems, Germany) by the second derivative maximum method. C_t values of replicates were averaged.

Determination of gene expression was performed as relative quantification against housekeeping genes using the equation according to the $2^{-\Delta\Delta C_t}$ method¹⁰⁵. Calibrator normalization was performed with wild-type samples set to 100%.

Primer sequences are listed in the appendix (see 5.3)

3.2.2.7 TOPO cloning

TOPO cloning (pCR[®]II-TOPO[®], pCR[®]4-TOPO[®], pCR[®]-XL-TOPO) was conducted according to the manufacturer's recommendation. After transformation, 2 μ l of the reaction was added to either DH5 α or 10-beta chemically competent cells and incubated for 30 minutes on ice. After heat-shock of cells at 42°C for 30 seconds, SOC medium was added (250 μ l for DH5 α , 900 μ l for 10-beta) and incubated for 1 hour at 37°C with slow agitation. 50-150 μ l of the reaction was subsequently plated on LB Agar plates with the desired antibiotics and incubated at 37°C over night in an incubator for colony growth.

To check correct insertion of the PCR product into the vector, a “colony PCR” was performed with available M13-primer (supplied in the TOPO cloning kits by Invitrogen) or similar primers binding within the vector sequence (according to 3.2.2.1). Briefly, colonies were picked from the LB plate with a pipette tip, dipped into the PCR reaction mix and subsequently streaked to a new LB plate for later recovery of this colony. PCR positive colonies (displaying the expected product) were cultured over night in 5 ml LB medium and plasmid was purified according to 3.2.1.4. Plasmid DNA was afterwards again checked by restriction digests and sequenced to proof the insert sequences (see 3.2.2.2).

3.2.2.8 Ligation

For ligation of DNA fragments, plasmids were restriction digested with the desired enzymes. After incubation, the fragment containing the vector backbone was incubated with 1 µl shrimp alkaline phosphatase (SAP) for 30 min at 37°C and a subsequent inactivation step for 15 minutes at 65°C to dephosphorylate the vectors ends. Digests were separated by a 1% TAE gel. Fragments were cut out of the gel and were purified with the QIAquick Gel Extraction Kit (Qiagen, Germany) according to the manufacturer’s recommendations. Ligation was performed with T4 ligase and the supplied ligation buffer (Fermentas, Germany) and a vector to insert ratio of 1:3 in a 20 µl reaction mix. Ligation was incubated over night in a temperature gradient (ice to room temperature). 2-4 µl were added to chemically competent cells (10-beta, New England Biolabs) and the reaction was incubated for 30 minutes on ice. After heat-shock for 30 seconds at 42°C, 900 µl SOC medium was added to the reaction and incubated for 1 hour at 37°C with slow agitation. 50 – 150 µl were plated on LB Agar with the desired antibiotics and incubated at 37°C in an incubator over night.

Correct ligation was checked by colony PCR and restriction digests of purified plasmid DNA while inserts were sequenced for sequence confirmation.

3.2.2.9 Gateway cloning

The Gateway cloning system from Invitrogen was used to express exogenous tagged P1xnd1 *in vitro*. The system utilizes the ability of recombination between

attB, attP, attL, attR sites that simplifies the directed insertion of DNA sequences into different tagged vectors. The modified pSlo1.1K (purchased from Bio&Sell) was used as an entry clone to directly clone the full-length cDNA of *Ptxnd1* in both forms (wild type and *Ali34*) into the desired expression vectors by the use of LR clonase II (Invitrogen, Germany) according to the kits manual. The cDNA was additionally cloned into the pDonrTM201 vector using BP clonase II (Invitrogen, Germany) following the manufacturer's instructions.

3.2.2.10 Transfection methods

The fibroblast cell lines L929 and NIH3T3 were transfected using LipofectamineTM 2000, LipofectamineTM LTX or the electroporation system NeonTM Transfection System (Invitrogen, Germany). All protocols were tested with multiple experimental setups. For transfection reagents an initial cell density range between 1×10^4 - 1×10^5 cells/well to a 24-well *Primaria*TM plate was used and cells were incubated over night in a humidified incubator at 37°C and 5% CO₂. Subsequently cells were transfected with varying plasmid concentrations (range 0.2 µg-1.5 µg/well) with 2 µl LipofectamineTM 2000 or with 1-2 µl LipofectamineTM LTX in Opti-MEM®-I (Invitrogen, Germany) according to the manufacturer's manual. For electroporation, a cell density range between 1×10^5 - 3×10^5 per reaction was used to be electroporated with 0.5 - 2 µg plasmid DNA. Two pulses at 1200 mA for 20 ms were applied and cells were subsequently plated on 24 well *Primara*TM plates.

3.2.2.11 Western Blot

For Western blot analysis, polyacrylamide gels with varying percentage were used to separate proteins in denatured conditions. For the assessment of molecular weights, SpectraTM Multicolor Broad Range Protein Ladder (Fermentas, Germany) was used. After gel electrophoresis (initial step 60V for 30 minutes and 80-100V until end), proteins were blotted on a Hybond-P PVDF membrane (GE Healthcare, Germany) that was activated in 100% methanol for 10 seconds, transferred to ddH₂O, incubated for 5 minutes and was subsequently equilibrated with Whatman[®] paper (Biometra, Germany) in transfer buffer. Blotting was performed at 200 mA for 2 hours. Subsequently, protein transfer was confirmed by Ponceau

S staining. Membranes were blocked over night in 10% skimmed milk in TBST at 4°C. Primary antibodies were used according to manufacturer's recommendations. After five times washing in TBST for 5 minutes, membranes were incubated in HRP-conjugated secondary antibodies for 3 hours at RT. Membranes were again washed five times for 5 minutes in TBST. Detection was performed using the Western Lightning[®] Plus-ECL Kit (Perkin Elmer, USA). Visualization of bands was performed using Amersham[™] Hyperfilm ECL autoradiography films (GE-Healthcare, Germany).

3.2.3 Genotyping

3.2.2.1 *Ali34*

Isolated DNA was amplified by PCR with the designed genotyping forward primer 5'-gtggcacacaccttaatcc-3' and reverse primer 5'-ttgcagtgagtcagatgtgc-3'. The product was restriction digested by PstI (Fermentas, Germany) for 2h at 37°C and was subsequently analysed on a 2% agarose gel. Restriction digest generates 158/112 bp fragments for the wild-type allele and 270 bp for the mutant allele. The digests were confirmed on a 2% TAE gel

3.2.2.2 *Aga2*

Isolated DNA was amplified by PCR with the designed genotyping forward primer 5'-ggcaacagtcgcttcaccta-3' and reverse primer 5'-ggaggtcttggtggtttgt-3' spanning the entire intron 50 *Col1a1*. The product was cleaved using MspA1I yielding 156bp and 75bp fragments in wild type mice and 231bp / 156bp and 75bp fragments in heterozygous *Aga2* and confirmed on a 2% TAE gel.

3.2.4 Cell culture methods

3.2.4.1 Primary fibroblast cell culture

For the analysis of mouse embryonic fibroblasts (MEFs) of the *Ali34* mouse line, 14.5 dpc old embryos were used for isolation. For this purpose, pregnant female

mice were euthanized by cervical dislocation and the uteri containing the embryos were removed and transferred to sterile PBS. All further steps were performed under a sterile working bench. Embryos were dissected in PBS and yolk sacs were used for genotyping. Extremities were removed, washed in fresh PBS twice and subjected to a 70 μ m cell strainer placed in a Petri dish containing DMEM culture medium supplemented with 10% FCS, 2 mM L-Glutamine and antibiotics (Penicillin / Streptomycin 100U/ml each). Subsequently, tissue was dissociated through the cell strainer by applying mechanical pressure. After dissociation, fibroblasts in DMEM culture medium were transferred to 15 ml Falcon tubes and pelleted at 4°C for 10 minutes at 1,200 rpm with subsequently plating in a T25 cm² cell culture flask. Cells were incubated in a humidified incubator at 37°C and 5% CO₂ with media change twice a week. Cells were passaged after reaching confluence by detachment with 0.25% trypsin/EDTA and splitting 1:5 in a new culture flask. For all assays, MEFs between the second and fifth passage were used and plated in 24-well *Primaria*TM plates at an initial cell density of 1x10⁵ cells/well.

For primary *Aga2* cardiac and pulmonary fibroblasts, 6-12 day old animals were euthanized by decapitation. Tissues were excised, immediately placed in ice-cold HBSS and brought under a sterile working bench for subsequent preparation steps. Tissues were minced with scissors to pieces of approximately 1-2 mm and washed 3 times with HBSS buffer. To remove debris and loosely attached contaminating cells, the pieces were subjected to a 5 minute predigesting step with 0.1% collagenase IV (Sigma Aldrich, Germany) at 37°C. The supernatant was discarded and the remaining tissue was digested in fresh 0.1% collagenase IV mixture for 30 minutes at 37°C twice. Digested cells were filtered through a 70 μ m cell strainer, filled up with equal amounts of DMEM supplemented with 10% FCS, 2 mM L-Glutamine and antibiotics (Penicillin / Streptomycin 100U/ml each) and pelleted by centrifugation for 10 minutes at 1200 rpm. The pellet was resuspended in DMEM culture medium and cells were plated in a T25 cm² cell culture flask for 1 hour. Afterwards, non-adherent cells were removed by rinsing with PBS and fresh media was added to the attached cells. The fibroblasts were incubated in a humidified incubator at 37°C and 5% CO₂ with media change twice a week. After reaching confluence, the cells were passaged by detachment with 0.25% trypsin/EDTA solution and splitting 1:2 or 1:3 in new flasks.

Cultures were used for the experiments between the first and third passage and therefore seeded on Lumox™ 24-well plates (Greiner, Germany) for ICC studies and on standard 24-well plates for RNA isolation, with an initial density of 1×10^5 cells/well. After 48 hours of incubation, cells were stimulated with ascorbic acid (50 µg/ml) for another 24 hours before deployed for further studies.

3.2.4.2 Primary osteoblast cell culture assay

A more detailed description of all assays is available in the PhD thesis of Dr. Frank Thiele.

For the analysis of a comprehensive osteoblast cell culture system through a three week culture period, 40 three to six day old mice were decapitated (20 *Ali34/+* and 20 wild-type controls), briefly immersed in 70% ethanol and subsequently stored in ice cold PBS. All further steps were performed under a sterile laminar flow. Calvariae were dissected by removing the skin. After calvarial detachment from the head, excessive tissue was removed and the remaining tissue was subjected to a 15 ml Falcon tube. Decalcification was performed with 4 mM EDTA (pH 7.0) in PBS for 7 minutes at 37°C and supernatant was discarded. After a predigestion step in 2 ml 0.1% collagenase IV solution for 7 minutes at 37°C in a water bath, calvariae were digested in 5 ml 0.1% collagenase IV solution with occasionally agitation for 30 minutes at 37°C using a water bath twice. Supernatant was filtered through a 44 µm cell strainer and 20 ml culture medium was added. Subsequently cells were pelleted by centrifugation for 10 minutes at 1,200 rpm at RT. After cell resuspension, cells were counted using an improved Neubauer counting chamber. Cells were plated in T12.5 cm² cell culture flasks, 6-well plates and 24-well plates according for the different assay requirements for every measurement day (T0, T3, T9, T15, T21).

For the assessment of proliferation, metabolic activity, protein content and ALP activity, one 24-well Lumox™ plate was used for each measurement day. The metabolic activity of the cells was assessed by adding *Resazurin (CellQuant-Blue™* Reagent, Biotrend Chemikalien, Germany) to the culture medium. Fluorescence intensity being proportional to the metabolic activity was analysed with a Tecan-Safire² (Tecan, Germany). Subsequently, cells were lysed and centrifuged to separate the nucleic and cytosolic fraction. The nucleic fraction was

used to determine the proliferative rate by using *Quant-iT™* ds DNA Assay Kit (Invitrogen, Germany) The supernatant is used for determination of the protein content and ALP activity. Protein content data was assessed with the BCA Protein Assay Kit (Thermo Scientific, Germany). ALP activity was quantified by 4-nitrophenylphosphate (PNPP) as described¹⁰⁶.

The analysis of collagen secretion and deposition was performed on 6-well *Primaria™* plates after stimulation of osteoblasts with 50 µg/ml ascorbic acid 24 hours before the measurements. Analysis was conducted by adding the Sircol™ Dye reagent (Tebu-bio, Germany). Collagen secretion was analysed by use of the supernatant colorimetrically. Subsequently, incorporated collagen in the ECM (collagen deposition) was analysed colorimetrically after dissolving the precipitate. For the analysis of matrix mineralization, cells on 6-well *Primaria™* plates were fixed in 4% PFA, air dried and stored at RT. Mineralization of the extracellular matrix was determined using Alizarin Red¹⁰⁷. The dye is dissolved with cetylpyridinium chloride and the degree of matrix mineralization was analysed colorimetrically, since the amount of bound Alizarin is proportional to the amount of calcified matrix.

Nodule quantification was performed in T12.5 cm² cell culture flasks. Flasks are placed under a stereomicroscope and transmitted light images are taken. The development of nodule-like structures in the culture was quantified by analyzing the images after conversion into binary files using ImageJ.

RNA isolation for gene expression analysis was performed from single wells of 24-well *Primaria™* plates with the RNeasy Mini Kit (see 3.2.1.2). Subsequently, RNA was reverse transcribed into cDNA and applied for qRT-PCR (see 3.2.2.5 and 3.2.2.6). 13 genes that are key factors in bone biology and important for development and maturation of bone cells, matrix synthesis and cell-cell interaction were analysed.

3.2.4.3 Primary pancreatic islet culture

Mice were euthanized by CO₂. Afterwards animals were dissected and the common bile duct was clamped. Subsequently, pancreas was infiltrated with collagenase P (Roche, Germany) f.c. 1 mg/ml. After removal of the pancreas from the gut, the organ was kept in a tube containing collagenase solution on ice until

subjected to a 37°C water bath for 15 minutes. After the digestion step, pancreata were placed on ice under a sterile working bench. 10-12 ml HBSS buffer containing 1% antimycotic solution and 1% BSA (G-solution) was added to the digest, followed by centrifugation for 2 minutes at 1,620 rpm. The supernatant was discarded and the digested pancreatic tissue was resuspended in 10-12 ml G-solution. Subsequently, the solution was filtered through a metal strainer and again centrifuged for 2 minutes at 1,620 rpm. Supernatant was removed and the pellet was resuspended in 15% Optiprep™ (Sigma, Germany) followed by 6 ml G-solution to separate the islets from the remaining tissue. The mix was incubated for 10 minutes at RT and afterwards centrifuged for 10 minutes at 1.700 rpm. The upper phase containing the islets was removed and filtered into a 70 µm cell strainer that was subsequently rinsed with G-solution into a petri dish. Isolated islets were picked with a 200 µl pipette and 50 islets were subjected to a new petri dish containing culture medium (RPMI-1640 containing 1% antimycotic solution and 10% FCS) each.

3.2.4.4 Cell line culture

Both, L929 and NIH3T3, stable fibroblast cell lines were used for transfection assays and for standard immunocytochemical stainings. Maintenance of the cells were performed in T75 cm² cell culture flasks with DMEM containing 10% FCS, 2 mM L-Glutamine and antibiotics and were incubated in a humidified incubator at 37°C and 5% CO₂. After reaching confluence, cells were detached with 0.25% trypsin/EDTA, pelleted by centrifugation at 4°C for 10 minutes at 1,200 rpm, resuspended and split 1:40. Cultures used for RNA isolation were plated on standard 24-well plates, with an initial density of 1x10⁵ cells/well. For ICC studies, cells were plated on glass coverslips placed in standard 24-well plates, with an initial density of 1x10⁵ cells/well.

3.2.5 Histological methods

3.2.5.1 Tissue preparation for paraffin sections

Mice were euthanized by carbon dioxide. The skin was removed and the organs of interest were isolated and fixed in 4% PFA/PBS for 30 min – 24 h according to the desired applications. For the preparation of bone, most of the muscle and connective tissue were removed and subsequently decalcified for 14 days in 0.5 M EDTA. After decalcification bones were minimized to a total length of approximately 0.5 cm to achieve better adhesion on the slides. Tissue was incubated for 2h in 25%, 50%, 75% and 95% EtOH at RT each. Solution was changed to 100% ethanol and the tissue was incubated o.n. at RT. Afterwards incubation was continued for 0.5 h at 37°C and 60°C in xylene and was then transferred into a xylene/paraffin mix (1:1) incubated o.n. at 60°C. The cover was removed for evaporation of the remaining xylene for 48 h. The tissue was embedded in an appropriate plastic rack and stored at 4°C. Sections (5 µm) were cut with a RM2165 microtome (Leica Instruments, Heidelberg, Germany) and placed on slides (SuperFrost® Plus, Menzel-Gläser, Braunschweig, Germany). Prior to histological stainings, sections were deparaffinised in two changes of xylene and rehydrated through 100%, 95%, 75%, 50% EtOH with a final step in ddH₂O.

3.2.5.2 Tissue preparation for cryosections

Mice were euthanized by carbon dioxide. The skin was removed and the organs of interest were isolated and fixed in 4% PFA/PBS for 30 min. Tissue was washed three times in PBS for 5 min. Specimens were incubated in 10% and 20% sucrose in PBS for 2 h and in 30% sucrose in PBS o.n. at 4°C. The next day, tissue was transferred to OCT/30% sucrose (2:1) for 2 h before embedded in OCT on dry ice. Tissue was stored at -80°C. 7 µm sections were cut, air dried and were subjected to two changes of PBS prior to stainings.

3.2.5.3 H&E staining

Sections were incubated 10 min in Mayer's Haematoxylin (Sigma, Germany) and subsequently washed for 10 min in running tap water. Afterwards, sections were dipped 10 times in 95% EtOH and counterstained with Eosin Y for 20 seconds. In the following, sections were dehydrated through 75%, 95%, 100% EtOH, cleared in xylene for 10 min and finally mounted with Entellan mounting medium (Merck, Germany).

3.2.5.4 Alcian blue staining

Staining was performed for 15 minutes in alcian blue staining solution. Subsequently sections were washed in running tap water for 2 minutes, rinsed in ddH₂O and counterstained with nuclear fast red for 5 minutes. Sections were again washed in double distilled water for 2 minutes, dehydrated in 95% and 100% EtOH, cleared in two changes of xylene for 5 minutes each and mounted with Entellan mounting medium.

3.2.5.5 Safranin O staining

Sections were stained in Weigert's iron haematoxylin working solution for 10 minutes and washed in running tap water afterwards. Sections were then incubated for 5 minutes in fast green staining solution, subsequently immersed for 10-15 seconds in 1% acetic acid and stained for 5 minutes in Safranin O staining solution. Sections were quickly dehydrated in 95% and 100% EtOH, cleared in xylene for 2 minutes and finally mounted with Entellan mounting medium.

3.2.5.6 TRAP staining

Samples were incubated for 20 minutes in TRAP-buffer, followed by incubation in filtered and prewarmed TRAP staining solution for 1 – 1.5 hours at 37°C. Staining was stopped by incubation in ddH₂O for 2 minutes. Counterstaining was performed by incubation in Weigert's Iron haematoxylin working solution for 5

minutes. Sections were briefly washed in ddH₂O and finally mounted in Fluoromount™ aqueous mounting medium (Sigma, Germany).

3.2.5.7 Immunohistochemistry on paraffin sections

To block exogenous peroxidase, sections were incubated in 0.3% H₂O₂ in methanol for 30 minutes. After washing in PBS antigen retrieval was performed. Except for type I collagen stainings (15 minute incubation in proteinase K (10 ng/μl) at 37°C), sections were cooked for 20 minutes in citric acid buffer pH 6.0 and cooled down in the same solution for another 20 minutes. The appropriate Vectastain Elite ABC Kit (Biozol, Germany) was used according to the kits manual. Primary antibodies were incubated as depicted in table 4. For visualisation, sections were incubated in DAB staining solution (Sigma, Germany) until specific staining was visible. Counterstaining was performed with Mayer's Haematoxylin (Sigma, Germany) for 1 minute followed by subsequent bluing in 0.1% sodiumbicarbonate for 1 minute. Sections were quickly dehydrated, cleared in xylene and mounted in Entellan mounting medium (Merck, Germany). Staining was analysed on an Axioplan 2 microscope (Zeiss, Germany) with light supplier HBO 100 (Zeiss, Germany) and photographed with AxioCam H RC (Zeiss, Germany).

Table 4. Antibody dilution, incubation conditions and buffers used for IHC on paraffin sections.

Antibody	Dilution	Incubation	used buffer
PECAM-1	1:200	3 hours, RT	PBST
Plxnd1	1:100	5 hours, RT	PBS

3.2.5.8 Immunohistochemistry on cryosections

For fluorescent staining, specimens were blocked in 5% BSA in either PBS or PBST (see table 5) o.n. at 4°C. After removing excess blocking solution, primary antibodies were applied on the slides and incubated according to table 5. After incubation, sections were washed three times in PBS or PBST for 5 minutes. Adequate secondary antibodies were applied at a 1:400 dilution together with DAPI (1:1000) in PBS or PBST and incubated in the dark for 2 hours at room

temperature. After five washes in PBS or PBST for 10 minutes, sections were mounted with Vectashield[®] Mounting Medium (Biozol, Germany), sealed with nail polish the next day and stored in the dark at 4°C.

Table 5. Antibody dilution, incubation conditions and buffers used for IHC on cryosections.

Antibody	Dilution	Incubation	used buffer
PECAM-1	1:200	o.n. 4°C	PBST
Plxnd1	1:200	o.n. 4°C	PBS
VEGF	1:200	o.n. 4°C	PBST
Col1	1:200 – 1:500	o.n. 4°C	PBST
Insulin	1:200	o.n. 4°C	PBST
Glucagon	1:200	o.n. 4°C	PBST
Laminin	1:500	o.n. 4°C	PBST

3.2.5.9 Immunocytochemistry

After removing the medium, cells were briefly washed in two changes of PBS. Cells were subsequently fixed in 4% PFA/PBS for 10 minutes at 4°C or in ice-cold methanol for 6 minutes at -20°C and washed with PBS twice. Blocking was performed in 5% BSA/PBS for at least 2 h RT or over night at 4°C. Primary antibodies were used as stated below (table 6). After incubation with the primary antibody, cells were washed three times in PBS for 5 minutes. Secondary antibodies were applied at a dilution of 1:400 together with DAPI (1:1000) and incubated for 2 hours at RT in the dark. Finally, cells were washed five times in PBS for 5 minutes, cover slips were removed from the well and mounted with Vectashield[®] Mounting Medium (Biozol, Germany) to glass slide (SuperFrost[®] Plus, Menzel-Gläser, Braunschweig, Germany). Stainings were analysed on an Axioplan 2 microscope (Zeiss, Germany) with light supplier HBO 100 (Zeiss, Germany) and photographed with AxioCam H RC (Zeiss, Germany).

Table 6. Antibody dilution, incubation conditions and buffers used for ICC.

Antibody	Dilution	Incubation	used buffer
goat-anti-Plxnd1	1:100	o.n. 4°C	PBS
mouse-anti- α -tubulin	1:500	o.n. 4°C	PBS/PBST
mouse-anti- β -actin	1:500	o.n. 4°C	PBS/PBST
rabbit-anti-His	1:200	o.n. 4°C	PBS
rabbit-anti-GFP	1:200	o.n. 4°C	PBS

3.2.5.10 SEM analysis

For scanning electron microscopy (SEM), hearts were additionally subjected to a maceration protocol to remove cellular components and ECM elements, thereby preserving and exposing the remaining collagen structure^{108,109}.

Briefly, bisected hearts were fixed in 2.5% glutaraldehyde for 6 days and immersed in 2 M NaOH for additional 6 days. NaOH maceration solution was changed every second day.

Subsequently, hearts were washed in several changes of distilled water to remove cellular debris. Tissue was further immersed in 1% tannic acid for 3 hours, rinsed in distilled water for several hours and postfixed in 1% OsO₄ for 1 hour. Samples were dehydrated in a graded series of 25%, 50%, 70%, 95% and 100% EtOH. Finally, specimens were critical-point-dried, coated with platinum and observed under a JEOL JSM 6300F scanning electron microscope (JEOL, Japan).

3.2.6 Skeletal stainings

Skeletal preparation was performed with an Alcian blue/Alizarin red staining solution. Alcian blue as a phthalocyanine dye contains copper and stains glycosaminoglycans, the major compartment of cartilage bluish. The dye forms a reversible electrostatic bond with the anionic sites of the polysaccharide. Alizarin red forms - together with calcium - an alizarin red S-calcium chelate complex.

After preparation the mice were first dehydrated in 100% ethanol for seven days and subjected to 100% acetone for another three days. After acetone removal, mice were briefly washed with water and then incubated for 21 days in the Alcian blue/Alizarin red staining solution (1 volume of Alizarin red, Alcian blue, glacial

acetic acid each, together with 17 volumes EtOH). Remaining tissue was destained and macerated in 1% KOH/20% glycerol at 37°C for 1 day and afterwards stored in the same solution at RT, until tissue was cleared. Skeletons were transferred in dilution series of glycerol (20%, 50%, 80%) in water to a final storage at 100% glycerol. Stainings were photographed using a microscope MZ APO with light supplier KL 1500 LCD and camera DFC 320, Leica.

3.2.7 Methods within the GMC

3.2.7.1 Animal housing and caretaking

Both mutant lines were generated in the Munich ENU mutagenesis screen⁸⁶. Maintenance of both mouse lines was performed by continuous matings of heterozygous males with wild type *C3HFeB/FeJ* female mice.

Mouse husbandry was conducted under a continuously controlled specific-pathogen-free (SPF) hygiene standard in compliance with the Federation of European Laboratory Animal Science Associations (FELASA) protocols. Mice received standard rodent nutrition and water *ad libitum* and all animal experiments were performed under the approval of the responsible animal welfare authority.

3.2.7.2 Cardiovascular phenotyping

Heart function and performance was investigated in living mice utilizing the cardiovascular screen of the German Mouse Clinic (GMC) as described previously¹¹⁰.

The secondary screen comprised echocardiography followed by an ECG analysis and was performed with six *Aga2^{severe}* and six wild type control mice at the age of 10 and 11 days. Left ventricular function was determined by transthoracic echocardiography using high-frequency ultrasound biomicroscopy with a Vevo 660 30-MHz transducer and 30 Hz frame rate (VisualSonics, Canada). The shaved and isoflurane (1%) anesthetized mice (Baxter, Germany) were fixed in supine position on a heated platform to maintain a body temperature of 36–38°C monitored via a rectal thermometer (Indus Instruments, USA). Left ventricular parasternal short-axis views were obtained in M-mode imaging at the papillary

muscle level. Four recordings were performed and measurements were averaged from four cardiac cycles of each record for the left ventricular end-diastolic internal diameter (LVEDD) and the left ventricular end-systolic internal diameter (LVESD) using the leading-edge convention, as suggested by the American Society of Echocardiography¹¹¹. Fractional shortening was calculated as $FS (\%) = [(LVEDD - LVESD) / LVEDD] \times 100$ and ejection fraction as $EF (\%) = [7 / (2.4 + LVEDD) \times LVEDD^3] - [7 / (2.4 + LVESD) \times LVESD^3]$ as previously described^{112,113}.

3.2.7.3 Dymorphological phenotyping

The dymorphology screening in the GMC includes the analysis of morphological alterations in a whole body check up at the age of 9 weeks. Therefore 20 (10 males and 10 females) mutant as well as 20 (10/10) control mice were analysed as previously described^{94,114}. In addition, a *Clickbox* test was performed to analyse the mice's ability to hear a sound of 20 kHz that is classified into six categories (0 = no reaction, 1 = no Preyer reflex, 2 = retarded reaction, 3 = normal reaction, 4 = strong reaction, 5 = particularly strong reaction).

For pQCT analysis mice were sacrificed and weight and length of the mice were recorded. The leg was positioned into the specimen holder in the centre of the gantry opening and fixed with a plastic mould. Both left and right distal femoral metaphysis and diaphysis were examined obtaining volumetric bone mineral density, content and area of trabecular, cortical and total bone. After a first scout measurement a reference line was set at the most distal point of the femur. 3.0 mm proximal from the reference line two slices were taken at 0.25 mm intervals and 6.0 mm proximal of the reference line one slice was taken to receive cross sections of the metaphysis and diaphysis. By means of this slices the circumference and area of both metaphysis and diaphysis were evaluated.

Measurements were performed using a Stratec XCT Research SA+ (Stratec Medizintechnik GmbH, Pforzheim, Germany). Photons emitted by the X-ray tube are detected by 12 semiconductor detectors. The spatial resolution was set to 70 μm .

Data analysis after scanning implies, to define the regions of interest by separating the femur from the patella. The CT slices were analysed using contour mode 1, cortmode 1, and peelmode 2 to evaluate trabecular and cortical parameters. For

detection of the outer contour of bone a threshold was set at 350 mg/cm³ and the trabecular bone region was defined by setting an inner threshold to 450 mg/cm³.

3.2.7.4 Behaviour screen

The Open Field (OF) test was carried out according to the standardised phenotyping screens developed by the EUMORPHIA partners and is available at www.empress.har.mrc.ac.uk and was previously described¹¹⁴

3.2.7.5 Neurology screen

Screening was performed using the modified SHIRPA protocol (original by Rogers et al.¹¹⁵). Assessment of each animal at the age of 10 weeks began with observation of undisturbed behaviour, the investigation of locomotor activity and motor behaviour as described recently^{114,116}. In addition grip strength of fore limbs and all limbs as well as rotarod performance were tested¹¹⁷.

3.2.7.6 Eye screen

The posterior parts of both eyes were examined by funduscopy. After pupil dilation with one drop of atropine (1%), the mouse is grasped firmly in one hand and clinically evaluated using a head-worn indirect ophthalmoscope (Sigma 150 K, Heine Optotechnik, Herrsching, Germany) in conjunction with a condensing lens (90D lens, Volk, Mentor, OH, USA) mounted between the ophthalmoscope and the eye.

For slit lamp biomicroscopy mice were examined for eye abnormalities as previously described¹¹⁸.

For histological analysis eyes were fixed 24 hours in Davidson solution, dehydrated and embedded in plastic medium. Transverse 2 µm sections were cut with an ultramicrotome, stained with methylene blue and basic fuchsine and evaluated with a light microscope.

3.2.7.7 Clinical chemical screening

For the analysis of blood based parameters blood samples were taken and analysed from isoflurane-anesthetized mice by puncturing the retro-orbital sinus with non-heparinised capillaries as described recently⁹³. In the primary screen, 21 different parameters were measured including various enzyme activities, as well as plasma concentrations of specific substrates and electrolytes.

In addition number and size of red blood cells, white blood cells, and platelets are measured by electrical impedance and haemoglobin by spectrophotometry.

A second sample was collected from all animals tested for blood based parameters, in order to retest parameter showing deviations in the first test, to check to check the reproducibility of the first results, and to provide the steroid screen with a plasma sample.

For the intraperitoneal glucose tolerance test mice were fasted for 16 to 18 hours overnight, injected with 2 g of glucose/kg body weight and blood samples were taken 15, 30, 60, 90 and 120 minutes after glucose injection as described⁹³.

3.2.7.8 Pathological phenotyping

Within the pathology screening mice were sacrificed with CO₂ at the age of 19-20 weeks. The animals were analysed macroscopically and weighed (<http://www.geocities.com/virtualbiology/>). The thymus and left lobe of the liver were measured. Blood samples were taken, centrifuged and the serum was saved at -20°C. Tails were preserved at -70°C for further genetic analysis. X ray of the complete bone structure was taken (Hewlett Packard, Cabinet X-Ray System Faxitron Series). Following a complete dissection, all organs were fixed in 4% buffered formalin and embedded in paraffin for histological examination. Two-µm-thick sections from skin, heart, muscle, lung, brain, cerebellum, thymus, spleen, cervical lymph nodes, thyroid, parathyroid, adrenal gland, stomach, intestine, liver, pancreas, kidney, reproductive organs, and urinary bladder were cut and stained with haematoxylin and eosin (H&E). For statistical analysis the T-test was used. A p-value of < 0.05 was interpreted as significant.

3.2.7.9 Expression profiling

Genome-wide cDNA-chip based expression profiling was performed with 16-weeks old animals during the primary screening of the GMC as well as from hearts and lungs of 11-days old *Aga2/+^{severe}* and control mice.

cDNA microarrays were produced in-house and hybridised using a Cy3/Cy5 dual colour approach as recently described^{119,120}. A full description of the microarray probes is available in the GEO database under GPL4937¹²¹.

Statistical analyses were performed using TM4 Microarray software suite including MIDAS (Microarray Data Analysis System) for normalization¹²² and SAM (Significant Analysis of Microarrays) for determination of genes showing significant differential regulation¹²³. The false discovery rate (FDR) - which is the percentage of genes identified by change - was estimated by calculating 1000 permutations of the measurements and the cut-off for discrimination of the top differentially expressed genes with reproducible up- or down regulation was set below 10% false positives (FDR). *In silico* analysis of differentially expressed genes was performed using EASE, a module of the DAVID database¹²⁴, assigning genes to Gene Ontology (GO) functional categories. EASE analysis includes a Bonferroni multiplicity correlation and evaluates the set of differentially expressed genes for over-representation of biological processes. In depth analysis and description of the denoted genes for molecular function and pathological involvements was additionally done using BiblioSphere Pathway Edition.

3.2.7.10 pO₂ measurements

Blood samples from four *Aga2^{severe}* as well as six *Aga2^{mild}* and 15 wild type control mice at the age of 8 to 11 day were collected to measure blood gas parameters. Animals were decapitated and blood leaking from the arteria carotis was directly soaked into an 85 µl blood gas capillary (Kabe, Germany). Blood pH, pO₂ and pCO₂ was immediately determined by direct measurement using an ABL5 blood gas analyzer (Radiometer, Germany) and the corresponding parameters O₂ saturation, carbon dioxide concentration (HCO₃⁻) and actual base excess (ABE) were automatically calculated.

3.2.8 Alendronate treatment

Alendronate treatment was performed using *Aga2/+* and control mice. Beginning with birth (P0), weight and size of the animals were recorded daily. Mice were grouped randomly into a treatment group receiving 0.03 mg/kg/week alendronate (Sigma, Germany) and a control group receiving the same amount of physiological saline solution. Injections started at 1 dpp by intermittent subcutaneous administration at 3, 5, 8, 10 and 12 dpp of 0.01 mg/kg/week. Prior to every injection, mice weight was recorded to calculate the exact amount of alendronate, which had to be administered. The maximal injection volume was set to 10 μ l per mouse. At 14 dpp or when *Aga2/+* mice were identified as *Aga2/+^{severe}*, mice were anaesthetized and bone densitometry was performed using the LaTheta LCT-100ATM μ CT (Bruker, Germany). 3D reconstruction was performed with the 3D Doctor software (Able Software Corp., USA). Rib fractures were counted according to the appearance of callus formation.

3.2.9 Imaging techniques

Aga2/+ animals were subcutaneously injected with 0.67 nmol AngiosenseTM750 and/or OsteosenseTM680 (Perkin Elmer, USA). One hour after injection, mice were subjected to FMT-XCT analysis. The hybrid FMT-XCT system was build around a micro-CT system (explore Locus, GE HealthCare, Ontario, Canada) featuring a ~1m outer diameter rotating gantry. FMT utilized two diode laser sources (680 nm, 750 nm, B&W Tek, Newark, DE, USA) and a back-illuminated cooled CCD camera in trans-illumination arrangement. For each transmission image the laser power was set to an optimal value using automatic gain control (AGC) to maximize the dynamic range of the system, the delivered power did not exceed laser standard for tissue exposure. Spectral selection was based on a six-position filter wheel positioned in front of the camera lens with filters to collect excitation and fluorescence photons in the 680 nm and 750 nm band combinations. Electromechanical linear stages (Thorlabs, Newton, NJ, USA) were used to scan a system of lenses so that a collimated laser beam was mildly focused in patterns onto the tissue surface for each gantry rotation position. The FMT components were placed orthogonal to the X-ray source and detector detection axis. By

rotating the gantry, both FMT and XCT raw data could be obtained over the full 360° range. For each source position, approximately 1-5 sec data collection time was required depending on the strength of the fluorescence signals observed and corresponding AGC settings. Each source position generated 2 x 512 x 512 data pairs, considering the 512x512 independent detectors established by the CCD camera and the two spectral measurements performed per fluorochrome.

Four hours after injection, mice were euthanized, frozen and embedded as previously described¹²⁵. Both bright field and fluorescent pictures were taken after every slice (250 µm) with a CCD camera. Images were analysed using the ImageJ software.

3.2.10 Blood plasma collection

Four-weeks old *Aga2/+* and wild type control mice were sacrificed with CO₂. Subsequently, mice were dissected to collect the entire blood from the vena cava using heparinised syringes and transferred to a 1.5 ml reaction tube. For plasma collection, heparinised blood was centrifuged at 13,000 rpm for 2 minutes at 4°C. The upper phase containing blood plasma was subdivided for adiponectin (20 µl), insulin (20 µl), osteocalcin (20 µl) ELISA measurements as well as for the clinical chemical screen of the GMC (130 µl) and for the metabolomics platform (50 µl twice).

3.2.11 ELISA-measurements

3.2.11.1 Insulin ELISA

The insulin Elisa kit was purchased from Mercodia (Sweden). The procedure was done according to the manufacturer's manual. Briefly, 10 µl blood plasma were mixed with 10 µl calibrator solution and 100 µl enzyme conjugate was added. After 2 hours incubation on a plate shaker (700-900 rpm) at room temperature, plates were washed six times with 700µl wash buffer. Subsequently, 200 µl TMB substrate was added and the plate was incubated for 15 minutes at RT. 50 µl stop solution was added to the reaction and the OD was measured at 450 nm in a plate reader (GeniusPRO, Tecan, Germany).

3.2.11.2 Osteocalcin ELISA

Osteocalcin measurements were conducted using the BTI Mouse Osteocalcin EIA Kit (Biomedical Technologies, Inc., USA). According to the kits manual, 5 µl plasma sample was diluted with 20 µl sample buffer. 100 µl osteocalcin antiserum was added to the reactions and incubated o.n. at 4°C. The next day, the plate was washed 5 times with the supplied PBS washing buffer. 100 µl Streptavidin-Horseradish peroxidase was added and incubated for 30 minutes at room temperature, followed by the addition of 100 µl TMB solution and an incubation for 15 minutes in the dark at RT. Afterwards, 100 µl stop solution was added and absorption was subsequently measured in a plate reader (GeniusPRO, Tecan, Germany).

3.2.11.3 Adiponectin ELISA

For the analysis of adiponectin levels, the Quantikine[®] Mouse Adiponectin/Acrp30 Immunoassay (R&D Systems, Germany) was used, according to the manufacturer's manual. Briefly, samples were diluted 1:2000 prior to the experiment. 50 µl of the diluted sample was added to 50µl assay diluent and incubated for 3 hours at RT. The plate was washed 5 times with 400µl wash buffer. Mouse adiponectin conjugate (100 µl) was added and incubated for 1 hour at room temperature. Plates were washed again for 5 times with wash buffer. Substrate solution (100 µl) was added, incubated in the dark for 30 minutes at RT and the reaction was stopped with 100µl stop solution. Absorption was measured at 450 nm in a plate reader (GeniusPRO, Tecan, Germany).

3.2.12 Blood glucose evaluation

Blood glucose levels were analysed from blood plasma samples. Measurements were performed with the blood glucose analyser Ascenia Elite (Bayer, Germany) with the supplied sensor strips.

3.2.13 Statistical analysis

Mean values, standard deviations and standard error of the mean (SEM) were determined from the indicated sample size (n). Regarding the primary screen of the GMC and the bone densitometry data obtained by μ CT measurements, one-way ANOVA analysis was performed to check for statistical significance. pQCT analysis as well as fracture rate, weight and size data of the alendronate treatment were statistically analysed using the Student's t-test. The remaining *Aga2/+* data was tested applying the non-parametric Mann-Whitney U test. The analysis tool from Excel as well as the StatView software (SAS cooperation) was used for the different tests. P-values below 0.05 were chosen to be significant and significance-ranking was grouped according to the following classification: * = $p \leq 0.05$, ** = $p \leq 0.01$, *** = $p \leq 0.001$.

4. Results

4.1 *Ali34*

4.1.1 Phenotypical characterisation of *Ali34* during embryogenesis

Preliminary phenotyping data on *Ali34* embryos (during my diploma thesis) revealed defects in vascular patterning and vertebral development that partially coincide with recently published knockout studies⁸⁸⁻⁹⁰. To confirm alterations observed in *Ali34* during embryogenesis and to compare the data with the knockout phenotypes, additional skeletal preparations of embryos at 18.5 dpc were analysed to perform statistical evaluation (Table 7).

Table 7. Summary of skeletal phenotypes observed during late embryogenesis

	+/+ (n=15)	<i>Ali34</i>/+ (n=26)	<i>Ali34</i>/<i>Ali34</i> (n=13)
sternal bones	-	8	13
crooked formation	-	8	10
enhanced ossification	-	-	5
fusion	-	-	2
Xiphoid process	-	-	13
split ossification	-	-	5
broadening	-	-	8
vertebrae	-	-	13
cervical malformation	-	-	3
thoracic malformation	-	-	13
lumbar malformation	-	-	11
sacral malformation	-	-	1
exencephaly	-	-	3

Mispatterning of developing vertebral bodies was the most prominent skeletal hallmark of homozygous *Ali34* embryos, occurring in the cervical to lumbar region in all analysed specimens (Figure 10A). The absence of calvarial bones was evident in 23% of all cases. Analysis of earlier developmental stages (9.5 dpc) revealed that exencephaly is caused by a defective neural tube closure (Figure 10B). Furthermore, the crooked formation of sternbrae, a so far not described phenotype for *Ptxnd1* knockouts is in conjunction with a shifted arrangement of ribs to the sternum and was fully penetrant in homozygous embryos. Alterations in the sternbrae varied from crooked formation to complete fusion of the sternal bones. Furthermore, the xiphoid process in all embryos exhibited either splitting or

broadening with complete ossification (Figure 10C). Interestingly, also *Ali34*^{+/+} embryos showed sternbral alterations (31%), however defects were restricted to a slightly crooked arrangement. Another phenotype described for *Plxnd1* knockouts was the development of a persistent truncus arteriosus (PTA), a congenital form of heart disease caused by defective remodelling of the outflow tract. To assess if this phenotype was also observable in *Ali34*, hearts were dissected prior to skeletal staining. All homozygous embryos displayed the described failed septation of the truncus arteriosus into the pulmonary artery and the aorta (Figure 10D). As PTA can cause cyanosis and heart failure, the phenotype is considered to be causative for neonatal lethality in both *Ali34* and *Plxnd1* knockouts.

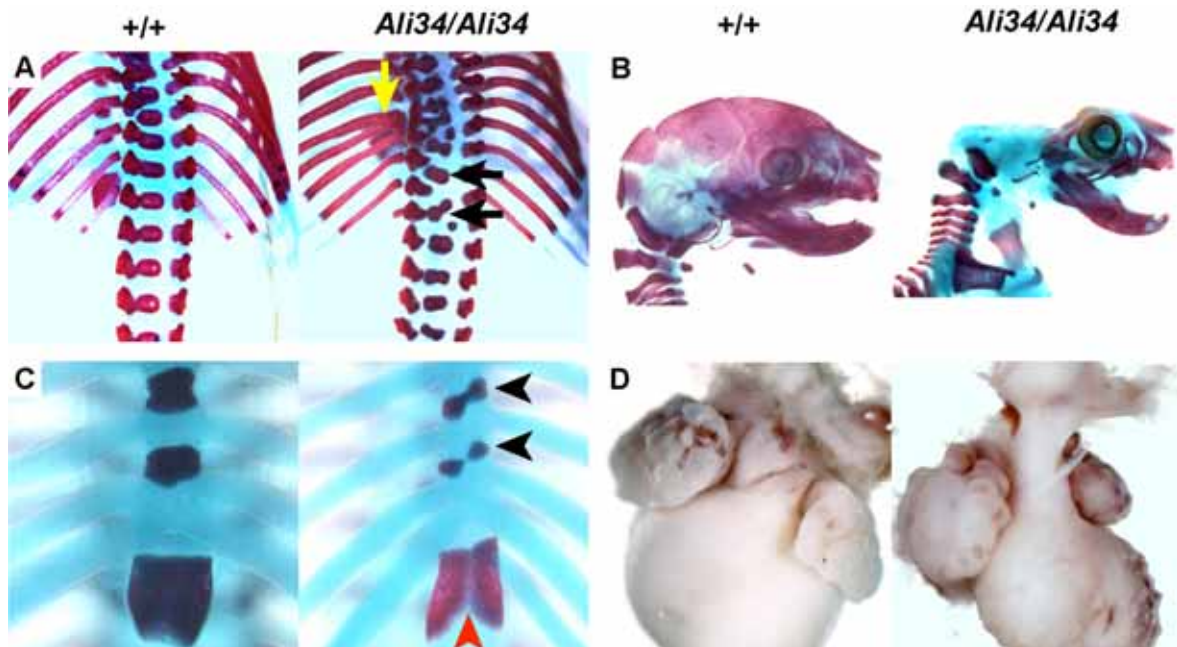


Figure 10. *Plxnd1*^{*Ali34/Ali34*} phenotypes during embryogenesis.

A Vertebral column phenotype comprises vertebral body malformations (black arrows) and rib fusions (yellow arrow) in homozygous embryos. **B** Additionally, 23% of all homozygous E18.5 embryos display exencephaly. **C** Sternal bones exhibit a crooked formation (black arrowheads) and possessed malformed xiphoid processes (red arrowhead). **D** In all *Plxnd1*^{*Ali34/Ali34*} embryos a persistent truncus arteriosus is evident.

As whole mount PECAM antibody staining of 10.5 and 12.5 dpc embryos displayed the recently reported vascular mispatterning⁸⁸⁻⁹⁰ (Figure 11A), antibody stainings on histological sections were analysed to link defective blood vessel guidance to *Plxnd1* expression. To clarify, if *Plxnd1*^{*Ali34*} was still evident in embryonic tissue, homozygous *Ali34* embryos were stained for *Plxnd1* and compared with wild-type littermates at 12.5 dpc. The mutated protein was evenly expressed in intersomitic vessels (Figure 11B). Furthermore, PECAM antibody

stainings showed abnormal blood vessel invasion into the developing somites (Figure 11C), indicating that repulsive signalling through Plxnd1 got lost due to truncation of the protein in *Ali34*, while expression is not altered. In *Ali34/+* embryos no alteration in blood vessel patterning was observed at this stage (not shown).

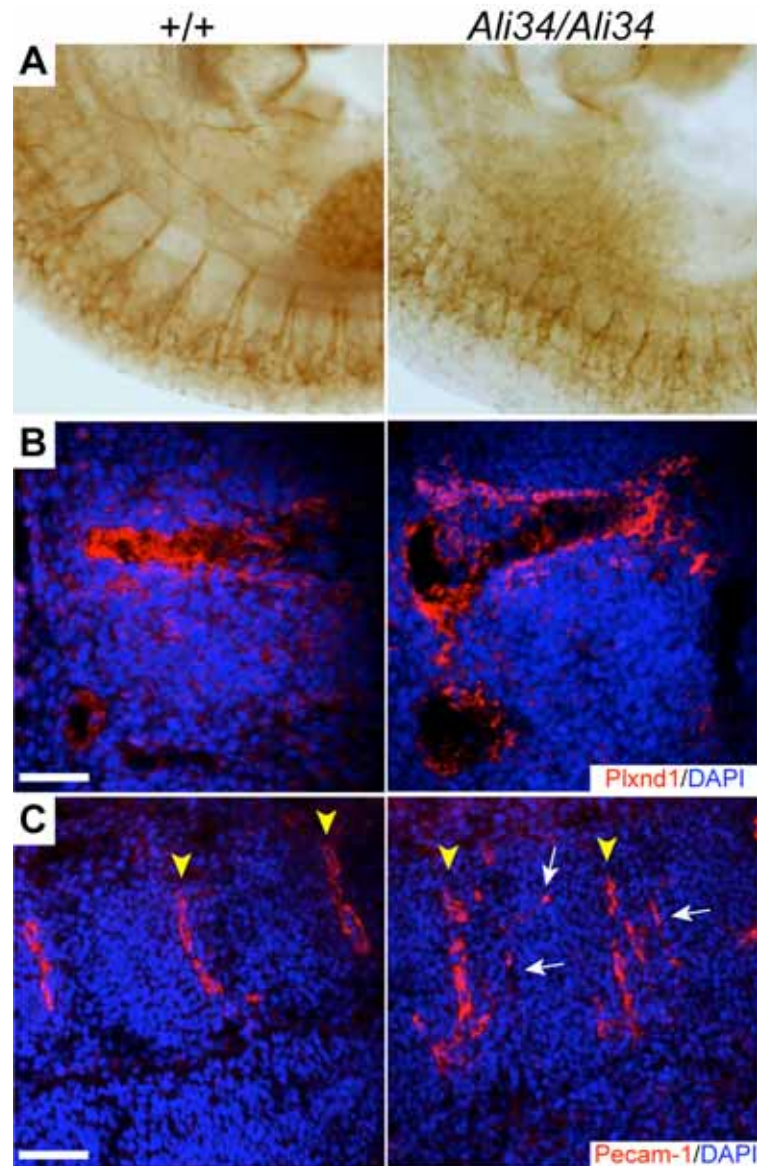


Figure 11. Immunohistochemical stainings of 12.5 dpc embryos.

A Whole mount Pecam-1 antibody staining of wild type and *Ali34/Ali34* embryos. In the developing somites excessive blood vessel invasion is seen in the homozygous embryos. **B** Positive staining of Plxnd1 is evident in homozygous *Ali34* embryos in the region of the developing somites lining the intersomitic blood vessels, indicating that Plxnd1^{*Ali34*} is still expressed. **C** Pecam-1 staining of the same region exhibits blood vessel invasion into the normally avascular somites (white arrows) in homozygous embryos, while intersomitic vessels (yellow arrowheads) are wild-type like. Scale bars in B = 50 μm; C = 100 μm.

To further investigate Plxnd1 expression during embryogenesis, additional antibody stainings were conducted. The protein was detectable in the dorsal root

ganglia and its surrounding vasculature, as well as in the notochord and main vessels (Figure 12A,B). In addition, *Plxnd1* was also evident in the developing heart, especially in the regions of the outflow tract and the developing atria (Figure 12C). Finally, also the lung endothelium displayed *Plxnd1* positive regions (Figure 12D).

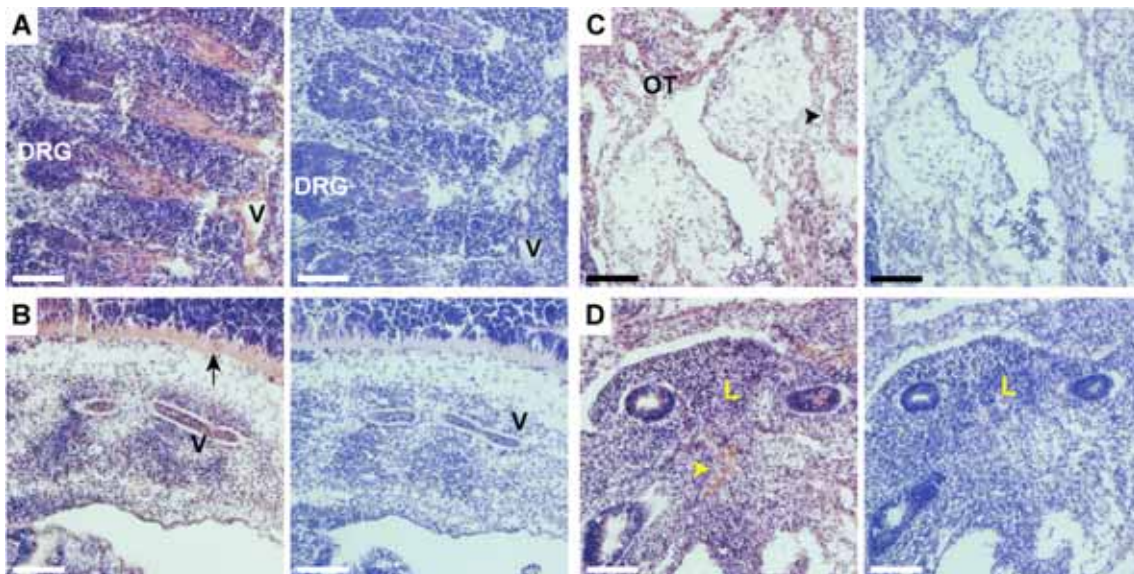


Figure 12. *Plxnd1* expression analysis in 11.5 dpc embryos.

Plxnd1 staining was evident in the dorsal root ganglia (DRG) and in the intersomitic vessels (A), in the notochord (black arrow) and main vessels (V) developing adjacent to the somites (B), in the developing heart where the outflow tract (OT) and atria (arrowhead) displayed intensive staining (C) and the lung endothelium (yellow arrowhead) (D). The second pictures of A-D display the corresponding negative controls. Scale bars = 100 μ m. V = main blood vessel; L = Lung tissue. Scale bars = 100 μ m.

In summary, the various phenotypes reported for *Plxnd1* knockouts were confirmed in *Ali34*. In addition, exencephaly as well as sternal bone alterations were identified for the first time. Antibody staining in 11.5 dpc embryos pointed to a more general impact of *Plxnd1* in angiogenic and also neuronal processes in other organs.

4.1.2 Characterisation of the bone phenotype in *Ali34*/+

4.1.2.1 Development and severity of the skeletal phenotype

Previously obtained data (see my diploma thesis and PhD thesis by Dr. Thomas Lisse) characterised phenotypical hallmarks of non-inflammatory osteoarthritis and chondrodysplasia, as well as the development of osteophytes and ankylosis in

heterozygous mutants (Figure 13). Phenotypes were initially observable at the age of 4 weeks by outer inspection. Thus, it seemed reasonable that bone alterations were caused in a currently unknown developmental manner.

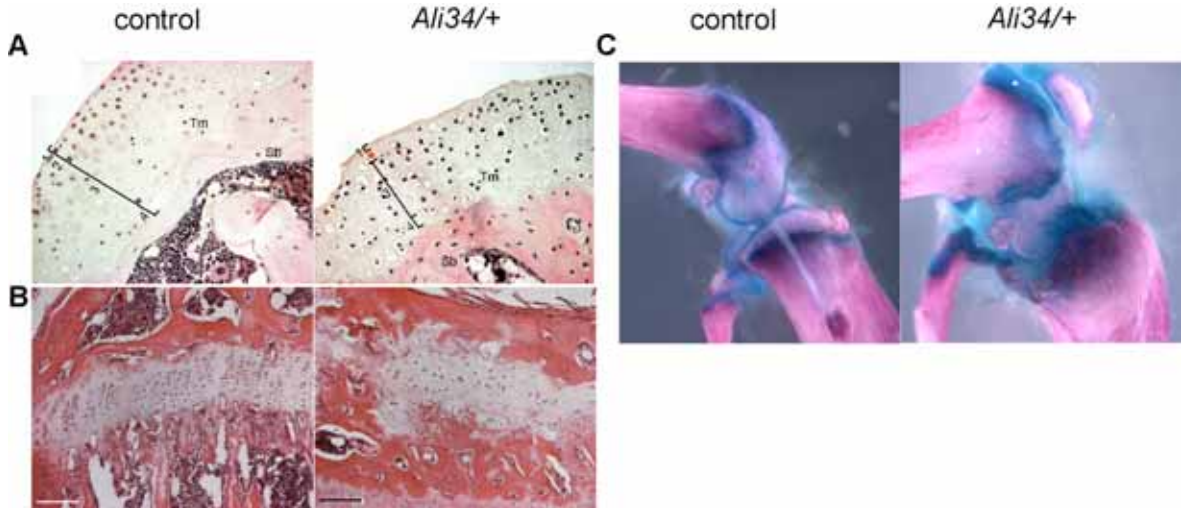


Figure 13. Phenotypical hallmarks known from previous characterisations.

A Osteoarthrosis is evident in 8-weeks old *Ali34/+* tibial and femoral bones. Additional to the bone erosion, the intermediate zone of the articular cartilage is missing. **B** Chondrodysplasia phenotype in *Ali34/+* shows complete depletion of the chondrogenic process, where only hypertrophic chondrocytes are sparsely distributed in the epiphyseal plate. **C** Thickening of the knee joint is evident in *Ali34/+* animals with concurrent appearance of osteophytes at the medial and lateral portion of the tibia. Furthermore, the tibial epiphyseal plate is not detectable, while the femoral growth plate displays malformation compared to wild-type controls. Tm = tidal mark; Sb = subchondral bone. Scale bars = 200 μ m

As *Ali34/+* embryos did not show alterations in their hindlimb bones, newborn mice were subsequently analysed. Comparison of skeletal stainings between *Ali34/+* and wild-type mice revealed no observable alterations in bone composition (Supplemental Figure 1). The overall length of the hindlimb bones appeared normal and the cartilaginous portion of both tibia and femur revealed no alterations in their shape. Histological analysis by H&E staining also ruled out defects in endochondral bone formation. In contrast to the wild-type like development of *Ali34/+* newborn mice, alterations were observable between the age of one and two weeks. In conjunction with the development of the secondary ossification centre arising shortly after birth, cartilage canals invaded the epiphysis. In *Ali34* these canals appeared to be misguided through parts of the epiphyseal plate, connecting the primary and the secondary ossification centre in both tibial and femoral bones. Notably, in the middle of both bones mispatterning was observed first (Figure 14 A,B). In two weeks old mutant hindlimb bones alcian blue staining, visualizing cartilaginous tissue revealed bony structures, which replaced cartilage

and divided the growth plate. Furthermore, nearby chondrocytes in close proximity exited the general columnar formation in a proximal-distal manner and tended to orientate to newly formed bone (Figure 14C). Alterations in the VEGF expression of *Ali34/+* chondrocytes, which might also influence endochondral bone formation were excluded as the invading cartilage canals exhibited strong VEGF expression (Figure 14D).

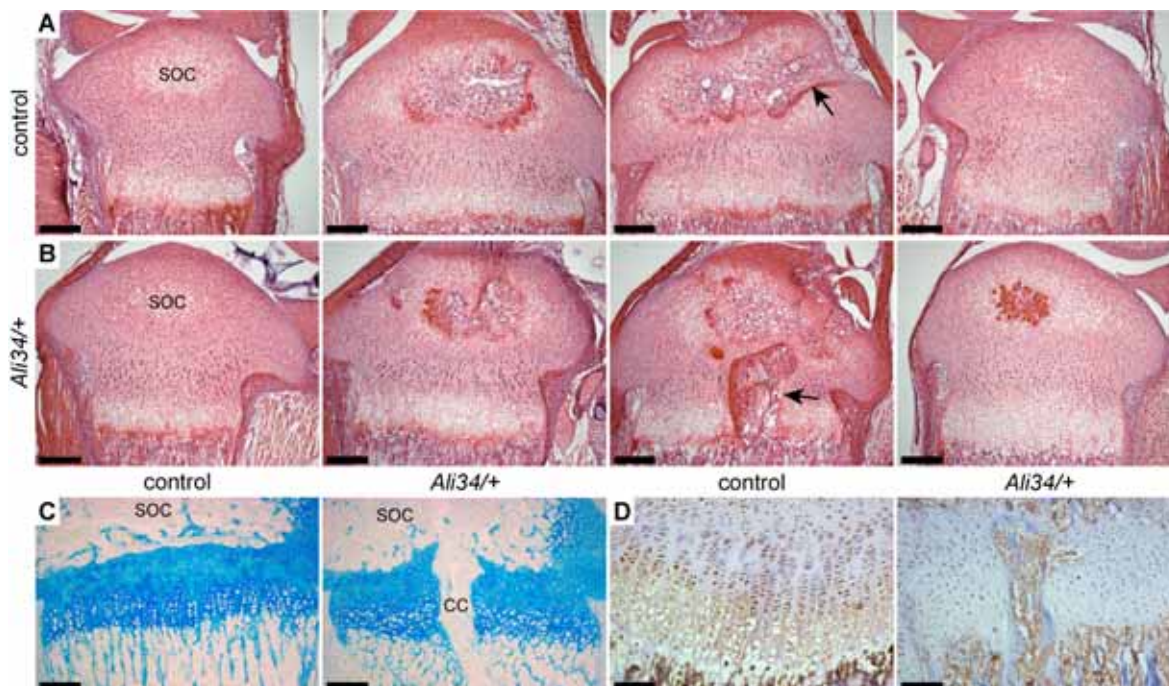


Figure 14. Cartilage canal misguidance results in ectopic bone formation.

A,B Sections through the tibial bone of one week old control (**A**) and *Ali34/+* (**B**) mice stained with H&E. While cartilage canals in wild types invade the future secondary ossification centre only, mutant bones exhibit canal misguidance through the epiphyseal growth plate (arrow) only visible in the inner portion of the bone. **C** Alcian blue staining of two weeks old wild type and *Ali34/+* tibial bones. While control mice display a continuous staining of the growth plate, *Ali34/+* mice show depletion of cartilaginous tissue at misguided cartilage canals forming ectopic bone. **D** VEGF staining of two weeks old mice exhibits no alterations between control and mutant chondrocytes. Notably, cartilage canals display strong VEGF staining. CC = cartilage canal; SOC = secondary ossification centre. Scale bars in A,B = 200 μ m; C,D = 100 μ m.

Screening of 2-weeks old *Ali34/+* hindlimb bones confirmed that every heterozygous animal displayed cartilage canal misguidance with ectopic bone formation. In addition, transverse sections identified that the number and area of ectopic bone formation through the endochondral plate varied between different hindlimb bones (Figure 15A). This observation correlated with longitudinal sections where severity of the chondrodysplasia phenotype was dependent on the number of observable ectopic bone formation events. Analysis of skeletal stainings identified broadening of the tibial surface already in 2-weeks old *Ali34/+* mice.

Additionally, alizarin red staining clearly visualized the amount of ectopic bone growing through the epiphyseal plate (Figure 15B-D).

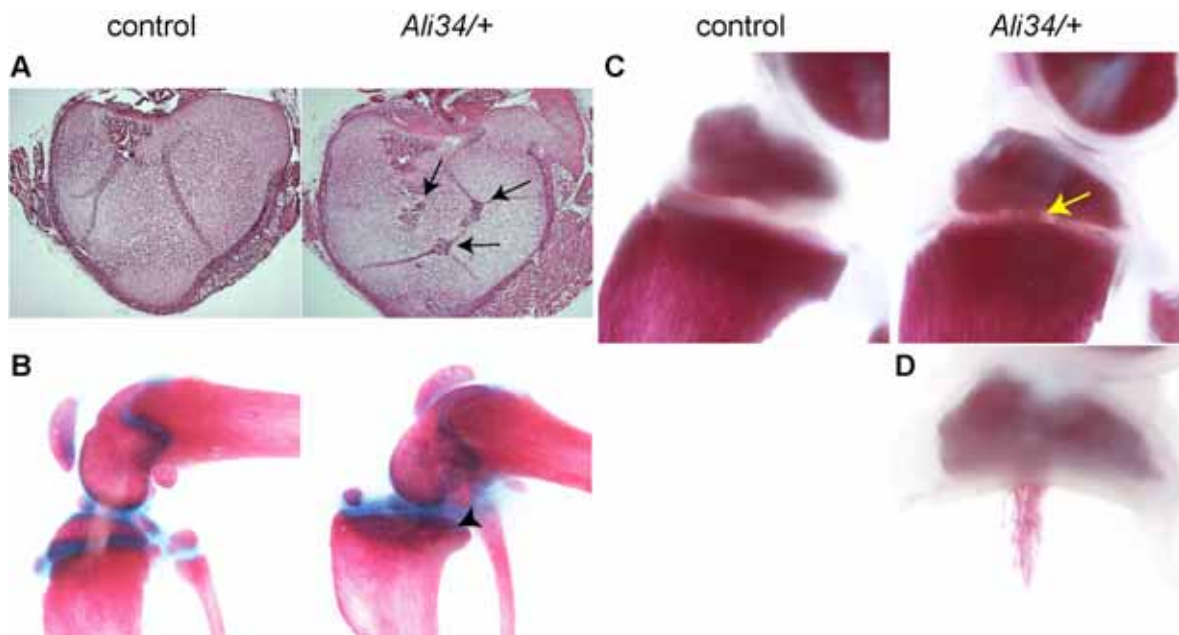


Figure 15. Phenotypes in 2-weeks old *Ali34/+* mice.

A Transverse sections through the tibial growth plate exhibit numerous ectopic bone formation events in *Ali34/+* (black arrows) while wild-type cartilage does not show bone formation. **B** Skeletal staining displayed broadening of the tibial surface with a reduction in secondary ossification centre height and a nearly absent epiphyseal plate already in 2-weeks old in *Ali34/+* animals. **C** Alizarin red stainings confirmed ectopic bone formation to be exclusively evident in *Ali34/+* mice (yellow arrow). **D** The growth plate was removed from a mutant tibial bone to better visualize ectopic bone formation.

Given the fact that bone disrupts the growth plate of long bones, it seemed reasonable that other bones were also affected. To proof this hypothesis, the remaining main long bones (radius, ulna, humerus) were analysed histologically. While radius and ulna were not affected, the proximal growth plate of the humerus also displayed ectopic bone formation (Figure 16). Unlike the hindlimb bones, no broadening or skeletal rearrangements were detected in the glenohumeral joint. To follow up the growth plate alterations found in all heterozygous *Ali34* animals at the age of 2 weeks, further analyses of 4- and 8-weeks old mice were performed to correlate their ankylotic phenotype to the observations from 2-weeks old animals.

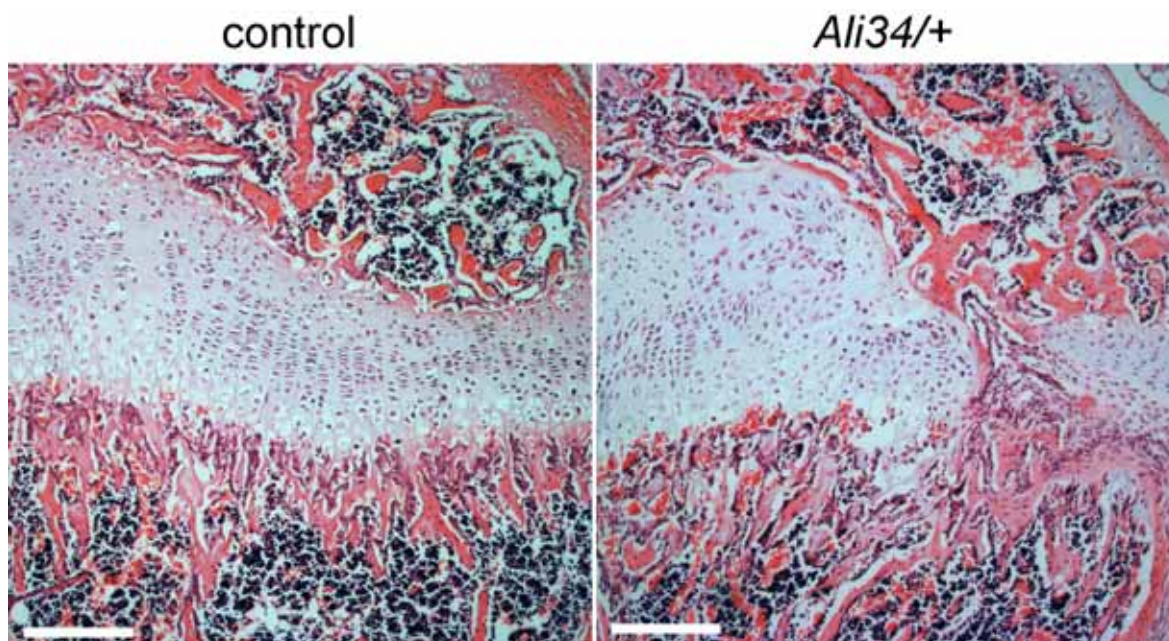


Figure 16. Epiphyseal plate of the proximal humerus of 2-weeks old animals.

H&E staining of the proximal humeral epiphysis in two weeks old wild type and *Ali34/+* mice. Ectopic bone formation is evident in *Ali34/+* growth plates connecting the secondary with the primary ossification centre. Scale bars: 200 μ m

In 4-weeks old mutants, further disruption of the growth plate was evident. The epiphyseal plate was reduced in length and proliferating chondrocytes either tended to orientate to the newly ectopic bone instead of following the normal proximal-distal columnar development or the newly formed bone shifted the cartilage into the primary ossification centre where it was progressively replaced by compact bone (Figure 17A, 18 B). Additionally, subchondral sclerosis with enhance compact bone formation was evident in areas of ectopic bone formation. Consequently, an increase in bone width was favoured over length, while cortical bone formation was enhanced. In addition, the articular cartilage of 4-weeks old *Ali34/+* hindlimb bones already displayed the absence of the intermediate zone as it was previously reported for older animals (Figure 17B). TRAP staining revealed no obvious alterations in the overall number and distribution of osteoclasts in *Ali34/+* hindlimb bones (Figure 17C). In 8-weeks old mice, further broadening of the metaphyseal area was observed as well as a progressive depletion of the cartilaginous zone of the epiphyseal plate (Figure 18A). In severely affected 8-weeks old *Ali34/+* animals, a split of the epiphyseal plate was evident, resulting in two independent zones of bone formation leading to osteophytes enclosing the joint cavity at the lateral portion. Thus, the two parts of the growth plate can vary in their potential to further follow the chondrogenic lineage. As shown in figure 18B,

bone formation was arrested at the medial portion of the tibia due to loss of resting and proliferating chondrocytes. Subchondral sclerosis was visible in the metaphysis, resulting in imbalanced bone formation at the primary spongiosa. However, the lateral part of the epiphyseal plate still followed the endochondral process, resulting in the osteophytic phenotype enclosing the knee joint. Secondary ossification centres of both hindlimb bones appeared flattened, with enhanced compact bone formation.

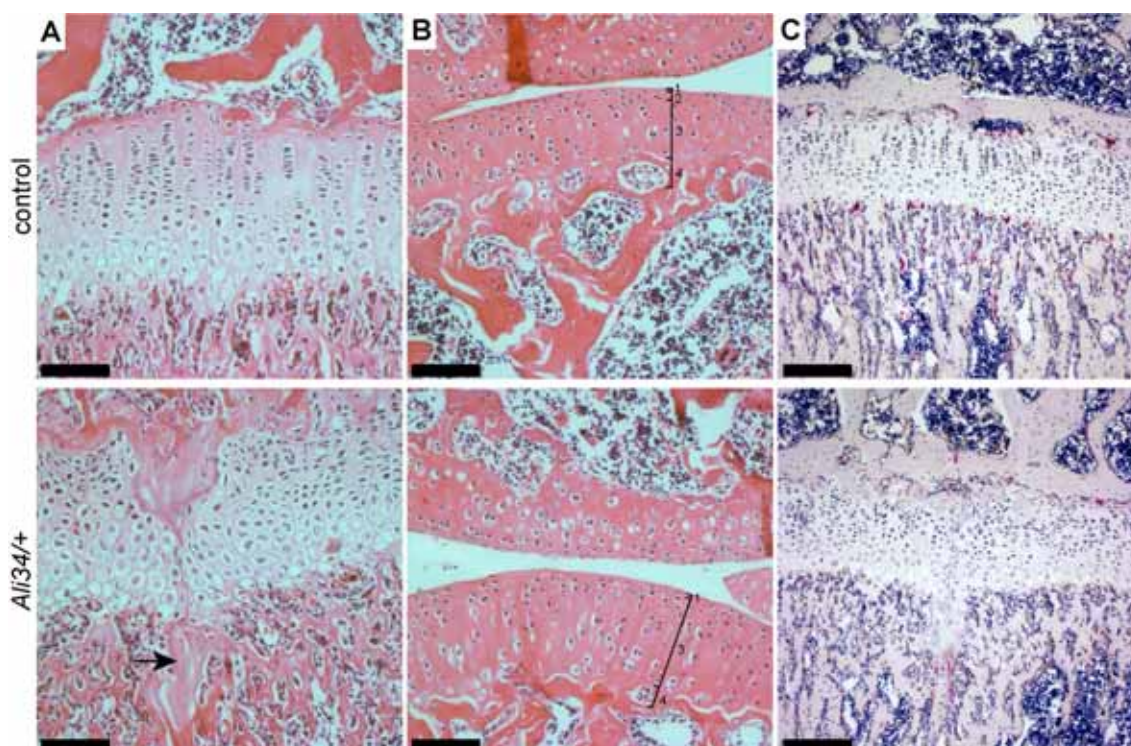


Figure 17. Histological analysis of 4-weeks old *Ali34/+* hindlimb bones.

A H&E staining of the tibial growth plate. Mutants exhibit ectopic bone formation that appeared to be causative for subchondral sclerosis due to compact bone formation beneath the growth plate with irregular columnar development of chondrocytes (arrow). In addition, the proximo-distal length of the growth plate is reduced in mutants. **B** H&E staining of the articular cartilage. The absence of the intermediate zone (2) is evident in *Ali34/+*. **C** TRAP staining displays no alterations in osteoclast number in *Ali34/+* compared to controls. Scale bars in A,B = 100 μ m, C = 200 μ m.

Although femora of *Ali34/+* also displayed ectopic bone formation through the growth plate, the development of osteophytes was never observed. However, subchondral sclerosis was favoured, thus reducing the amount of trabecular bone at the chondro-osseous junction. Additionally, fibrotic tissue was evident in the synovial joint cavities, separating the articular surface of the tibial and femoral bone only in severely affected knee joints. Interestingly, fibrosis could be correlated to the osteoarthritic phenotype, which was exclusively recognizable in severely affected knee joints. Further following up the effects on the knee joints of

older *Ali34*^{+/+} animals identified the development of calcified tissue inside the joint cavity in 17-weeks old mice (Supplemental Figure 2).

Taken together, the initiation of the observable hindlimb phenotype can be traced back to early neonatal developmental defects in bone formation. Depending on the amount of misguided cartilage canals, which result in ectopic bone formation through the epiphyseal plate, hindlimb phenotypes strongly varied in their occurrence and severity, while the most severe forms displayed a progressive destruction of the whole knee joint.

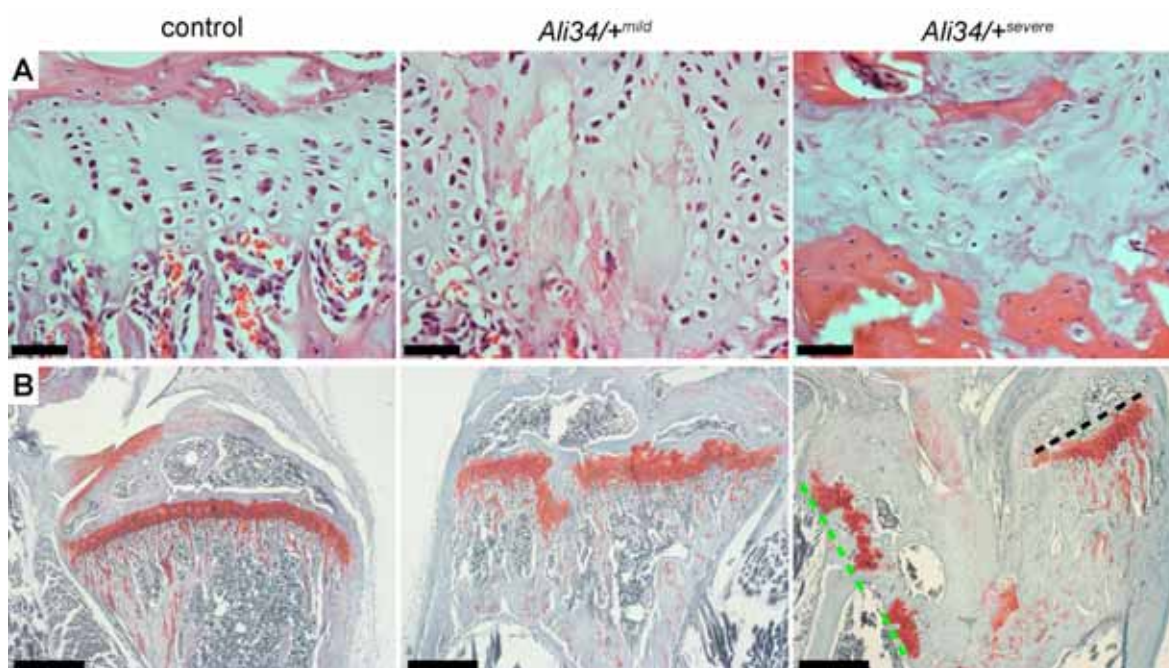


Figure 18. Histological analysis of 8-weeks old *Ali34*^{+/+} hindlimb bones.

A H&E stainings of hindlimb bones of 8-weeks old mice. The regular columnar formation is disturbed in mildly affected animals, while *Ali34*^{+/+ severe} growth plates are depleted of cartilaginous tissue. **B** Safranin O stainings of wild type controls in comparison to mildly and severely affected *Ali34*^{+/+ mild} tibial bones. In *Ali34*^{+/+ mild} the growth plate is partially dislocated. In *Ali34*^{+/+ severe} one part of the growth plate (green dotted line) is arrested. The second part builds up bone, developing osteophytes (black dotted line). Scale bars in A = 50 μ m, B = 1000 μ m.

4.1.2.2 C57BL/6J outcross analysis

During positional cloning of the *Ali34* mutation, it became evident that the phenotype of shortened hindlimb bones and stiffening of the knee joint vanished when mice were outcrossed to *C57BL/6J* or other inbred strains (see PhD thesis of Dr. Thomas Lisse). Additionally, hindlimb bone defects in *Ptxnd1* knockouts on different genetic backgrounds were not reported^{89,90}. Based on these facts and in conjunction with the knowledge that *Ali34*^{+/+} animals on the *C3HFeB/FeJ*

background displayed a gradual severity the hypothesis arised, that minor defects might also be detectable in outcrossed mutants. For this purpose, *Ali34/+* animals were outcrossed on *C57BL/6J* for a total of four generations while every generation was analysed. As the first generation results in 50% *C57BL/6J* background, 93.75% were statistically achieved in the fourth generation.

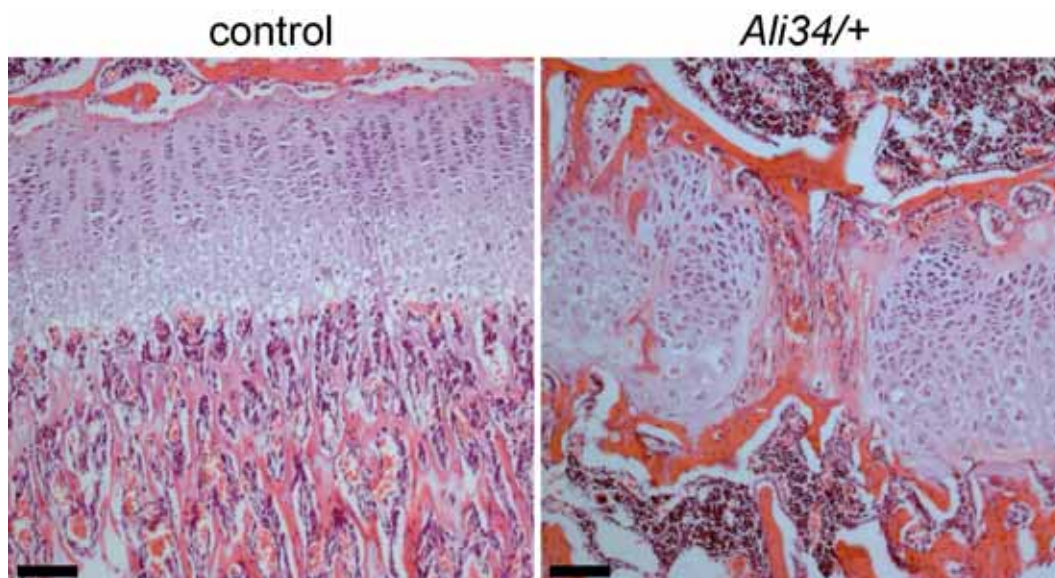


Figure 19. Ectopic bone formation in *Ali34/+* outcrossed to the *C57BL/6J* inbred strain. Two weeks old mutant mice outcrossed to the *C57BL/6J* inbred strain also display ectopic bone formation caused by cartilage canal misguidance. Trabecular bone formation is disturbed, but broadening of the bone is only slightly enhanced. Scale bars = 100 μ m.

Throughout every generation, ectopic bone formation varying in size and number was evident in *Ali34/+* hindlimb bone sections (Figure 19). Additionally, chondrocytes also orientated to newly formed bone with slight broadening of the tibial bone, although not to a comparable extent as observed for *Ali34* on the pure *C3HFeB/FeJ* background. Analysis of the hindlimb bone length revealed only a trend towards shortening. Furthermore, the development of osteophytes as well as ankylosis and osteoarthritis were never observed in these animals. In summary, blood vessel mispatterning, which caused ectopic bone formation in the epiphyseal plate was still evident in *Ali34/+* animals outcrossed onto the *C57BL/6J* genetic background. Further effects observed for the *C3HFeB/FeJ* background were not confirmed.

4.1.2.3 Expression analysis

To verify the alterations observed on the morphological level, expression analysis of several bone and cartilage markers, as well as *Plxnd1* and its putative downstream targets was performed with cDNA obtained from one week old animal hindlimb bones.

Preliminary data of three animals per genotype showed that *Plxnd1* expression was not regulated among the samples (Figure 20A). Notably, a trend towards upregulation of *Mmp9* and *Col1a1*, accounting for cartilage matrix degradation and bone formation, was identified (Figure 20B,C). This trend was mainly caused by one *Ali34/+* probe (*Ali34/+* 3) that especially displayed elevated expression levels only for those two genes. Additionally, the three main VEGF-A isoforms were equally expressed in both wild type and *Ali34/+* tissue (Figure 20D-E). In all other markers tested, expression levels revealed no significant alterations between mutant and control samples.

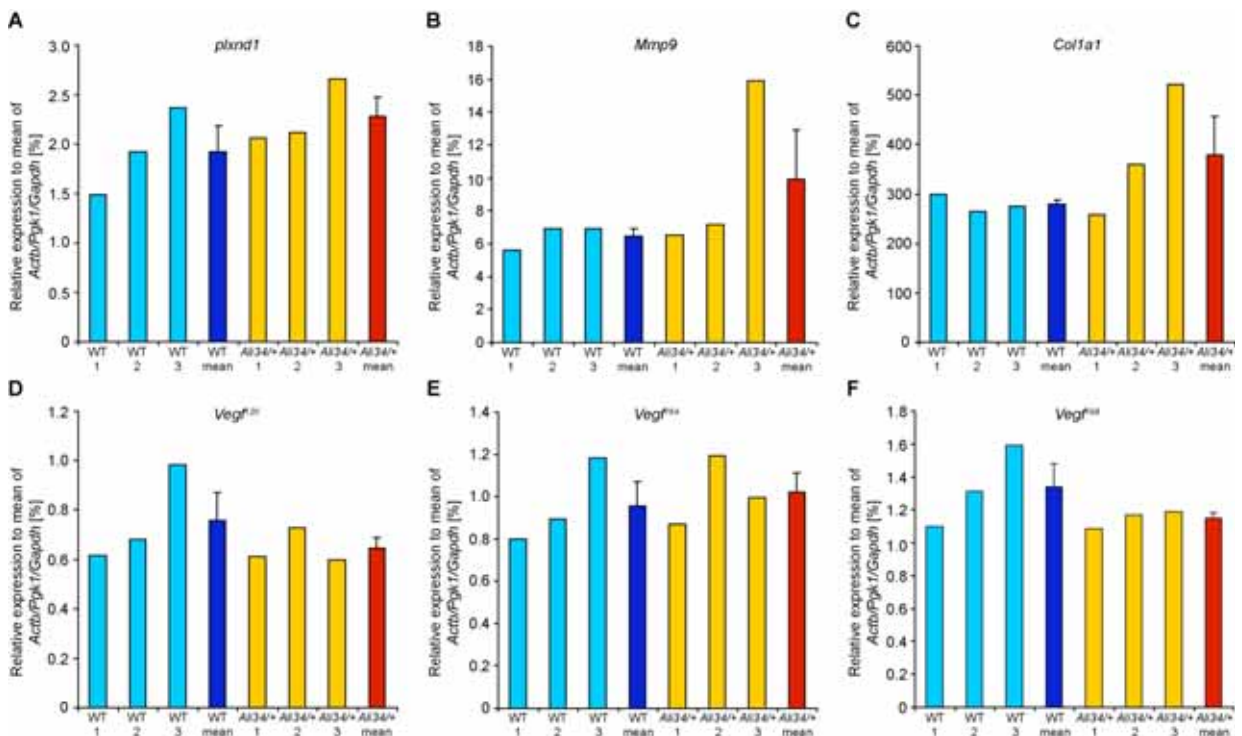


Figure 20. qRT-PCR analysis of one week old hindlimb bone samples.

Relative expression of three wild type (light blue) and three *Ali34/+* samples (orange) with their corresponding mean values (dark blue and red) to the mean of the housekeeping genes *Actb*, *Pgk1* and *Gapdh*. **A** *Plxnd1*, **B** *Mmp9*, **C** *Col1a1*, **D** *Vegf¹²⁰*, **E** *Vegf¹⁶⁴*, **F** *Vegf¹⁸⁸*. Error bars are represented as SEM.

Taken together, an elevated matrix degradation process, as well as an increased amount of cartilage canals in conjunction with bone formation was suggested by preliminary qRT-PCR data. However, more samples have to be analysed, to obtain significant results because variation in different *Ali34/+* animals regarding *Mmp9* and *Col1a1* expression was very high.

4.1.2.4 *In vitro* analysis of primary osteoblasts

As *Plxnd1* expression was already reported for osteoblasts^{89,90}, a possible direct phenotype on osteoblasts was hypothesised. For example, a reduced nodule formation, necessary for the development of osteocyte like structures during the cell culture period might be evident. A comprehensive *in vitro* primary osteoblast culture system was utilized to identify possible alterations in *Ali34/+* osteoblasts (experiments were performed in collaboration with Dr. Frank Thiele). In 9 different quantifiable assays, general properties of cell growth as well as the analysis of bone specific parameters at the functional, protein and transcriptional level were assessed throughout a three weeks culture period in a kinetic fashion.

For metabolic activity, protein content and ALP activity no alterations could be detected at all time points analysed (Figure 21A-C). Furthermore, collagen secretion and deposition displayed wild-type like values (Figure 21D,E). The formation of nodules, which was hypothesized to reveal potential alterations, showed no reduction compared to wild-type cells (Figure 21F). Finally, expression analysis of 14 different genes identified no alterations in *Ali34* (Supplemental Table 1).

All in all, intrinsic effects caused by the *Ali34* mutation on osteoblasts can be ruled out as none of the measured parameters displayed alterations at least in the first three weeks of the culture.

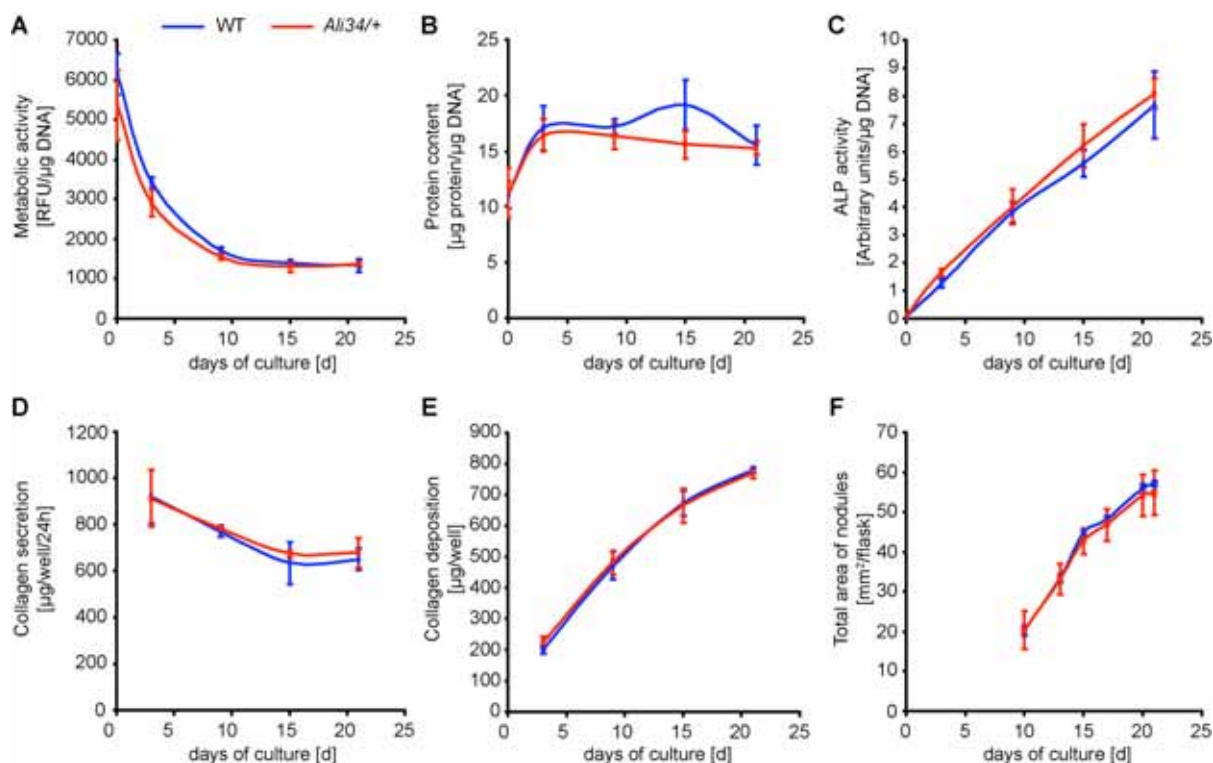


Figure 21. Data evaluation of the *in vitro* assays in primary osteoblasts of *Ali34/+* and controls.

A The metabolic activity displays no alterations between *Ali34/+* and control cells. **B** Protein content and **C** ALP activity is unchanged in both groups. **D**, **E** Collagen secretion and deposition are wild-type like. **F** Nodule formation in both control and *Ali34/+* osteoblasts reveals no alterations throughout the culture period. Error bars represent SEM values.

4.1.3 Primary Screen of the GMC

Given the broad spectrum of *Plxnd1* expression, *Ali34* was analysed in the primary screen of the GMC to identify possible new phenotypes which are linked to the underlying mutation. For each GMC pipeline 40 animals (20 wild type, 20 *Ali34/+* subdivided into 10 males and 10 females) were screened in the GMC standard workflow (Figure 9).

4.1.3.1 Dysmorphology screen

The Dysmorphology screen investigates the general morphological appearance of the body and the skeleton by outer inspection, X-ray analysis and by DXA, as well as hearing ability by the clickbox test. While *Ali34/+* animals performed wild-type like in the clickbox test and did not show alterations in the general appearance apart from the already known hindlimb phenotypes, DXA parameters displayed alterations in body composition (Table 8). Measurements for BMD in both sexes

showed a trend towards decreased values, while male *Ali34/+* BMC values were significantly decreased. Female mice displayed a tendency towards a decreased BMC. Furthermore, body weight and fat mass reduction in *Ali34/+* animals was evident. All other parameters revealed no significant differences among the analysed groups. For a detailed analysis of both BMD and BMC parameters obtained by DXA, and to quantify alterations in the knee joints of *Ali34/+* mice, secondary screening by pQCT was chosen as a sequentially next step (Figure 22). Previous data (PhD thesis by Dr. Thomas Lisse) already gave a general hint on expected alterations in bone parameters. With the possibility to genotype every mouse and the knowledge that every heterozygous animal displays ectopic bone formation, a more detailed view could be achieved. 17-weeks old *Ali34/+* animals were subdivided into two groups (*Ali34/+^{mild}* (n=8), *Ali34/+^{severe}* (n=9)) by means of their ankylosis phenotype and compared to their wild type littermates (n=10). For all mice, femoral metaphysis (two slices) and diaphysis (one slice) data were collected (Table 9).

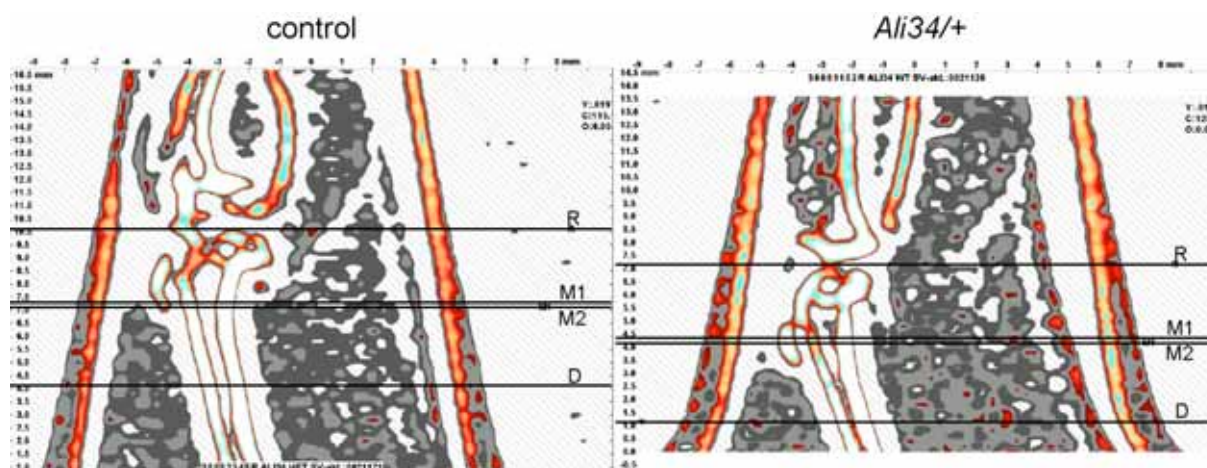


Figure 22. Scout view of the pQCT measurement.

During the scout view a generalized picture of the whole hindlimb is generated. A reference line is set on the top of the femoral articular surface (line labelled as R). Afterwards the program sets two lines in the metaphysis (lines labelled with M1 and M2) and a third line (D) in the femoral diaphysis at a defined distance from the reference line. In these three lines in depth scanning was performed.

When comparing all *Ali34/+* animals with wild-type controls highly significant increased values were obtained in total bone content (+10.69%), total bone density (+7.95%), cortical content (+14.18%) and cortical density (+10.75%), whereas trabecular density (-13.47%) and endosteal circumference (-4.75%) were decreased. Subdivision according to the phenotypic occurrence revealed, that apart from cortical and trabecular density parameters, all other changed values were related to severely affected *Ali34/+* mice. Additionally, animals with ankylosis

exhibited an increased total area (+13.59%) which were traced back to increased cortical area (+23.36%) and periosteal circumference (+6.22%) values. Diaphyseal parameters, showing the effect of possible bone maintenance alterations or altered force distributions also revealed changes compared to wild type. In the comparison of all heterozygous animals with controls, content and area parameters were significantly increased, while the entire density values were decreased. Furthermore, periosteal and endosteal circumference were both increased in all *Ali34/+* mice.

Table 8. Bone and weight-related quantitative parameters by DXA.

Parameter	control		<i>Ali34/+</i>		ANOVA genotype p-value
	male (n=10)	female (n=10)	male (n=10)	female (n=10)	
BMD [mg/cm ²]	55 ±1	56 ±2	52 ±2	53 ±1	n.s.
sBMD [10 ⁻³ x cm ²]	1.76 ±0.03	1.91 ±0.03	1.77 ±0.03	1.99 ±0.04	n.s.
BMC [mg]	589 ±23	587 ±41	513↓ ±50	516 ±40	*
Bone content [%]	1.89 ±0.04	1.99 ±0.11	1.72 ±0.14	1.92 ±0.10	n.s.
Body length [cm]	10.15 ±0.08	10.20 ±0.08	10.20 ±0.11	10.05 ±0.09	n.s.
Body weight [g]	31.06 ±0.64	29.41 ±0.99	29.62 ±0.86	26.59↓ ±0.71	*
Fat mass [units]	7.70 ±0.70	8.74 ±1.27	5.96 ±1.02	6.13 ±1.15	*
Fat content [units x 100/g]	24.53 ±1.78	29.00 ±3.49	19.60 ±2.87	22.36 ±3.46	n.s.
Lean mass [units]	16.58 ±0.39	13.91 ±0.77	16.95 ±0.74	14.11 ±0.73	n.s.
Lean content [units x 100/g]	53.61 ±1.71	47.93 ±3.53	57.63 ±2.76	53.71 ±3.39	n.s.

Results

Table 9. pQCT parameters

Parameter	+/+	<i>Ali34/+</i>	<i>Ali34/+</i> (sev.)	<i>Ali34/+</i> (mild)	t-test				
	(A) (n=10)	(B) (n=17)	(B1) (n=9)	(B2) (n=8)	A-B	A-B1	A-B2		
metaphysis	Total Content [mg]	2.535 ±0.048	2.806 ±0.060	3.331 ±0.114	2.589 ±0.040	***	***	n.s.	
	Total Density [mg/cm ³]	677.374 ±12.794	731.203 ±9.843	788.695 ±16.944	707.457 ±10.126	***	***	*	
	Total Area [mm ²]	3.753 ±0.045	3.85 ±0.076	4.263 ±0.180	3.679 ±0.063	n.s.	**	n.s.	
	Cortical Content [mg]	2.193 ±0.065	2.504 ±0.062	3.057 ±0.113	2.276 ±0.041	***	***	n.s.	
	Cortical Density [mg/cm ³]	824.828 ±5.902	913.498 ±8.096	947.395 ±17.653	899.498 ±7.945	***	***	***	
	Cortical Area [mm ²]	2.65 ±0.068	2.746 ±0.071	3.269 ±0.169	2.53 ±0.040	n.s.	**	n.s.	
	Trabecular Content [mg]	0.344 ±0.023	0.302 ±0.013	0.273 ±0.023	0.313 ±0.015	n.s.	*	n.s.	
	Trabecular Density [mg/cm ³]	311.718 ±3.067	269.723 ±3.440	274.842 ±7.222	267.609 ±3.795	***	***	***	
	Trabecular Area [mm ²]	1.104 ±0.074	1,104 ±0.040	0.994 ±0.077	1.15 ±0.045	n.s.	n.s.	n.s.	
	Periosteal circumference [mm]	6.863 ±0.041	6.935 ±0.067	7.29 ±0.151	6.789 ±0.058	n.s.	**	n.s.	
	Endosteal circumference [mm]	5.267 ±0.083	5.017 ±0.075	5.007 ±0.157	5.021 ±0.085	*	n.s.	*	
	diaphysis	Total Content [mg]	2.153 ±0.039	2.284 ±0.049	2.391 ±0.123	2.249 ±0.049	*	n.s.	n.s.
		Total Density [mg/cm ³]	1023.230 ±9.123	986.130 ±7.952	953.788 ±11.480	996.480 ±8.889	**	***	*
		Total Area [mm ²]	2.110 ±0.047	2.326 ±0.059	2.513 ±0.140	2.266 ±0.060	**	*	*
Cortical Content [mg]		2.098 ±0.037	2.218 ±0.047	2.313 ±0.120	2.188 ±0.047	*	n.s.	n.s.	
Cortical Density [mg/cm ³]		1132.870 ±4.776	1118.576 ±5.711	1108.438 ±11.521	1121.820 ±6.442	*	*	n.s.	
Cortical Area [mm ²]		1.852 ±0.034	1.986 ±0.048	2.094 ±0.129	1.952 ±0.047	*	n.s.	*	
Trabecular Content [mg]		0.056 ±0.004	0.067 ±0.003	0.079 ±0.005	0.063 ±0.003	*	**	n.s.	
Trabecular Density [mg/cm ³]		221.750 ±5.684	201.352 ±3.573	189.338 ±6.112	205.196 ±3.998	**	***	*	
Trabecular Area [mm ²]		0.258 ±0.020	0.338 ±0.017	0.416 ±0.033	0.313 ±0.018	**	**	*	
Periosteal circumference [mm]		5.142 ±0.058	5.392 ±0.067	5.604 ±0.151	5.324 ±0.069	**	*	*	
Endosteal circumference [mm]		2.797 ±0.055	3.054 ±0.055	3.281 ±0.100	2.982 ±0.058	**	**	*	

4.1.3.2 Behaviour screen

In the behaviour screen, 9-weeks old mice were analysed in the *Open Field* test to investigate possible alterations in unconditioned behaviour. Two weeks later, *Prepulse Inhibition* (PPI) assessed sensorimotor gating. As *Plxnd1* is also evident in neuronal tissue, possible effects were hypothesised. Analysis of the *Open Field* test revealed a significant reduction in the total distance travelled in the second and third measurement period. Rearing frequency and moved distances in either the centre or the periphery do not show significant changes (Table 10). Additionally, PPI identified no alterations in *Ali34/+* mice.

Table 10. Results of the behavioural observations in the Open Field test

Parameter	Control		Mutant		Male+Female		Anova
	male (n=10)	female (n=10)	male (n=10)	female (n=10)	control (n=20)	mutant (n=20)	
Distance Travelled [cm] - 5 min	2751.96 ±294.85	2971.92 ±399.34	2634.41 ±364.44	2409.22 ±304.55	2861.94 ±242.89	2521.82 ±232.57	n.s
Distance Travelled [cm] - 10 min	2993.28 ±200.13	2816.25 ±248.24	2417.75 ±279.28	2310.89 ±252.8	2904.77 ±156.5	2364.32 ±183.74	*
Distance Travelled [cm] - 15 min	2798.84 ±181.81	2858.24 ±158.85	2333.06 ±257.23	2489.41 ±201.17	2828.54 ±117.7	2411.24 ±159.93	*
Distance Travelled [cm] - 20 min	2695.13 ±189.36	2565.02 ±190.99	2055.23 ±169.01	2523.46 ±166.72	2630.08 ±131.74	2289.35 ±127.41	n.s
Distance Travelled [cm] - total	11239.19 ±736.19	11211.45 ±870.47	9440.4 ±1018.27	9733.02 ±874.56	11225.32 ±554.83	9586.71 ±654.1	n.s
Rearing [fre- <i>quency]</i> - 5 min	5.9 ±1.72	7.9 ±2.96	4.9 ±2.19	5.1 ±2.07	6.9 ±1.68	5 ±1.47	n.s
Rearing [fre- <i>quency]</i> - 10 min	13.4 ±3.2	10.2 ±3.44	10 ±3.26	9.8 ±3.3	11.8 ±2.32	9.9 ±2.26	n.s
Rearing [fre- <i>quency]</i> - 15 min	17.8 ±3.45	15.6 ±3.86	11.6 ±3.49	14.9 ±3.12	16.7 ±2.53	13.25 ±2.31	n.s
Rearing [fre- <i>quency]</i> - 20 min	16.9 ±3.24	18.6 ±3.87	10.6 ±2.58	16.8 ±3.93	17.75 ±2.47	13.7 ±2.4	n.s
Rearing [fre- <i>quency]</i> - total	53.8 ±10.65	52.1 ±12.98	37.1 ±10.64	46.5 ±11.58	52.95 ±8.17	41.8 ±7.73	n.s

4.1.3.3 Neurology screen

The neurology screen analyses the overall neurological reflexes to determine neurological functions of a mouse by SHIRPA-analysis at the age of 9 weeks. In addition, grip strength and rotarod performance were analysed to investigate muscle strength and motor coordination.

In the primary screen, the SHIRPA protocol revealed no significant differences in neurological issues. Tendencies towards abnormal gaiting and hind feet claspings

were observed only for males. Grip strength of forepaws as well as all paws was wild-type like. In the rotarod analysis, *Ali34/+* male mice displayed a significant reduction in their performance (Figure 12A) throughout all three experiments (Figure 12B).

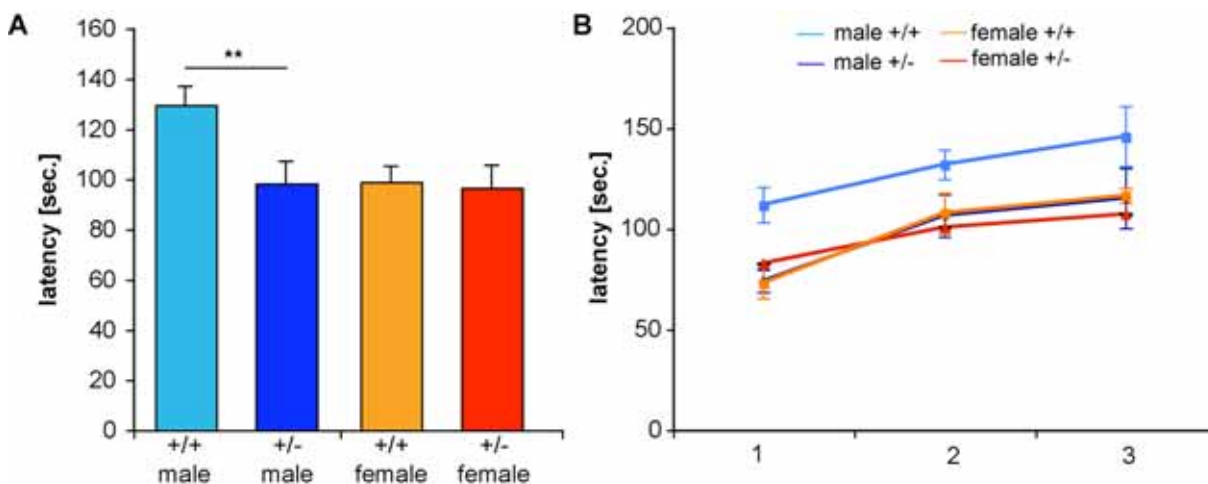


Figure 23. Results of the primary neurology screening in the GMC.

A Results of the rotarod analysis display a significant reduction in performance in male *Ali34/+* mice. **B** Overview of the three experiments performed with the same animals. Males display the significant reduction throughout all tests.

4.1.3.4 Eye screen

The eye screening of the GMC includes the investigation by funduscopy, slit lamp biomicroscopy, laser interference biometry (LIB), histology and general morphology. As the retinal vasculature develops postnatal, increased angiogenesis as observed in the secondary ossification centre development seemed to be conceivable.

Results of the screen did not identify alterations in the funduscopy. Instead of a possible vessel mispatterning, vessel attenuation, which is a general observable hallmark of mice on the *C3HFeB/FeJ* background, was confirmed also for *Ali34/+* mice. Axial eye lengths of male mutants exhibited a slight significant increase, while females showed no alterations. For all other tests, *Ali34/+* were comparable to their wild-type controls.

4.1.3.5 Clinical chemical screen

The aim of the clinical chemical screen is the detection of haematological changes, defects of various organ systems, and changes in metabolic pathways and electrolyte homeostasis by means of suitable laboratory diagnostic tools. In summary, 21 clinical-chemical, 10 haematological parameters and glucose tolerance are measured and compared between both groups. In addition a second blood sample was analysed to verify alterations of the first blood sample test.

The first blood sample analysis revealed significant regulation of inorganic phosphorus creatinine, cholesterol, triglycerides and free fatty acids (NFEA). Verification by the second blood sample (Table 11) only displayed a minor but significant reduction in cholesterol levels in *Ali34/+*. Changes of all other parameters were not confirmed.

Table 11. Clinical chemical parameters of the second blood sample.

Parameter	Control (A)		Mutant (B)		genotype <i>p-value</i>
	Male (n=10)	Female (n=10)	Male <i>p-value</i>	Female (n=10)	
Calcium [mmol/l]	2.29 ±0.01	2.28 ±0.02	2.28 ±0.01	2.31 ±0.02	n.s.
inorg. Phosphorus [mmol/l]	1.1 ±0.09	1.22 ±0.08	1 ±0.04	1.18 ±0.1	n.s.
Creatinine [mg/dl]	0.2 ±0.02	0.2 ±0.02	0.2 ±0.01	0.2 ±0.02	n.s.
Urea [mg/dl]	61.8 ±3.54	55.7 ±1.87	60.9 ±1.19	59.2 ±2.18	n.s.
Cholesterol [mg/dl]	162.8 ±3.91	116.1 ±3.6	153.8 ±3.64	108.1 ±2.1	*
Triglycerides [mg/dl]	373 ±19.4	277 ±26.5	321 ±20.5	285 ±18.8	n.s.
NEFA [mmol/l]	1.6 ±0.08	1.9 ±0.06	1.5 ±0.03	1.8 ±0.06	n.s.
LDH [U/l]	283.9 ±12.86	216.9 ±21.33	292.7 ±17.21	247.5 ±28.73	n.s.

4.1.3.6 Molecular phenotyping

The molecular phenotyping screen provides comparative genome-wide expression profiling of personally chosen organs. The analysis of regulated genes is intended to support the understanding of underlying mutations on the molecular level and potentially provides new insights into mammalian gene function¹²⁰. Based on the

findings in *Ali34/+* and with respect to the already known phenotypes of homozygous *Ali34* embryos as well as previously published knockouts, bone and heart tissue of three wild type and *Ali34/+* mice were applied to the screen respectively.

Eight regulated genes were identified for heart tissue (Supplemental Figure 3). Estimation of the number of false positive results by the false discovery rate (FDR) was calculated to 0.3%. Classification by means of molecular functions and biological processes using the PANTHER classification identified three genes (*Col1a1*, *Gabra1*, *Lyzs*) failing to interact between each other. Additional GO-term analysis, screening the datasets for potential under- or over-representation of certain annotations, detected no differences due to a too small number of regulated genes. Analysis of the dataset obtained from bone tissue identified 70 genes which are differentially regulated compared to wild type with a FDR of 6.0% (Supplemental Figure 4). Classification and GO-term analysis revealed motor activity, actin binding, structural constituent of cytoskeleton and ATP binding to be over-represented molecular functions (Table 12). Additionally, several genes were identified to be annotated with the *Wnt*-signalling pathway, cell adhesion and oxidative phosphorylation.

Table 12. GO term analysis of regulated genes in *Ali34/+* bone tissue

Term	Genes	z-Score
motor activity	<i>Myl2</i> , <i>Myh8</i> , <i>Myh7</i> , <i>Myh4</i> , <i>Myh2</i> , <i>Myh1</i>	10.18
actin binding	<i>Actn2</i> , <i>Myh1</i> , <i>Myh4</i> , <i>Myh7</i> , <i>Myh8</i> , <i>Tnni2</i> , <i>Tpm2</i> , <i>Wasf2</i>	9.31
structural constituent of cytoskeleton	<i>Des</i> , <i>Tnni2</i> , <i>Tnnt3</i> , <i>Tpm2</i>	7.76
ATP binding	<i>Ass1</i> , <i>Atp2a1</i> , <i>Chd7</i> , <i>Ckmt2</i> , <i>Dicer1</i> , <i>Myh1</i> , <i>Myh2</i> , <i>Myh4</i> , <i>Myh7</i> , <i>Myh8</i> , <i>Tbk1</i> , <i>Tnni2</i>	5.31

4.1.3.7 Pathology screen

In the pathological screen of the GMC, mutants are weight primarily and investigated macroscopically. Afterwards, general histological analysis of all organs is performed to possibly identify novel phenotypes at the microscopical level.

Besides the confirmation of the hindlimb bone phenotype, one animal displayed a fusion of vertebral bodies between the lumbar and sacral vertebral column. The screen additionally identified novel cardiac phenotypes, while all other organs

showed no abnormalities. Interestingly, the heart weight of *Ali34/+* animals with severe knee joint phenotypes was significantly reduced. In addition, dilatation of the auricle (2/12), focal fibrosis in the pericardium (1/12) and bifurcation of the aortic arch (1/12) were identified in *Ali34/+* mice. The underlying data indicated that *Ali34/+* also displayed minor prevalence towards cardiac defects, although with a very low penetrance.

Taken together, the primary screen of the GMC confirmed the already known bone phenotypes of *Ali34/+* animals and expression analysis detected 70 regulated genes in bone tissue. Additionally, the behavioural and neurological analysis identified a reduction of movement and a reduced rotarod performance in *Ali34/+* males which were both attributed to the stiffening of the knee joints. Furthermore, the eye screen detected a reduced axial eye length in male mutants. Cholesterol, analysed in the clinical chemical screen, exhibited slightly reduced values and finally, pathological observations additionally identified cardiac defects with low penetrance in heterozygous mutants.

4.1.4 Protein analysis

The fact, that *Plxnd1*^{*Ali34*} was still expressed in homozygous embryos led to a more in depth analysis of the proteins distribution. In conjunction with the transcriptional analysis, the 48 amino acid truncation (Figure 24A) did not result in posttranscriptional degradation like nonsense-mediated decay. *In silico* analysis of protein domains along *Plxnd1* revealed, that all known active binding sites were still present in *Ali34* except a putative PDZ binding motif at the C-terminal end (Figure 24B). With the availability of a functional *Plxnd1* antibody, Western blot analysis confirmed the expression of the protein in adult *Ali34/+* cardiac tissue (Figure 24C).

transfection system for electroporation. Different approaches were tested, whereby the electroporation system revealed the best transfection efficiency (approximately 50%). Unfortunately, cells transfected with either *Plxnd1*^{WT} or *Plxnd1*^{Ali34} appeared as rounded condensed cells similar to apoptotic cells within the first 30 hours post transfection (Figure 25A). In addition, confirmation stainings with the Plxnd1 antibody identified that the exogenous GFP-tagged protein does not fully co-localize with the available Plxnd1 antibody (Figure 25B). The exogenous protein rather accumulated close to the nuclei and was hardly detectable at the membrane of the cells. As the vector sequences were confirmed to be correct and no frameshifts in the expression were obtained, other mechanisms might be accountable for the altered expression.

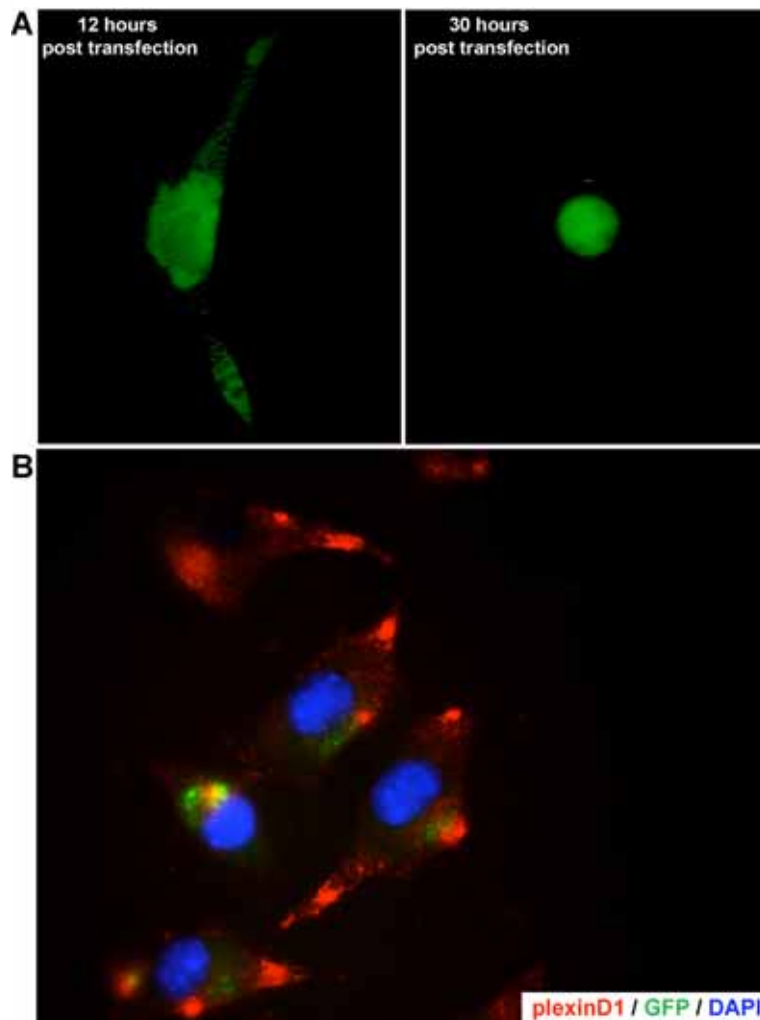


Figure 25. Overexpression of Plxnd1 in L929 fibroblasts.

A Exogenous expression of GFP tagged Plxnd1 is visible 12 hours post transfection, but cells might undergo cell death after 30 hours. **B** Exogenous expression only partially co-localizes with staining pattern obtained by Plxnd1 antibody staining.

4.1.4.2 *In vitro* analysis of mouse embryonic fibroblasts

To study the spatial distribution of the endogenous Plxnd1 protein *in vitro*, mouse embryonic fibroblasts were isolated. With the availability of a Plxnd1 antibody, which was confirmed to detect both the wild type and mutant protein stainings were performed to analyse possible alterations in the cytoplasmic filamentous arrangement. Additionally, RhoGTPase activity assays should also be applied to identify if the proposed binding partner Rac1 or other small GTPases still bind to the cytoplasmic domain of Plxnd1^{Ali34}.

Antibody stainings were performed to analyse β -actin filament structure as well as α -tubulin arrangement in the different genotypes. Indeed, β -actin filaments were found to be less dense in fibroblasts of homozygous animals, while heterozygous cells were comparable to controls. However, collapsed cells as described previously^{126,127} were not increased in fibroblasts of homozygous animals. Plxnd1 antibody staining displayed an enhancement in the endoplasmatic reticulum and the Golgi apparatus. With the help of α -tubulin antibody stainings, Plxnd1 was found to be localized in parallel to filaments suggesting a trafficking of the protein along tubulin towards the transmembrane.

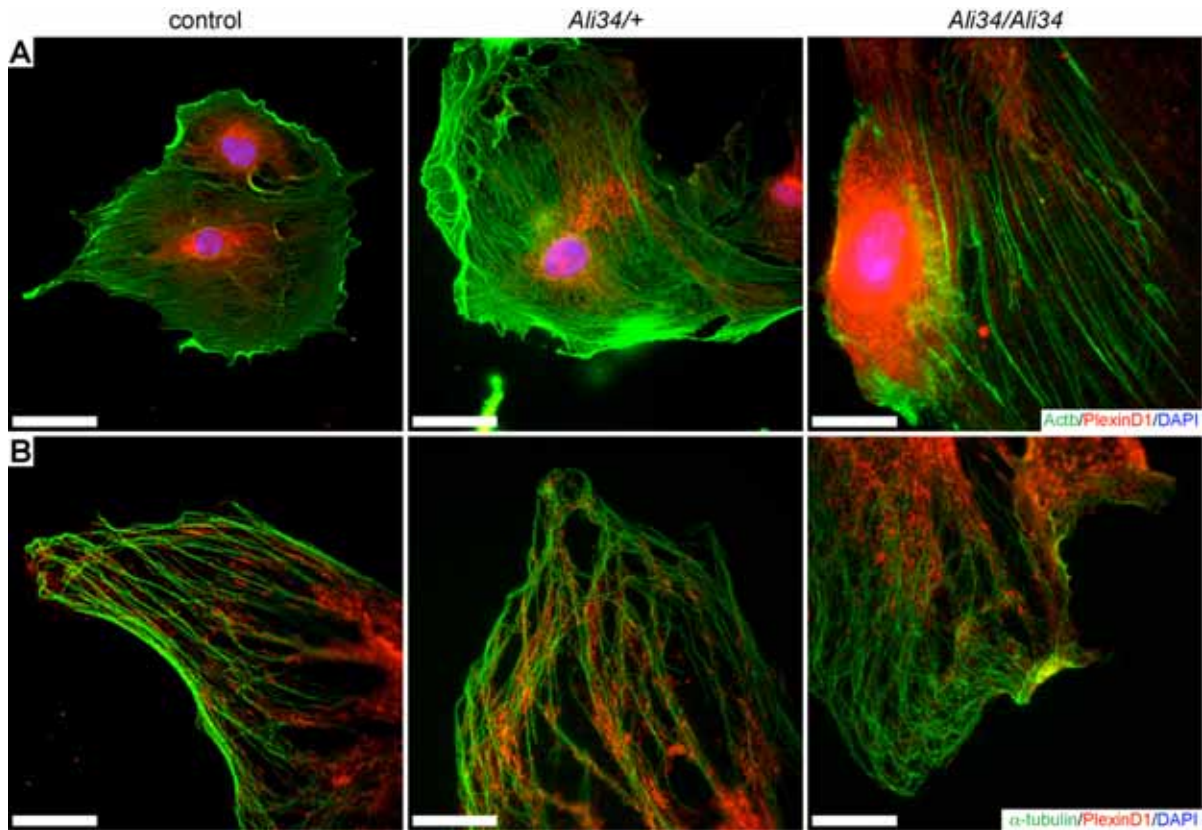


Figure 26. Cellular localisation of Plxnd1 in mouse embryonic fibroblasts.

A Double-immunostaining of Plxnd1 (red) and β -actin (green) in wild-type, heterozygous and homozygous *Ali34* fibroblasts. **B** Double-immunostaining of Plxnd1 (red) and α -tubulin (green) in wild-type, heterozygous and homozygous *Ali34* fibroblasts. Plxnd1 appears to be localized along the tubulin fibres in all cells. For the detection of nuclei, all samples were stained with DAPI (blue). Scale bars = 20 μ m.

4.1.5 Following steps

Based on the current knowledge and the preliminary work several further steps are currently in progress.

For further assessment of bone specific phenotypes caused by the *Plxnd1* mutation in *Ali34*, in depth bone histomorphometric methods are planned to receive more detailed data of the *in vivo* situation. This includes the analysis of hindlimb bones at multiple time points (2, 4, 8, 16 weeks) by TRAP and van Kossa staining and their computed analysis of scanned sections according to published standards^{128,129}. In addition the recently established assays for the analysis of isolated osteoclasts (with the help of Dr. Laura Helming) as well as a co-culture assay of osteoblasts and osteoclasts will be utilised to investigate possible bone cell specific phenotypes *in vitro*. Osteoclast differentiation assays as well as activity/resorption assays will be applied for the monoculture. For co-culture experiments, possible defects in cell-cell interactions will be analysed with

Plxnd1^{Ali34/Ali34} osteoblasts in the presence of wild-type osteoclasts and vice versa. Additionally co-cultures of both *Plxnd1*^{Ali34/Ali34} osteoblasts and osteoclasts will also be investigated.

Regarding protein biochemistry, several *in vitro* assays are planned. This includes activity assays for the different RhoGTPases (Rac1, Cdc42, RhoA) as well as the analysis of R-Ras activity *in vitro*. Furthermore, co-immunoprecipitations should shed light on potential binding defects at the different cytoplasmic domains of *Plxnd1*^{Ali34}. In case that all bindings can be confirmed for the mutant protein, further analysis of the PDZ binding motif will be indispensable and will have major impact on the understanding of Plxnd1 signalling.

Western blot analysis of His-tagged endogenous Plxnd1 will be performed on different cellular fractions to verify membrane association of the mutant protein. In addition, stable cell lines will be created to achieve more consistent conditions where alterations in spatial distribution of the protein can be analysed more specifically.

4.2 *Aga2*

4.2.1 Phenotypical classification of *Aga2/+*

As described recently⁹¹ two different phenotypes were discernable upon *Aga2/+* offsprings resembling different types of OI.

The first group was characterised by diastrophic limbs, long bone and rib cage fractures, generalised decrease in DXA-based bone parameters and slight changes in body composition with a 20% reduction in body weight compared to wild-type littermates. Further clinical features comparable to type III and IV OI were also described previously⁹¹. Mice displayed wild-type like lifetime and were classified as mildly affected *Aga2* (*Aga2/+^{mild}*). The second group of *Aga2/+* animals exhibit the same phenotypic features observable for the mildly affected animals. In addition, pectus excavatum, gasping and cyanosis were further hallmarks as well as platyspondyly, edema of eyes and eczema. As the most typical criteria for the phenotypic classification, mice had a strong physique deficit with a body weight reduction to about 50% compared to wild-type littermates and appeared weak and asthenic. These mice resemble phenotypic features of severe type III OI as well as type II OI and entirely succumbed to postnatal lethality, 6 – 11 days after birth. Based on the observations, these mice displayed a more severe progression of OI and were subsequently termed *Aga2/+^{severe}*.

This morphological diversity was discernable starting between 6 – 11 dpp. Classification of progeny was done prior to experiments and depended on body weight and severity of symptoms.

4.2.2 Bisphosphonate treatment during neonatal development

Antiresorptive drugs are routinely applied among patients with osteoporotic features. A previous approach with the administration of the bisphosphonate alendronate (see PhD thesis by Dr. Thomas Lisse) addresses the question if long term application could rescue the bone phenotype of *Aga2/+* animals. Indeed, bone parameters measured by bone densitometry were improved in mutant mice and the fractures were reduced to 50% after treatment for 16 weeks (see PhD

thesis by Dr. Thomas Lisse). In contrast, neonatal lethality rate was unaffected upon the treated *Aga2/+* group compared with the saline treated control group.

To address, whether alendronate significantly improves bone structure already during neonatal development, a more detailed analysis was performed to evaluate bone parameters after a two weeks administration period starting with birth of the mice. In addition, the survival rate was recorded to clarify if the bone phenotype is directly causal for lethality in *Aga2*.

For this purpose wild-type controls and *Aga2/+* animals were randomly grouped into q treatment group receiving alendronate (wild type (n=21), *Aga2/+* (n=16)) and a control group receiving saline injections (wild type (n=17), *Aga2/+* (n=14)). To standardise alendronate application, mice were subcutaneously injected 1, 3, 5, 8, 10 and 12 after birth. Additionally, weight and size of all analysed animals were recorded daily. *Aga2/+^{severe}* animals were identified by their reduced body weight and size. When severely affected animals were recognised, μ CT measurements were subsequently performed to receive bone densitometric data. For all other animals (wild type and *Aga2/+^{mild}*) μ CT measurements were performed at the age of 14 days.

Evaluation of the weight and size curves during the 2-weeks period identified initial differences between wild-type and *Aga2/+* animals after 3 days (Figure 27A, B) and progressed until the end of the period. Interestingly, *Aga2/+^{severe}* animals were indistinguishable from *Aga2/+^{mild}* animals 12-24 hours before death. Severely affected animals displayed stagnancy in both body weight and size or even a reduction in both parameters. Fracture rates, which were counted from callus formations, visible in the 3D reconstruction of the thoracic region (Supplemental Figure 5A) of the generated μ CT images, exhibited a significant reduction (p=0.022) for all alendronate treated *Aga2/+* animals compared to the saline treated control group (Figure 27C). Interestingly, subdivision of mildly and severely affected animals revealed a significantly reduced fracture rate only in the treated *Aga2/+^{severe}* mice (p=0.014), while *Aga2/+^{mild}* animals showed a trend towards reduction (p=0.234). The survival rate of *Aga2/+* animals was not improved by the reduced fracture rate (Figure 27D), indicating that lethality might be caused by bone-independent mechanisms.

Analysis of μ CT pictures additionally identified perfusions in lungs of *Aga2/+^{severe}* animals, which were persistent in treated and untreated mice. In *Aga2/+^{mild}* mice,

these observations were not observed, suggesting a specific pathological trait in lethal animals. (Supplemental Figure 5B).

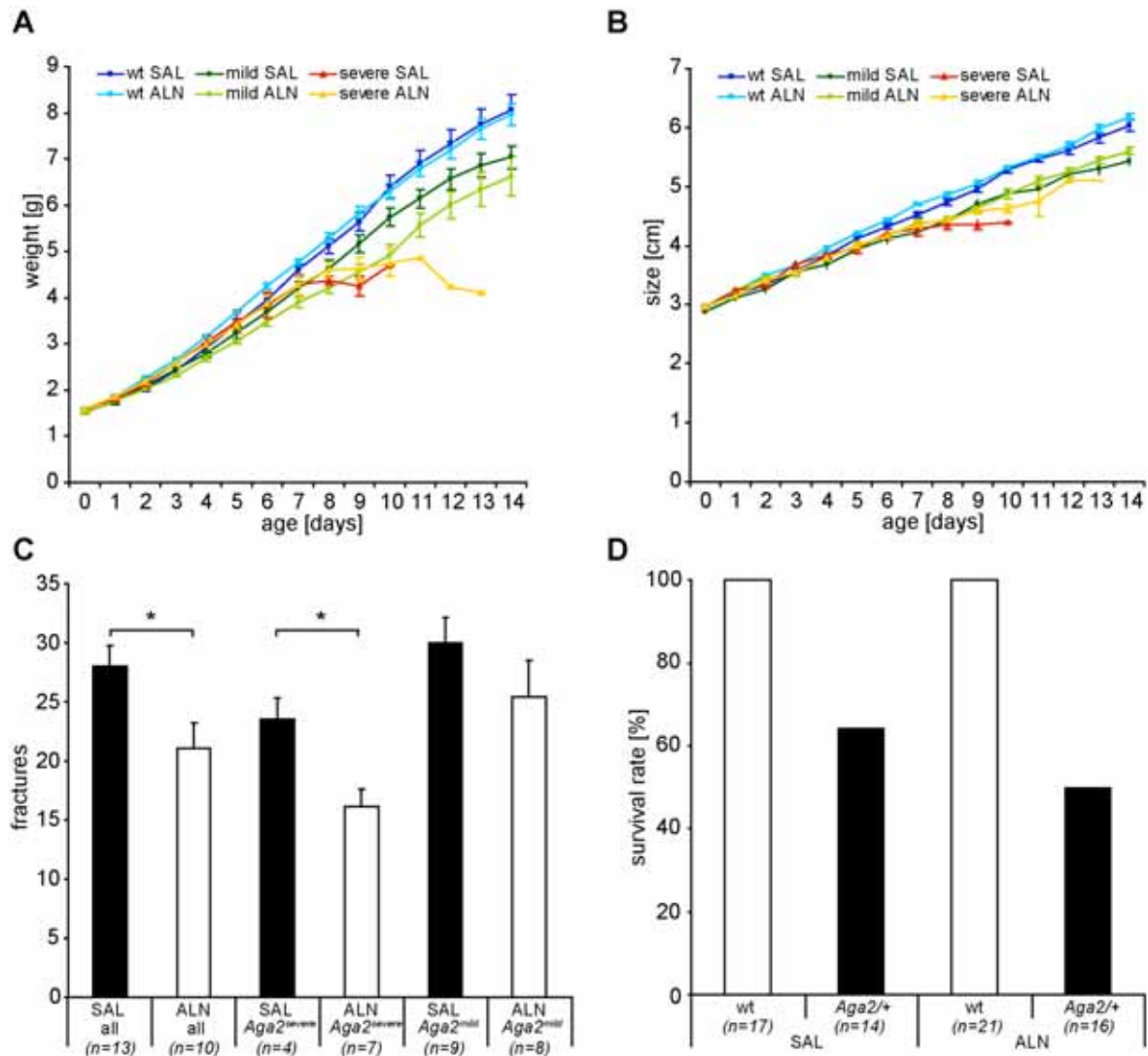


Figure 27. Alendronate treatment in *Aga2*^{+/+} newborn mice.

A Weight curve of all groups during the application period. *Aga2*^{+/+} display weight reduction as early as 3 dpp while alendronate treatment has no effect on weight compared to saline treated mice. *Aga2*^{+/+}^{severe} animals are indistinguishable from *Aga2*^{+/+}^{mild} until 24 hours before death. **B** Size curve of all groups during the 14 days period. All *Aga2*^{+/+} mice display a size reduction after 3 days. As with the weight data, *Aga2*^{+/+}^{severe} values drop 24 hours prior to death. **C** Fractures observable in the rib cage of *Aga2*^{+/+} animals in the control (SAL) and the treatment (ALN) group. Data is further subdivided into *Aga2*^{+/+}^{mild} and *Aga2*^{+/+}^{severe}. **D** Survival rate of the analysed animals reveals no improvement by alendronate (ALN) administration in *Aga2*^{+/+}. Error bars represent SEM-values. SAL: saline treated control group; ALN: alendronate treated group. * = $p < 0.05$

Whole body bone densitometry was performed by a LaTheta μ CT. *Aga2*^{+/+}^{severe} animals were not analysed due to heterogeneous weight and size parameters caused by the different days of death. Therefore, only *Aga2*^{+/+}^{mild} animals were analysed and compared to wild-type controls. Trabecular (-5%), cortical (-2%) and total BMD (-3%) values were significantly reduced in *Aga2*^{+/+}^{mild} animals compared to controls (Figure 28A). In addition, alendronate treated *Aga2*^{+/+} mice displayed an

improvement in cortical and total BMD compared to the saline group, while trabecular BMD tended to decrease. Furthermore, BMC data displayed a significant reduction for trabecular (-24%), cortical (-7%) and total (-8%) parameters (Figure 28B). Alendronate application did not improve content parameters during the treatment period.

As fractures appeared to be most frequent in the thoracic region of newborn animals, additional μ CT measurements were performed focusing on the thoracic region of the animals. This more specific analysis showed effects of alendronate on *Aga2/+* animals. Cancellous BMC and BMD values were significantly reduced (-56% and -25% respectively) in alendronate treated mutant mice. In addition, cancellous volume was reduced (-43%) compared to untreated *Aga2/+* animals (Figure 28C). Regarding the cortical parameters, content (-27%) and volume (-28%) values were declined upon treated mutant mice (Figure 28D). Wild-type controls displayed no treatment effects.

In summary, alendronate treated neonatal mice showed tendencies towards decreased fracture rates and an improvement in bone structure, suggesting a milder bone phenotype. However, the survival rate of treated *Aga2/+* animals was not improved suggesting other causative alterations that lead to the increased neonatal lethality.

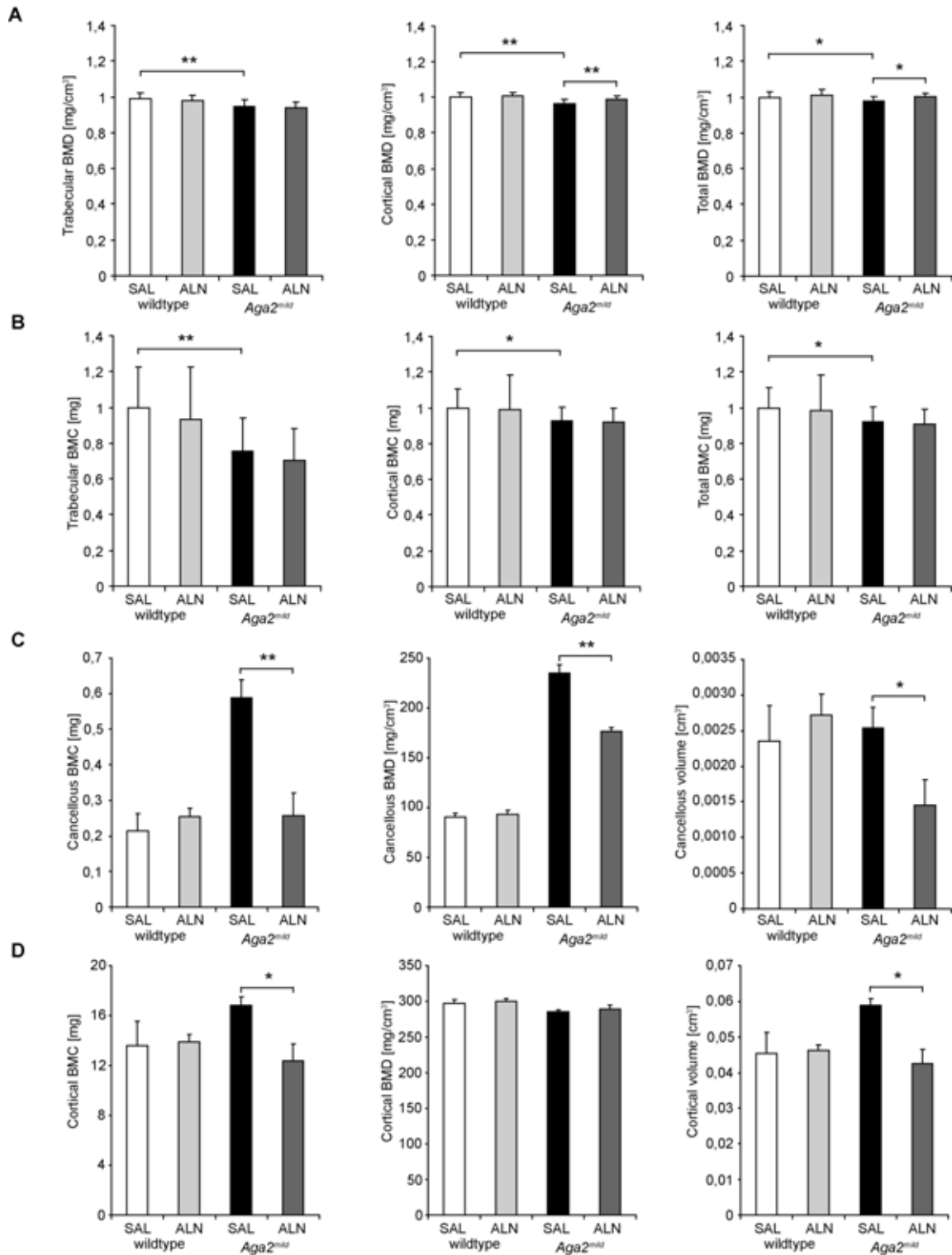


Figure 28. Evaluation of bone densitometric data obtained by μ CT measurements.

A BMD values of the trabecular, cortical and total portion in wild type and *Aga2/+^{mid}* saline and alendronate treated animals respectively. **B** Trabecular, cortical and total BMC values in wild-type and *Aga2/+^{mid}* animals of both groups. **C** Cancellous BMC, BMD and volume of all analysed groups in the thoracic region. **D** Cortical BMC, BMD and volume values in wild-type and *Aga2/+^{mid}* mice of all groups in the thoracic region. Error bars represent SEM values. * = $p < 0.05$; ** = $p < 0.01$

4.2.3 Cardiovascular defects in OI

4.2.3.1 Cardiovascular phenotyping of *Aga2/+*

Cardiac distress is generally observed in human OI patients⁸⁰. During the primary screen of the GMC, ECG analysis was performed on 14-weeks old *Aga2/+^{mild}* animals (Table 13).

Increased heart rates could be observed for *Aga2/+* mice of both sexes compared to controls. In addition, J-T intervals and QRS amplitudes were increased in the mutant group. While alterations in the QRS amplitudes were mainly caused by enhanced Q and declined S values, the increased J-T values claimed for alterations in ventricle repolarisation.

Table 13. Results of the primary cardiovascular phenotyping

Parameter	Wild type (A)		<i>Aga2</i> (B)		A~B	
	male (n=10)	female (n=9)	male (n=10)	female (n=10)	male p-value	female p-value
Heart rate (bpm)	471.9 ±17	529.4 ±15	572.4 ±9.6	573.9 ±7.9	< 0.001	< 0.05
JT interval (ms)	3.6 ±0.3	3.6 ±0.1	4.4 ±0.1	4.6 ±0.3	< 0.05	< 0.05
Q amplitude (mV)	0.01 ±0	0.02 ±0.01	0.05 ±0.01	0.05 ±0	< 0.01	< 0.01
R amplitude (mV)	2.15 ±0.11	2.06 ±0.17	1.86 ±0.08	2.04 ±0.13	n.s.	n.s.
S amplitude (mV)	-0.28 ±0.12	-0.83 ±0.18	-1.37 ±0.15	-1.3 ±0.19	< 0.001	< 0.05
QRS amplitude (mV)	2.48 ±0.09	2.88 ±0.23	3.24 ±0.14	3.34 ±0.16	< 0.01	= 0.058

As cardiac complications are generally observed in type III OI patients that die during childhood⁸⁰, secondary screening of *Aga2/+^{severe}* mice at the age of 10 days was performed to further ascertain possible cardiac defects that might account for perinatal lethality (in collaboration with Dr. Frank Thiele and Dr. Anja Schrewe). Ultrasound analysis revealed significant functional and anatomical alterations in *Aga2/+^{severe}* mice. While the left ventricular enddiastolic internal diameter (LVEDD) was comparable to wild-type littermates, left ventricular endsystolic internal diameter (LVESD) values significantly increased in *Aga2/+^{severe}* (Figure 29A). Fractional shortening (FS) and ejection fraction (EF), relating to the diastolic and systolic diameter, indicating the potential ejected blood volume, were both

significantly decreased in the analysed mice compared to their control littermates. As *Aga2*^{+*severe*} mice displayed a strong reduction in size and weight, the combination of the equal LVEDD values together with the increased LVESD suggested morphological abnormalities and a possible cardiac muscle dilatation. B-mode analysis further corroborated that septal defects as well as cardiac hypertrophy are possible phenotypic alterations in *Aga2*^{+*severe*} animals. While the diastolic pictures (Figure 29B, D) revealed no alterations, the examination of the systole revealed a possible dilatation due to the failure of correct contraction of the left ventricle (Figure 29C, E).

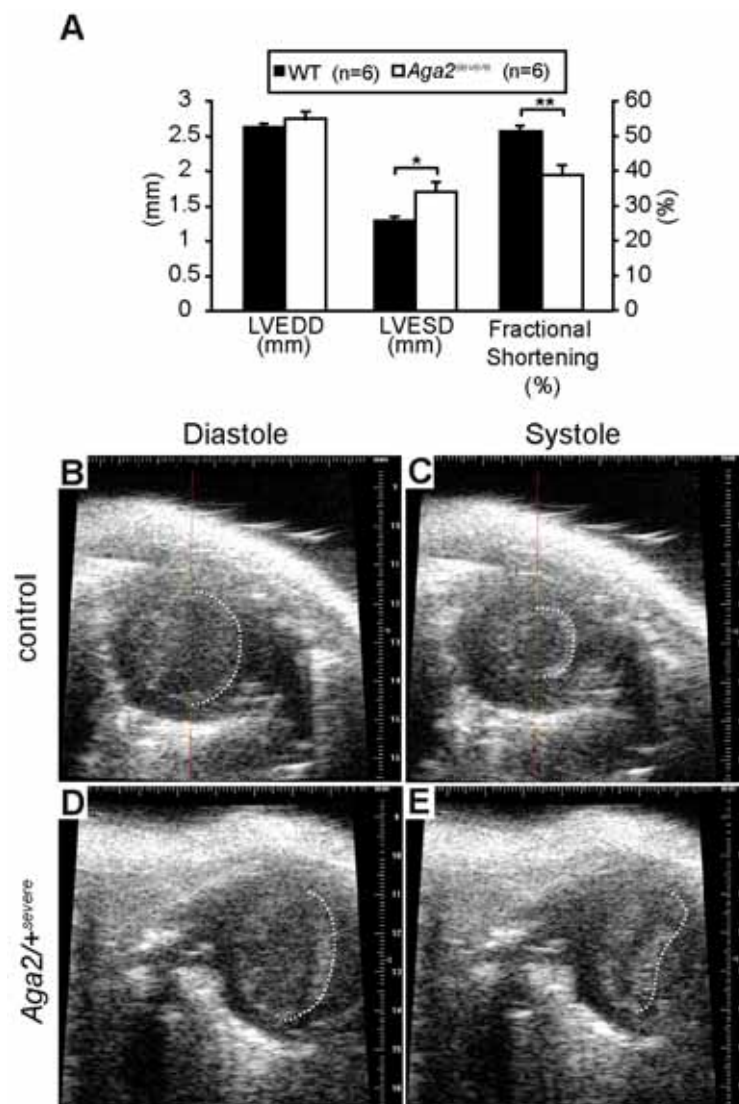


Figure 29. Ultrasound analysis at 10 dpp.

A Quantitative analysis of the ultrasound data. No alterations are detected in the left ventricular end-diastolic internal diameter (LVEDD) while left ventricular end-systolic internal diameter (LVESD) is significantly increased in *Aga2*^{+*severe*} mice compared to wild-type littermates. Fractional shortening is significantly reduced in severely affected *Aga2*^{+*severe*} animals. **B-E** B-mode analysis reveals septal deformation with a convex bulge into the left ventricle during the systole.

To further substantiate these findings, histological examination of *Aga2/+^{severe}* hearts was performed. General morphological analysis by H&E stainings revealed that, even though lethal *Aga2/+* animals displayed reduced body size and weight, the hearts were equally sized compared to wild-type controls (Figure 30A). Enlarged septa as well as right ventricular hypertrophy were evident in all analysed *Aga2/+^{severe}* mice. To correlate the observed morphological alterations with the underlying *Aga2* mutation, type I collagen antibody stainings on heart sections were performed. Analysis revealed that ten day old *Aga2/+^{severe}* animals exhibited a strongly reduced collagen staining in the entire myocardium. While wild-type controls displayed type I collagen staining in serial aligned fibres along myocardial muscles, a dispersed staining pattern with a loss of continuous collagen distribution was evident in lethal *Aga2/+^{severe}* cardiac tissue (Figure 30B). This was accompanied by a disordered cellular arrangement with type I collagen accumulation close to fibroblast nuclei. For the characterisation of alterations in the cardiac ECM and to solely visualise the collagen network, scanning electron microscopy (SEM) on macerated tissue was performed in collaboration with Dr. Frank Thiele. Ultrastructural analysis displayed an altered ratio between the main type I collagen fibrils appearing as broad strands and thinner fibrils mainly composed of smaller collagen types. These defects also resulted in an altered structural and spatial arrangement of the whole collagen network in *Aga2/+^{severe}* animals in the myocardial ECM (Figure 30C).

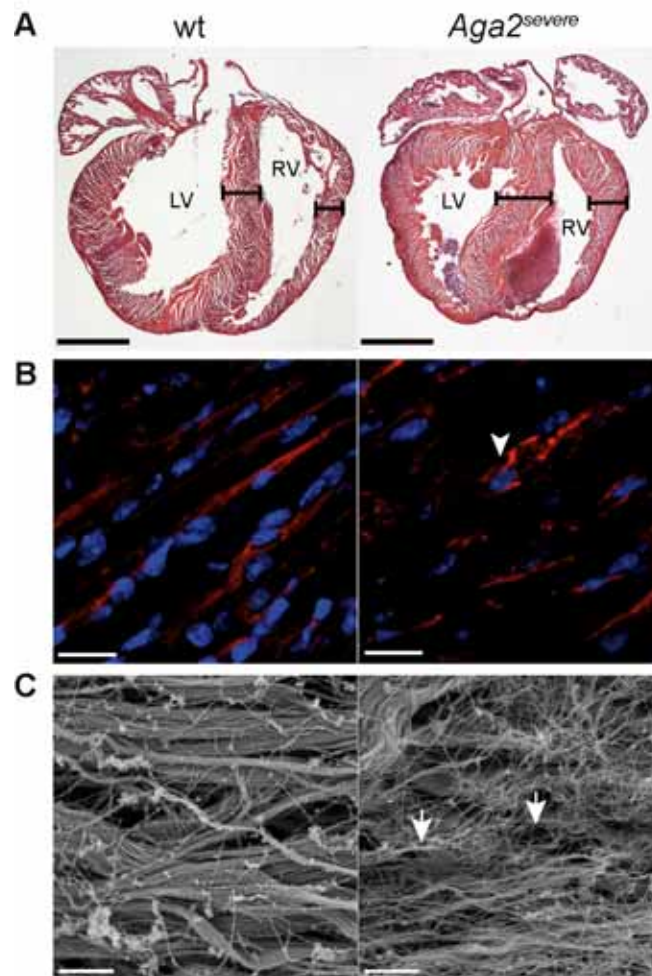


Figure 30. Histological analysis of cardiac phenotypes in *Aga2*.

A H&E staining reveals a thickened septal and right ventricular wall in *Aga2*^{severe} compared to wild types. In addition, heart size is nearly equal to controls. **B** Type I collagen antibody staining in the myocardium displays protein accumulation at fibroblasts in *Aga2*^{severe} (white arrowhead) and a dispersed staining pattern along the cardiac muscles while wild-type controls display a continuous pattern. **C** SEM pictures of the myocardial ECM exhibit a reduction in type I collagen fibrils in *Aga2*^{severe} while the content of smaller collagen fibres is still evident with a more pronounced disarrangement (white arrow).

Considering that the *Aga2* mutation results in a defective fibrillation of the type I collagen protein, hearts of *Col1a1*^{Mov13/+} and *Col1a1*^{BrillV/+} mice (provided by Joan Marini) were investigated for possible defects in the myocardial extracellular matrix. Haploinsufficiency of *Col1a1*^{Mov13/+}, resulting in mild type I OI symptoms¹³⁰, revealed a less intense type I collagen staining in the myocardium, while tissue integrity was still sustained. In contrast, *Col1a1*^{BrillV/+} mice, harbouring a glycine substitution in the core protein of type I collagen (G349C)¹³¹, and exhibit also an increased susceptibility for neonatal lethality, displayed major defects in their cardiac ECM integrity with a diffuse type I collagen staining pattern, while staining intensity was wild-type like (Figure 31).

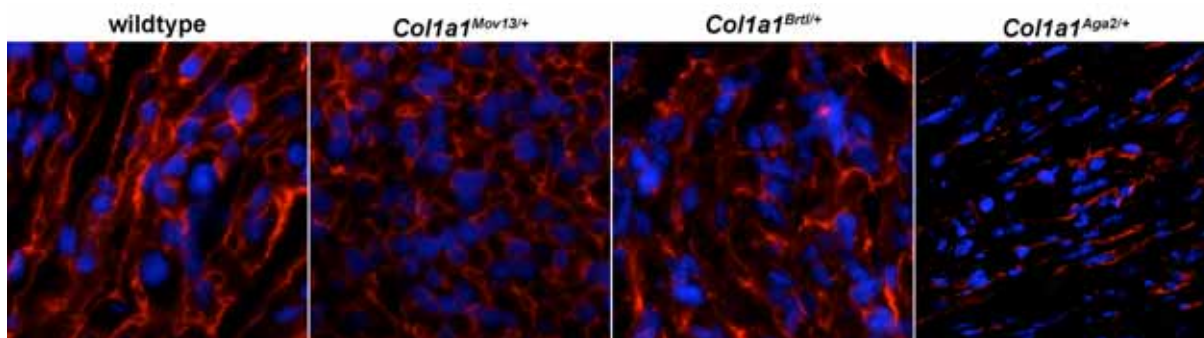


Figure 31. Myocardial ECM comparison between different murine OI models.

Type I collagen antibody staining displays a reduced staining intensity in *Col1a1*^{Mov13/+} hearts due to haploinsufficiency. *Col1a1*^{Brtll/+} mice display an altered staining pattern which is comparable with severely affected *Col1a1*^{Aga2/+} specimens while staining intensity is not obviously reduced compared to stainings of wild type controls.

As type I collagen also accounts for proper blood vessel wall morphology, PECAM antibody stainings on *Aga2*^{+/severe} were additionally performed. Overall, PECAM staining was reduced around blood vessels, indicating alterations in the tunica intima layer. This was additionally confirmed by a disordered cellular arrangement of endothelial cells (Figure 32).

In conclusion, besides minor alterations in *Aga2*^{+/mild} animals, *Aga2*^{+/severe} animals displayed major cardiac defects including septal defects and right ventricular hypertrophy. The observed alterations in type I collagen staining intensity as well as the altered spatial arrangement supported the hypothesis that the *Aga2* mutation is directly linked to these pathophysiological defects.

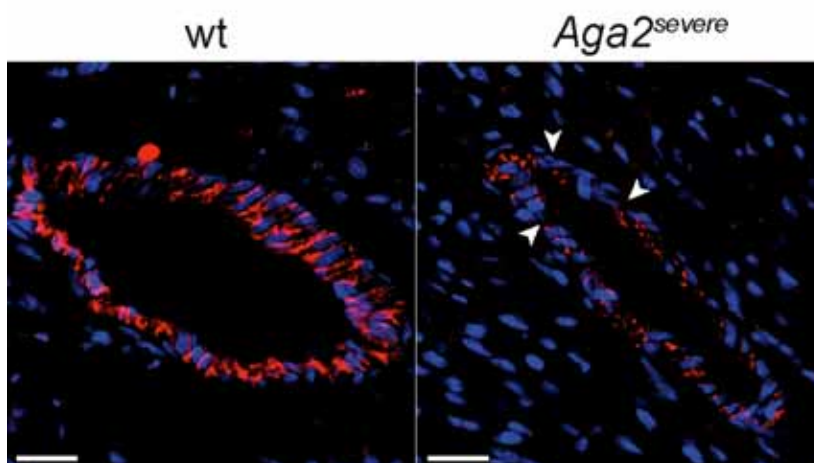


Figure 32. Immunohistochemical staining of PECAM-1 for morphological analysis of blood vessels.

PECAM antibody staining exhibits a strong reduction in *Aga2*^{+/severe} animals as well as loss of endothelial cell arrangement compared to wild types.

4.2.3.2 Comparison to human patient data

To assess whether defects observed for *Aga2/+* animals could be correlated to human OI patients, data from a longitudinal study of 46 children and young adults with type III and IV OI was dragged for comparison (data provided by Joan Marini) (Table 14). Echo and ECG analysis revealed that mild tricuspid regurgitation was the most common finding and occurred in over half of children for each type of OI. Combined mild mitral, pulmonic or aortic regurgitations with additional tricuspid valve defects were confirmed for two type III and ten type IV patients. Two children with type III OI displayed mitral regurgitations without a concurrent pulmonic valve finding. Small intracardiac shunts were detected in 3 type III OI children who also had pulmonic valve regurgitation and all mild left-to-right flows across an atrial septal defect. Mild left atrial enlargement was reported in 2 type III (one also with premature atrial contractions (PACs)) and 3 type IV OI children. ECG analysis additionally identified sinus tachycardia, sinus tachycardia with Q waves, high right ventricular voltage, reduced PR voltage and premature atrial contractions for five type III OI patients. For type IV OI, two children with premature atrial contractions or sinus arrhythmia and high left ventricular voltage were identified. Valvular or cardiac chamber findings were evident in 78% (18/23) of the patients in both groups.

Results

Table 14. Echocardiogram and PFT findings in children with type III and IV OI.

ID = patient identification number, Type = OI type, Age = age range during serial testing, T = tricuspid valve, M = mitral valve, A = aortic valve, P = pulmonic valve (+ = mild regurgitation, ++ = moderate regurgitation, MVP = mitral valve prolapse, I = insufficiency, - = normal). LV = left ventricle, LA = left atrium (DIL = dilated, L>R = left to right shunt, - = normal). Restr = restrictive lung disease, Obstr = obstructive lung disease (+ = mild, ++ = moderate, +++ = severe, ++++ = very severe, - = normal). Spine = degrees of curvature, Pam = pamidronate (+ = received during testing period).

ID	Type	Mutation	Age	T	ECHOCARDIOGRAM					PFT			Pam
					M	P	A	LV	LA	Restr	Obstr	Spine	
1	IV	α1 (I) gly88glu	17-23	+	MVP	+/I	+/I	-	-	+	-	15-25	
2	IV	α1 (I) gly844ala	12	+	+	+	-	-	-	+	-	10	+
3	IV	α1 (I) gly13asp	9-13	+	+	-	+	-	-	++	-	10-40	+
4	IV	α1 (I) gly352ser	13-19	+	+	-	-	-	-	+	-	25-40	
5	IV	unknown	12-16	+	+	-	-	-	DIL	-	+	25-45	
6	IV	α1 (I) gly589ser	10-14	+	+	-	-	-	-	++	-	40-60	
7	IV	α2 (I) gly244ser	8-10	+	+	-	-	-	-	+	-	15	+
8	IV	α1 (I) gly448ser	5-8	+	+	-	-	-	-	-	-	15-30	+
9	IV	α2 (I) gly511ser	10-17	+	-	+	-	-	-	-	-	15-20	+
10	IV	α2 (I) gly922ser	10-17	+	-	-	+	-	-	+++	-	10-15	
11	IV	unknown	5-7	+	-	-	-	-	-	-	-	10-15	
12	IV	α2 (I) gly238ser	9-11	+	-	-	-	-	-	-	+	10	+
13	IV	unknown	10-13	+	-	-	-	-	-	+	-	15	+
14	IV	α2 (I) gly238ser	7-12	+	-	-	-	-	-	+	-	10-20	+
15	IV	α2 (I) gly121asp	4	+	-	-	-	-	-	-	-	0	
16	IV	α2 (I) Δ E16	7-11	+	-	-	-	-	-	-	-	15-20	+
17	IV	α1 (I) thr1120ile	16	-	-	-	-	-	-	+++	-	10	
18	IV	α1 (I) gly523cys	18-21	-	-	-	-	-	-	++	-	30-45	
19	IV	α2 (I) gly268ser	16-19	-	-	-	-	-	-	++	-	40-55	
20	IV	α2 (I) gly238ser	3-9	-	-	-	-	-	-	-	-	0	+
21	IV	α1 (I) gly136arg	14	-	-	-	-	-	-	-	-	0-10	
22	IV	α1 (I) pro1266his	7-9	-	-	-	-	-	DIL	-	+	10	
23	IV	α1 (I) gly589ser	16	-	-	-	-	-	DIL	+	-	42	
24	III	α1 (I) gly187ala	4-8	+	+	+	-	-	-	+	+	10-45	+
25	III	α2 (I) gly106val	11	+	+	-	-	-	DIL	-	-	0	
26	III	α1 (I) gly217ser	6-8	+	-	-	-	-	-	+	+	10-20	+
27	III	unknown	7-8	+	-	-	-	-	-	++	-	15	
28	III	α2 (I) gly247cys	15-20	+	-	-	-	-	-	+++	-	60-70	
29	III	α2 (I) gly337ser	10-14	+	-	-	-	-	-	-	-	15-35	+
30	III	unknown	12-16	+	-	-	-	-	-	-	+	10-25	
31	III	α1 (I) gly898ser	4-7	+	-	-	-	-	-	+	-	0-30	+
32	III	α1 (I) Δ E41	5	+	-	-	-	-	-	-	-	15	
33	III	α2 (I) gly703arg	6-8	+	-	-	-	-	-	-	-	10-20	
34	III	unknown	11-13	+	-	-	-	-	L>R	++	-	20-25	
35	III	α1 (I) gly154arg	9-12	+	-	-	-	-	-	++	-	35-55	+
36	III	α1 (I) gly193ser	7-12	+	-	-	-	-	-	+	++	20-70	+
37	III	α1 (I) gly25val	12-17	+	-	-	-	-	L>R	++	++	40-50	
38	III	α2 (I) gly898val	12-18	+	-	-	-	-	L>R	+++	-	0-50	
39	III	α1 (I) gly76glu	12-13	-	++	-	-	-	-	++	-	25-35	+
40	III	α1 (I) gly997ser	4-6	-	+	-	-	-	-	-	-	0	+
41	III	α1 (I) gly286arg	12	-	-	-	-	-	-	-	++	20	+
42	III	α2 (I) gly370ser	14	-	-	-	-	-	DIL	-	-	55	
43	III	α1 (I) gly232ser	7	-	-	-	-	-	-	-	-	20	+
44	III	α1 (I) Δ E33-36	11-16	-	-	-	-	-	-	+	-	30-70	
45	III	α1 (I) gly589ser	5-10	-	-	-	-	-	-	-	+	0	+
46	III	α2 (I) gly250ser	9-14	-	-	-	-	-	-	++++	-	20-50	

4.2.4 Pulmonary defects in OI

4.2.4.1 Pulmonary phenotyping of *Aga2/+*

The leading cause of death among type III OI patients are pulmonary complications⁸⁰. Furthermore, reports on patients with milder types of OI exhibit reduced pulmonary functions which are mainly considered to be secondary to bone deformities. The primary lung screen of the GMC investigated spontaneous breathing patterns during rest and activity in 15-weeks old mice. Comparison of *Aga2/+^{mild}* animals with their littermate controls revealed higher specific values for tidal volume and minute ventilation. In addition, respiratory rates at rest and activity displayed lower values with a normal adaptation from rest to activity. Due to the defects found in respiratory rates, expiratory time was extended and flow rates were reduced in *Aga2/+^{mild}* mice. In conjunction with the reduced body weight of mildly affected animals together with rib cage deformities, the phenotypes observed in this screen could not be exclusively linked to a primary phenotype caused by the *Col1a1* mutation (Supplementary Table 2).

As *Aga2/+^{severe}* animals exhibited enhanced cardiac dysfunction compared with mildly affected mutants, it seemed reasonable that pulmonary impairment could also be enhanced. Unfortunately, lung function tests could not be performed in 10-days old animals due to their small body size. Therefore, morphological analysis was performed to evaluate possible pulmonary distress (in collaboration with Dr. Frank Thiele). General macroscopical analysis identified that *Aga2/+^{mild}* and *Aga2/+^{severe}* animals displayed comparable number of rib cage fractures that were equally distributed. Interestingly, only *Aga2/+^{severe}* mice displayed haemorrhagic lungs, while lungs of mildly affected animals were found to be wild-type like (Figure 33 A). Subsequent histological analysis by H&E stainings revealed bleedings in the alveolar space of the lung parenchyma, equally distributed in the whole organ of lethal mice. In addition, pneumonia with infiltration of polymorphonuclear neutrophils (PMN), the occurrence of alveolar macrophages as well as pleurisy was evident exclusively in *Aga2/+^{severe}* animals (Figure 33B). As cardiac data already shed light on blood vessel defects in *Aga2/+^{severe}*, PECAM antibody staining was utilised to visualise the vascular network in the lung parenchyma. While lungs of *Aga2/+^{mild}* mice revealed an intact capillary network comparable to

wild-type controls, PECAM positive cells were hardly detectable in $Aga2/+^{severe}$. This was particularly observed in regions with excessive alveolar bleedings (Figure 33C). Only non-infiltrated alveoli displayed PECAM staining indicating an intact capillary network.

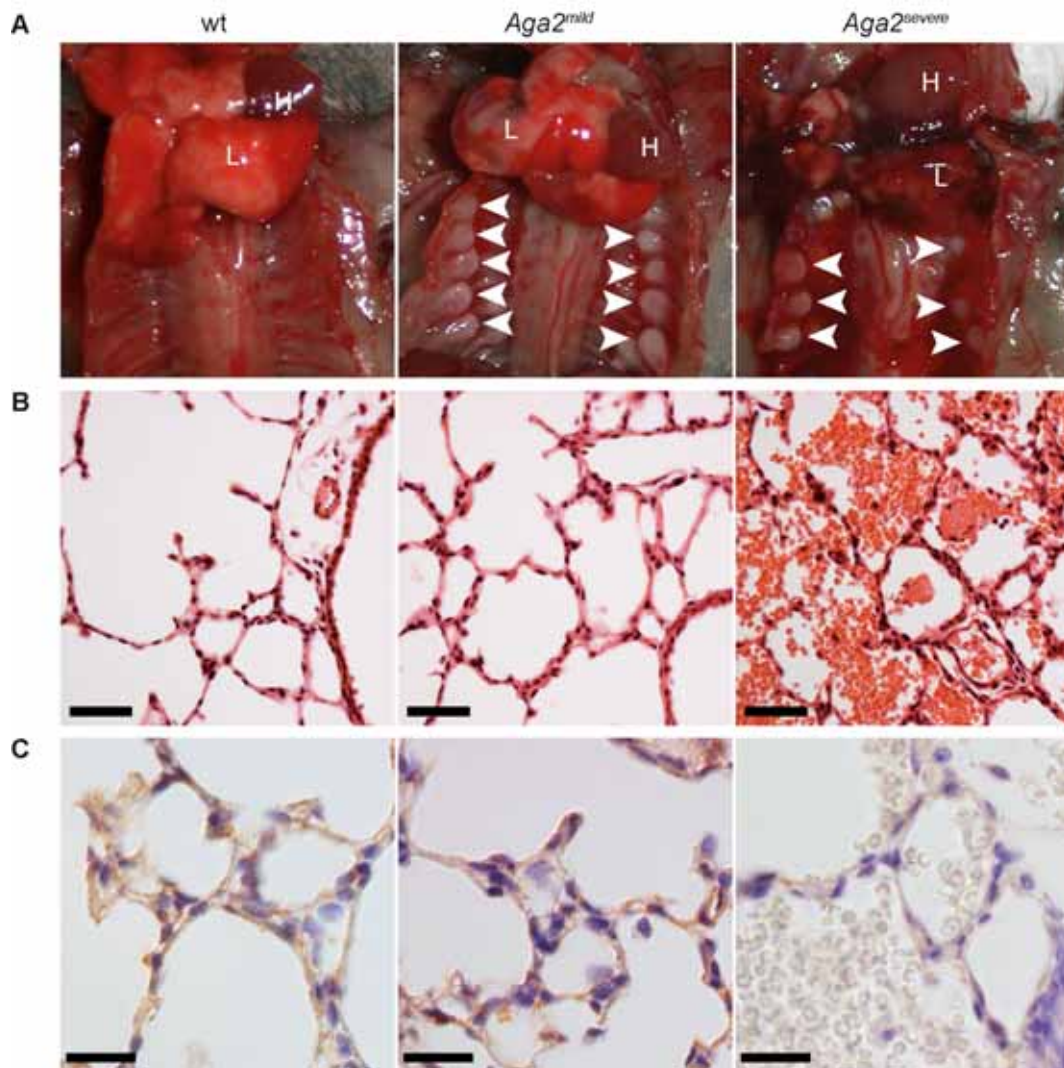


Figure 33. Histological analysis of lung tissue in $Aga2/+^{mild}$ and $Aga2/+^{severe}$.
A Macroscopical analysis of thoraces of wild type, $Aga2/+^{mild}$ and $Aga2/+^{severe}$ mice. White arrowheads indicate callus formation at the ribs. H&E staining of transversal sections of wild type, $Aga2/+^{mild}$ and $Aga2/+^{severe}$. **B** H&E staining of transversal sections of wild type, $Aga2/+^{mild}$ and $Aga2/+^{severe}$. **C** PECAM staining on lung tissue of wild type, $Aga2/+^{mild}$ and $Aga2/+^{severe}$. H = heart; L = lung; Scale bars in **B** = 100 μ m; **C** = 50 μ m.

4.2.4.2 Comparison to human patient data

Human OI patients participating in the aforementioned longitudinal study (see 4.2.3.2) underwent lung function tests to identify the effects of scoliosis onto pulmonary function. 36 of the 46 patients (78.3%) developed scoliosis greater than

10°, with a mean curvature of approximately 25° (range 0-70°). 10 patients additionally required spinal instrumentation to stabilise curve progression. Overall observations showed that OI patients with scoliosis had a progressive decline of forced vital capacity (FVC), tidal lung capacity (TLC) and vital capacity (VC) values in conjunction with increased curvature (Figure 34A-C). This is in agreement with prior studies from other cohort studies. However, pulmonary function parameters displayed marginal declines in patients with no obvious pathological spine curvature (<20%) and dropped abruptly in patients after 30° of curvature; thereafter, the decline was gradual (Figure 34D-F)

Notably, pulmonary function parameters declined significantly with age for all OI patients, including lung volumes and flow rates (FVC: $r = -0.5$, $P < 0.001$; VC: $r = -0.5$, $P < 0.001$; TLC: $r = -0.5$, $P < 0.001$), from nearly normal at the age of 4 to about half of predicted values by age 20 years (Figure 35A). All but 2 participants who had three or more pulmonary function tests (PFTs), displayed a progressive decline of percent predicted FVC over time. The decline of FVC, TLC and VC with age was significantly greater for type III than the milder type IV OI patients.

Although scoliosis contributes to PFT decline in OI, significant decline also occurred in the absence of scoliosis (Figure 35B). Lung function declined significantly in 20 participants who had minimal scoliosis ($\leq 10^\circ$ curvature) at one or more time points during the study ($p = 0.008$) to about 60% of values of younger patients. All of the participants who had significant lower airway obstruction had more severe scoliosis. Those with mild scoliosis had restrictive disease but no significant obstructive disease.

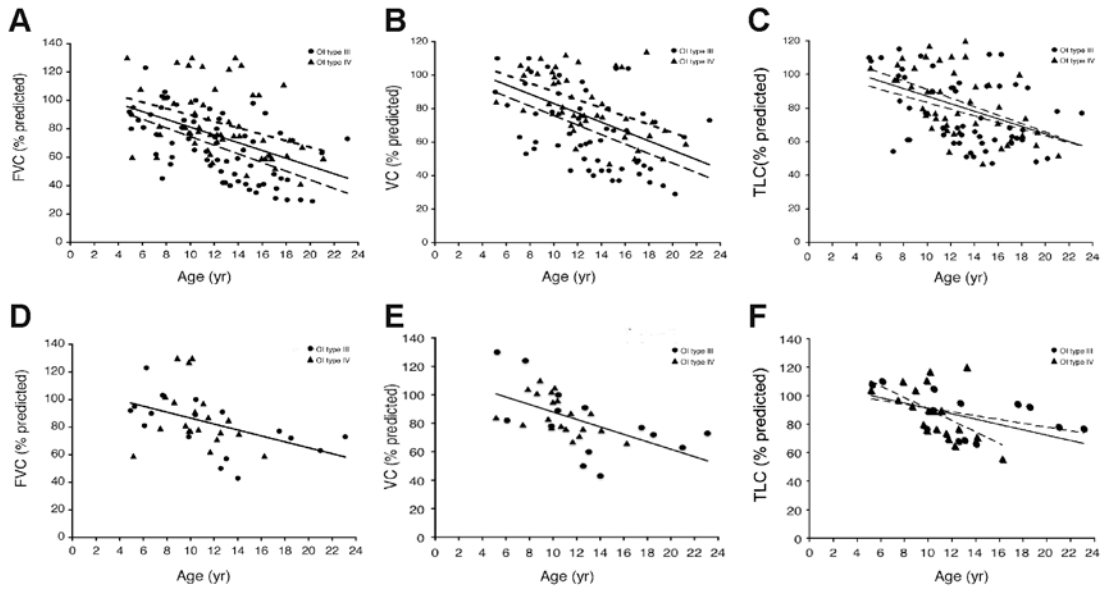


Figure 34. Relationship of age to lung volume and function in type III and IV OI patients. Lung volume and function declines in childhood in the patient cohort as a whole, as well as in types III and IV OI patients considered separately. Pulmonary function also declines significantly in children with types III and IV OI who have less than 10° scoliosis. **A-C** PFT results on all children in study population. **D-F** PFT results on participants with less than 10° scoliosis. (A,D) Forced vital capacity (% predicted), **B, E** Vital capacity (% predicted) and **C, F** total lung capacity (% predicted). The regression lines for the total population (solid line), type III OI (long hatch line) and type IV OI (short hatch line) are shown.

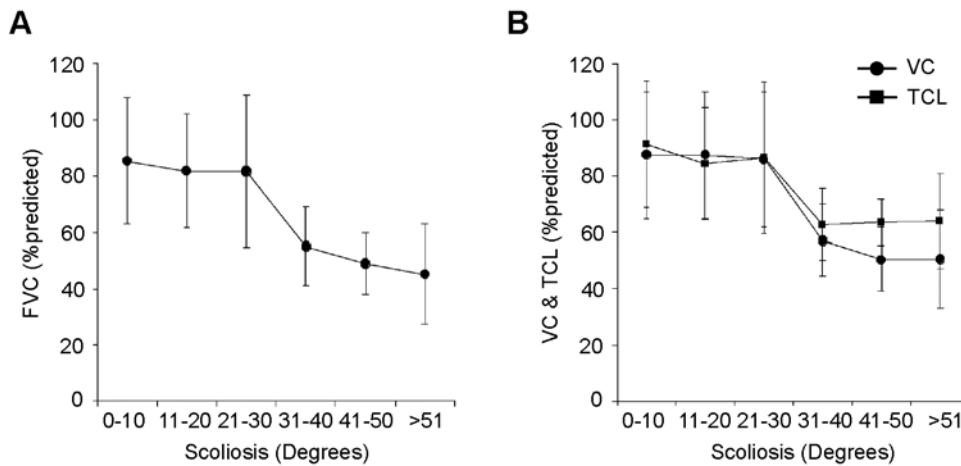


Figure 35. Relationship of scoliosis to lung volume and function in patients with types III and IV OI. Pulmonary function parameters drop significantly in OI patients after 30 degrees of curvature. **A** Forced vital capacity (% predicted) and **B** vital capacity and total lung capacity (% predicted) in comparison to the degree of scoliosis in patients with osteogenesis imperfecta types III and IV.

4.2.5 Blood gas analysis in *Aga2*

The observed cardiac and pulmonary defects observed in *Aga2*^{+*severe*} mice, led to the assumption that both phenotypes might be associated with each other. For this purpose, blood gas parameters were analysed in *Aga2*^{+*mild*} and *Aga2*^{+*severe*} animals at the age of 8 to 11 days and compared with their wild type littermates (Figure 36) (experiments were performed in collaboration with Dr. Frank Thiele). Indeed, pO₂ arterial pressure was declined to 56% in *Aga2*^{+*severe*} mice, while mildly affected animals exhibited wild-type like values. Data for pCO₂ were concurrently increased to 140% in *Aga2*^{+*severe*}. Calculation of oxygen saturation revealed a 61% decrease in severely affected mice, whereas *Aga2*^{+*mild*} values were normal. The observed alterations further substantiated that the cardiopulmonary system has a major impact on lethality in *Aga2*^{+*severe*} mice. Additionally, the altered values for pO₂ and pCO₂ suggested that hypoxia could be a further phenotypical hallmark in severely affected animals.

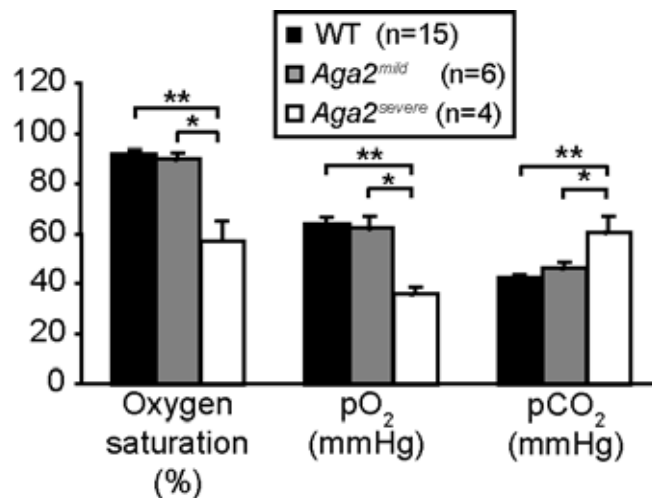


Figure 36. Blood gas analysis of wild type, *Aga2*^{+*mild*} and *Aga2*^{+*severe*}. *Aga2*^{+*severe*} animals exhibit reduced oxygen saturation and a declined partial oxygen pressure (pO₂) while partial carbon dioxide (pCO₂) pressure is increased.

4.2.6 *In vivo* imaging of the cardiopulmonary systems in *Aga2*⁺

As all experiments on perinatal *Aga2*⁺ mice required the killing of mice, *in vivo* imaging could help to visualise the progressive development of *Aga2*^{+*severe*} phenotypes in heart and lung tissue. In collaboration with the Institute of Biomedical Imaging (Dr. Volomidir Ermolayev and Angelique Ale), *Aga2*⁺ animals

were therefore analysed in a pilot study by combining FMT and μ CT imaging techniques. Mice were injected with fluorescent dyes for the vascular system and bone tissue (AngiosenseTM 750 and OsteosenseTM 680, Perkin Elmer, USA). As measurements by FMT were not performed before on newborn mice, methods needed to be established. After measurements, mice were subsequently euthanized, embedded, sectioned and analysed by means of fluorescent signal detection.

Preliminary analysis of the combined FMT and μ CT data displayed multiple fractures in the rib cage of *Aga2/+* animals but signal recognition of bone and vascular tissue appeared inaccurate (data not shown).

To further correct the signal visualisation, threshold calculations have to be applied that will result in a more accurate detection after 3D reconstruction. To support the evaluation of the FMT analysis, images of the slicing experiment will be consulted to define true signals. In the fluorescent imaging, AngiosenseTM 750 signals were detected in both wild-type and *Aga2/+^{mild}* animals. The main lung vessels could be detected as well as a diffuse signal all over the lung tissue. In contrast, *Aga2/+^{severe}* animals lacked signals in the lung. The corresponding bright field images clearly showed that *Aga2/+^{severe}* had excessive bleedings in the lung parenchyma. This indicated that bleedings do not generate enough fluorescent signals for detection.

In summary, the *in vivo* imaging techniques applied for *Aga2/+* mice determined alterations in the vasculature of severely affected animals. Proper 3D reconstruction and measurements of one mouse at different time points (e.g. 3, 5, 7, 9 dpp) might be an indispensable next step towards the assessment of the initial effect that accounts for perinatal lethality in *Aga2/+^{severe}* mice.

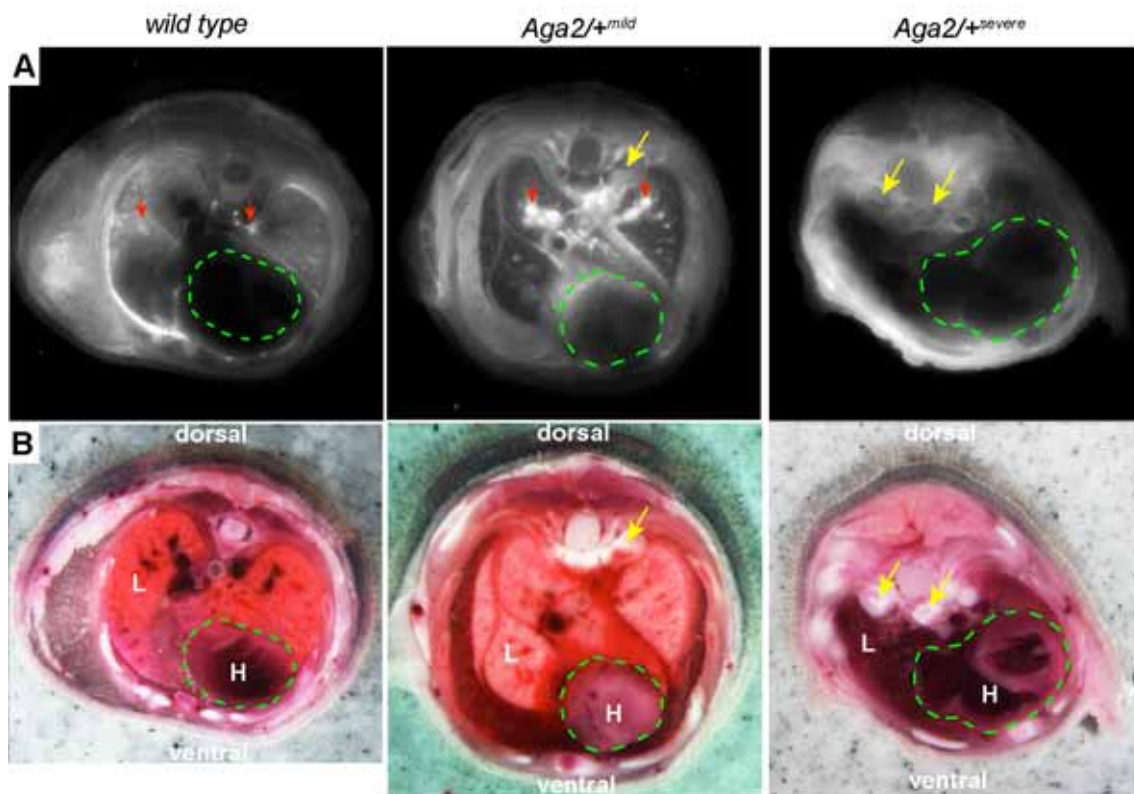


Figure 37. *Aga2/+* slicing images.

A Angiosense™ signalling in wild type, *Aga2/+^{mild}* and *Aga2/+^{severe}*. Signalling is apparent in both control and *Aga2/+^{mild}* lungs (red arrow) but vanished in lung tissue (L) of *Aga2/+^{severe}* mice. Callus formation (yellow arrows) was never observed in wild-type controls. Note that the heart (H) encircled by green dotted lines is enlarged in *Aga2/+^{severe}*. **B** Corresponding bright field images of A

4.2.7 Expression profiling of heart and lung tissue of *Aga2/+^{severe}*

As macroscopical and microscopical characterisation of *Aga2/+^{severe}* animals identified a variety of pathophysiological phenotypes, molecular analysis of heart and lung tissue was a continuative next step to unravel the mechanisms accounting for the increased neonatal lethality in *Aga2*. As the molecular phenotyping screen in the GMC could not identify any regulated genes in lung tissue of 17-weeks old *Aga2/+^{mild}* animals, genome-wide transcriptome analysis of heart and lung tissue was performed with *Aga2/+^{severe}* animals in comparison to wild-type littermates at the age of 11 days. Experiments and data analysis was done in collaboration with Dr. Frank Thiele and Dr. Marion Horsch.

In heart tissue, 48 significantly regulated genes were identified compared to wild type with a false discovery rate (FDR) of 0.5% (Supplemental Figure 6). GO term analysis of differentially expressed genes revealed an association for altered ECM composition and remodelling (Supplemental Table 3). *Col1a1* was the most

prominently regulated gene, showing a 2.5 fold downregulation in *Aga2^{severe}* in three independent probes on the chip assay. This data was confirmed by 4 fold *Col1a1* repression compared to wild type by qRT-PCR (Supplementary Figure 7). In addition, *Col1a2*, encoding for the $\alpha 2$ chain of the type I collagen protein, was concomitantly downregulated in *Aga2/+^{severe}* animals. Furthermore, *Col2a1* and *Col3a1* expression as well as key factors of collagen fibrillogenesis and matrix assembly (*Dpt*, *Mfap4*) were downregulated indicating a reduced collagen network in the myocardium already observed in SEM analysis. Upregulation of *Col8a1*, *Tgm2* and *Ctgf* indicated pronounced ECM remodelling. Changes in metabolic pathways and alteration of oxygen supply were suggested by upregulation of *Egln3*, *Ldha*, *Aldoa*, *Eno1*, *Gapdh* and *Pgm2*, indicating hypoxia. Consistent with the histological examinations, markers for hypertrophy (*Nppa*, *Slc25a4*) were upregulated.

Data obtained from *Aga2/+^{severe}* lung tissue revealed reproducible and significant regulation of 149 genes with a FDR of 0% (Supplemental Figure 8). In contrast to cardiac tissue, GO term analysis revealed that ECM-related transcripts (*Col3a1*, *Col5a1*, *Mfap2*, *Tnc*, *Dpt*) were upregulated, while *Ctgf* displayed a significant downregulation (Supplemental Table 4). Interestingly, *Col1a1* transcripts were not significantly altered in *Aga2/+^{severe}* lung tissue. Additional qRT-PCR of the *Col1a1* transcript in lung tissue samples displayed only tendencies towards downregulation to 75% compared to wild-type controls (Supplemental Figure 7). Furthermore, *Wnt11*, *Tgfbi* and *Ltbp3*, markers for inflammation and wound healing exhibited increased expression levels, as did hypoxia markers, such as *Pltp*, *Cd248*, *AR*, *Gdf10* and *Prkce*. Downregulation of pro-angiogenic markers such as *Ang* and *Cxcl12* supported the loss of the capillary network observed in *Aga2/+^{severe}*, while upregulation of *Agt* hinted for hypertension.

4.2.8 *Col1a1* expression analysis

4.2.8.1 *In vitro* analysis of primary cardiac and pulmonary fibroblasts

As previous experiments claimed for an intrinsic effect of the underlying *Col1a1* mutation in *Aga2*, *in vitro* analysis was utilized to decipher alterations on the cellular level without systemic influences (experiments performed by Frank Thiele).

As fibroblasts are the major collagen producing cells in both tissues, primary cardiac and pulmonary fibroblasts of *Aga2/+^{mild}* and *Aga2/+^{severe}* were isolated and compared to wild type controls. Immunocytochemistry on stimulated cardiac fibroblasts revealed a uniform staining pattern in wild type as well as *Aga2/+^{mild}* cells with extracellular type I collagen secretion, while reduced staining intensity was noticeable for fibroblasts of mildly affected animals (not shown). In contrast, a tremendous reduction in type I collagen protein in *Aga2/+^{severe}* was detectable. Furthermore, remaining collagen tended to accumulate intracellularly (Figure 38A). To verify results obtained on the protein level, qRT-PCR was performed to analyse expression levels of *Col1a1* in fibroblasts. In conjunction with the previous findings, *Col1a1* was reduced to 25% in *Aga2/+^{severe}*, while *Aga2/+^{mild}* expression was reduced to 65% compared to wild-type controls (Figure 38C).

As whole-genome transcriptome analysis on whole lung tissue already suggested, type I collagen antibody staining displayed no observable alterations among the different pulmonary fibroblast cultures (Figure 38B). In addition qRT-PCR further substantiated, that *Aga2/+^{severe}* fibroblasts possessed 75% *Col1a1* expression compared to wild type controls, while *Aga2/+^{mild}* expression was calculated to 90% (Figure 38C).

Taken together, the analysis of intrinsic effects in primary cardiac and pulmonary fibroblasts *in vitro* revealed that *Aga2/+^{severe}* animals displayed a tremendous downregulation of the *Col1a1* transcript in resulting in a dispersed protein staining pattern and substantial alteration both intracellularly as well as in the extracellular matrix deposition in cardiac fibroblasts. Lung fibroblasts as well as both cell types in *Aga2/+^{mild}* animals displayed only marginal changes.

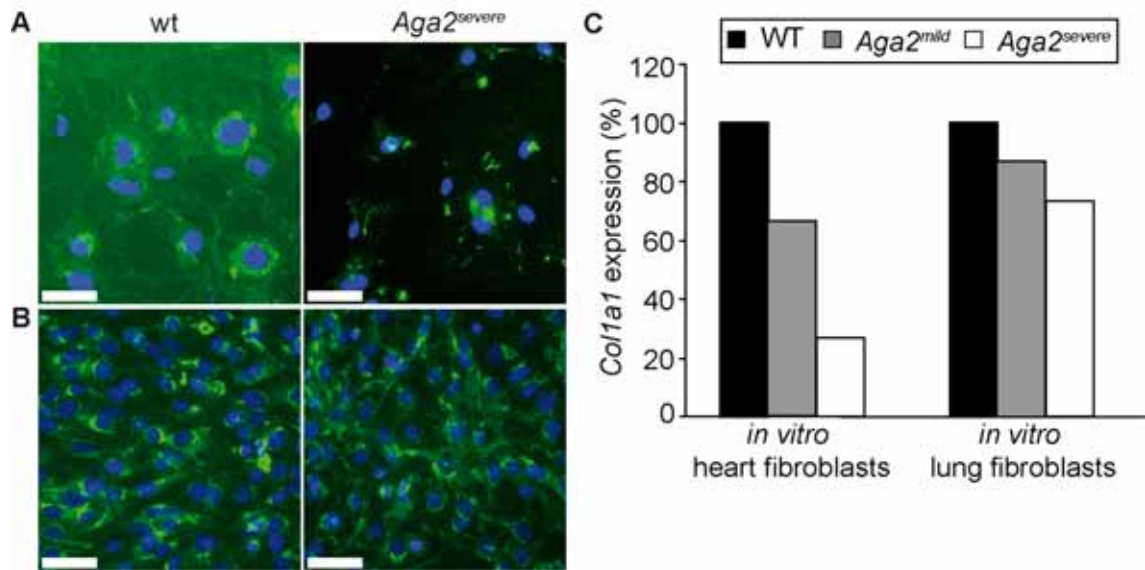


Figure 38. *In vitro* culture of primary heart and lung fibroblasts and expression analysis by qRT-PCR.

A, B ICC for type I collagen (green) on heart fibroblasts (**A**) and lung fibroblasts (**B**) counterstained with DAPI (blue). **C** Overall *Col1a1* expression assessed by qRT-PCR of *in vitro* cultivated primary heart and lung fibroblasts.

4.2.8.2 Onset of *Col1a1* downregulation and allele-specific *Col1a1* expression

The tremendous reduction of *Col1a1* transcripts in *Aga2/+^{severe}* animals led to the assumption that the downregulation closely correlates with the occurrence of lethality. To ascertain this hypothesis, hearts of 14.5 and 20.5 dpc embryos as well as newborns at 1, 3 and 6 dpp were isolated and RNA was analysed by qRT-PCR (Figure 39A) (experiments were performed in collaboration with Dr. Frank Thiele). Throughout all developmental stages, *Col1a1* expression was decreased to 55-70% compared to wild-type littermates. These observed reduction in the expression levels were in close conjunction with the results obtained for *Aga2/+^{mild}* *in vivo* and *in vitro* respectively. At 6 dpp, the first *Aga2/+^{severe}* was identified by outer inspection. Expression analysis of this single mutant mouse clearly showed a downregulation to 25% compared to the wild type controls.

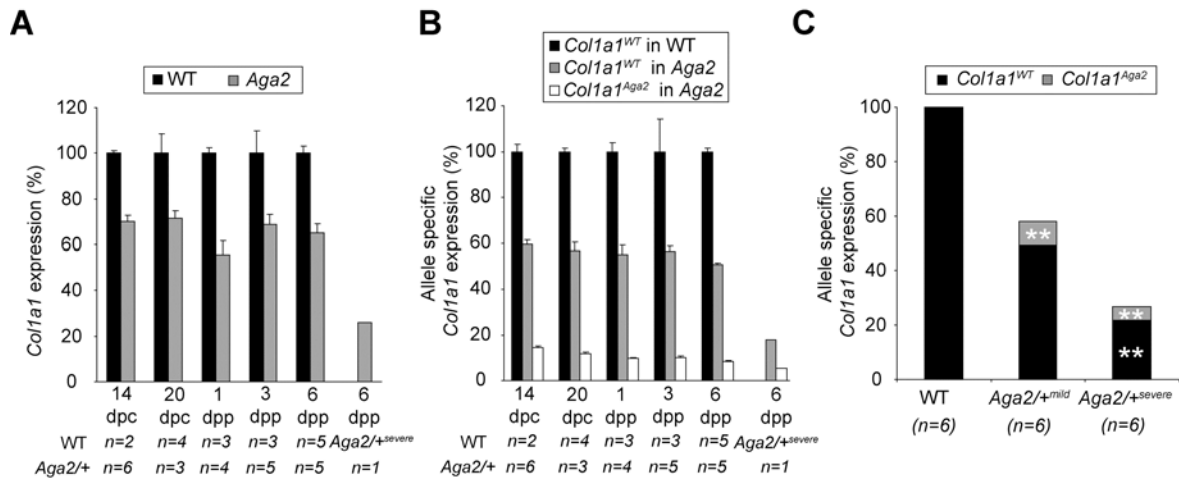


Figure 39. *Col1a1* expression in hearts during perinatal development.

A During embryogenesis and until 3 dpp, *Aga2*^{+/+} mice appear to express *Col1a1* at equal levels with the already known downregulation compared to their wild-type littermates. At 6 dpp, the first *Aga2*^{+/severe} animal was identified, with a reduction in *Col1a1* expression to 25%. **B** Allele specific *Col1a1* expression displays a downregulation of the *Col1a1*^{Aga2} allele in all *Aga2*^{+/+} animals to approximately 10% until 3 dpp. The *Aga2*^{+/severe} animal additionally displays a dramatic downregulation of the *Col1a1*^{WT} allele to 20% and a further downregulation of the *Col1a1*^{Aga2} allele to 5%. **C** Allele specific *Col1a1* expression analysis of 11-days old animals confirms the observations of younger mice shown in B.

As *Aga2*^{+/+} mice were genetically identical by means of inbred strain background and *Aga2*^{+/severe} animals appear in all matings that were set up, possible alterations in the two *Col1a1* allele was hypothesised. Therefore, the analysis of both *Col1a1* alleles was designed to discriminate between different downregulation mechanisms. As the *Col1a1*^{Aga2} transcript was elongated for 16 bp at exon 50, *Col1a1*^{WT} and *Col1a1*^{Aga2} shared the same forward primer but differ in their reverse primer, thus qRT-PCR analysis could distinguish between both alleles. Embryonic and postnatal cardiac tissue was used for the initial experiments.

Compared to the wild-type expression of *Col1a1*^{WT}, all *Aga2*^{+/+} embryos as well as newborns at 1 and 3 dpp exhibited 50-60% of *Col1a1*^{WT} expression (Figure 39B). This showed clearly that the wild-type allele was fully expressed in *Aga2*^{+/+} cardiac tissue at these time points. Solely, the reduced expression of the *Col1a1*^{Aga2} allele to 10% accounted for the observed reduction in total *Col1a1* expression for all *Aga2*^{+/+} heart samples to 60-70% compared to wild-type controls. In 6-days old animals, where the first *Aga2*^{+/severe} mouse was identified, *Aga2*^{+/mild} animals still displayed normal *Col1a1*^{WT} allele expression (50%) and a reduction in *Col1a1*^{Aga2} to 10%. Interestingly, *Aga2*^{+/severe} exhibited a further reduction of *Col1a1*^{Aga2} to 5% and in addition a strong downregulation of *Col1a1*^{WT} to 20% (Figure 40B).

These novel findings were further analysed for all other *Aga2/+* samples at the age of 10-11 days to confirm these observations. Indeed, all *Aga2/+^{severe}* animals showed a reduction of the *Col1a1^{WT}* allele, resulting in a total *Col1a1* expression of 25% compared to controls (Figure 39C).

As the *Col1a1^{Aga2}* allele tended to be silenced in all *Aga2/+* animals nonsense-mediated decay (NMD) could be a possible explanation of the specific downregulation. Emetine is known to block NMD, resulting in the ability to entirely detect usually degraded transcripts. *In vitro* analysis of emetine treated pulmonary fibroblasts revealed a total restoration of *Col1a1^{Aga2}* and therefore also of the complete *Col1a1* expression to wild type like values could be obtained in all *Aga2/+* animals (Figure 40). Emetine treatment of cardiac fibroblasts did not provide reliable results, as expression in treated cells varied extremely among each other.

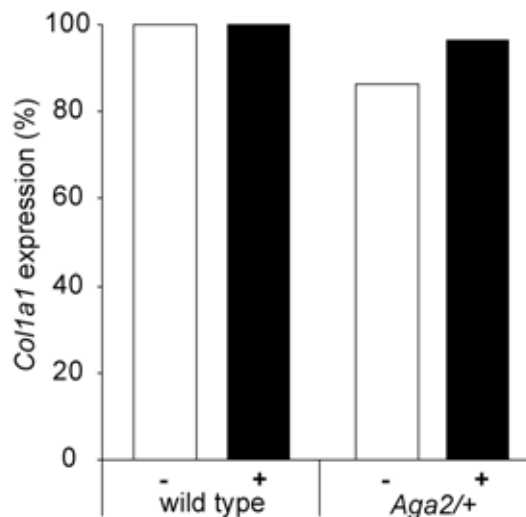


Figure 40. Emetine treatment of pulmonary fibroblasts.

Wild type and *Aga2/+* pulmonary fibroblasts cultures were either treated (+) or not treated (-) with emetine. While untreated *Aga2/+* cells display approximately 80% *Col1a1* expression compared to wild-type controls, emetine treatment restored the expression to nearly wild-type values.

In summary, the onset of the tremendous *Col1a1* downregulation in *Aga2/+^{severe}* hearts was confirmed as early as 6 dpp. While *Aga2/+^{mild}* animals expressed the wild-type allele (*Col1a1^{WT}*) to 50% and only the mutant allele (*Col1a1^{Aga2}*) was downregulated, severely affected animals also displayed a downregulation of *Col1a1^{WT}*. As shown by emetine treatment, at least downregulation of the *Col1a1* transcript in pulmonary fibroblast is caused by nonsense mediated decay. Further analysis on cardiac fibroblasts of both *Aga2/+^{mild}* and *Aga2/+^{severe}* will be required

to identify possible other mechanisms accounting for the downregulation in cardiac tissue of *Aga2*/^{severe}.

4.2.9 Conditional gene targeting

Although, the identification of bone-independent mechanisms leading to death in *Aga2* was well-defined during this thesis, effects of the skeletal malformations on the whole organism cannot be fully excluded. To bypass the severe bone phenotype in *Aga2*, conditional gene targeting would be a valuable tool to analyse the mutations effect on every single organ that contributes to the known phenotypes.

For this purpose, a gene-targeting construct was designed which enables the conditional expression of the *Col1a1*^{*Aga2*} allele after Cre-mediated excision of the wild type allele (Figure 41). Generally, insertion of the targeting vector should result in wild type *Col1a1* expression in the absence of Cre-recombinase throughout the entire organism. With the help of Cre mouse lines, recombination will replace the wild type sequence with the generated sequence harbouring the *Aga2* mutation. *In silico* analysis was performed to ensure that no currently known regulatory element will be disturbed by the insertion of loxP sites into the intronic region of intron 49 and the upstream region of the *Col1a1* 3'UTR. Furthermore the complete annotated 3'UTR region was added to both allele sequences to ensure proper transcription and translation of the *Col1a1* gene. Currently, cloning of the targeting vector is performed. Based on repetitive sequences along the *Col1a1* gene, the 5' homologous arm had to be subcloned in parts and needs to be religated. Cloning of the wild type and mutant allele as well as the frt-Neo-frt sequence and the 3' homologous arm is finished. Due to overlapping of multiple restriction sites in the already existing parts of the whole targeting vector it is not possible to start ligation of the different subsequences as long as cloning of the 5' homologous arm is not finished.

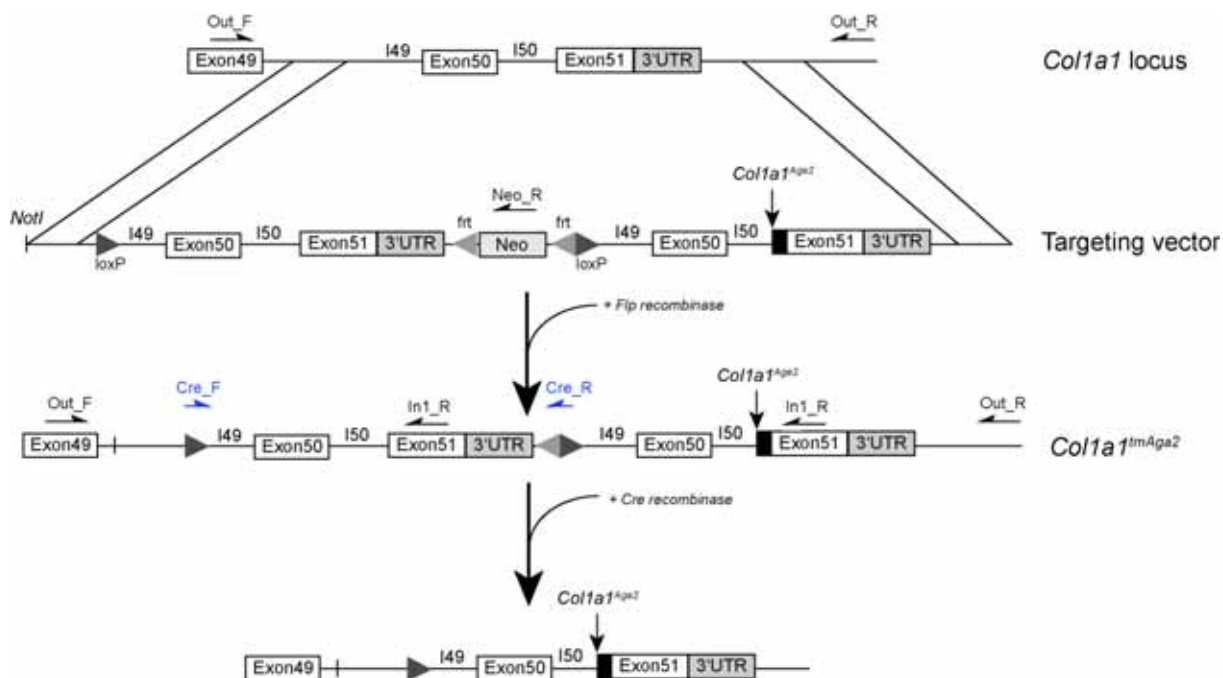


Figure 41. General strategy for gene targeting the *Col1a1^{Aga2}* locus.

In the targeting vector, the wild-type sequence is flanked by loxP sites and an additional frt-flanked neomycin resistance cassette for ES cell selection. Afterwards the mutant sequence including the *Aga2* mutation is placed. After homologous recombination, the neomycin resistance is removed by Flp recombinase. Confirmation can be obtained by long range PCR with the outlined primer (Out_F, In1_R, Out_R). For the detection of the loxP-flanked wild-type segment PCR analysis with Cre_F and Cre_R can be applied. After Cre-mediated excision of the wild-type segment, the mutated sequence will be expressed.

4.2.10 Metabolic phenotypes in *Aga2*

4.2.10.1 General strategy

Recent studies elegantly showed that leptin coregulates bone mass, appetite and energy expenditure^{104,132-134}. In addition, it seemed most likely that bone evolves as an endocrine organ that regulates energy metabolism. This hypothesis was confirmed by studies investigating the bone specific hormone osteocalcin^{4,135}. Subsequent studies by Ferron *et al.*⁹⁷ and Fulzele *et al.*⁹⁹ showed that not only osteocalcin producing osteoblasts alone but the interaction with bone resorbing osteoclasts together have a major impact on β -cell function through osteocalcin signalling (Figure 42). While active osteocalcin levels were at least partially regulated by signalling through the insulin receptor (InsR), the acidic environment during bone resorption by osteoclasts favours osteocalcin activation by decarboxylation of glutamic acid residues (Glu-Ocn). Active osteocalcin enhances β -cell proliferation, insulin secretion as well as insulin sensitivity. Therefore,

defects in both bone cell types do not only cause alterations in bone homeostasis, they also potentially affect pancreatic islet functions.

Observations that people with type 1 diabetes displayed significantly reduced bone mass were already assessed during the 1970s¹³⁶, but the impact of type 2 diabetes on bone is however controversially discussed. Generally, a reduced skeletal quality was observed while BMD values were stable or even slightly enhanced¹³⁷⁻¹⁴⁰. Admittedly, these studies always focus on diabetes as the primary incidence. A reverse experimental approach setting osteoporotic features as the point of origin is still missing.

Postmenopausal women exhibiting osteoporotic features, people with early onset osteoporosis as well as patients suffering from osteogenesis imperfecta (OI) routinely receive antiresorptive drugs like bisphosphonates or Denosumab, a monoclonal antibody against RANKL to inhibit rapid bone loss. These drugs target mainly osteoclasts resorption activity by either enhancing apoptosis or inhibiting differentiation of these cells. This causes a reduction of acidic areas at the bone surface where osteocalcin can be decarboxylated, which eventually leads to a reduction in β -cell function⁹⁷.

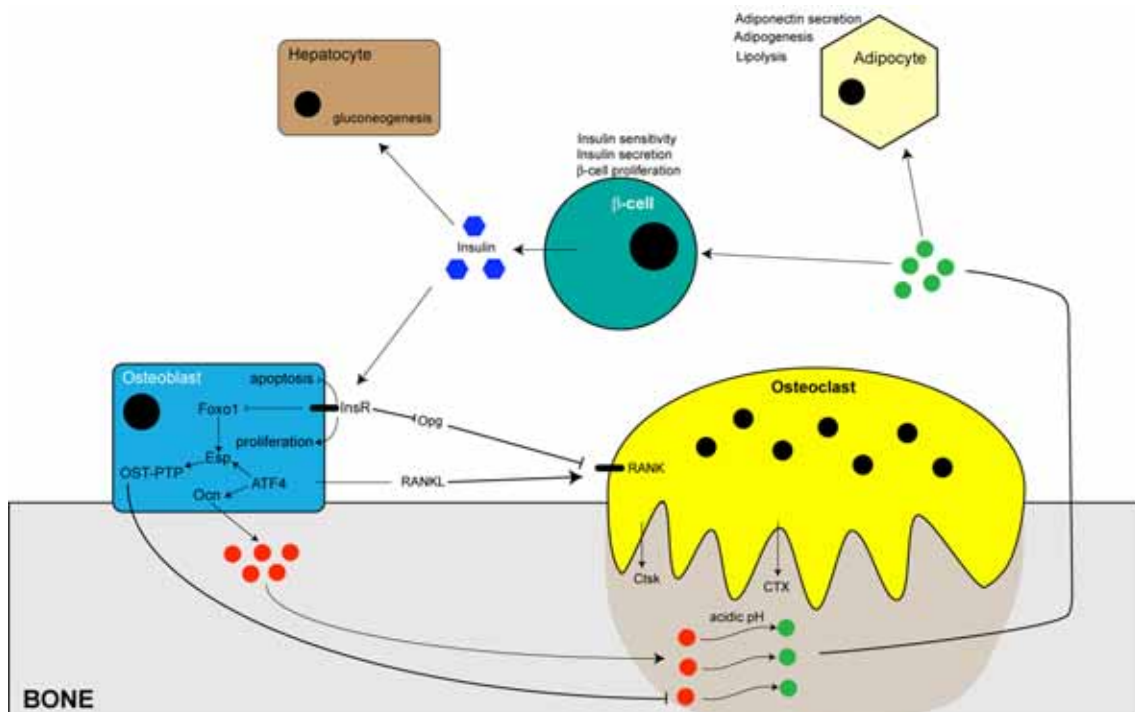


Figure 42. General model for the interaction between bone and β -cells.

Insulin (blue hexagons) signals through its receptor (InsR) in osteoblasts, thus enhancing proliferation and blocking the expression of *Foxo1*, thereby reducing the amount of OST-PTP, an inhibitor of osteocalcin activation. Inactive osteocalcin (red circles) is incorporated into the bone matrix and is released by osteoclast mediated resorption. An acidic pH in the resorption pits of osteoclasts activates osteocalcin (green circles). Active osteocalcin controls adipocyte and β -cell function.

To investigate the effects of primary caused BMD reduction and loss of bone quality and to assess the effects of bisphosphonate administration on energy metabolism, an experimental setup was designed utilizing the *Aga2* mouse line (Figure 43).

Based on the higher apoptotic rates of osteocalcin producing osteoblasts in *Aga2/+* mice⁹¹, possible defects in blood glucose homeostasis and a reduction in active osteocalcin leading to a reduced β -cell function were hypothesised. Therefore, three main questions should be tackled by this approach:

- (1) Do antiresorptive drugs have an impact on the energy metabolism with special interest on the β -cell function in *Aga2*?
- (2) Can long term treatment with bisphosphonates lead to a type 2 diabetic phenotype in *Aga2*?
- (3) Are investigated effects on *Aga2* comparable to human patients?

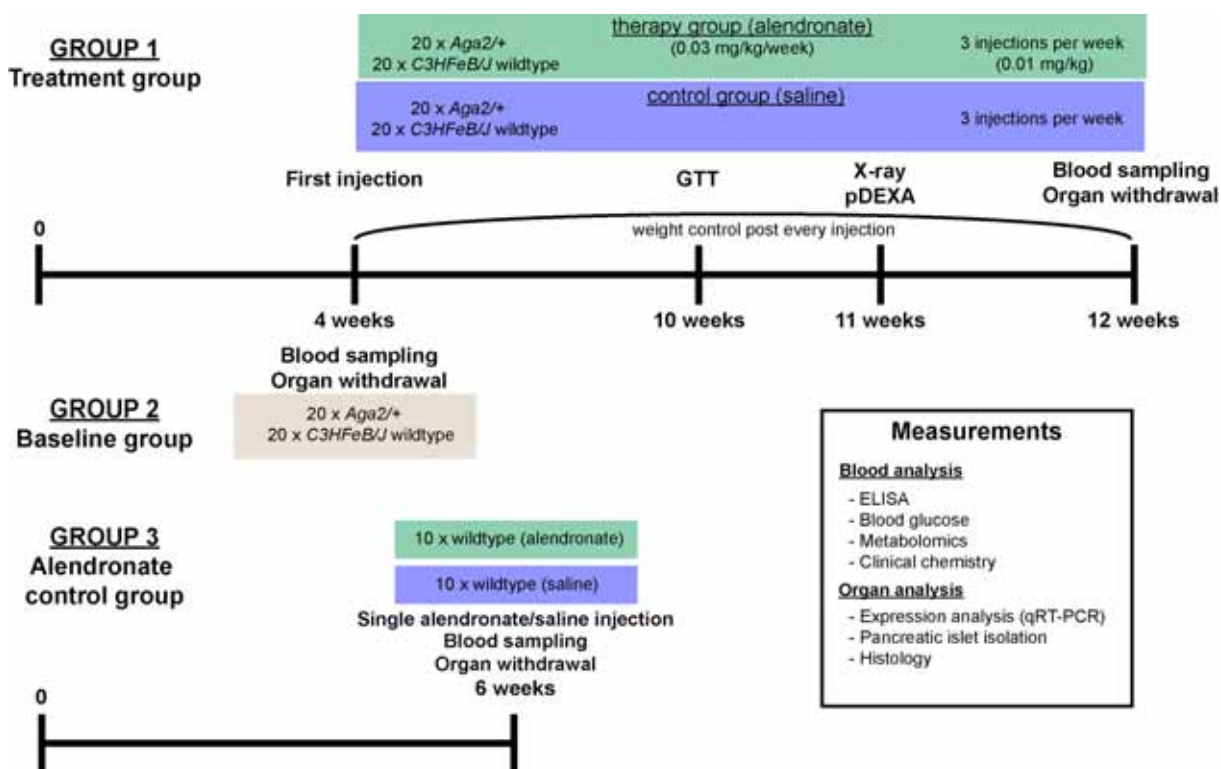


Figure 43. Timetable for the systemic metabolic phenotyping of *Aga2*.

Starting at four weeks of age, animals are randomly subjected to either the treatment or the control group (GROUP 1). These animals will be injected intermittently throughout an eight week period. At the age of 10 weeks a GTT will be performed, X-ray and pDEXA measurements will be executed at the age of 11 weeks. Subsequently, mice will be euthanized and analysed (Measurement box). Animals of the second group (GROUP 2) will be euthanized at the age of 4 weeks to obtain baseline parameters equal to GROUP 1. In a third approach (GROUP 3), six weeks old animals will be injected once with alendronate and saline to verify possible direct effects of alendronate on β -cell function.

4.2.10.2 Experimental setup

Overall three main experimental groups will be analysed during this study. The first experiment will be divided into 4 groups (10 animals per group) with wild type littermates and *Aga2/+* animals, both treated with the bisphosphonate alendronate or untreated receiving equal amount of a physiological saline solution. Alendronate administration will start at the age of 4 weeks with three intermittent injections of 0.01 mg/kg per week for a period of 8 weeks. Animals will be euthanized at the age of 12 weeks and subsequently analysed for a variety of parameters that are specified below (Figure 44). In parallel, a second group of *Aga2/+ x C3HeB/FeJ* matings will be analysed at the age of 4 weeks to receive “baseline” values. Data obtained from this group should identify possible effects caused by the *Aga2/+* mutation independent from treatment and will be performed with *Aga2/+* and their wild type littermates (10 animals per group). Mice will be euthanized and the same parameters will be analysed as investigated for the first experimental groups. In a third approach 10 wild type animals will be analysed for possible direct effects of alendronate on β -cells against control animals (saline injection). A single injection (0.01 mg/kg) will be applied at the age of six weeks. The mice will be euthanized the next day with subsequent blood glucose and plasma insulin analysis. Pancreata will be subjected to histological analysis and expression analysis by qRT-PCR.

The analysis outlined in figure 43 comprises a detailed analysis of the metabolism, pancreatic function as well as the investigation of bone parameters. Weight progression during treatment will be monitored prior to every bisphosphonate/saline injection.

Within in the dysmorphology screen of the GMC the primary and tertiary screening will be utilized. General morphological observations will be assessed by X-ray and DXA measurements. Bone densitometric data will be used to analyse the improvement of bone density upon alendronate treatment. In addition, ELISA measurements for CTX-I, leptin, adiponectin, osteocalcin, Rankl and Opg will be performed to analyse differences in bone metabolism as well as possible rescue mechanisms controlled by leptin and/or adiponectin. In addition, insulin ELISA and blood glucose determinations will be performed to monitor possible dysfunction in glucose homeostasis. Clinical chemical will additionally monitor possible effects of

either the *Col1a1^{Aga2}* mutation or the bisphosphonate treatment on the whole organism. At the age of 11 weeks (after 7 weeks of treatment), mice will be subjected to a glucose tolerance test for the analysis of potential deficits in insulin secretion induced by a glucose injection. Furthermore, a panel of 163 parameters including different types of acylcarnitines, glycerophospholipids and shingolipids as well as amino acids and hexose will be analysed in the metabolomics screening. This screening will provide an overarching analysis of the metabolome in all groups. In addition, isolated pancreatic islets will be investigated *in vitro*. The experiments include the counting of islets and their general morphological appearance, analysis of insulin secretion in dependence on different glucose concentrations in the culture medium as well as transcriptional analysis by qRT-PCR. Further expression analysis is also intended for whole pancreatic and bone tissue to investigate effects on the transcriptional level caused by the *Col1a1^{Aga2}* mutation and alendronate. Finally, histological examination will be conducted to analyse morphological differences as well as protein expression in pancreata and bone.

4.2.10.3 Preliminary results

The entire experimental setup was designed very recently, thus only some preliminary data regarding the baseline values are available.

Aga2/+ animals depicted alterations in the metabolism screen of the GMC (Supplemental Table 5). Especially mutant male mice appeared to consume less food, thus had a reduced energy uptake and displayed a reduced metabolized energy per day. Correlated to the body weight, energy uptake and metabolized energy were wild-type like. In *Aga2/+* females, food consumption was comparable to wild types, resulting in an inclined energy uptake correlated to their body weight. In conjunction, the metabolized energy per day correlated to body weight also exhibited increased values. Additionally, the *in vitro* analysis of osteoblasts (see PhD thesis by Dr. Frank Thiele) showed that osteocalcin expression was downregulated in cultured osteoblasts (Supplemental Table 6).

To investigate effects caused by the *Aga2* mutation, plasma osteocalcin, adiponectin and insulin levels were analysed by ELISA measurements (Figure 44 A-C). While osteocalcin and adiponectin levels were comparable to wild type

controls, insulin levels of *Aga2*^{+/+} animals were significantly decreased ($p=0.0008$) to 24.6% of control values. As decreased insulin values are often accompanied with increased blood glucose levels, available plasma samples were tested for this parameter (Figure 44D). Interestingly, blood glucose levels in mutant animals also exhibited significantly reduced values ($p=0.003$) compared to their wild type littermates suggesting that insulin secretion in *Aga2*^{+/+} mice is sufficient for glucose homeostasis maintenance.

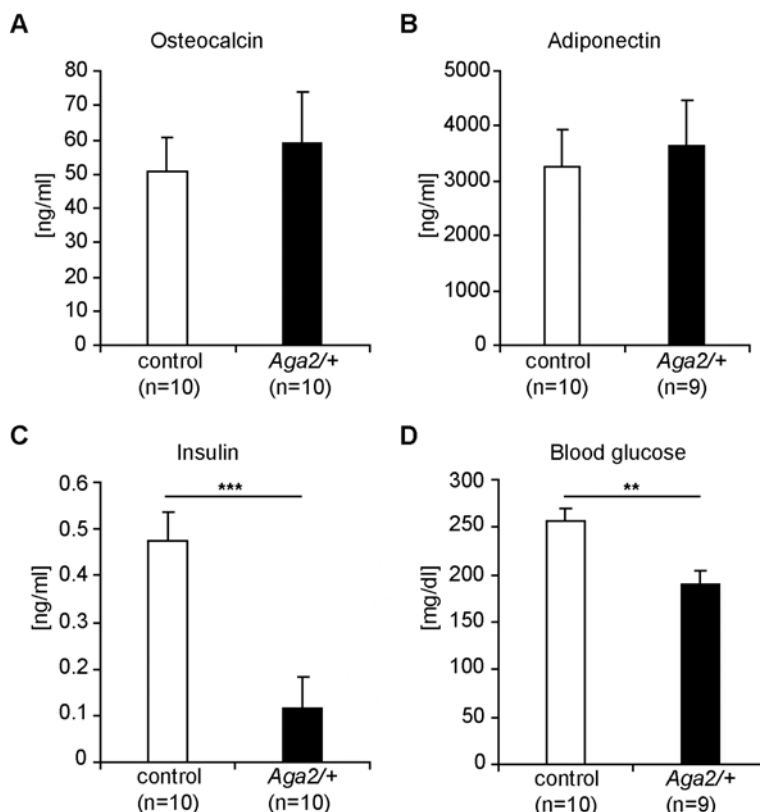


Figure 44. ELISA and blood glucose analysis in 4-weeks old mice.

A Osteocalcin ELISA of 4-weeks old control and *Aga2*^{+/+} animals depicting no alterations. **B** Adiponectin ELISA of the same animals with no obvious alteration. **C** Insulin ELISA of the same animals depict a reduction to 25% of control samples in *Aga2*^{+/+}. **D** Blood glucose levels in *Aga2*^{+/+} mice are significantly reduced. Error bars represent SEM values. ** = $p<0.01$; *** = $p<0.001$.

To confirm decreased insulin levels on the microscopical level and to generally analyse the pancreatic morphology and integrity of its ECM, various antibody stainings were conducted. General morphological observations of islets distribution in the pancreas as well as general morphological appearance with respect to number and size of the islets revealed no striking differences. In addition, the partitioning of α - and β -cells was not altered in *Aga2*^{+/+} (Figure 45A). However, a reduced insulin staining intensity was generally observed in mutant islets compared to controls (Figure 45 A-D). As shown for heart and lung tissue in *Aga2*^{+/+} animals, the *Col1a1*^{*Aga2*} mutation had an impact on vessel integrity. Thus,

additional antibody stainings for PECAM-1 were performed but lacked any alterations (Figure 46B). The analysis of the extracellular matrix which is most prominent in the exocrine part of the pancreas displayed no major structural alterations as shown by type I collagen and laminin stainings (Figure 45C, D). A possible reduction of type I collagen protein in the ECM could not be validated by the analysed sections (Figure 45 C).

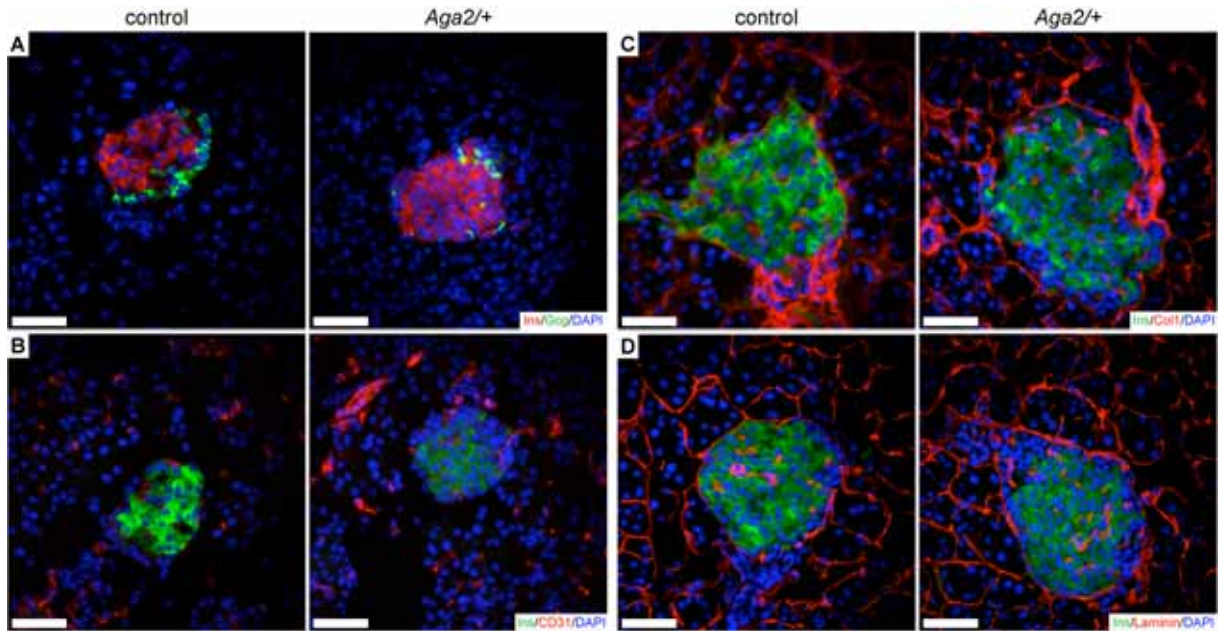


Figure 45. Immunohistochemical analysis of pancreata in 4-weeks old mice.

A Double-staining of insulin (red) and glucagon (green), **B** Insulin (green), CD31 (red), **C** insulin (green), type I collagen (red) and **D** insulin (green) and laminin (red) of wild type and *Aga2/+* sections. All sections are counterstained with DAPI (blue). Merely, insulin stainings appeared reduced in *Aga2/+* specimens. All other stainings are wild-type like. Scale bars = 50 µm.

Finally, qRT-PCR results from a first batch of isolated pancreatic islets (experiments performed in collaboration with Davide Cavanna) interestingly displayed wild-type like expression of both insulin genes in *Aga2/+* (Figure 46A, B). Furthermore, *Gcg*, *Ccdk4* and *Ccnd2* were not regulated between both groups (Figure 46C-E). Solely, but not surprising, *Col1a1* transcripts displayed a trend towards downregulation in *Aga2/+* islets, although significance failed due to a high variance in wild type samples (Figure 46F).

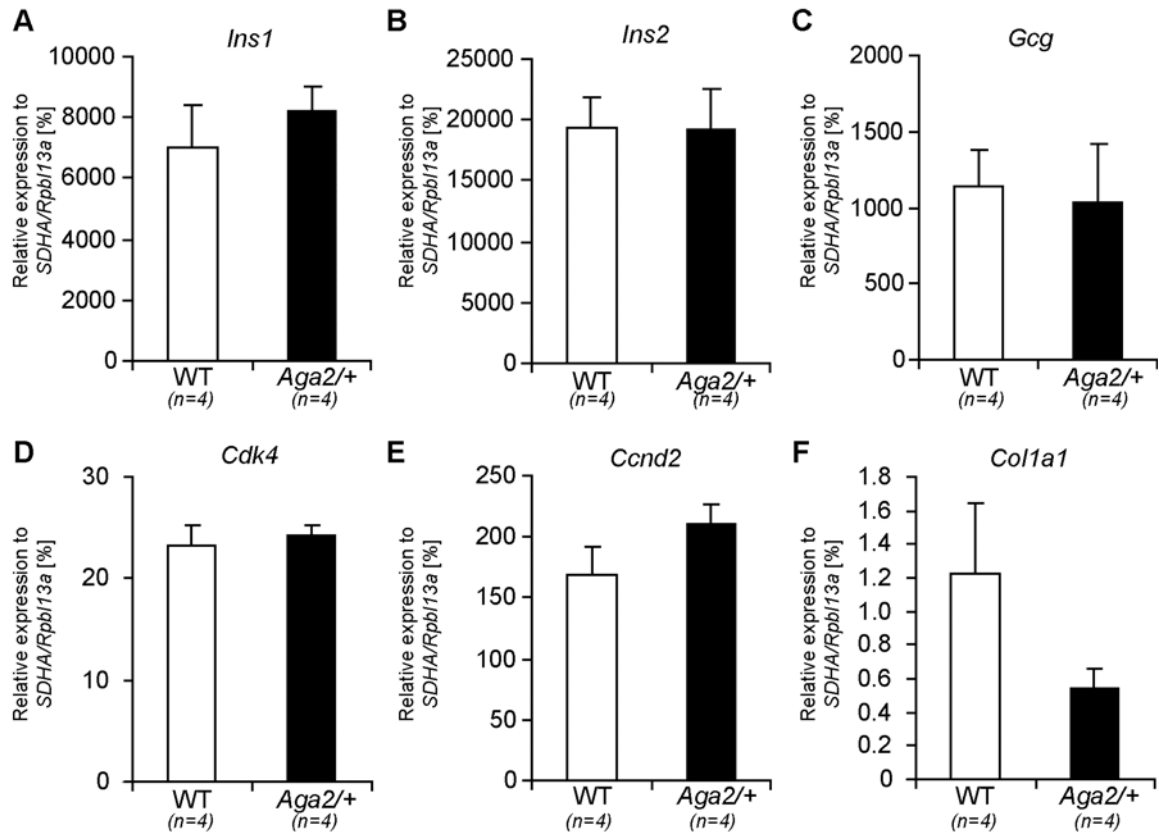


Figure 46. qRT-PCR analysis of isolated pancreatic islets of 4-weeks old mice.

Relative expression of **A** insulin-1 (*Ins1*), **B** insulin-2 (*Ins2*), **C** glucagon (*Gcg*), **D** Cyclin-dependent kinase 4 (*Cdk4*), **E** CyclinD2 (*Ccnd2*) and **F** *Col1a1* to the mean value of the housekeeping genes *SDHA* and *Rpbl13a*. No significant alterations are observed, although *Col1a1* values tend to decrease in *Aga2/+*.

Taken together, preliminary results obtained for the “baseline” cohort exhibited a significant decrease of insulin levels in blood plasma which was confirmed by histological examination but was negated by expression analysis of isolated pancreatic islets. In addition to the declined insulin values also the blood glucose concentration was reduced, suggesting an overall balanced glucose homeostasis in *Aga2/+* animals. Significant effects based on the type I collagen protein as well as the *Col1a1* transcripts could so far not be determined in *Aga2/+*.

4.2.11 Following steps

Besides the new experimental setup investigating potential metabolic phenotypes in *Aga2*, the work on the gene targeting for the *Aga2* mutation is currently in process.

The finished construct will be transfected into ES cells. The available ES cells on a mixed *C57BL6/J* and *129/Sv* background. After validation of correct homologous

recombination of the targeting vector into the *Col1a1* locus by PCR screening and Southern blot analysis, the neomycin cassette will be removed by applying general Flp deletion on the ES cells. Generation of chimeras will be performed as described by the EUCOMM protocol (available at <http://www.eucomm.org/information/protocols/>). After germline verification, *Col1a1^{tmAga2}* mice have to be outcrossed to *C3HFeB/FeJ* for ten generation to achieve a statistically 100% pure background as for the ENU mouse line, since progeny of outcrossed *Aga2* mutants to the *C57BL6/J* background resulted in reduced *Aga2*/+ littermates. Thus it is most likely that those animals already die prenatally. During the outcross mice should be investigated for potential phenotypes caused by the insertion of the targeting vector. After outcross has been finished, mice will be crossed with a general Cre-deleter mouse line. For this purpose, the *Tg(CMV-Cre)1Nagy* line could be used¹⁴¹. This mouse line should confirm the phenotypes already described for the ENU mutant line. Additionally, this Cre-line is also available as tamoxifen inducible¹⁴². The resulting conditional mouse line would be of great interest to investigate the effects of the *Aga2* mutation during adulthood, especially when peak bone mass was reached (approximately after 16 weeks). It will furthermore serve as a good model for the analysis of cardiopulmonary defects in later stages. For cell specific Cre deletion, the *Tg(Col1a1-cre)1Kry*¹⁴³ line will be used to achieve *Col1a1^{Aga2}* expression specifically in osteoblasts. This mouse line will be used to identify the effects of the skeletal manifestations on other organ systems, especially for heart and lung. As all other phenotypes could be traced back to fibroblast defects in different organs, other specific Cre-lines have to be used. Unfortunately, no organ and fibroblast specific Cre line is currently available. Recently, a tamoxifen inducible fibroblast specific Cre line was reported where expression is driven by the control of a 6-kb transcriptional enhancer from the far-upstream region of the mouse pro α 2(I)collagen gene¹⁴⁴. This Cre-deleter mouse line will result in *Col1a1^{Aga2}* expression in all fibroblasts, exacerbating the discrimination of organ specific defects but without skeletal defects.

All different conditional targeted mouse lines should be analysed prior to their lethality rate and overall appearance. Afterwards, every mouse line should be subjected to the primary screen of the GMC to evaluate the effects of cell specific expression of *Col1a1^{Aga2}* in a systemic view.

5. Discussion

5.1 *Ali34*

The functional analysis of *Plxnd1* recently discovered phenotypes that were mainly traced back to endothelial misguidance including cardiac defects and vertebral body malformations. Additionally, *Plxnd1* was found to play a major role in tumor angiogenic processes as well as in immunological traits. Up to date, studies were entirely conducted on complete null-alleles.

In the ENU mutant line *Ali34* various novel bone dysmorphologies were characterised leading to a stiffening of the knee joints caused by defective bone formation in the hindlimb bones. These phenotypes were related to a point mutation in *Plxnd1* causing a premature stop codon resulting in a 48 amino acid shortened protein. Interestingly, all known phenotypes during embryogenesis were confirmed for *Ali34*. Moreover, a systemic analysis of heterozygous *Ali34* animals further characterised the progression of the bone phenotype and additionally identified similar phenotypes observed for homozygous mice with more moderate occurrence. Finally, analysis of the protein was conducted to identify which domain in the cytoplasmic portion of *Plxnd1* is causative for the described phenotypes.

5.1.1 *Plxnd1*'s role during embryogenesis

The phenotypic characterisation of *Ali34* during embryogenesis has shown that the truncation of the cytoplasmic domain of *Plxnd1*^{*Ali34*} is sufficient to phenocopy the recently described defects of *Plxnd1* knockouts^{88-90,145}. Moreover, homozygous *Ali34* embryos additionally display exencephaly and alterations in the development of the sternbrae. As *Plxnd1*^{*Ali34*} is still expressed in homozygous embryos at the designated sites and spatial arrangement on the cellular level is not altered as shown by immunocytochemistry of homozygous MEFs, it seems reasonable that the extracellular Sema-domain of *Plxnd1* which interacts with different class 3 semaphorins might still be functional, but downstream signalling is diminished due to the truncation of the cytoplasmic domain of *Plxnd1*^{*Ali34*}.

Proper angiogenesis is at least partially controlled by guidance cues through binding of Sema3e to *Plxnd1* independently of co-receptors such as *Nrp1* or

Nrp2¹⁴⁵. In *Sema3e*^{-/-} and *Plxnd1*^{-/-} mutants, aberrant blood vessel migration into the developing somites is caused by defective repulsive signalling through the semaphorin-plexin complex as it was also observed in the zebrafish mutant *out of bounds (obd)*¹⁴⁵⁻¹⁴⁸. Homozygous *Ali34* embryos resemble the reported phenotypes, although the expression pattern of *Plxnd1* visualized by immunofluorescence was not altered compared to wild-type controls. Based on this observation, the effect of the truncated cytoplasmic domain in *Plxnd1*^{*Ali34*} seems to be sufficient to abolish the transduction of the repulsive signalling in endothelial growth cone cells. Angiogenic sprouting in *Ali34* as well as in *Plxnd1* knockouts has dramatic effects in later embryonic stages. In the most recent studies by Kanda *et al.*⁸⁹ and Zhang *et al.*⁹⁰, the developing vertebral column displays malformations in the cervical to lumbar vertebrae with varying appearance. These defects in ossification are also observable for *Ali34*, indicating that hypervascularisation of the cartilage anlagen results in severe skeletal dysplasia. Furthermore, the skeletal defects seem to be uniquely driven by the endothelial expression of *Plxnd1* as it was shown for conditional endothelial specific depletion of *Plxnd1*⁹⁰.

The crooked formation of the sternal bones might also be correlated to defective neoangiogenesis. As sternal bone formation initially occurs approximately at 14.5 dpc after the sternal bars are fused, possible vascular mispatterning might also be accountable for both sternal bone alterations as well as the malformation of the xiphoid process. Interestingly, *Sema3e* knockout studies never observe sternal bone phenotypes while another class 3 semaphorin - *Sema3a* - was shown to develop a comparable phenotype as observed for *Ali34*¹⁴⁹. This might indicate a possible *Sema3a*-*Plxnd1* signalling as *Sema3a* is expressed in both endothelial cells and osteoblasts^{150,151}. At least for cardiac tissue this binding was reported *in vivo* with the requirement of the Nrp1 co-receptor^{88,147} and *in vitro* for primary endothelial cells⁹⁰. Therefore it might be possible that the *Sema3a*/Nrp1/*Plxnd1* complex is also evident during sternal development.

The potential of *Plxnd1* to interact with different types of class 3 semaphorins in the presence or absence of neuropilins, makes it a multifaceted protein in different tissue types. As *Plxnd1* expression is not exclusively restricted to endothelial cells during embryogenesis other observed phenotypes like exencephaly might also be traced back to neuronal defects. While the *Sema3e*-*Plxnd1* complex also acts as a

repellent in neurons, the additional binding of Nrp1 as a co-receptor was found to generate attractive cues during neuronal circuit formation¹²⁶. However, neuronal defects were never reported for *Plxnd1* knockouts where neurofilament stainings appeared wild-type like. As *Ali34* exhibits the phenotype of exencephaly in 23% of all homozygous embryos, a possible effect on neuronal cell migration seems feasible. Neural tube closure requires neural crest cell migration that in turn is driven by RhoA mediated reorganisation of actin filaments¹⁵². As the *Sema3c/Nrp1/Plxnd1* complex is responsible for attractive neural crest cell migration during cardiac development¹⁵³, it might also be accountable for proper neural tube closure. Furthermore, exencephaly was also reported for *Plxnb2* knockout embryos¹⁵⁴ with an 87.7% penetrance, suggesting only a minor or redundant effect of *Plxnd1*, as the penetrance was calculated to 23%. In addition, with regard to the low penetrance in *Ali34*, a further possibility that might explain this additional phenotypic trait and the absence in *Plxnd1* knockouts could be a different genetic background among the different lines that was also reported to play a role in *Sema3a* and *Sema3c* signalling^{155,156}.

Another striking phenotype observable for homozygous *Ali34* embryos was the incomplete septation of the cardiac outflow tract resulting in a persistent truncus arteriosus (PTA). This is in conjunction with *Plxnd1* knockouts, which also entirely resembling these phenotypes in general and conditional loss of function mice respectively^{88,90} and are thought to be sufficient to account for neonatal lethality. It is not surprising that the potential of *Plxnd1* to bind different class 3 semaphorins is also evident in cardiac development. While the initial migration of cardiac neural crest cells under the control of the transcription factor *Foxc1*¹⁵⁷ and *Plxna2* signalling¹⁵⁸ was obviously not disturbed by *Plxnd1* signalling⁸⁸, *Sema3c* deficient mice display septation defects¹⁵⁵. This indicates, that *Plxnd1* might act downstream of the neural crest migration process by interacting with *Sema3c* and its co-receptors in cardiac outflow tract development^{88,150,159}. Notably, inhibition of *Nrp1* only was shown to be insufficient in generating outflow tract phenotypes¹⁵⁹, while *Nrp1* and *Nrp2* inactivation together can resemble the observed phenotypes of either *Sema3c* or *Plxnd1* deficient mice^{88,145,155}. A connection to VEGFs, that are also known to contribute to outflow tract morphology was also recently suggested by competitive binding of *Sema3a* and *Sema3c* to *Nrp1* also crucial for VEGF¹⁶⁵ binding to its receptor VEGFR2 (KDR)⁸⁸.

As *Sema3c* expression is restricted to the region of the outflow tract, other phenotypes observable in *Ali34* and *Plxnd1* knockout hearts have to be caused by other signalling defects including *Plxnd1* signal transduction. Although not shown for hearts of homozygous *Ali34* embryos in detail, *Plxnd1* deficiency causes a condensed and discontinuous atrial myocardium as well as thin-walled and enlarged atria⁹⁰. Based on the overall morphology of homozygous *Ali34* hearts that is reminiscent to the reported phenotypes it is assumable that these defects are also evident.

Taken together, the phenotypes observed for homozygous *Ali34* embryos resembled the known knockout phenotypes that can be traced back to the interaction of different class 3 semaphorins (*Sema3a*, *Sema3c*, *Sema3e*). The diverse spatial expression patterns as well as the different requirements of the co-receptors *Nrp1* and *Nrp2* for class 3 semaphorins to bind to *Plxnd1* clearly show that cardiac development, neural tube closure and vascularisation is controlled by different interactions and signalling cues. Based on the fact that the *Ali34* mutation only causes a 48 amino acid truncation of *Plxnd1*, this ENU mutant mouse line is a perfect model for studying the cytoplasmic signalling driving vascular pathfinding.

5.1.2 *Plxnd1* signalling affects bone development and maintenance

Apart from the diverse patterning defects during embryogenesis in homozygous *Ali34* mice that die shortly after birth, *Ali34/+* mice were viable and display numerous skeletal abnormalities. This includes the defective guidance of cartilage canals during the development of the secondary ossification centre in the large long bones (tibia, femur, humerus) that eventually resulted in ectopic bone formation through the epiphyseal growth plate. The phenotypic severity, based on the frequency of ectopic bone formation events in the growth plate, ranges from mild broadening of the tibial surface up to the development of osteophytes at the tibia, loss of proper endochondral bone formation, ankylosis and osteoarthritis. Furthermore, subchondral sclerosis was a commonly observed alteration in all *Ali34/+* hindlimb bones.

The initiation of the primary phenotype was evaluated to be present shortly after birth. A prerequisite of the formation of the secondary ossification centre is the formation of cartilage canals during the first days of life¹⁶⁰⁻¹⁶². It is, however, still

unknown which process is the driving force for the initiation of such cartilage canals. One model claims for a VEGF-independent formation of canals from the surrounding perichondrium¹⁶³. It is believed that the disintegration of cartilage and the formation of canals is mainly governed by matrix metalloproteinases (e.g. Mmp9, Mmp13, Mmp14)^{164,165}. Admittedly, Alvarez and co-workers describe VEGF signalling to be required for neovascularisation in the middle of the epiphysis to control proper chondrocyte hypertrophy as well as bone formation¹⁶³. Another model also accepts the requirements of matrix metalloproteinases during the formation process, but suggested a VEGF-A isoform gradient in the epiphysis to be crucial for canal guidance and proper secondary ossification centre development¹⁶⁶. Based on the findings in *Ali34*, cartilage canal formation is not disturbed by *Plxnd1* signalling, as the formation itself was found to be normal. In addition, qRT-PCR analysis revealed that none of the crucial factors, namely Mmp9, Mmp13 and the main VEGF-A isoforms are generally regulated. However, results in some *Ali34/+* specimens show an upregulated expression of matrix metalloproteinases which might cause increased cartilage canal formation and explain the enhanced cartilage disintegration, taking place when more canals develop through the epiphysis and the growth plate in more severely affected animals. Furthermore, the equal ratio of the different VEGF-A isoforms clearly shows that blood vessel guidance during cartilage canal development is independent of these factors. This leads to the hypothesis that disturbed *Plxnd1* signalling does not change the overall microenvironment of the perichondral and epiphyseal tissue. In conjunction with this, studies of mouse models expressing only single VEGF isoforms display either reduced or delayed vascular invasion into the epiphysis that results in defects in secondary ossification centre development, but defective canal guidance was never observed^{102,166,167}. A further model hypothesised a quiescent angiogenic process including blood vessel formation through the epiphysis in a VEGF independent manner, whereby a reactionary angiogenic process requiring proper VEGF signalling is regulating bone formation^{163,168}. The observations made in *Ali34* further corroborate this model, as patterning is disturbed while the initiation and bone formation processes are wild-type like.

After cartilage canals penetrate into the epiphyseal plate, bone formation was recognised in *Ali34/+*. Chondrocytes in close proximity to the ectopic bone were

shown to exit the proliferative phase. Subsequently, the loss of isogenic group development results in a distorted not columnar-like alignment of the chondrocytes as well as irregular chondrocyte hypertrophy and orientation to the newly formed bone. Notably, ablation of *Rac1*, a potential interaction partner at the cytoplasmic domain of *Plxnd1* in chondrocytes, also results in loss of isogenic groups in the growth plate although to a much larger extent and independent of any ectopic bone formation¹⁶⁹. As *Plxnd1* expression was also found in chondrocytes, an effect on chondrocyte formation and guidance processes through the epiphyseal growth plate might be conceivable.

Osteoblast expression of *Plxnd1*⁸⁹ was analysed by an *in vitro* assay system in *Ali34*. None of the analysed parameters revealed defects throughout the three weeks culture period. These results clearly showed that the interactions between osteoblast/osteoblast and osteoblast/osteocyte-like cells accounting for nodule formation are not disturbed by a defective *Plxnd1* signalling. It is however noteworthy, that pre-osteoblasts express other semaphorins like *Sema3b*, *4c*, *5b* and *6c* that do not bind to *Plxnd1*¹⁷⁰, which might suggest that osteoblast-osteoblast communication is not *Plxnd1*-dependent. Furthermore, osteoclasts were shown to be capable for *Sema3a* and *Nrp1* expression^{171,172}. Based on the current findings in *Ali34/+* mice, number and overall appearance of osteoclasts is not altered. Further experiments that calculate standard histomorphometric parameters (see ^{128,129}) as well as calcein labelling to evaluate the bone formation rate would be reasonable next steps towards a more in depth analysis of potential alterations of bone homeostasis in *Ali34*.

The hindlimb bone phenotype in *Ali34/+* mice can be classified into two severity grades. Mildly affected animals developed a slight broadening of the tibial surface with a minor reduction in overall length. In addition, subchondral sclerosis as well as a reduction in the tibial epiphyseal portion was observable. This phenotypic occurrence was related to a low number of misguided cartilage canals during secondary ossification centre development. In contrast, severely affected *Ali34/+* animals display an enhanced broadening of the tibial surface area and partial depletion of their tibial epiphyseal growth plates resulting in strongly reduced bone length formation. These observations might be caused by numerous ectopic bone formation events during the first weeks. In addition, fibrotic tissue developed in the joint cavities at the age of 8 weeks that seem to differentiate into calcified tissue at

later stages. Based on these observations, it is most likely that mechanical forces have an additive effect on phenotype diversity. Due to the fact that bone mass and architecture are continuously adjusted according to experienced loads¹⁷³ and mechanical stimuli function as determinants for adaptive bone remodelling¹⁷⁴, structural changes of the whole knee joint are conceivable. Ectopic bone formation as it is shown for *Ali34* is likely to have a major impact on bone reconstruction mechanisms. Alterations in the distribution of forces onto the bone might explain the increase in cortical content and density as well as the increase in cortical area (also evident in the ratio between periosteal and endosteal circumference) shown by pQCT analysis in both metaphysis and diaphysis. In addition, subchondral sclerosis, evident in all *Ali34/+* hindlimb bones, further indicates that cortical bone formation is preferred. These features were recently described to be causative for the development of an osteoarthritic phenotype¹⁷⁵. As it is evident for mildly affected mutants, altered bone structure by itself is not sufficient to induce cartilage erosion. The appearance of both structural defects in bone composition and the development of osteophytes in severely affected *Ali34/+* mice however cause OA-like phenotypes. The upregulation of different interleukins, matrix metalloproteinases, as well as the upregulation of *Plxnb1*, *Flt1* and *Scya2* known regulators in angiogenesis and bone remodelling were recently reported to be associated with OA^{176,177}. Furthermore, cartilage hypertrophy in close conjunction with subchondral bone formation in the secondary ossification centre is also observable, contributing to the OA phenotype¹⁷⁸⁻¹⁸⁰. At least structural defects could be confirmed in *Ali34*. Although the characteristic genes associated with the progression of OA were not found to be regulated in bone tissue of *Ali34*, other genes like *Vcam-1* and *Wasf2*, responsible for angiogenic traits^{181,182}, indicating enhanced angiogenesis. As neoangiogenesis of the synovium and the osteochondral junction of the articular surface are typically observed in OA progression¹⁸³, a defective *Plxnd1* signalling might cause hypervascularisation, which indeed contributes to a more severe progression of OA by unknown mechanisms on the molecular level¹⁸⁴.

In summary the *Ali34* mutation in *Plxnd1* seems to cause cartilage canals mispatterning independently from VEGF signalling during the first week after birth. The number of misguided canals is most likely thought to determine the severity of the hindlimb bone phenotype in older *Ali34/+* animals. The development of

osteophytes as well as the progression of an OA-like phenotype in severely affected animals might be secondary due to excessive ectopic bone formation and accompanied altered force distribution on the hindlimb bones. To which extent *Plxnd1* signalling in chondrocytes, osteoblasts and osteoclasts contributes to the bone phenotype remains to be elucidated.

5.1.3 Systemic phenotypes of *Ali34*

Besides the alteration in bone development and maintenance, the primary screen of the GMC identified several additional phenotypes.

Behavioural and neurological phenotyping of *Ali34/+* were largely inconspicuous. Solely, male *Ali34/+* mice displayed a reduced travelling distance in the open field test and a reduced rotarod performance. Notably, the number of severely affected males with impaired movability was higher than females in both tests. Although *Plxnd1* is known to be expressed in neuronal tissue during adulthood, and is responsible for neuronal circuit formation^{126,185}, these phenotypes are considered to be secondary effects that are caused by the bone phenotype. However, further experimental setups have to be designed to completely rule out neuronal defects in *Ali34*.

In the eye screen, an increased axial length was detected in male mutants. As the development of the eye comprises three different types of embryonic tissues (neuroectoderm, mesoderm and surface ectoderm) a potential cellular migration or positioning defect during embryogenesis might be accountable for the phenotype but remains to be highly speculative. Unfortunately, retinal vascular mispatterning could not be determined in the screening as mice of the *C3HFeB/FeJ* inbred strain commonly display vessel attenuation^{186,187}. As retinal vascularisation develops through neoangiogenesis postnatally¹⁸⁸, *Plxnd1* might be a crucial regulator of the vascular patterning. Indeed, recent studies on *Plxnd1* and *Sema3e* in zebrafish and mouse mutants displayed angiogenic inhibition in the retina^{90,127,189}. Additionally, earlier studies engaging in this topic identified pathways, similar to that of the secondary ossification centre development^{101,166,190}. It is therefore conceivable, that *Ali34* mutants might display defects in retinal vascular patterning if maintained on another inbred strain.

Finally, cardiac defects were identified in the pathological screening of the GMC. These defects included the dilatation of the auricle, focal fibrosis in the pericardium and bifurcation of the aortic arch. Although the penetrance of these phenotypes was low, the parallels between cardiac defects in homozygous embryos and in the heterozygous adult animals are clearly perceptible and are not to be denied.

Taken together, systemic phenotypes besides bone are hardly detectable in heterozygous animals. Based on the fact that *Plxnd1* signalling is responsible for blood vessel sprouting in many organ systems, minor defects seem plausible. The retinal phenotype of *Ali34* mutants will have to be investigated in another inbred mouse strain, but heart defects, however with low penetrance, claim for more systemic defects that left unrecognized during the primary screen of the GMC

5.1.4 *Plxnd1*'s association to human diseases

To date, no specific human disease is related to mutations in *PLXND1*. Notably, several studies claim for a contribution of the *Plxnd1* signalling pathway to aetiology of several diseases.

Recently, a patient suffering from CHARGE syndrome (OMIM #214800) was found to harbour a missense mutation in *SEMA3E*¹⁹¹. The CHARGE syndrome, initially described in 1979 by Hall¹⁹² and named by Pagon in 1981, depict coloboma of the eye, hear defects, atresia of the choanae, retardation of growth and/or development, genital and/or urinary abnormalities, and ear abnormalities and deafness¹⁹³ and could be previously linked to mutations in the *CHD7* gene¹⁹². In contrast to homozygous *Plxnd1* null mice that die perinatally, *Sema3e* knockout mice are viable and resemble most of the described phenotypes of the CHARGE syndrome¹⁹⁴. However, based on the systemic phenotyping of *Ali34*, heterozygous mice might also be correlated to the disease although with milder impact.

Association to hereditary congenital facial palsy also known as Möbius syndrome 2 (OMIM %601471) was analysed. The disease is characterised by paralysis of cranial nerves, orofacial and limb malformations as well as defects in the skeletal muscles¹⁹⁵. As facial nerve defects are also commonly observed in patients of CHARGE syndrome, contribution of *PLXND1* seemed conceivable. Interestingly, chromosomal mapping of the disease in human patients revealed a linkage to 3q21-22, resembling a syntenic region of chromosome 6 in mouse also

containing *PLXND1*¹⁹⁶. As *Ali34* also displays malformation in the extremities and cranial nerve defects might also be possible, the *PLXND1* locus would be a possible candidate region to search for causative mutations. However, the evaluation of sequencing data in human patients revealed until now no causative mutation in either the coding or the non-coding sequence of *Plxnd1* as all putative polymorphisms were also found in the control groups^{197,198}.

In addition to the contribution of *PLXND1* to the development of the CHARGE syndrome, a more widespread association to different types of cancer was recently described. It was shown that *PLXND1*'s expression is increased both in malignant cells and its vasculature¹⁹⁹⁻²⁰¹. Additionally, Casazza and co-workers confirmed *PLXND1* expression in human colon carcinoma samples²⁰². Therefore, results suggested attractive signalling cues mediated by *PLXND1* in cancer development and metastatic spreading. Thus, defective *Plxnd1* signalling observable in *Ali34* might be capable to reduce the susceptibility of cancer development in this mouse line. Even though, the appearance of metastasis was not investigated in *Ali34* so far, it would be worth to follow up possible effects (see later).

In conclusion, diseases that are directly linked to *PLXND1* mutations were not observed yet. Nevertheless, phenotypes in homozygous *Plxnd1* null mice can be correlated to CHARGE syndrome. Amongst others, the potential of *PLXND1* to either induce or repeal angiogenic blood vessel sprouting might potentiate different defects in a variety of organ systems.

5.1.5 Impact of *Plxnd1*'s cytoplasmic region on intracellular signalling

Although *Plxnd1*^{*Ali34*} is truncated by only 48 amino acids and the protein is still associated to the membrane, the phenotypic analysis suggests a complete loss-of-function similar to reported knockout mouse lines. However, the preliminary analysis of the *Plxnd1*^{*Ali34*} protein confirmed that expression is not altered and that the protein is still transmembrane-bound. Based on these observations, a more sophisticated mechanism that might entail the underlying phenotypes in both *Ali34* and the reported knockout-lines is conceivable.

To unravel possible mechanisms, the cytoplasmic tail of *Plxnd1* has to be subdivided into its single domains. A RhoGTPase binding domain (RBD) located in

the middle of the cytoplasmic tail^{203,204} is flanked by two highly conserved RasGAP domains (C1 and C2)^{148,205} that specifically bind small monomeric GTPases of the R-Ras family²⁰⁶. The C-terminal end of the cytoplasmic region (~40-60 amino acids), lacks any known protein domain. Interestingly, a SEA-COOH motif at the very end of Plxnd1 is known to be capable for binding type I PDZ domains¹⁹⁴.

It was recently shown that the RBD of Plxnd1 interacts with GTP-bound Rnd2 and provokes the inactivation of the two nearby RasGAP domains²⁰⁷ due to sterical modifications. Only in conjunction with the binding of semaphorins at the extracellular part of Plxnd1, Rnd2 will be released and the RasGAP domains are capable for interacting with proteins of the Ras-family namely M-Ras and R-Ras^{126,194,207,208}. In the active state R-Ras GTPases maintain integrin-mediated cell adhesion to the ECM²⁰⁹. For instance, binding to Plxnb1 or Plxnd1 implies the inactivation of R-Ras, thus resulting in the loss of cell adhesion to the ECM^{207,210}. In addition, the RBD has a second important role in the downstream signalling of Plxnd1. After Rnd2 removal from the RBD, active RhoGTPases (e.g. Rac1, Cdc42, RhoA) can bind to the RBD^{203,211}. In the case of Rac1, it was recently reported that GTP-bound Rac1 binding antagonises actin stabilisation, thus promoting neural growth cone collapse^{204,212}. The active sites, capable for binding either R-Ras or RhoGTPases are still present in *Plxnd1*^{Ali34}. As it was preliminary shown for primary mouse embryonic fibroblasts *in vitro*, actin filaments appeared less dense in homozygous cells compared to *Ali34/+* and controls, but cell collapses were not observed. Additionally, the proposed tertiary structure²¹³ in Plxna1 further provokes the hypothesis, that the active sites are not sterically altered due to the loss of the 48 amino acids in the mutated protein. This would imply that neither the RBD nor the RasGAP domains are affected and possibly fulfil their intracellular functions. To proof this hypothesis it is necessary to perform GTPase binding assays in the future.

The C-terminal stretch harbouring a SEA-COOH motif in Plxnd1 is completely absent in *Ali34*. Among the different classes of plexins (A-D), specific motifs were identified for these regions and are thought to be specific modulators and/or effectors for plexin signalling¹⁹⁴. In the case of Plxnd1 it was recently shown that GIPC1, a further key player during angiogenesis^{214,215}, is able to bind to the SEA-COOH motif. As this binding motif is absent in *Ali34*, the proposed modulating and downstream effects provoked by GIPC1, might be at least crucial for the vascular

phenotype in mutant mice. To discriminate between defective Ras/Rho signalling and the impact of loss of GIPC1 interaction further binding assays with Plxnd1^{Ali34} have to be performed.

Based on the current knowledge on interactions at the C-terminal part of Plxnd1 a more directed analysis of the mutated protein is enabled and the effect of the truncated protein in *Ali34* will be beneficial for further investigations on the Plxnd1 signalling pathway.

5.1.6 Conclusion and future perspective

In conclusion, *Ali34* is the first known mouse model that harbours a point mutation in *Plxnd1*. While resembling the entire phenotypic characteristics of homozygous knockout mice, skeletal defects as well as faint alterations in the heart were identified during this thesis. Additionally, it is proposed that other tissues like lung and eye as well as some neuronal pathfinding cues might also be affected. On the molecular level, the characterisation of *Plxnd1*^{Ali34} is not finalised, while different hypotheses might be possible that explain the observable phenotypic traits. In addition, *Ali34* might be a suitable model for the comparison of known human diseases like CHARGE syndrome and Möbius syndrome 2 and different murine cancer models. Finally, the unravelling of the different intracellular events controlled by Plxnd1 signalling might lead to a better understanding in the progression of different types of cancer and their hypervascularisation.

Several further experimental setups might be useful to decipher Plxnd1's function. Bone histomorphometric methods and *in vitro* analysis of osteoclasts and osteoblast-osteoclast interactions are intended to identify possible bone-specific alterations caused by the *Plxnd1* mutation. With the analysis of the molecular mechanisms already planned (see 3.1.5) it will be possible to identify the causative domain steering vascular patterning. Apart from the already ongoing experiments, further characterisation of tissue-specific phenotypes could further elucidate Plxnd1's function. As it was not possible to receive the recently published conditional knockout mouse line⁹⁰, a further source was found at EUCOMM. This international knockout mouse consortium generated ES cells that harbour a *Plxnd1* knockout construct that can be conditionally targeted. The investigation of

this mouse line would enable the comparison to the available ENU mutant line *Ali34*. Additionally, the possibility to generate conditional knockouts would be a valuable tool to dissect *Plxnd1*'s function in different organ systems. Although endothelial-specific inactivation of *Plxnd1* phenocopies the known phenotypes during embryogenesis in classical knockouts⁹⁰, it is however assumable, that effects on bone might not entirely traced back to defective angiogenesis. Furthermore, neuronal specific knockout studies might also reveal unappreciated effects. For this purpose, the *Tg(Col2a1-cre)1Asz* line for chondrocytes²¹⁶, *Tg(Col1a1-cre)1Kry* for osteoblasts¹⁴³ and *Tg(Syn1-cre)671Jxm* for neuronal tissue²¹⁷ might be utilised for cell specific *Plxnd1* deletion. As EUCOMM mouse lines are maintained on a *C57BL6/J* inbred strain, possible retinal defects can be investigated as *C57BL6/J* mice do not resemble vessel attenuation like the *C3HFeB/FeJ* inbred strain¹⁸⁷.

Regarding the potential influence of *Plxnd1* in cancer progression, tumor induction or the crossing of *Ali34* to mouse models for different types of cancer might be beneficial. As enhanced *Plxnd1* expression was reported for different malignant cells and its vasculature the effect of the *Ali34* mutation might cause tumor suppression, thus potentially serving for a further progress in cancer treatment.

5.2 *Aga2*

Although Osteogenesis imperfecta is primarily described as a bone disorder, the majority of OI mortality and morbidity is caused by either respiratory or cardiac distress⁸⁰. However, these defects are generally considered secondary to skeletal deformities²¹⁸. Although a primary role for mutant collagen in cardiopulmonary complications has been suggested, a direct association to the aetiology of OI has not been demonstrated^{60,82,218,219}.

Comparable to the heterogeneity among the different types of OI in human patients, heterozygous *Aga2* mice exhibit two distinct severity grades. As *Aga2/+^{mild}* animals display a moderate progression of OI symptoms, *Aga2/+^{severe}* mice were shown to entirely succumb to perinatal lethality due to serious progression of OI during the first ten days of life. To investigate the pathological alterations leading to the heterogeneity among *Aga2/+* mice and to determine the primary cause of death in *Aga2/+^{severe}*, comprehensive analysis of the *Aga2* mutant line was conducted to decipher possible extra-skeletal effects of the *Col1a1* mutation. In addition, continuative studies were initiated to unravel possible effects of type I collagen mutations in the development of metabolic diseases.

5.2.1 Bone phenotype improvement has no effect on perinatal lethality

Rib cage fractures and scoliosis are the most prominent clinical features attributed to cardiopulmonary defects in OI. Thus, bisphosphonate treatment was conducted in *Aga2/+* newborns. Bisphosphonate treatment is a common tool to effectively suppress bone resorption and reduce bone turnover among women displaying postmenopausal osteoporosis by increasing bone mass and significantly lowering the susceptibility of fractures^{220,221}. In addition, patients with idiopathic juvenile osteoporosis and different types of OI receive antiresorptive drugs^{222,223}. The treatment of *Aga2/+* newborns with alendronate had to be conducted in a very limited timeframe (during the first ten days) to provoke bone improvements. As reported recently, bisphosphonates are capable to act rapidly on the bone metabolism^{223,224}. However, contrary to several studies on murine OI models^{225,226}, the effects of alendronate administration on *Aga2/+* newborns revealed only slight

effects. Notably, studies on *Col1a1^{BrIII}* and *Col1a2^{oim/oim}* mice, two other well-described murine OI models, focused on histomorphometric data of the femur. *Aga2/+* animals were analysed by μ CT measurements of the whole body and the thoracic region respectively. While DXA analysis in humans mainly focuses on the lumbar region²²⁷⁻²²⁹ where significantly increased values are observable, generally rare whole body DXA measurements reveal no significant improvement in bisphosphonate treated patients²³⁰. Therefore, the comparison of different murine as well as human studies with the effects shown for *Aga2/+* is rather difficult. Nevertheless, the reduction of fractures in treated *Aga2/+* mice clearly show, that alendronate has a positive effect on bone strength also after this minimal timeframe. The reduced values for cortical and cancellous content and volume in the thoracic region measurements implies reduced fracture rates in alendronate treated *Aga2/+* animals. The marginal decrease in cancellous density might be explained by the fact, that bisphosphonate treatment hampers cartilage resorption, thus provoking a less dense calcified matrix especially during fracture healing^{231,232}.

Although bone densitometric analysis could clearly show an improvement of the bone phenotype, lethality was equally observable in the treated and control group respectively. Additionally, μ CT image comparison between *Aga2/+^{mild}* and *Aga2/+^{severe}* identified diminished signals in the pulmonary region of severely affected animals only, thus further corroborating fracture-independent pathological effects.

In conclusion, the bone phenotype in *Aga2/+* animals was mildened due to the administration of alendronate during a two week period. However, lethality rate could not be reduced.

5.2.2 Cardiac defects in *Aga2/+*

In hearts and primary cardiac fibroblasts, a tremendous downregulation of *Col1a1* and the consequential type I collagen protein were confirmed by transcriptional and histological examinations. For both *Aga2/+^{mild}* and *Aga2/+^{severe}*, the expression of the mutant *Col1a1^{Aga2}* allele was reduced to a minimum, while severely affected animals additionally exhibit a decline of the wild-type allele. While silencing of *Col1a1^{Aga2}* by nonsense-mediated decay might be within the realms of possibility,

the reduction of both *Col1a1* alleles is based on other mechanisms. The comparison of other OI models further corroborates that structural defects in *Col1a1* leads to a worsening of the cardiac ECM in OI. While the cardiac ECM of *Aga2/+^{mild}* animals (~60% expression compared to controls) are comparable with *Col1a1^{Mov13/+}* mice (haploinsufficiency) with no obvious structural defects, the hearts of *Aga2/+^{severe}* as well as perinatal lethal *Col1a1^{BrtlV/+}* mice display a reduction in type I collagen expression and secretion into the ECM accompanied by dramatic structural defects of the myocardium. Cardiac complications investigated for the *oim* mouse model, harbouring a *Col1a2* mutation²³³ also reported a downregulation of type I collagen²³⁴ but these mice display no perinatal lethality and the formation of *Col1a1* homotrimers can partially rescue the myocardial defects²³⁵, thus resembling similar phenotypes observed for *Aga2/+^{mild}* animals. Moreover, the *post mortem* investigation of two lethal fetuses resembling type II OI also hint to a reduced type I collagen amount in cardiac tissue through analysis by SEM and TEM analysis. However, validation by transcriptional analysis is lacking²¹⁹. Due to the accumulation of defective type I collagen in primary cardiac fibroblasts of *Aga2/+^{severe}*, potential regulatory mechanisms might account for the coordinated downregulation of both *Col1a1* alleles that are not based on ER-stress, as those markers were not upregulated in these cells. The resistance of cardiac fibroblasts to undergo apoptosis through *Bcl-2* triggered signalling was recently described²³⁶. Indeed, the upregulation of *Cox6a1*, a suppressor of Bax-mediated cell death²³⁷, as well as apoptotic markers that were not regulated in *Aga2/+^{severe}*, were in conjunction with these findings. However, another mechanism which might explain cardiac defects could be identified. Since *Mt1*, a known positive regulator of NfkappaB²³⁸ was strongly upregulated and active NfkappaB is capable to inhibit *Col1a1* and *Col1a2* expression²³⁹, the downregulation of both genes suggests a NfkappaB mediated downregulation of both type I collagen chains. Further corroboration was achieved by the downregulation of *Col3a1*, the minor fibrillar collagen of the cardiac ECM, which is important for crosslinking type I collagen fibres. Similarly, also *Dpt* and *Mfap4*, two important proteins for collagen fibrillogenesis and matrix assembly^{240,241} were downregulated in *Aga2/+^{severe}*. The collectivity of these observations is likely to be the basis of collagen protein reduction and disordered spatial arrangement in *Aga2/+^{severe}* cardiac tissue. A

normal collagen scaffold is needed for proper myocyte attachment to the ECM and spatial orientation, thus conferring myocardial stiffness and adequate ventricular function^{242,243}. Therefore, the collagen matrix abnormalities observed in *Aga2/+^{severe}* animals might lead directly to enlarged septa, right ventricular hypertrophy, reduced vessel integrity and impaired cardiac mechanics suggested by histological and ultrasound analysis. These considerations were also supported by upregulation of *Col8a1* and *Ctgf* that might simultaneously act as compensatory connective tissue mechanisms in severely affected hearts^{244,245}. Additionally, upregulation of *Nppa*, secreted by heart cells in response to stressors of the myocardium to modulate cardiac growth potentially leads to hypertrophy²⁴⁶. *Tgm2* expression, which increases during heart failure²⁴⁷ and *Slc25a4*, which is involved in cardioprotection of failing hearts²⁴⁸ additionally conveys the hypothesis that bone-independent mutational effects lead to functional impairments of *Aga2/+^{severe}* hearts.

5.2.3 Pulmonary complications in *Aga2*

Lung complications are also generally observed among the literature that accounts for morbidity in the majority of lethal OI cases⁸⁰. These observations are in conjunction with findings in *Aga2/+^{severe}*, which displayed enhanced haemorrhagic lungs, accompanied with pneumonia and pleurisy. Besides these observations, rib fractures were never found to cause lung damage due to invasion into the lung parenchyma. The morphological hallmarks were further corroborated by upregulation of *Wnt11*, *Tgfbi* and *Ltbp3*, three markers associated with inflammation and the Tgf β pathway²⁴⁹⁻²⁵¹. Upregulation of angiotensinogen and declined proangiogenic transcripts (*Ang*, *Cxcl12*, *Ctgf*) support the morphological observations of excessive bleedings and a reduced capillary network shown by PECAM stainings in *Aga2/+^{severe}*²⁵²⁻²⁵⁵. These pulmonary defects provoke respiratory impairments due to a reduced free alveolar space crucial for proper gas exchange, concomitantly leading to hypoxic conditions. Indeed, markers accountable for hypoxemia and hypoxia like *Pltp*, *Cd248*, *AR* and *Gdf10*²⁵⁶⁻²⁵⁹ exhibit inclined transcript levels. Elevated *Prkce* expression additionally may contribute to pulmonary vasoconstriction due to hypoxia²⁶⁰. This proposed pathological alterations leading to hypoxemic conditions were additionally

substantiated by blood gas analysis that revealed a significant decrease in pO₂ in conjunction with increased pCO₂ values specifically in *Aga2/+^{severe}* mice.

In contrast to the cardiac tissue, *Col1a1* expression in the lung as well as the second type I collagen strain (*Col1a2*) were not significantly hampered. Furthermore, nonsense-mediated decay, which was suggested to degrade *Col1a1^{Aga2}* was confirmed to be accountable for the marginal downregulation to ~75% compared to controls both *in vivo* and *in vitro*. Nevertheless, other ECM related transcripts were shown to be regulated in *Aga2/+^{severe}*. *Col3a1* and *Col5a1*, coding for minor collagen fibrils and *Dpt*, an important factor for collagen fibrillogenesis were upregulated^{261,262}. This might be a potential compensatory mechanism that preserves connective tissue integrity caused by the type I collagen reduction.

5.2.4 Functional linkage of cardiac and pulmonary defects in

Aga2/+^{severe}

The combinational observations of defects in hearts and lungs of *Aga2/+^{severe}* mice leads to the assumption that the pathological events are closely correlated. Additionally, bone phenotypes in *Aga2/+* animals might not contribute to the progression of the perinatal lethal form. This hypothesis is also corroborated by recent human studies on patients resembling the Ehlers-Danlos-Syndrome, which is also caused by mutations in *COL1A1* and *COL1A2*. Although these patients do not suffer from bone fractures, cardiac findings are commonly identified²⁶³⁻²⁶⁶.

Structural myocardial impairments obviously lead to remodelling processes in *Aga2/+^{severe}* hearts like septal and right ventricular hypertrophy. In addition, *Tgm2* and *Agt* (both upregulated in *Aga2/+^{severe}* hearts) are known to contribute to the development of hypertension^{267,268}. Whether a primary defect due to a fragile capillary network or the consequence of increased pulmonary blood pressure is accountable for the excessive bleedings observed for *Aga2/+^{severe}*, still remains to be elucidated. However, the existence of haemorrhages in the alveolar space induces hypoxia that in turn results in signals triggering the elevation of the pulmonary blood pressure.

In conclusion, these effects amplify each other, finally leading to death in *Aga2/+^{severe}* potentially by *cor pulmonale* (Figure 47). With respect to the

investigation of *Col1a1* downregulation in *Aga2/+^{severe}*, heart defects are suggested to be the primary elicitor of this vicious cycle, although further investigations are required to definitely validate this hypothesis.

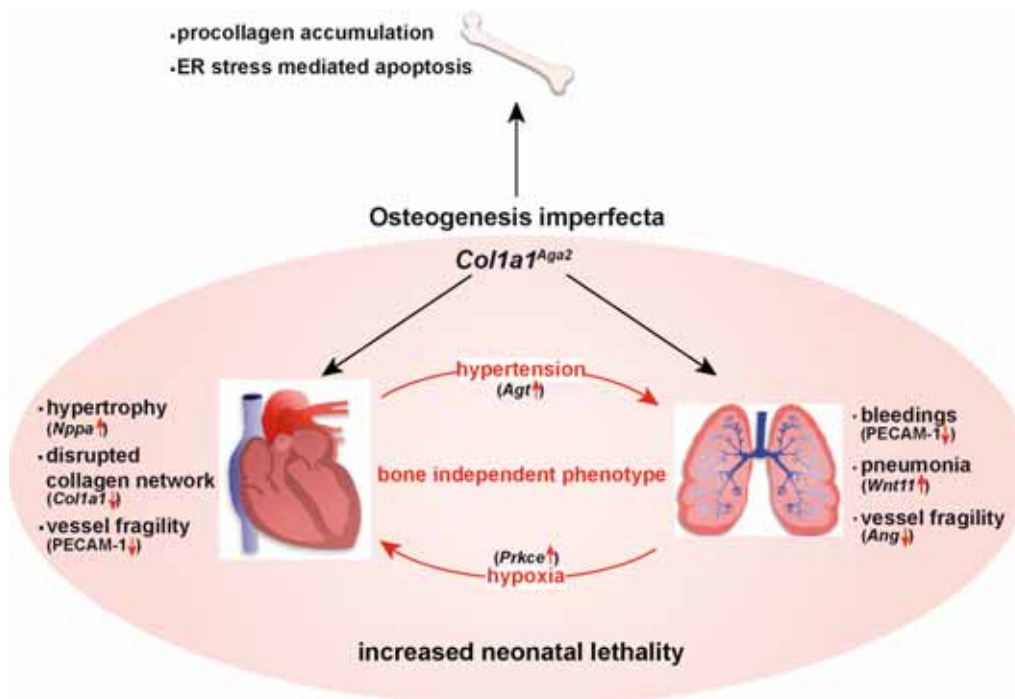


Figure 47. Schematic representation of the pathological processes provoked by the collagen mutation in *Aga2*.

In bone, the expression of *Col1a1^{Aga2}* leads to accumulation of malformed procollagen in the ER that causes the induction of UPR and triggers apoptosis. The bone independent phenotype is caused by downregulation of *Col1a1* in cardiac fibroblasts leading to a disrupted collagen network, accompanied with hypertrophy and vessel fragility. Cardiac alterations cause a vicious cycle of hypertension in heart, followed by bleedings and hypoxia in the lung leading to *cor pulmonale* in *Aga2/+^{severe}* mice.

5.2.5 Human patients with type III and IV OI

The pulmonary and cardiac findings in children and young adults with non-lethal types III and IV OI due to abnormal collagen structure support the interpretation that the findings in *Aga2/+^{mild}* mice correlate to pre-adult development in humans. The type III and IV OI children with documented structural abnormalities of type I collagen have significant abnormalities in pulmonary function that could not be correlated to functional cardiac impairments. Significant decline of total lung capacity and forced vital capacity occurs during childhood in OI patients without scoliosis, although at a slower rate than those with a more enhanced curvature (>30°). This data indicates a primary lung tissue dysfunction due to type I collagen defects and also corroborates the known worsening of OI lung function with

scoliosis^{81,269}. More than half of OI children studied have restrictive lung disease; many of those with moderate or greater severity do not have advanced scoliosis. About 20% of children studied have mild to moderate obstructive findings with or without restrictive disease.

Valvular regurgitation was documented in a study of OI adults with types I, IV and III OI²⁷⁰, 95% of whom have combinations of tricuspid, mitral and aortic valvular regurgitation. Cardiac abnormalities in OI appear to begin in childhood for children with collagen structural abnormalities, although cardiopulmonary function at rest was normal in children with type I OI, who have reduced levels of normal collagen²⁷¹. Most (70%) of the study population presented here had valvular regurgitation, almost all involving mild tricuspid regurgitation with about one-third of these children also having mild mitral regurgitation. Paediatric tricuspid regurgitation is likely to be related to annular dilation of primary origin, as it occurs without heart failure or elevated pulmonary artery pressures. While 5 children had dilated left atria and 3 had atrial shunting on echocardiography, 5 of these children had no or minimal functional lung abnormality. Although these results rather mimic findings in *Aga2/+^{mild}* animals with moderate cardiac and pulmonary impairments, they however clearly indicate that OI aetiology of cardiopulmonary defects are caused by bone independent effects.

Nevertheless, follow-up of this longitudinal patient population will be required for progression of findings and contribution to OI morbidity and mortality.

5.2.6 Osteoporosis in *Aga2* – Connection to type 2 diabetes?

Studies examining diabetic conditions as a result of osteoporosis are lacking or are not well defined to date. The experimental approach presented here should initially discover the potential effects of osteoporosis in the OI mouse model *Aga2* on energy metabolism with specific attention to a potential type 2 diabetic phenotype. Bisphosphonate treatment to rescue the bone phenotype in mutant mice should additionally investigate the impact of antiresorptive drugs on the recently reported connection between bone and pancreatic β -cells^{97,99}.

Preliminary results on *Aga2/+* mice showed that especially male mice displayed a balanced energy uptake in conjunction with the metabolised energy compared to their body weight. In contrast, female *Aga2/+* animals appeared to be

hypermetabolic, an also observed feature in human OI patients²⁷². Besides the overall metabolic activity in *Aga2*, insulin and blood glucose levels are significantly decreases compared to wild-type controls at the age of 4 weeks. This observation suggests that although *Aga2*^{+/+} mice display a reduction in insulin secretion to one fourth, its sensitivity is able to maintain an even lower blood glucose level as observed for controls. This might be in conjunction with the lower food uptake in *Aga2*^{+/+} males. Expression analysis of isolated pancreatic islets further corroborates this hypothesis, as insulin expression – that is known to be uncoupled from secretion, overall proliferation markers and also the second main hormone glucagon were not regulated among *Aga2*^{+/+} mice. Conformable to these results, osteocalcin as well as adiponectin levels are wild-type like, although it has been shown by *in vitro* analysis, that osteocalcin expression is reduced in *Aga2*^{+/+} osteoblasts (PhD thesis of Dr. Frank Thiele). Compared to the recently published effects of osteocalcin on β -cell function, proliferation and insulin secretion, it can be assumed that the reduction of insulin secretion might be not induced entirely by primary effects of the *Col1a1* mutation in *Aga2*. Nevertheless, osteocalcin levels have to be judged cautiously as the ELISA measurements cannot distinguish between the active (Glu-Ocn) and the inactive (Gla-Ocn) form. Further analysis, for instance by mass spectrometry, could give more insight into the active/inactive ratio of osteocalcin in *Aga2*^{+/+} mice. The analysis of 10-weeks old mice by GTT will additionally reveal how mutant mice respond to increased blood glucose levels. The analysis of direct effects on the pancreatic ECM was also initiated. Immunohistochemical analysis revealed that the type I collagen amount might only be slightly decreased (similar to *Aga2*^{+/mild} heart and lung values). Major defects in ECM composition and structure were also not observable as shown by laminin stainings. However, a trend towards reduction of *Col1a1* transcripts was determined by expression analysis in isolated islets. As type I collagen was only found to be co-localised with PECAM stainings inside the islets, a general conclusion about the whole pancreatic tissue is not possible so far. The following qRT-PCR analyses on whole pancreatic tissue will therefore be more precisely. The general outcome of this study is currently highly hypothetical. Nevertheless, recently proposed models^{97,99,135,273-276} (see Figure 44 for overview) support the hypothesis that “external” mutational defects affecting bone in combination with the administration of bisphosphonates might have a major impact on the metabolic

bone-pancreas axis that possibly results in a type 2 diabetic phenotype. The complete analysis of untreated 4-weeks old *Aga2/+* mice will be invaluable to assess the effects of the underlying *Col1a1* mutation on the energy metabolism and to define a more precise estimation on the outcome of the alendronate treatment.

However, the treatment with alendronate will result in reduced bone resorption induced by osteoclasts apoptosis. This will in fact influence the ratio between active and inactive osteocalcin. The reduced Glu-Ocn levels might lead to a reduced β -cell proliferation, insulin secretion and sensitivity. Together with the decreased plasma insulin values found in *Aga2/+* animals, this additive effect might drive into pathophysiological conditions possibly leading to a diabetic phenotype. In addition to the pancreatic phenotype, a reduced plasma insulin level also feedbacks on osteoblasts through insulin receptor signalling⁹⁹. If impaired, it would lead to a reduction in osteoblast proliferation, thus counteracting on the bisphosphonates action. Indeed, the knowledge that type I diabetic patients suffer from dramatic reduction in BMD and a loss of bone quality, loss of insulin signalling in osteoblasts have to be taken into account¹³⁶.

Taken together, the upcoming investigation of metabolic defects in *Aga2* in combination with bisphosphonate administration might be an important next step to further characterise systemic effects in the aetiology of OI and to study the effects of long-term bisphosphonate treatment that is commonly applied in people with primary osteoporotic phenotypes.

5.2.7 Conclusion and future perspective

The systemic analysis of the OI mouse model *Aga2* could identify primary defects caused by the *Col1a1* mutation in heart and lung tissue that is accountable for perinatal lethality in a subgroup of heterozygous mutants (*Aga2/+^{severe}*). In addition, the comparison to human patients suffering from type III and IV OI with moderate to severe clinical manifestations that are comparable with *Aga2/+^{mild}* mice, support the results of bone-independent dysfunctions leading to impairments in the cardiac and respiratory system. The data presented here should make clinicians more attentive for extra-skeletal examinations of OI patients and may provide insights for novel therapeutic approaches. The investigation of metabolic

phenotypes in *Aga2* animals is a reasonable next step towards the systemic analysis of OI as a multifactorial disease. Additionally, the bisphosphonate treatment of *Aga2* mimics standard bone phenotype rescue applications in humans and might help to evaluate long term effects that favour the progression of a diabetic phenotype.

To follow neonatal lethality in *Aga2*/^{severe} further investigations on the underlying mechanisms accounting for the downregulation of the *Col1a1*^{WT} allele are indispensable. The proposed influence of enhanced NfκB signalling could be analysed by activity assays of NfκB in cardiac fibroblasts *in vitro*. Additionally, ChIP assays could be utilised to proof for an enhanced binding of NfκB to the *Col1a1* promoter. The completion of the gene targeting vector to conditionally induce the *Col1a1*^{Aga2} mutation in different cell types and moreover in a temporal fashion will help to discriminate between intrinsic effects on different organ systems not only during development but also in terms of maintenance after a normal developmental phase. Complementation studies with other OI mouse models (e.g. *Col1a2*^{Oim}, *Col1a1*^{BritIV}, *Col1a1*^{Mov13}) or mutants harbouring mutations equal to human cases (Supplemental Figure 9) by using the ENU F1-archive could be a further approach to corroborate the findings in *Aga2* in a more general fashion.

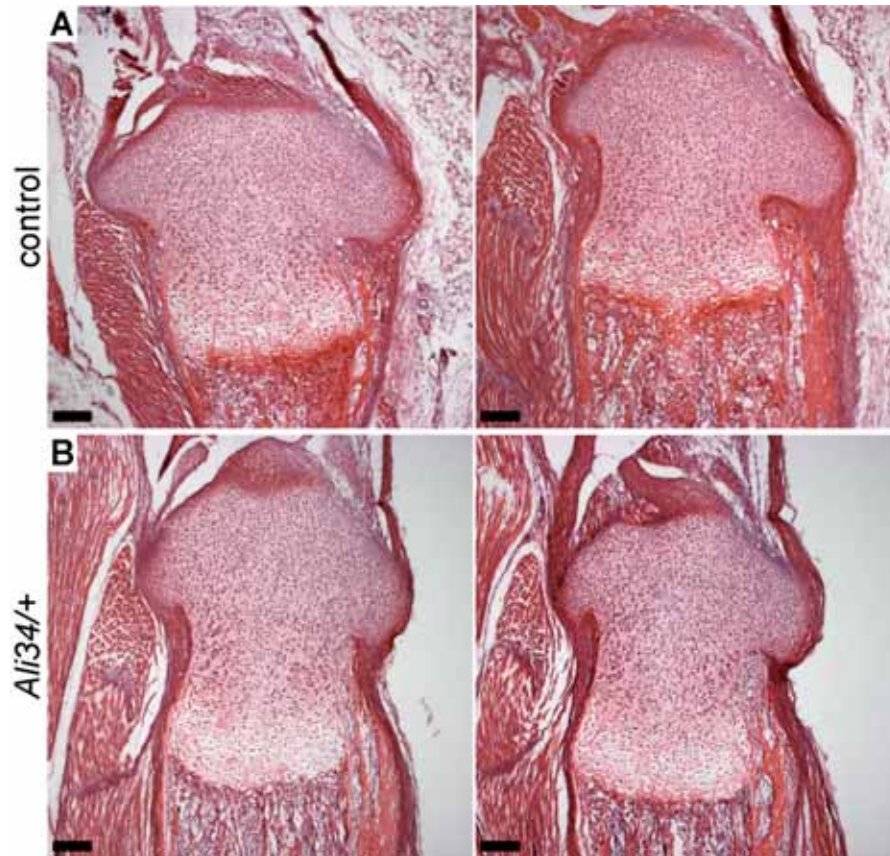
With respect to the metabolic phenotyping in *Aga2*, the general outcome of this study is currently not entirely predictable. However, if metabolic defects indicate an increased susceptibility for the development of a diabetic phenotype as a consequence of bisphosphonate treatment, human cohort studies could be utilised to evaluate potential congruency. As OI is a general connective tissue disorder that is accompanied by osteoporosis, the *Aga2* mouse line might primarily mimic only OI-related dysfunctions. Therefore, GWAS could be additionally analysed for loci that were identified to be susceptible for osteoporosis (e.g. Li *et al.*²⁷⁷). The obtained data can then be used to analyse further mouse models as well as the comparison of genes that are reported by GWAS directed for type 2 diabetes susceptibility (for review see²⁷⁸).

5.3 Final remarks

The systemic analysis of *Ali34* and *Aga2* during this thesis could confirmed several extraskkeletal features in both mutant mouse lines by systemic analysis. While the data obtained for *Ali34* claims for mild defects in other organ systems like the heart and the neuronal tissue, analysis of *Aga2* unravelled a recently unappreciated intrinsic effect of the *Col1a1* mutation in heart and lung tissue. In general, upcoming challenging experiments like the metabolic phenotyping in *Aga2* will be a reasonable next step towards the understanding of human diseases by mouse models.

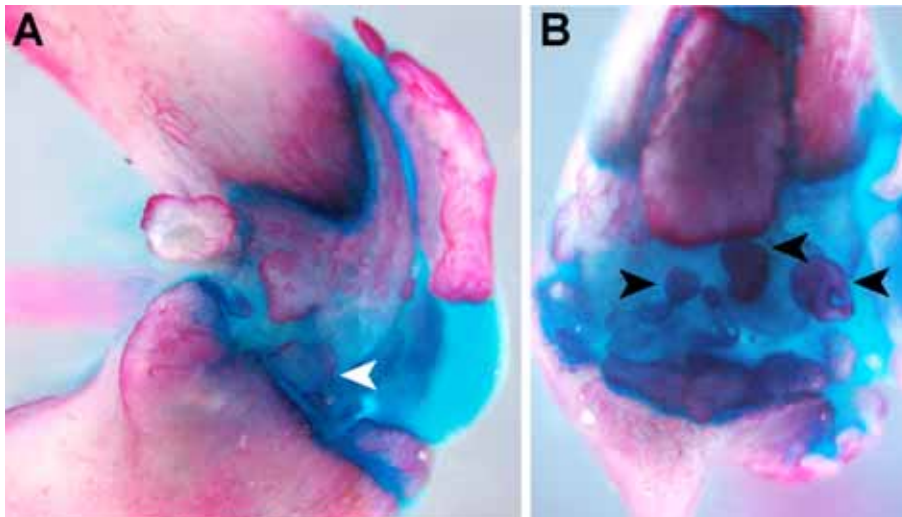
6. Appendix

6.1 Supplemental figures



Supplemental Figure 1. Analysis of newborn *Ali34/+* mice.

H&E stainings of **A** wild type and **B** *Ali34/+* tibial bones. No alterations in bone formation are determined.



Supplemental Figure 2. Skeletal staining of 17-weeks old *Ali34/+* hindlimb bones.

A Lateral view of the knee joint clearly shows progressive erosion of the articular cartilage as well as destruction of the SOC (white arrowhead). **B** Frontal view on the knee joint depicts calcified tissue inside the synovial cavity (black arrowheads).

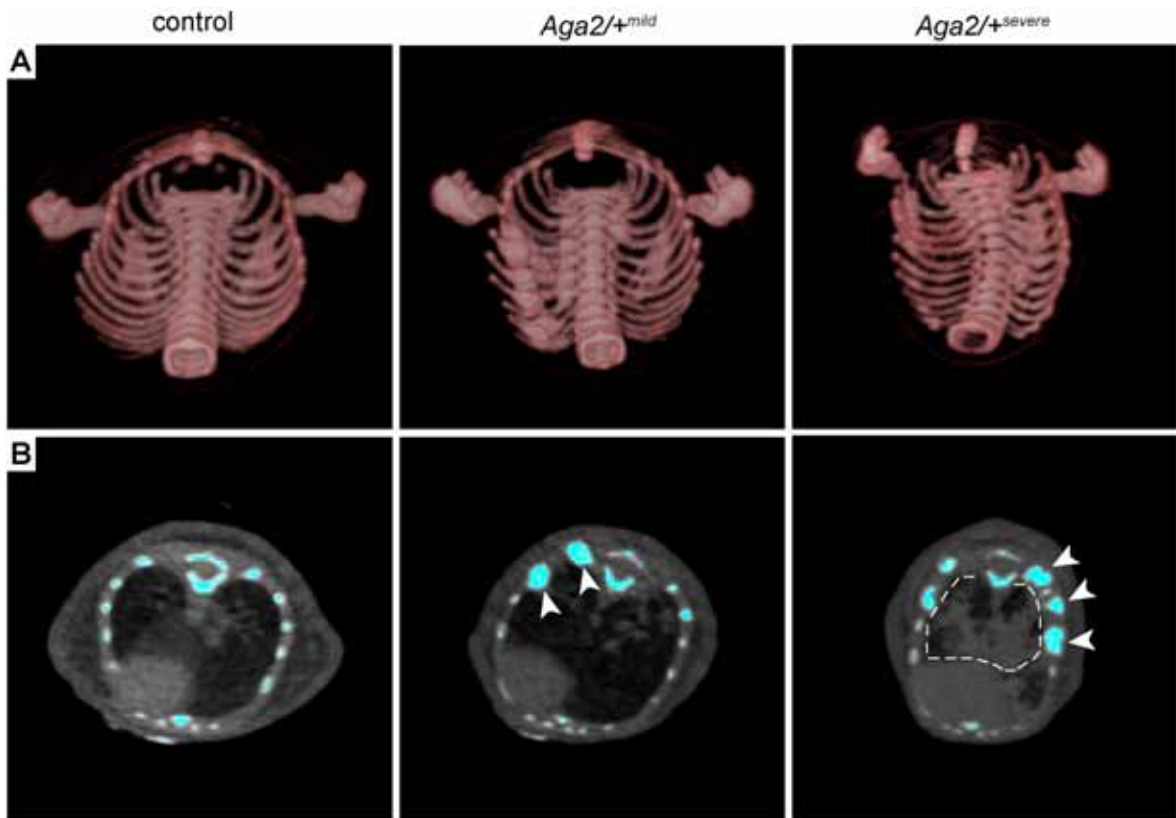
	-2.0 0.0 2.0				
Mean log2 ratio	<i>Ali34-1</i>	<i>Ali34-2</i>	<i>Ali34-3</i>	Gene symbol	Comment
0,50				<i>CR515097</i>	
0,45				<i>S1pr2</i>	Sphingosine-1-phosphate receptor 2
0,55				<i>CR515399</i>	
0,61				<i>CR515855</i>	
0,66				<i>Gabra1</i>	Gamma-aminobutyric acid receptor, subunit alpha 1
-0,55				<i>Col1a1</i>	Procollagen, type I, alpha 1
-0,46				<i>Lyzs</i>	Lysozyme
-0,45				<i>Ankrd23</i>	Ankyrin repeat domain 23

Supplemental Figure 3. Differentially expressed genes in heart tissue of *Ali34/+* animals.

Appendix

	-2.0	0.0	2.0		
Mean log2 ratio	Ali34-1	Ali34-2	Ali34-3	Gene symbol	Comment
0.57				<i>Ugcg11</i>	UDP-glucose ceramide glucosyltransferase-like 1
0.65				<i>Zc3hdc7</i>	Zinc finger CCH type domain containing 7
0.72				<i>Serp2</i>	Endoplasmic reticulum protein family member 2
0.61				<i>Vcam1</i>	Vascular cell adhesion molecule 1
0.72				<i>Prg2</i>	Proteoglycan 2, bone marrow
0.64				<i>Pdlim4</i>	PDZ and LIM domain 4
0.70				<i>Ppp2r5d</i>	Protein phosphatase 2, regulatory subunit B
0.56				<i>Ass1</i>	Argininosuccinate synthetase 1
0.74				<i>Hdlbp</i>	High density lipoprotein binding protein
0.62				AT30018C14Rik	
0.80				CR519355	
0.74				<i>Zfp385c</i>	zinc finger protein 385C
0.63				<i>Comm3</i>	COMM domain containing 3
0.67				<i>Wasf2</i>	WAS protein family, member 2
0.70				<i>Patk1b2</i>	Platelet-activating factor acetylhydrolase, isoform 1b
0.61				<i>R3hdm2</i>	R3H domain containing 2
0.58				<i>Ear1</i>	Eosinophil-associated, ribonuclease A family, member 1
-0.58				<i>mt-Ocr</i>	d-loop control region-mitochondrial
-0.51				CR521141	
-0.73				<i>Tnnt3</i>	Troponin T3, skeletal, fast
-0.54				CR521142	
-0.68				<i>Pgam2</i>	Phosphoglycerate mutase 2
-1.10				<i>Col2a1</i>	Procollagen, type II, alpha 1
-0.47				<i>Car3</i>	Carbonic anhydrase 3
-0.66				<i>Carp3</i>	Cysteine and glycine-rich protein 3
-0.50				<i>Postn</i>	Perostin, osteoblast specific factor
-0.68				<i>Gapd</i>	Similar to glyceraldehyde-3-phosphate dehydrogenase
-0.48				<i>Actn2</i>	Actinin alpha 2
-0.60				<i>Tpm2</i>	Tropomyosin 2, beta
-0.70				<i>Cox7a1</i>	Cytochrome c oxidase, subunit VIIa 1
-0.62				<i>mt-Cytb</i>	Cytochrome b, mitochondrial
-1.12				<i>Myf2</i>	Myosin, light polypeptide 2, regulatory
-0.62				<i>Myh7</i>	Myosin, heavy polypeptide 7
-0.54				<i>Ndn2</i>	N-myc downstream regulated gene 2
-0.57				<i>Cmya5</i>	Cardiomyopathy associated 5
-0.58				<i>Col11a1</i>	Procollagen, type XI, alpha 1
-0.57				<i>Mybpc2</i>	Myosin binding protein C, fast-type
-0.49				<i>Atpf1</i>	ATPase, inhibitory factor 1
-0.80				<i>Myh1</i>	Myosin, heavy polypeptide 1
-0.61				2900042B11Rik	
-0.62				<i>Col1a1</i>	Procollagen, type I, alpha 1
-0.62				<i>Cdgap</i>	Cdc42 GTPase-activating protein
-0.64				CR517976	
-0.69				Bx635876	
-0.73				<i>Myh4</i>	Myosin, heavy polypeptide 4
-0.61				<i>Cox8b</i>	Cytochrome c oxidase, subunit VIIIb
-0.78				<i>Ckmt2</i>	Creatine kinase, mitochondrial 2
-0.61				<i>Tbk1</i>	TANK-binding kinase 1
-0.73				<i>Des</i>	Desmin
-0.70				<i>Myh1</i>	Myosin, heavy polypeptide 1
-0.69				<i>Atp2a1</i>	ATPase, Ca++ transporting
-0.61				<i>Atp1b1</i>	ATPase, Na+K+ transporting, beta 1 polypeptide
-0.52				300002C10Rik	
-0.83				<i>Mb</i>	Myoglobin
-0.76				<i>Tnnt3</i>	Troponin T3, skeletal
-0.84				CR515557	
-0.66				<i>Cryab</i>	Crystallin, alpha B
-0.57				<i>Aldoa</i>	Aldolase 1, A isoform
-0.50				<i>Gapdh</i>	Glyceraldehyde-3-phosphate dehydrogenase
-0.60				CR516647	
-0.63				<i>Art1</i>	ADP-ribosyltransferase 1
-0.75				<i>Tnnt3</i>	Troponin T3
-0.72				<i>Tnni2</i>	Troponin I
-0.54				<i>Trdn</i>	Tradin
-0.66				4930546H06Rik	
-0.67				<i>Aldoa</i>	Aldolase 1, A isoform
-0.67				<i>Fhl1</i>	Four and a half LIM domains 1
-0.72				<i>Myh8</i>	Myosin, heavy polypeptide 8
-0.76				<i>Myh2</i>	Myosin, heavy polypeptide 2
-0.62				1110019822Rik	

Supplemental Figure 4. Differentially expressed genes in bone tissue of *Ali34/+* animals.

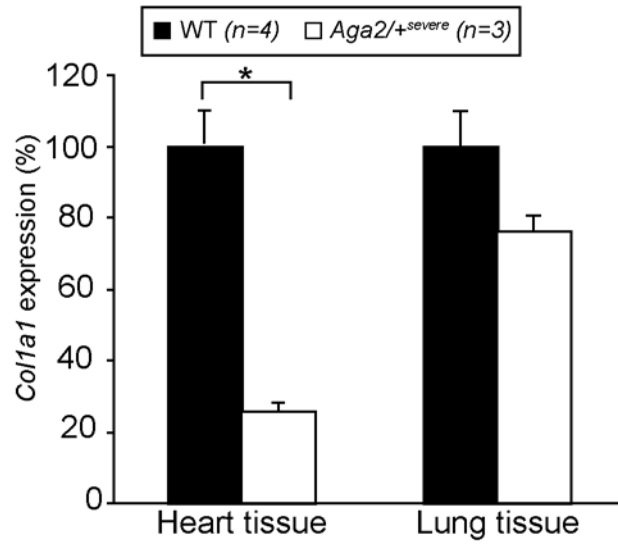


Supplemental Figure 5. μ CT pictures of alendronate treated animals.

A 3D reconstruction of wild type, *Aga2*^{+mild} and *Aga2*^{+severe} mice. Callus formation is visible in both mutants. **B** Single picture of the μ CT scan of the same animals. Callus formation is evident (white arrowheads). Additionally, *Aga2*^{+severe} animals display perfusion in the lung tissue (encircled by dotted line).

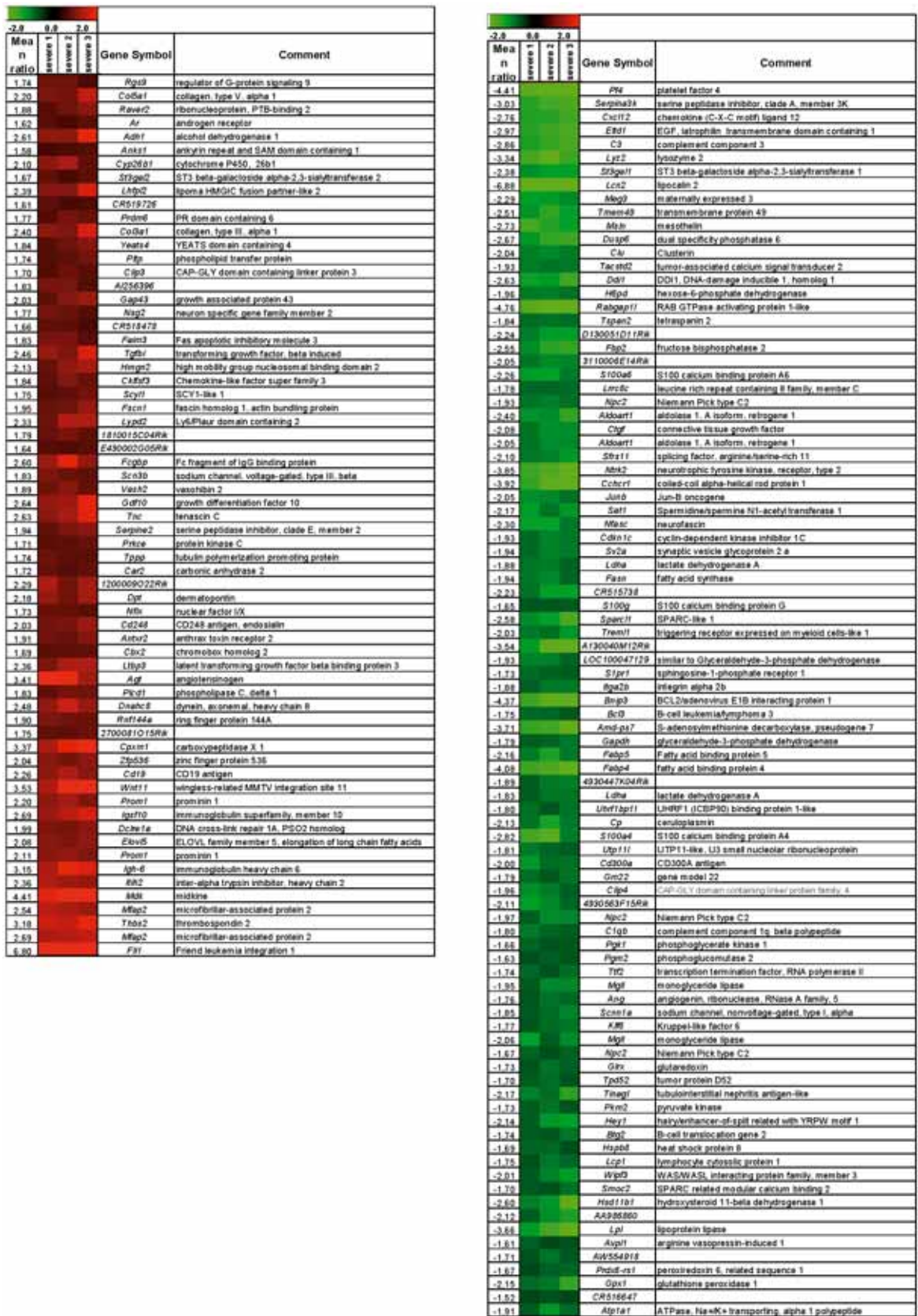
Mean ratio	Heatmap			Gene Symbol	Comment
	severe 1	severe 2	severe 3		
-2.51				<i>Col1a1</i>	collagen, type I, alpha 1
-2.23				<i>Mfap4</i>	microfibrillar-associated protein 4
-1.86				<i>Col1a2</i>	collagen, type I, alpha 2
-1.82				<i>Col1a2</i>	collagen, type I, alpha 2
-2.31				<i>Tbk1</i>	TANK-binding kinase 1
-2.25				<i>Psmc1</i>	protease 26S subunit, ATPase 1
-2.32				<i>Col3a1</i>	collagen, type III, alpha 1
-1.85				<i>Atoh8</i>	atonal homolog 8
-2.18				<i>Col1a1</i>	collagen, type I, alpha 1
-1.74				<i>Ptger1</i>	Prostaglandin E receptor 1
-1.66				<i>Col1a2</i>	collagen, type I, alpha 2
-2.14				<i>Dpt</i>	dermatopontin
-2.02				<i>Col2a1</i>	collagen, type II, alpha 1
-1.50				<i>Rabgef1</i>	RAB guanine nucleotide exchange factor 1
-2.01				<i>Col1a1</i>	collagen, type I, alpha 1
-1.57				<i>Gas1</i>	growth arrest specific 1
-1.82				<i>Mf1</i>	myeloid leukemia factor 1
-1.78				<i>Tinf2</i>	Terf1 (TRF1)-interacting nuclear factor 2
-1.69				<i>Col1a2</i>	collagen, type I, alpha 2
-1.45				<i>Cdgap</i>	Cdc42 GTPase-activating protein
-2.56				<i>DOH4S114</i>	DNA segment, human D4S114
1.60				<i>Rbm3</i>	RNA binding motif protein 3
1.48				<i>Pgm2</i>	phosphoglucomutase 2
1.51				<i>Egln3</i>	EGL nine homolog 3
1.73				<i>Lpl</i>	lipoprotein lipase
1.53				<i>Gorasp1</i>	golgi reassembly stacking protein 1
1.62				<i>Gapdh</i>	glyceraldehyde-3-phosphate dehydrogenase
1.46				<i>Mgll1</i>	monoglyceride lipase
1.68				<i>3110006E14Rik</i>	
1.69				<i>Fabp5</i>	fatty acid binding protein 5
3.11				<i>Mt1</i>	metallothionein 1
1.45				<i>Clc5</i>	chloride intracellular channel 5
1.59				<i>2310056P07Rik</i>	
1.53				<i>Atp4a</i>	ATPase, H ⁺ /K ⁺ exchanging, gastric, alpha polypeptide
1.59				<i>Slc25a4</i>	solute carrier family 25, member 4
1.46				<i>Utp11</i>	UTP11-like, U3 small nucleolar ribonucleoprotein
1.70				<i>CR516017</i>	
1.78				<i>Rad17</i>	RAD17 homolog
1.47				<i>CR519105</i>	
1.54				<i>Tgm2</i>	transglutaminase 2, C polypeptide
1.55				<i>Eno1</i>	enolase 1
1.94				<i>Glu1</i>	glutamate-ammonia ligase
1.73				<i>Aldoa1</i>	aldolase 1, A isoform, retrogene 1
1.71				<i>CR518500</i>	
3.10				<i>Ctgf</i>	connective tissue growth factor
1.70				<i>Gapd</i>	similar to glyceraldehyde-3-phosphate dehydrogenase
1.68				<i>Aldoa</i>	aldolase 1, A isoform
1.78				<i>CR516962</i>	
1.58				<i>Cox6a1</i>	cytochrome c oxidase, subunit VI a, polypeptide 1
1.78				<i>Slc5a10</i>	solute carrier family 5, member 10
1.86				<i>Aldoa1</i>	aldolase 1, A isoform, retrogene 1
1.82				<i>Ldh1</i>	lactate dehydrogenase A
2.03				<i>Aldoa</i>	aldolase 1, A isoform
2.04				<i>Col3a1</i>	collagen, type VIII, alpha 1
1.75				<i>Ldha</i>	lactate dehydrogenase A
2.07				<i>Nppa</i>	natriuretic peptide precursor type A

Supplemental Figure 6. Differentially expressed genes in heart tissue of *Aga2/4^{severe}*.



Supplemental Figure 7. qRT-PCR data of *Col1a1* expression in heart and lung tissue of *Aga2*^{+severe}.

The analysed samples conducted to the expression profiling are additionally measured by qRT-PCR to verify the data. Error bars represent SEM values. * = $p < 0.01$.



Supplemental Figure 8. Differentially expressed genes in lung tissue of *Aga2+^{severe}*.

6.2 Supplemental tables

Supplemental Table 1. Gene expression analysis of *in vivo* cultured primary osteoblasts in *Ali34/+*.

Gene	Group	Timepoint after stimulation				
		Expression in [%] to mean of <i>Actb/Pgk1/Gapdh</i>				
		0	3	9	15	21
<i>Alpl</i>	control	0.78	4.32	1.99	22.94	4.83
	<i>Ali34/+</i>	1.05	4.90	1.78	18.62	2.50
<i>Bglap1</i>	control	0.29	3.54	2.16	17.00	7.82
	<i>Ali34/+</i>	0.33	2.79	2.56	14.06	4.02
<i>Col1a1</i>	control	698.4	1278.8	532.5	1173.9	452.4
	<i>Ali34/+</i>	743.7	1189.5	575.0	1137.4	308.9
<i>Cst3</i>	control	21.66	31.02	28.09	55.86	65.05
	<i>Ali34/+</i>	23.44	33.13	32.60	60.82	65.82
<i>Pdpr</i>	control	2.80	2.71	7.04	7.34	5.96
	<i>Ali34/+</i>	2.71	2.47	8.17	6.97	6.07
<i>Fos</i>	control	0.21	0.23	0.13	0.37	0.26
	<i>Ali34/+</i>	0.22	0.22	0.17	0.35	0.30
<i>Fosl2</i>	control	2.20	1.92	1.89	1.60	2.05
	<i>Ali34/+</i>	2.09	2.03	1.71	1.55	1.78
<i>Ibsp</i>	control	0.16	15.78	6.49	93.18	30.93
	<i>Ali34/+</i>	0.25	15.83	4.68	81.69	14.84
<i>Mmp13</i>	control	5.86	44.00	100.81	48.44	47.48
	<i>Ali34/+</i>	6.69	39.61	111.22	47.32	40.61
<i>Sp7</i>	control	6.61	2.94	2.70	7.78	2.19
	<i>Ali34/+</i>	7.37	2.19	3.57	7.09	1.31
<i>Runx2</i>	control	0.80	0.73	0.73	1.06	0.71
	<i>Ali34/+</i>	0.82	0.59	0.91	1.06	0.60
<i>Spp1</i>	control	91.54	90.52	518.10	230.44	254.12
	<i>Ali34/+</i>	100.72	73.21	579.28	227.64	227.17
<i>Twist1</i>	control	1.75	2.12	2.50	0.88	0.81
	<i>Ali34/+</i>	2.17	1.88	2.93	0.91	0.71

Supplemental Table 2. Spontaneous breathing pattern during rest and activity in *Aga2/+^{mild}*.
Data are represented as mean \pm SEM.

Parameter	Control (A)		<i>Aga2/+</i> (B)		A~B	A~B
	Male (n=6)	Female (n=5)	Male (n=6)	Female (n=5)	Male p-value	Female p-value
Rest						
f [1/min]	333.1 ± 7.2	334.7 ± 5.4	290.1 ± 10.6	345.0 ± 15.7	**	n.s.
TV [ml]	0.20 ± 0.01	0.19 ± 0.01	0.20 ± 0.01	0.18 ± 0.01	n.s.	n.s.
sTV [μ l/g]	5.7 ± 0.1	6.7 ± 0.3	9.4 ± 0.5	10.3 ± 0.4	***	***
MV [ml/min]	63.9 ± 2.3	62.6 ± 3.5	55.3 ± 1.4	60.8 ± 4.0	n.s.	n.s.
sMV [ml/min/g]	1.8 ± 0.1	2.2 ± 0.1	2.5 ± 0.1	3.4 ± 0.2	***	**
Ti [ms]	53.5 ± 1.4	53.2 ± 0.6	58.4 ± 2.2	51.7 ± 2.2	n.s.	n.s.
Te [ms]	127.1 ± 3.7	126.2 ± 2.4	149.6 ± 5.9	123.6 ± 6.9	**	n.s.
Ti/TT	0.30 ± 0.01	0.30 ± 0.01	0.28 ± 0.01	0.30 ± 0.01	n.s.	n.s.
PIF [ml/s]	6.6 ± 0.2	6.4 ± 0.3	6.2 ± 0.3	6.6 ± 0.4	n.s.	n.s.
PEF [ml/s]	3.6 ± 0.1	3.6 ± 0.2	3.5 ± 0.2	3.7 ± 0.3	n.s.	n.s.
MIF [ml/s]	3.8 ± 0.2	3.6 ± 0.2	3.5 ± 0.2	3.6 ± 0.2	n.s.	n.s.
MEF [ml/s]	1.6 ± 0.1	1.5 ± 0.1	1.4 ± 0.1	1.5 ± 0.1	n.s.	n.s.
Activitiy						
f [1/min]	463.7 ± 5.3	468.0 ± 7.9	428.5 ± 10.5	480.6 ± 10.4	*	n.s.
TV [ml]	0.21 ± 0.01	0.21 ± 0.01	0.20 ± 0.01	0.18 ± 0.01	n.s.	n.s.
sTV [μ l/g]	6.0 ± 0.2	7.2 ± 0.4	9.3 ± 0.4	10.2 ± 0.6	***	**
MV [ml/min]	95.6 ± 3.6	95.8 ± 3.4	85.2 ± 1.4	87.2 ± 3.9	n.s.	n.s.
sMV [ml/min/g]	2.7 ± 0.1	3.3 ± 0.1	3.9 ± 0.1	4.9 ± 0.3	***	***
Ti [ms]	41.9 ± 0.7	41.2 ± 0.5	43.6 ± 0.9	38.4 ± 0.4	n.s.	**
Te [ms]	87.6 ± 0.9	87.1 ± 1.9	96.8 ± 2.6	86.6 ± 2.7	**	n.s.
Ti/TT	0.32 ± 0.01	0.32 ± 0.01	0.31 ± 0.01	0.31 ± 0.01	n.s.	n.s.
PIF [ml/s]	8.6 ± 0.3	8.6 ± 0.3	8.1 ± 0.2	8.4 ± 0.4	n.s.	n.s.
PEF [ml/s]	5.2 ± 0.2	5.2 ± 0.2	4.9 ± 0.2	5.0 ± 0.3	n.s.	n.s.
MIF [ml/s]	5.0 ± 0.2	5.0 ± 0.2	4.6 ± 0.1	4.8 ± 0.2	n.s.	n.s.
MEF [ml/s]	2.4 ± 0.1	2.4 ± 0.1	2.1 ± 0.1	2.1 ± 0.1	**	n.s.

Supplemental Table 3. GO-Term analysis of differentially expressed genes in hearts of *Aga2*^{+/severe} mice.

GO-term	Gene symbol
Cell communication	<i>Col1a2, Col2a1, Col8a1, Ctgf, Dpt, Glul, Gorasp1, Mfap4, Ptger1, Tbk1, Tgm2</i>
Cell growth and/or maintenance	<i>Apt4a, Cdgap, Clic5, Ctgf, Fabp5, Gas1, Lpl, Rad17, Scl25a4, Tinf2</i>
Organogenesis	<i>Col1a1, Col1a2, Col2a1, Col3a1, Col8a1, Ctgf, Fabp5</i>
Cell adhesion	<i>Col1a2, Col2a1, Col8a1, Ctgf, Dpt, Mfap4</i>
Energy pathways	<i>Aldoa, Cox6a1, Eno1, Gapd, Ldha, Scl25a4</i>
Carbohydrate metabolism	<i>Aldoa, Eno1, Gapd, Ldha, Pgm2</i>
Protein metabolism	<i>Egln3, Lpl, Psmc1, Tbk1, Tgm2</i>
Response to stress	<i>Ctgf, Mgl, Rad17, Tinf2</i>
Skeletal development	<i>Col1a1, Col1a2, Col2a1, Ctgf</i>
Epidermal differentiation	<i>Col1a1, Ctgf, Fabp5</i>
Lipid metabolism	<i>Fabp5, Lpl, Mgl</i>
Apoptosis	<i>Egln3, Tgm2</i>
Signal transduction in Golgi apparatus	<i>Clic5, Gorasp1</i>
Hormone activity	<i>Nppa</i>

Supplemental Table 4- GO-Term analysis of differentially expressed genes in lungs of *Aga2*^{+/severe} mice.

GO-term	Gene symbol
cell growth and/or maintenance	<i>Ar, Atp1a1, Bcl3, Btg2, Cbx2, Cdkn1c, Cp, Ctgf, Cxcl12, Dusp6, Fabp4, Fli1, Fscn1, Gap43, Hmgn2, Junb, Lcn2, Lpl, Mdk, Nfix, Pgm2, Pltp, S100A6, scn3b, Scnn1a, Sv2a, Tacstd2, Tgfb1</i>
cell surface receptor-linked signal transduction	<i>Agt, C3, Cd19, Ctgf, Cxcl12, Etd1, Gap43, Gdf10, Itga2b, Ltbp3, Ntrk2, Pf4, Rgs9, Tacstd2, Wnt11</i>
organogenesis	<i>Ang, Ar, Col3a1, Ctgf, Fabp5, Fli1, Gap43, Gdf10, Hey1, Mdk, Ntrk2, Pf4, S100a6</i>
Response to stress	<i>Btg2, C1qb, C3, CD19, Clu, Ctgf, Cxcl12, Dclre1a, Gap43, Gpx1, Mgl, Pf4</i>
Protein metabolism	<i>Bcl3, Col5a1, Dusp6, Itih2, Lpl, Ntrk2, Prkce, Scyl1, Serpine2</i>
Immune response	<i>C1qb, C2, Cd19, Clu, Cxcl12, Fcgbp, Mgl, Pf4</i>
Lipid metabolism	<i>Clu, Fabp5, Fasn, Hsd11b1, Lpl, Mgl, Plcd1, Pltp</i>
Oxidoreductase activity	<i>Cp, Fasn, Glrx, Gpx1, H6Pd, Hsd11b1, Ldha, Msln</i>
Wound response	<i>C3, Cd19, Ctgf, Cxcl12, Gap43, Mgl, Pf4</i>
Energy pathway	<i>Fbp2, H6pd, Ldha, Pdk1, Pkm2</i>
Neurogenesis	<i>Gap43, Hey1, Mdk, Ntrk2, S100a6</i>
Apoptosis	<i>Bnip3, Clu, Dusp6, Prkce</i>
Inflammatory response	<i>C3, Cxcl12, Mgl, Pf4</i>
Angiogenesis	<i>Ng, Ctgf, Pf4</i>
Embryogenesis and morphogenesis	<i>Tpd52, Wnt11</i>
Epidermal differentiation	<i>Ctgf, Fabp5</i>

Supplemental Table 5. Metabolic parameters of *Aga2/+^{mild}*.
Data are represented as mean \pm SEM.

Parameter	Control (A)		Mutant (B)		A~B p-value
	Male (n=6)	Female (n=5)	Male (n=6)	Female (n=5)	
Body weight [g]	32.8 ± 0.58	33.9 ± 1.02	21.9 ± 0.61	20.8 ± 0.45	***
Rectal body temperature [°C]	35.9 ± 0.06	36.4 ± 0.04	35.4 ± 0.25	36.0 ± 0.04	**
Food consumption [g/day]	4.3 ± 0.12	4.49 ± 0.1	3.01 ± 0.25	4.42 ± 0.29	***
Energy uptake [kJ/day]	76.9 ± 2.19	84.8 ± 3.69	53.7 ± 4.47	78.8 ± 5.24	***
Energy uptake BW¹ [kJ/g/day]	2.35 ± 0.08	2.62 ± 0.13	2.44 ± 0.18	3.8 ± 0.27	**
Feces production [g/day]	1.05 ± 0.02	1.12 ± 0.04	0.8 ± 0.05	0.9 ± 0.03	***
Energy content feces [kJ/g]	15.5 ± 0.06	15.5 ± 0.05	15.4 ± 0.08	15.3 ± 0.03	*
Metabolised energy [kJ/day]	59.4 ± 1.87	69.3 ± 1.47	40.6 ± 3.85	63.7 ± 4.84	***
Metabolized energy [kJ/g/day]	1.81 ± 0.06	2.06 ± 0.11	1.84 ± 0.16	3.07 ± 0.25	**
Food assimilation coefficient [%]	77.2 ± 0.32	78.6 ± 0.42	74.9 ± 1.66	80.5 ± 0.73	n.s.

Supplemental Table 6. Gene expression analysis of *in vivo* cultured primary osteoblasts in *Aga2/+*.

Gene	Group	Timepoint after stimulation				
		Expression in % to mean of <i>Actb/Pgk1/Gapdh</i>				
		0	3	9	15	21
<i>Alpl</i>	control	6.8	8.6	6.6	31.4	8.0
	<i>Aga2/+</i>	8.1	9.2	7.1	14.4	2.4
<i>Bglap1</i>	control	1.3	7.4	15.4	32.5	16.3
	<i>Aga2/+</i>	1.4	5.3	16.2	15.8	4.5
<i>Col1a1</i>	control	1302.6	1633.4	980.3	1182.8	507.7
	<i>Aga2/+</i>	1221.7	1370.0	650.4	676.3	271.4
<i>Cst3</i>	control	51.0	45.3	45.2	91.0	75.4
	<i>Aga2/+</i>	45.1	47.9	49.5	91.9	68.4
<i>Pdpr</i>	control	4.8	3.4	10.4	5.4	4.3
	<i>Aga2/+</i>	8.2	5.7	8.8	5.7	5.6
<i>Fos</i>	control	0.8	0.5	0.5	0.5	0.4
	<i>Aga2/+</i>	0.7	0.6	0.5	0.6	0.5
<i>Fosl2</i>	control	5.6	3.4	3.3	2.4	2.1
	<i>Aga2/+</i>	4.6	3.0	2.5	2.2	2.5
<i>Ibsp</i>	control	0.6	30.7	15.2	103.7	39.6
	<i>Aga2/+</i>	0.6	17.4	12.6	46.0	9.0
<i>Mmp13</i>	control	37.4	42.7	145.1	74.7	64.4
	<i>Aga2/+</i>	79.1	62.0	69.7	54.3	46.5
<i>Sp7</i>	control	5.2	2.1	4.6	5.9	1.5
	<i>Aga2/+</i>	4.8	2.5	2.4	2.5	0.4
<i>Runx2</i>	control	2.3	0.9	1.9	1.5	0.9
	<i>Aga2/+</i>	1.9	1.2	1.1	1.0	0.6
<i>Spp1</i>	control	64.4	66.0	533.1	368.1	283.9
	<i>Aga2/+</i>	98.8	61.2	302.1	218.1	230.7
<i>Twist1</i>	control	3.5	2.1	3.6	3.9	2.5
	<i>Aga2/+</i>	4.2	2.8	2.8	3.6	2.2

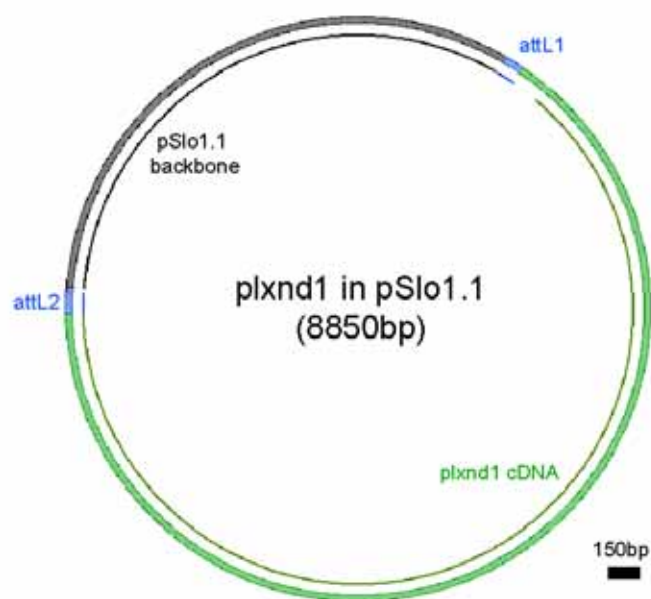
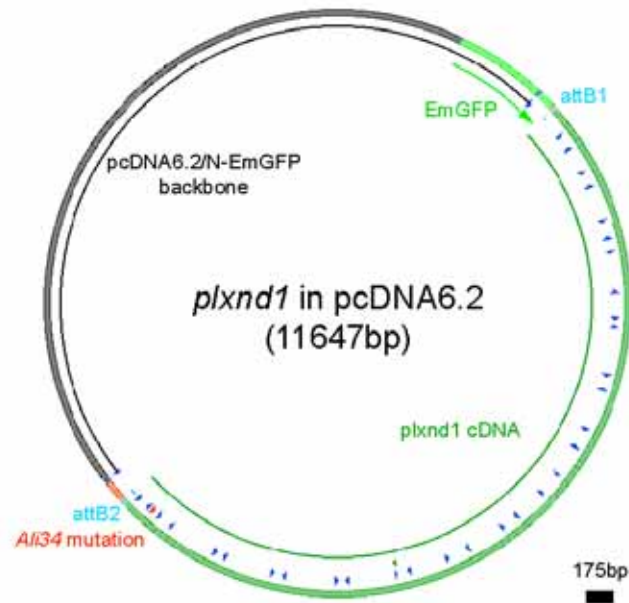
6.3 Primer sequences

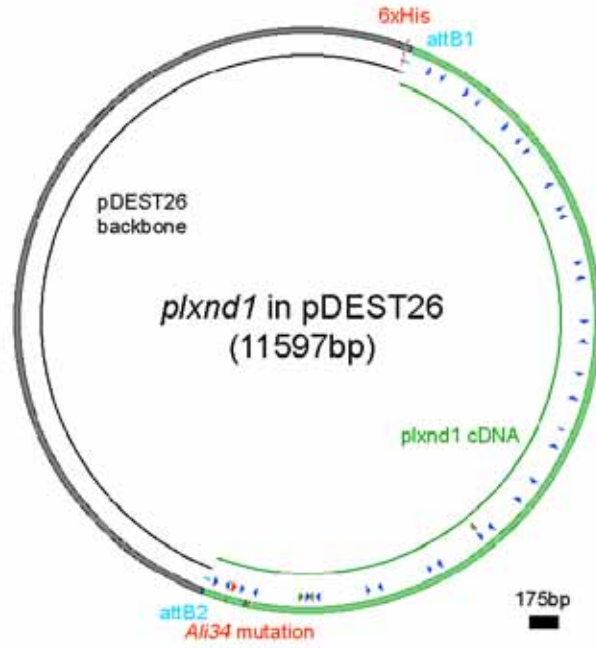
Primer name		Sequence (5'-->3')
<i>Ali34 Genotyping</i>	F	GTGGCACACACCTTTAATCC
	R	TTGCAGTGAGTCAGATGTGC
<i>Aga2 Genotyping</i>	F	GGCAACAGTCGCTTCACCTA
	R	GGAGGTCTTGGTGGT'TTTGT
<i>Ali34 SDM</i>	F	CATGGCTGAGATTTAGAAATATGCTAAGAGG
	R	GCCACGTTTGTGTTGAACCTCATTCT
<i>Aga2 SDM</i>	F	ACCCTCTCCCGCAGTCTTCATTACACCA
	R	CATTACCAAGGTAGGAATGAAGTGAGGCTCA
<u>qRT-PCR Primer</u>		
<i>Col10a1</i>	F	CATCTCCCAGCACCAGAATC
	R	ACTGGAATCCCTTTACTCTTTATGG
<i>Postn</i>	F	CCGCAGTGATGCCTATTGA
	R	GCGAATGTCAGAATCCAGGT
<i>Cdc42</i>	F	TTTGATACTGCAGGGCAAGA
	R	TCTCAGGCACCCACTTTTCT
<i>Rac1</i>	F	CGTGCAAAGTGGTATCCTGA
	R	GACAGCACCGATCTCTTTCG
<i>Lect1</i>	F	TCTCTGAACTGGAAGGCAAGA
	R	TGGATTTCTTTTGGATACATGG
<i>Sox9</i>	F	GCTCTGGAGGCTGCTGAA
	R	CTGAGATTGCCAGAGTGCT
<i>Col2a1</i>	F	CAGCTGGAGTCAAGGGAGAT
	R	ACCTTGTGCACCAGCCTCT
<i>Cdgap</i>	F	GAGTTACCAGACAACAAGAGAAAGC
	R	TTCCACTGACAGCCTCTGG
<i>Plxnd1</i>	F	TCAGAGGAGATCGTGTGTGC
	R	GGGCAGCACATAGGAGAACT
<i>Ctgf</i>	F	AGTGTGCACTGCCAAAGATG
	R	TTCCAGTCGGTAGGCAGCTA
<i>Mmp9</i>	F	AAGGACGGTTGGTACTGGAA
	R	CCACATTTGACGTCCAGAGA
<i>Col1a1</i>	F	CCAAGAAGACATCCCTGAAGTC
	R	TTGGGTCCCTCGACTCCT
<i>Col1a1^{WT}</i>	F	GATGGATTCCCGTTCGAGTA
	R	AGTTCCGGTGTGACTCGTG
<i>Col1a1^{Aga2}</i>	F	GATGGATTCCCGTTCGAGTA
	R	GACTCTGGTGTGAATGAAGACG
<i>Alp</i>	F	TTGTGCCAGAGAAAGAGAGAGAC
	R	TTGGTGTATATGTCTTGGAGAGG
<i>Bglap</i>	F	GACCTCACAGATGCCAAGC
	R	GACTGAGGCTCCAAGGTAGC
<i>Cst3</i>	F	CGTAAGCAGCTCGTGGCT
	R	CAGAGTGCCTTCCTCATCAGA
<i>Pdpr</i>	F	CAGATAAGAAAGATGGCTTGCC
	R	CTCTTTAGGGCGAGAACCCTTC
<i>Fos</i>	F	CAACACACAGGACTTTTGCG
	R	TCAGGAGATAGCTGCTCTACTTTG
<i>Fosl2</i>	F	AGATGAGCAGCTGTCTCCTGA
	R	TCCTCGGTCTCCGCCT
<i>Ibsp</i>	F	AGGAAGAGGAGACTTCAAACGA
	R	TGCATCTCCAGCCTTCTTG
<i>Mmp13</i>	F	GCAGTTCCAAAGGCTACAACCTT
	R	TCATCGCCTGGACCATAAAG
<i>Sp7</i>	F	TCTCTGCTTGAGGAAGAAGCTC
	R	TTGAGAAGGGAGCTGGGTAG
<i>Runx2</i>	F	AGTCAGATTACAGATCCAGGC
	R	GCAGTGTATCATCTGAAATACG
<i>Spp1</i>	F	AGCAAGAACTCTTCCAAGCA
	R	TGGCATCAGGATACTGTTTCATC

Primer name		Sequence (5'-->3')
<i>Twist1</i>	<i>F</i>	GCTCAGCTACGCCTTCTCC
	<i>R</i>	ACAATGACATCTAGGTCTCCGG
<i>Acp5</i>	<i>F</i>	CACCGCCAAGATGGATTCT
	<i>R</i>	TCCTCAAAGGTCTCCTGGAA
<i>Itgav</i>	<i>F</i>	AATGGGGATGATTACGCAGA
	<i>R</i>	GCAATATCATTGAAGCCATCC
<i>Ctsk</i>	<i>F</i>	ATATGTGGGCCAGGATGAAA
	<i>R</i>	TCATCATAGTACACACCTCTGCTG
<i>mcsf</i>	<i>F</i>	TGCCCTTCTTCGACATGG
	<i>R</i>	TTGACTGTCGATCAACTGCTG
<i>Rank</i>	<i>F</i>	ATGCGAACCAGGAAAGTACC
	<i>R</i>	CCTTGCCTGCATCACAGAC
<i>Ins1</i>	<i>F</i>	GCAAGCAGGTCATTGTTTCA
	<i>R</i>	CACTTGTGGGTCTCCACTT
<i>Ins2</i>	<i>F</i>	CAGCAAGCAGGAAGCCTATC
	<i>R</i>	GCTCCAGTTGTGCCACTTGT
<i>Gcg</i>	<i>F</i>	AGGCTCACAAGGCAGAAAAA
	<i>R</i>	CAATGTTGTTCCGGTTCCTC
<i>Cdk4</i>	<i>F</i>	TGGGGAAAATCTTTGATCTCAT
	<i>R</i>	GGTCAGCATTTCCAGTAGCAG
<i>Ccnd2</i>	<i>F</i>	CTCTGTGCGCTACCGACTTC
	<i>R</i>	GGCTTTGAGACAATCCACATC
<i>VEGF¹²⁰</i>	<i>F</i>	CAACATCACCATGCAGATCA
	<i>R</i>	TTGTACATTTTTTCTGGCTTTG
<i>VEGF¹⁶⁴</i>	<i>F</i>	CAACATCACCATGCAGATCA
	<i>R</i>	TCACAGTGATTTTTCTGGCTTT
<i>VEGF¹⁸⁸</i>	<i>F</i>	AATCCTGGAGCGTTCACTGT
	<i>R</i>	TCACATCTGCAAGTACGTTTCG
<i>CD-31</i>	<i>F</i>	CAGCCATTACGGTTATGATGA
	<i>R</i>	TCCCAGAGCTTGGTGAGG
<i>qRT-PCR housekeeping gene primer</i>		
<i>Actb</i>	<i>F</i>	GCCACCAGTTCGCCAT
	<i>R</i>	CATCACACCCTGGTGCCTA
<i>Pgk1</i>	<i>F</i>	GAGCCCATAGCTCCATGGT
	<i>R</i>	ACTTTAGCGCCTCCCAAGA
<i>Gapdh</i>	<i>F</i>	TGGAGAAACCTGCCAAGTATG
	<i>R</i>	CATTGTCATACCAGGAAATGAGC
<i>SDHA</i>	<i>F</i>	GCAATTTCTACTCAATACCCAGTG
	<i>R</i>	CTCCCTGTGCTGCAACAGTA
<i>RpbII</i>	<i>F</i>	TGAAGCCTACCAGAAAGTTTGC
	<i>R</i>	GCCTGTTTCCGTAACCTCAA

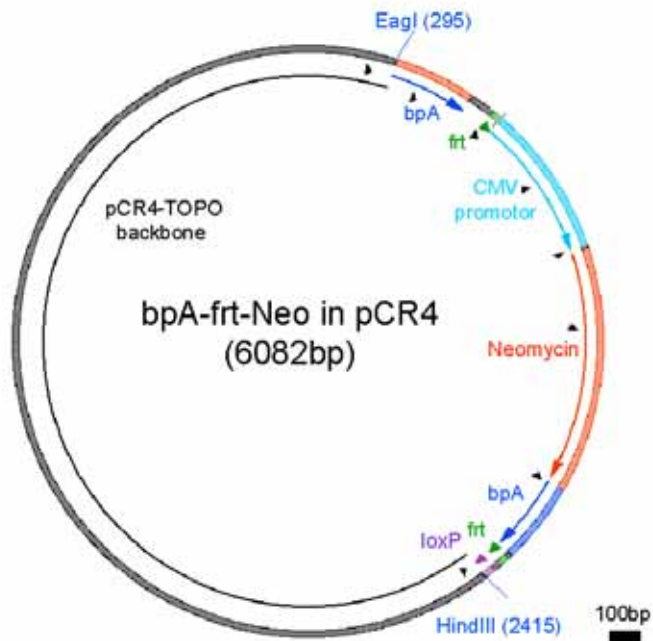
6.4 Plasmid constructs

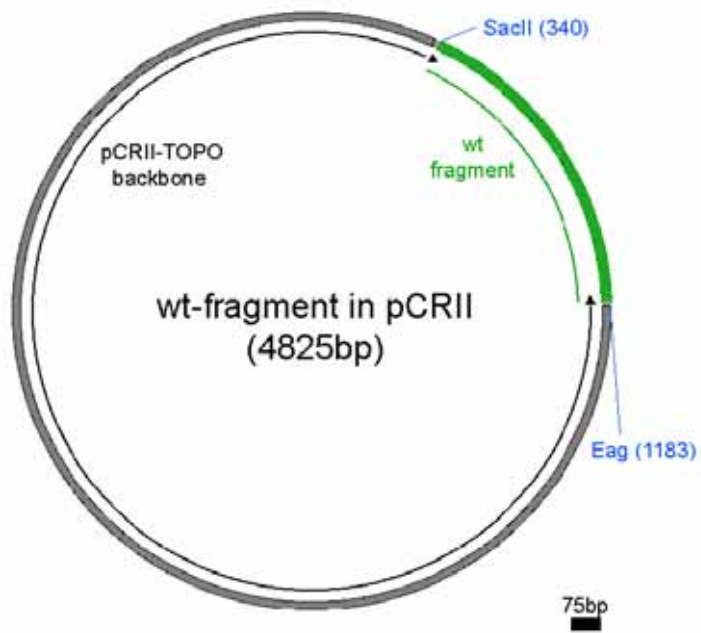
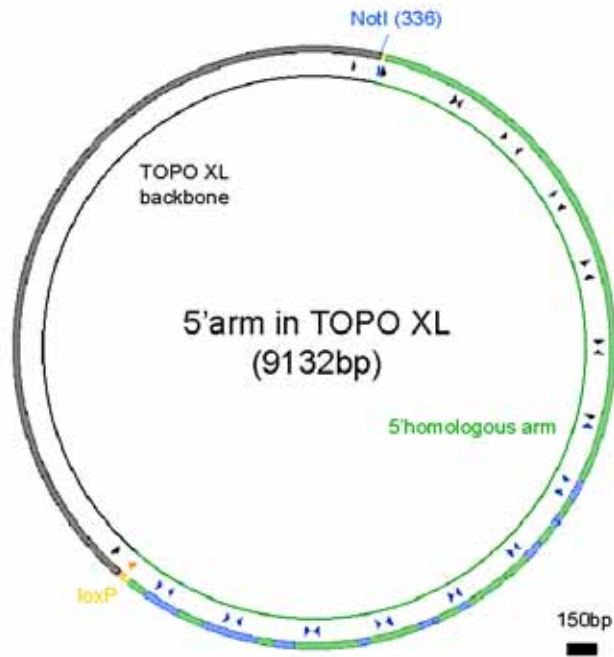
Ali34 plasmids

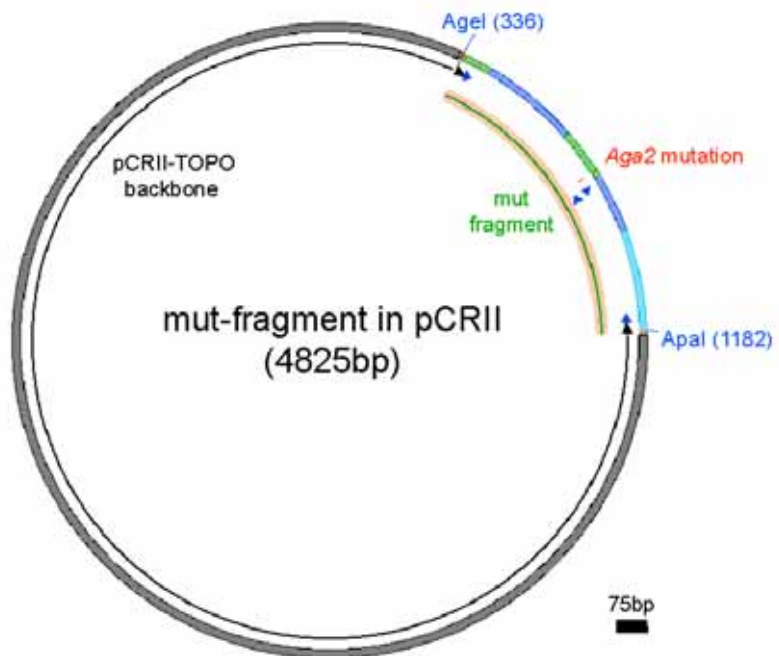
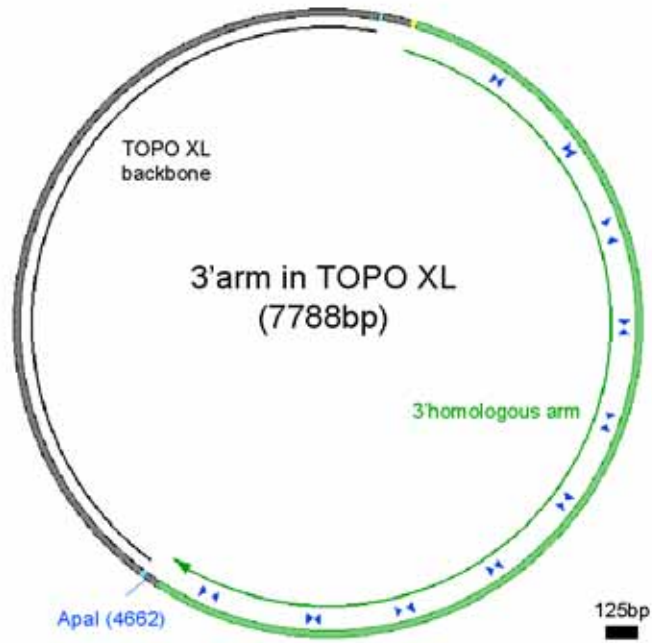




Aga2 plasmids







7. References

1. Steele, D.G. & Bramblett, C.A. *The anatomy and biology of the human skeleton*, (Texas A&M University Press, College Station, 1988).
2. Buckwalter, J.A., Glimcher, M.J., Cooper, R.R. & Recker, R. Bone biology. I: Structure, blood supply, cells, matrix, and mineralization. *Instr Course Lect* **45**, 371-386 (1996).
3. Marks Jr., S.C. & Hermey, D.C. *in Principles of bone biology pp. 3-14*, (Academic Press, San Diego, 1996).
4. Lee, N.K., *et al.* Endocrine regulation of energy metabolism by the skeleton. *Cell* **130**, 456-469 (2007).
5. Bryan, G.J. *Skeletal anatomy, Third Edition p.6*, (Churchill Livingstone, 1996).
6. Chai, Y. & Maxson, R.E., Jr. Recent advances in craniofacial morphogenesis. *Dev Dyn* **235**, 2353-2375 (2006).
7. Karsenty, G. & Wagner, E.F. Reaching a genetic and molecular understanding of skeletal development. *Dev Cell* **2**, 389-406 (2002).
8. Mariani, F.V. & Martin, G.R. Deciphering skeletal patterning: clues from the limb. *Nature* **423**, 319-325 (2003).
9. Hall, B.K. & Miyake, T. Divide, accumulate, differentiate: cell condensation in skeletal development revisited. *Int J Dev Biol* **39**, 881-893 (1995).
10. Horton, W.A. Skeletal development: insights from targeting the mouse genome. *Lancet* **362**, 560-569 (2003).
11. Olsen, B.R., Reginato, A.M. & Wang, W. Bone development. *Annu Rev Cell Dev Biol* **16**, 191-220 (2000).
12. Cohen, M.M., Jr. The new bone biology: pathologic, molecular, and clinical correlates. *Am J Med Genet A* **140**, 2646-2706 (2006).
13. Shapiro, F. Bone development and its relation to fracture repair. The role of mesenchymal osteoblasts and surface osteoblasts. *Eur Cell Mater* **15**, 53-76 (2008).
14. Hartmann, C. A Wnt canon orchestrating osteoblastogenesis. *Trends Cell Biol* **16**, 151-158 (2006).
15. Goldring, M.B., Tsuchimochi, K. & Ijiri, K. The control of chondrogenesis. *J Cell Biochem* **97**, 33-44 (2006).
16. Kornak, U. & Mundlos, S. Genetic disorders of the skeleton: a developmental approach. *Am J Hum Genet* **73**, 447-474 (2003).
17. Kugler, J.H., Tomlinson, A., Wagstaff, A. & Ward, S.M. The role of cartilage canals in the formation of secondary centres of ossification. *J Anat* **129**, 493-506 (1979).
18. Lee, E.R., *et al.* Enzymes active in the areas undergoing cartilage resorption during the development of the secondary ossification center in the tibiae of rats ages 0-21 days: I. Two groups of proteinases cleave the core protein of aggrecan. *Dev Dyn* **222**, 52-70 (2001).
19. Eyre, D.R., Weis, M.A. & Wu, J.J. Articular cartilage collagen: an irreplaceable framework? *Eur Cell Mater* **12**, 57-63 (2006).
20. Zuscik, M.J., Hilton, M.J., Zhang, X., Chen, D. & O'Keefe, R.J. Regulation of chondrogenesis and chondrocyte differentiation by stress. *J Clin Invest* **118**, 429-438 (2008).
21. Horowitz, M.C., Bothwell, A.L., Hesslein, D.G., Pflugh, D.L. & Schatz, D.G. B cells and osteoblast and osteoclast development. *Immunol Rev* **208**, 141-153 (2005).

22. Hesse, L., *et al.* Tissue-nonspecific alkaline phosphatase and plasma cell membrane glycoprotein-1 are central antagonistic regulators of bone mineralization. *Proc Natl Acad Sci U S A* **99**, 9445-9449 (2002).
23. Datta, H.K., Ng, W.F., Walker, J.A., Tuck, S.P. & Varanasi, S.S. The cell biology of bone metabolism. *J Clin Pathol* **61**, 577-587 (2008).
24. Bonewald, L.F. Mechanosensation and Transduction in Osteocytes. *Bonekey Osteovision* **3**, 7-15 (2006).
25. Bonewald, L. Osteocytes as multifunctional cells. *J Musculoskelet Neuronal Interact* **6**, 331-333 (2006).
26. You, L., *et al.* Osteocytes as mechanosensors in the inhibition of bone resorption due to mechanical loading. *Bone* **42**, 172-179 (2008).
27. Duncan, R.L. & Turner, C.H. Mechanotransduction and the functional response of bone to mechanical strain. *Calcif Tissue Int* **57**, 344-358 (1995).
28. Pavalko, F.M., *et al.* A model for mechanotransduction in bone cells: the load-bearing mechanosomes. *J Cell Biochem* **88**, 104-112 (2003).
29. Tarbell, J.M., Weinbaum, S. & Kamm, R.D. Cellular fluid mechanics and mechanotransduction. *Ann Biomed Eng* **33**, 1719-1723 (2005).
30. Bonewald, L.F. & Johnson, M.L. Osteocytes, mechanosensing and Wnt signaling. *Bone* **42**, 606-615 (2008).
31. Ellies, D.L., *et al.* Bone density ligand, Sclerostin, directly interacts with LRP5 but not LRP5G171V to modulate Wnt activity. *J Bone Miner Res* **21**, 1738-1749 (2006).
32. Lin, C., *et al.* Sclerostin mediates bone response to mechanical unloading through antagonizing Wnt/beta-catenin signaling. *J Bone Miner Res* **24**, 1651-1661 (2009).
33. Miller, S.C. & Jee, W.S. The bone lining cell: a distinct phenotype? *Calcif Tissue Int* **41**, 1-5 (1987).
34. Everts, V., *et al.* The bone lining cell: its role in cleaning Howship's lacunae and initiating bone formation. *J Bone Miner Res* **17**, 77-90 (2002).
35. Kawaguchi, N. & Noda, M. Mitf is expressed in osteoclast progenitors in vitro. *Exp Cell Res* **260**, 284-291 (2000).
36. Yavropoulou, M.P. & Yovos, J.G. Osteoclastogenesis--current knowledge and future perspectives. *J Musculoskelet Neuronal Interact* **8**, 204-216 (2008).
37. Lerner, U.H. New Molecules in the Tumor Necrosis Factor Ligand and Receptor Superfamilies with Importance for Physiological and Pathological Bone Resorption. *Crit Rev Oral Biol Med* **15**, 64-81 (2004).
38. Boyle, W.J., Simonet, W.S. & Lacey, D.L. Osteoclast differentiation and activation. *Nature* **423**, 337-342 (2003).
39. Franzoso, G., *et al.* Requirement for NF-kappaB in osteoclast and B-cell development. *Genes Dev* **11**, 3482-3496 (1997).
40. Boyce, B.F. & Xing, L. Biology of RANK, RANKL, and osteoprotegerin. *Arthritis Res Ther* **9 Suppl 1**, S1 (2007).
41. Lacey, D.L., *et al.* Osteoprotegerin ligand is a cytokine that regulates osteoclast differentiation and activation. *Cell* **93**, 165-176 (1998).
42. Miyazaki, T., Tanaka, S., Sanjay, A. & Baron, R. The role of c-Src kinase in the regulation of osteoclast function. *Mod Rheumatol* **16**, 68-74 (2006).
43. McHugh, K.P., *et al.* Mice lacking beta3 integrins are osteosclerotic because of dysfunctional osteoclasts. *J Clin Invest* **105**, 433-440 (2000).

44. Frattini, A., *et al.* Defects in TCIRG1 subunit of the vacuolar proton pump are responsible for a subset of human autosomal recessive osteopetrosis. *Nat Genet* **25**, 343-346 (2000).
45. Kornak, U., *et al.* Loss of the CIC-7 chloride channel leads to osteopetrosis in mice and man. *Cell* **104**, 205-215 (2001).
46. Teitelbaum, S.L. & Ross, F.P. Genetic regulation of osteoclast development and function. *Nat Rev Genet* **4**, 638-649 (2003).
47. Gelb, B.D., Shi, G.P., Chapman, H.A. & Desnick, R.J. Pycnodysostosis, a lysosomal disease caused by cathepsin K deficiency. *Science* **273**, 1236-1238 (1996).
48. Buckwalter, J.A., Glimcher, M.J., Cooper, R.R. & Recker, R. Bone biology. II: Formation, form, modeling, remodeling, and regulation of cell function. *Instr Course Lect* **45**, 387-399 (1996).
49. Hill, P.A. Bone remodelling. *Br J Orthod* **25**, 101-107 (1998).
50. Harada, S. & Rodan, G.A. Control of osteoblast function and regulation of bone mass. *Nature* **423**, 349-355 (2003).
51. Gori, F., *et al.* The expression of osteoprotegerin and RANK ligand and the support of osteoclast formation by stromal-osteoblast lineage cells is developmentally regulated. *Endocrinology* **141**, 4768-4776 (2000).
52. Hofbauer, L.C., Kuhne, C.A. & Viereck, V. The OPG/RANKL/RANK system in metabolic bone diseases. *J Musculoskelet Neuronal Interact* **4**, 268-275 (2004).
53. Khosla, S. Minireview: the OPG/RANKL/RANK system. *Endocrinology* **142**, 5050-5055 (2001).
54. Hofbauer, L.C. & Schoppet, M. Clinical implications of the osteoprotegerin/RANKL/RANK system for bone and vascular diseases. *JAMA* **292**, 490-495 (2004).
55. Sattler, A.M., Schoppet, M., Schaefer, J.R. & Hofbauer, L.C. Novel aspects on RANK ligand and osteoprotegerin in osteoporosis and vascular disease. *Calcif Tissue Int* **74**, 103-106 (2004).
56. Superti-Furga, A., Bonafe, L. & Rimoin, D.L. Molecular-pathogenetic classification of genetic disorders of the skeleton. *Am J Med Genet* **106**, 282-293 (2001).
57. Fuchs, H., Lisse, T., Abe, K., Hrabé de Angelis, M. *Screening for bone and cartilage phenotypes in mice.*, (Wiley-VCH, Weinheim, 2006).
58. Malloy, P.J. & Feldman, D. Genetic disorders and defects in vitamin d action. *Endocrinol Metab Clin North Am* **39**, 333-346, table of contents (2010).
59. Karsenty, G. The complexities of skeletal biology. *Nature* **423**, 316-318 (2003).
60. Rauch, F. & Glorieux, F.H. Osteogenesis imperfecta. *Lancet* **363**, 1377-1385 (2004).
61. Sack, K.E. Osteoarthritis. A continuing challenge. *West J Med* **163**, 579-586 (1995).
62. Feldmann, M., Brennan, F.M. & Maini, R.N. Role of cytokines in rheumatoid arthritis. *Annu Rev Immunol* **14**, 397-440 (1996).
63. Horton, W.E., Jr., Bennion, P. & Yang, L. Cellular, molecular, and matrix changes in cartilage during aging and osteoarthritis. *J Musculoskelet Neuronal Interact* **6**, 379-381 (2006).
64. Chapman, K., *et al.* Osteoarthritis-susceptibility locus on chromosome 11q, detected by linkage. *Am J Hum Genet* **65**, 167-174 (1999).

65. Greig, C., *et al.* Linkage to nodal osteoarthritis: quantitative and qualitative analyses of data from a whole-genome screen identify trait-dependent susceptibility loci. *Ann Rheum Dis* **65**, 1131-1138 (2006).
66. Hunter, D.J., Demissie, S., Cupples, L.A., Aliabadi, P. & Felson, D.T. A genome scan for joint-specific hand osteoarthritis susceptibility: The Framingham Study. *Arthritis Rheum* **50**, 2489-2496 (2004).
67. Leppavuori, J., *et al.* Genome scan for predisposing loci for distal interphalangeal joint osteoarthritis: evidence for a locus on 2q. *Am J Hum Genet* **65**, 1060-1067 (1999).
68. Loughlin, J., *et al.* Stratification analysis of an osteoarthritis genome screen-suggestive linkage to chromosomes 4, 6, and 16. *Am J Hum Genet* **65**, 1795-1798 (1999).
69. Cohen, M.M., Jr. Pfeiffer syndrome update, clinical subtypes, and guidelines for differential diagnosis. *Am J Med Genet* **45**, 300-307 (1993).
70. Ho, A.M., Johnson, M.D. & Kingsley, D.M. Role of the mouse ank gene in control of tissue calcification and arthritis. *Science* **289**, 265-270 (2000).
71. Kuurila, K., Grenman, R., Johansson, R. & Kaitila, I. Hearing loss in children with osteogenesis imperfecta. *Eur J Pediatr* **159**, 515-519 (2000).
72. Paterson, C.R., Monk, E.A. & McAllion, S.J. How common is hearing impairment in osteogenesis imperfecta? *J Laryngol Otol* **115**, 280-282 (2001).
73. Petersen, K. & Wetzel, W.E. Recent findings in classification of osteogenesis imperfecta by means of existing dental symptoms. *ASDC J Dent Child* **65**, 305-309, 354 (1998).
74. Sillence, D.O., Senn, A. & Danks, D.M. Genetic heterogeneity in osteogenesis imperfecta. *J Med Genet* **16**, 101-116 (1979).
75. Glorieux, F.H. Osteogenesis imperfecta. *Best Pract Res Clin Rheumatol* **22**, 85-100 (2008).
76. Baldrige, D., *et al.* CRTAP and LEPRE1 mutations in recessive osteogenesis imperfecta. *Hum Mutat* **29**, 1435-1442 (2008).
77. Barnes, A.M., *et al.* Lack of cyclophilin B in osteogenesis imperfecta with normal collagen folding. *N Engl J Med* **362**, 521-528 (2010).
78. Morello, R., *et al.* CRTAP is required for prolyl 3- hydroxylation and mutations cause recessive osteogenesis imperfecta. *Cell* **127**, 291-304 (2006).
79. Marini, J.C. Diseases of Bone and Mineral Metabolism - Chapter 16 - Osteogenesis imperfecta, in www.endotext.org. (ed. Frederick, S.) (Endotext.org, 2010).
80. McAllion, S.J. & Paterson, C.R. Causes of death in osteogenesis imperfecta. *J Clin Pathol* **49**, 627-630 (1996).
81. Widmann, R.F., *et al.* Spinal deformity, pulmonary compromise, and quality of life in osteogenesis imperfecta. *Spine* **24**, 1673-1678 (1999).
82. Shapiro, J.R., *et al.* Pulmonary hypoplasia and osteogenesis imperfecta type II with defective synthesis of alpha I(1) procollagen. *Bone* **10**, 165-171 (1989).
83. Thibeault, D.W., Pettett, G., Mabry, S.M. & Rezaiekhaligh, M.M. Osteogenesis imperfecta Type IIA and pulmonary hypoplasia with normal alveolar development. *Pediatr Pulmonol* **20**, 301-306 (1995).
84. Perkins, A.S. Functional genomics in the mouse. *Funct Integr Genomics* **2**, 81-91 (2002).

85. Waterston, R.H., *et al.* Initial sequencing and comparative analysis of the mouse genome. *Nature* **420**, 520-562 (2002).
86. Hrabe de Angelis, M.H., *et al.* Genome-wide, large-scale production of mutant mice by ENU mutagenesis. *Nat Genet* **25**, 444-447 (2000).
87. Justice, M.J., Noveroske, J.K., Weber, J.S., Zheng, B. & Bradley, A. Mouse ENU mutagenesis. *Hum Mol Genet* **8**, 1955-1963 (1999).
88. Gitler, A.D., Lu, M.M. & Epstein, J.A. PlexinD1 and semaphorin signaling are required in endothelial cells for cardiovascular development. *Dev Cell* **7**, 107-116 (2004).
89. Kanda, T., *et al.* PlexinD1 deficiency induces defects in axial skeletal morphogenesis. *J Cell Biochem* **101**, 1329-1337 (2007).
90. Zhang, Y., *et al.* Tie2Cre-mediated inactivation of plexinD1 results in congenital heart, vascular and skeletal defects. *Dev Biol* **325**, 82-93 (2009).
91. Lisse, T.S., *et al.* ER stress-mediated apoptosis in a new mouse model of osteogenesis imperfecta. *PLoS Genet* **4**, e7 (2008).
92. Beckers, J., Wurst, W. & de Angelis, M.H. Towards better mouse models: enhanced genotypes, systemic phenotyping and envirotype modelling. *Nat Rev Genet* **10**, 371-380 (2009).
93. Gailus-Durner, V., *et al.* Systemic First-Line Phenotyping. *Methods Mol Biol* **530**, 1-47 (2009).
94. Fuchs, H., *et al.* Phenotypic characterization of mouse models for bone-related diseases in the German Mouse Clinic. *J Musculoskelet Neuronal Interact* **8**, 13-14 (2008).
95. Fuchs, H., Schughart, K., Wolf, E., Balling, R. & Hrabe de Angelis, M. Screening for dysmorphological abnormalities--a powerful tool to isolate new mouse mutants. *Mamm Genome* **11**, 528-530 (2000).
96. Shannon, D.C., Riseborough, E.J., Valenca, L.M. & Kazemi, H. The distribution of abnormal lung function in kyphoscoliosis. *J Bone Joint Surg Am* **52**, 131-144 (1970).
97. Ferron, M., *et al.* Insulin signaling in osteoblasts integrates bone remodeling and energy metabolism. *Cell* **142**, 296-308 (2010).
98. Fukumoto, S. & Martin, T.J. Bone as an endocrine organ. *Trends Endocrinol Metab* **20**, 230-236 (2009).
99. Fulzele, K., *et al.* Insulin receptor signaling in osteoblasts regulates postnatal bone acquisition and body composition. *Cell* **142**, 309-319 (2010).
100. Schipani, E., Maes, C., Carmeliet, G. & Semenza, G.L. Regulation of osteogenesis-angiogenesis coupling by HIFs and VEGF. *J Bone Miner Res* **24**, 1347-1353 (2009).
101. Maes, C., *et al.* Increased skeletal VEGF enhances beta-catenin activity and results in excessively ossified bones. *EMBO J* **29**, 424-441 (2009).
102. Zelzer, E., *et al.* Skeletal defects in VEGF(120/120) mice reveal multiple roles for VEGF in skeletogenesis. *Development* **129**, 1893-1904 (2002).
103. Riggs, B.L., Khosla, S. & Melton, L.J., 3rd. Sex steroids and the construction and conservation of the adult skeleton. *Endocr Rev* **23**, 279-302 (2002).
104. Yadav, V.K., *et al.* A serotonin-dependent mechanism explains the leptin regulation of bone mass, appetite, and energy expenditure. *Cell* **138**, 976-989 (2009).
105. Livak, K.J. & Schmittgen, T.D. Analysis of relative gene expression data using real-time quantitative PCR and the 2(-Delta Delta C(T)) Method. *Methods* **25**, 402-408 (2001).

106. Bessey, O.A., Lowry, O.H. & Brock, M.J. A method for the rapid determination of alkaline phosphates with five cubic millimeters of serum. *J Biol Chem* **164**, 321-329 (1946).
107. Puchtler, H., Meloan, S.N. & Terry, M.S. On the history and mechanism of alizarin and alizarin red S stains for calcium. *J Histochem Cytochem* **17**, 110-124 (1969).
108. Macchiarelli, G., *et al.* A micro-anatomical model of the distribution of myocardial endomysial collagen. *Histol Histopathol* **17**, 699-706 (2002).
109. Ohtani, O., Ushiki, T., Taguchi, T. & Kikuta, A. Collagen fibrillar networks as skeletal frameworks: a demonstration by cell-maceration/scanning electron microscope method. *Arch Histol Cytol* **51**, 249-261 (1988).
110. Gailus-Durner, V., *et al.* Introducing the German Mouse Clinic: open access platform for standardized phenotyping. *Nat Methods* **2**, 403-404 (2005).
111. Sahn, D.J., DeMaria, A., Kisslo, J. & Weyman, A. Recommendations regarding quantitation in M-mode echocardiography: results of a survey of echocardiographic measurements. *Circulation* **58**, 1072-1083 (1978).
112. Collins, K.A., Korcarz, C.E. & Lang, R.M. Use of echocardiography for the phenotypic assessment of genetically altered mice. *Physiol Genomics* **13**, 227-239 (2003).
113. Teichholz, L.E., Cohen, M.V., Sonnenblick, E.H. & Gorlin, R. Study of left ventricular geometry and function by B-scan ultrasonography in patients with and without asynergy. *N Engl J Med* **291**, 1220-1226 (1974).
114. Fuchs, H., *et al.* Mouse phenotyping. *Methods* **53**, 120-135 (2011).
115. Rogers, D.C., *et al.* Behavioral and functional analysis of mouse phenotype: SHIRPA, a proposed protocol for comprehensive phenotype assessment. *Mamm Genome* **8**, 711-713 (1997).
116. Schneider, I., *et al.* Systematic, standardized and comprehensive neurological phenotyping of inbred mice strains in the German Mouse Clinic. *J Neurosci Methods* **157**, 82-90 (2006).
117. Jones, B.J. & Roberts, D.J. A rotarod suitable for quantitative measurements of motor incoordination in naive mice. *Naunyn Schmiedebergs Arch Exp Pathol Pharmacol* **259**, 211 (1968).
118. Favor, J. A comparison of the dominant cataract and recessive specific-locus mutation rates induced by treatment of male mice with ethylnitrosourea. *Mutat Res* **110**, 367-382 (1983).
119. Hegde, P., *et al.* A concise guide to cDNA microarray analysis. *Biotechniques* **29**, 548-550, 552-544, 556 passim (2000).
120. Horsch, M., *et al.* Systematic gene expression profiling of mouse model series reveals coexpressed genes. *Proteomics* **8**, 1248-1256 (2008).
121. Edgar, R., Domrachev, M. & Lash, A.E. Gene Expression Omnibus: NCBI gene expression and hybridization array data repository. *Nucleic Acids Res* **30**, 207-210 (2002).
122. Quackenbush, J. Microarray data normalization and transformation. *Nat Genet* **32 Suppl**, 496-501 (2002).
123. Tusher, V.G., Tibshirani, R. & Chu, G. Significance analysis of microarrays applied to the ionizing radiation response. *Proc Natl Acad Sci U S A* **98**, 5116-5121 (2001).
124. Dennis, G., Jr., *et al.* DAVID: Database for Annotation, Visualization, and Integrated Discovery. *Genome Biol* **4**, P3 (2003).

125. Sarantopoulos, A., Themelis, G. & Ntziachristos, V. Imaging the Bio-Distribution of Fluorescent Probes Using Multispectral Epi-Illumination Cryoslicing Imaging. *Mol Imaging Biol* (2010).
126. Chauvet, S., *et al.* Gating of Sema3E/PlexinD1 signaling by neuropilin-1 switches axonal repulsion to attraction during brain development. *Neuron* **56**, 807-822 (2007).
127. Sakurai, A., *et al.* Semaphorin 3E initiates antiangiogenic signaling through plexin D1 by regulating Arf6 and R-Ras. *Mol Cell Biol* **30**, 3086-3098 (2010).
128. Parfitt, A.M. Bone histomorphometry: standardization of nomenclature, symbols and units. Summary of proposed system. *Bone Miner* **4**, 1-5 (1988).
129. Revell, P.A. Histomorphometry of bone. *J Clin Pathol* **36**, 1323-1331 (1983).
130. Saban, J., *et al.* Heterozygous oim mice exhibit a mild form of osteogenesis imperfecta. *Bone* **19**, 575-579 (1996).
131. Forlino, A., Porter, F.D., Lee, E.J., Westphal, H. & Marini, J.C. Use of the Cre/lox recombination system to develop a non-lethal knock-in murine model for osteogenesis imperfecta with an alpha1(I) G349C substitution. Variability in phenotype in BrtlIV mice. *J Biol Chem* **274**, 37923-37931 (1999).
132. Ducy, P., *et al.* Leptin inhibits bone formation through a hypothalamic relay: a central control of bone mass. *Cell* **100**, 197-207 (2000).
133. Karsenty, G. & Oury, F. The central regulation of bone mass, the first link between bone remodeling and energy metabolism. *J Clin Endocrinol Metab* **95**, 4795-4801 (2010).
134. Shi, Y., *et al.* Dissociation of the neuronal regulation of bone mass and energy metabolism by leptin in vivo. *Proc Natl Acad Sci U S A* **105**, 20529-20533 (2008).
135. Ferron, M., Hinoi, E., Karsenty, G. & Ducy, P. Osteocalcin differentially regulates beta cell and adipocyte gene expression and affects the development of metabolic diseases in wild-type mice. *Proc Natl Acad Sci U S A* **105**, 5266-5270 (2008).
136. Levin, M.E., Boisseau, V.C. & Avioli, L.V. Effects of diabetes mellitus on bone mass in juvenile and adult-onset diabetes. *N Engl J Med* **294**, 241-245 (1976).
137. Adami, S. Bone health in diabetes: considerations for clinical management. *Curr Med Res Opin* **25**, 1057-1072 (2009).
138. Hofbauer, L.C., Brueck, C.C., Singh, S.K. & Dobnig, H. Osteoporosis in patients with diabetes mellitus. *J Bone Miner Res* **22**, 1317-1328 (2007).
139. Isidro, M.L. & Ruano, B. Bone disease in diabetes. *Curr Diabetes Rev* **6**, 144-155 (2010).
140. Yaturu, S. Diabetes and skeletal health. *J Diabetes* **1**, 246-254 (2009).
141. Miquerol, L., Gertsenstein, M., Harpal, K., Rossant, J. & Nagy, A. Multiple developmental roles of VEGF suggested by a LacZ-tagged allele. *Dev Biol* **212**, 307-322 (1999).
142. Hayashi, S. & McMahon, A.P. Efficient recombination in diverse tissues by a tamoxifen-inducible form of Cre: a tool for temporally regulated gene activation/inactivation in the mouse. *Dev Biol* **244**, 305-318 (2002).

143. Dacquin, R., Starbuck, M., Schinke, T. & Karsenty, G. Mouse alpha1(I)-collagen promoter is the best known promoter to drive efficient Cre recombinase expression in osteoblast. *Dev Dyn* **224**, 245-251 (2002).
144. Zheng, B., Zhang, Z., Black, C.M., de Crombrughe, B. & Denton, C.P. Ligand-dependent genetic recombination in fibroblasts : a potentially powerful technique for investigating gene function in fibrosis. *Am J Pathol* **160**, 1609-1617 (2002).
145. Gu, C., *et al.* Semaphorin 3E and plexin-D1 control vascular pattern independently of neuropilins. *Science* **307**, 265-268 (2005).
146. He, Z. & Tessier-Lavigne, M. Neuropilin is a receptor for the axonal chemorepellent Semaphorin III. *Cell* **90**, 739-751 (1997).
147. Kruger, R.P., Aurandt, J. & Guan, K.L. Semaphorins command cells to move. *Nat Rev Mol Cell Biol* **6**, 789-800 (2005).
148. Tamagnone, L., *et al.* Plexins are a large family of receptors for transmembrane, secreted, and GPI-anchored semaphorins in vertebrates. *Cell* **99**, 71-80 (1999).
149. Behar, O., Golden, J.A., Mashimo, H., Schoen, F.J. & Fishman, M.C. Semaphorin III is needed for normal patterning and growth of nerves, bones and heart. *Nature* **383**, 525-528 (1996).
150. Banu, N., Teichman, J., Dunlap-Brown, M., Villegas, G. & Tufro, A. Semaphorin 3C regulates endothelial cell function by increasing integrin activity. *FASEB J* **20**, 2150-2152 (2006).
151. Gomez, C., *et al.* Expression of Semaphorin-3A and its receptors in endochondral ossification: potential role in skeletal development and innervation. *Dev Dyn* **234**, 393-403 (2005).
152. Cummings, D.E., *et al.* A preprandial rise in plasma ghrelin levels suggests a role in meal initiation in humans. *Diabetes* **50**, 1714-1719 (2001).
153. Toyofuku, T., *et al.* Repulsive and attractive semaphorins cooperate to direct the navigation of cardiac neural crest cells. *Dev Biol* **321**, 251-262 (2008).
154. Deng, S., *et al.* Plexin-B2, but not Plexin-B1, critically modulates neuronal migration and patterning of the developing nervous system in vivo. *J Neurosci* **27**, 6333-6347 (2007).
155. Feiner, L., *et al.* Targeted disruption of semaphorin 3C leads to persistent truncus arteriosus and aortic arch interruption. *Development* **128**, 3061-3070 (2001).
156. Serini, G., *et al.* Class 3 semaphorins control vascular morphogenesis by inhibiting integrin function. *Nature* **424**, 391-397 (2003).
157. Seo, S. & Kume, T. Forkhead transcription factors, Foxc1 and Foxc2, are required for the morphogenesis of the cardiac outflow tract. *Dev Biol* **296**, 421-436 (2006).
158. Brown, C.B., *et al.* PlexinA2 and semaphorin signaling during cardiac neural crest development. *Development* **128**, 3071-3080 (2001).
159. Gu, C., *et al.* Neuropilin-1 conveys semaphorin and VEGF signaling during neural and cardiovascular development. *Dev Cell* **5**, 45-57 (2003).
160. Allerstorfer, D., *et al.* VEGF and its role in the early development of the long bone epiphysis. *J Anat* **216**, 611-624 (2010).
161. Blumer, M.J., Fritsch, H., Pfaller, K. & Brenner, E. Cartilage canals in the chicken embryo: ultrastructure and function. *Anat Embryol (Berl)* **207**, 453-462 (2004).

162. Blumer, M.J., Longato, S., Schwarzer, C. & Fritsch, H. Bone development in the femoral epiphysis of mice: the role of cartilage canals and the fate of resting chondrocytes. *Dev Dyn* **236**, 2077-2088 (2007).
163. Alvarez, J., Costales, L., Serra, R., Balbin, M. & Lopez, J.M. Expression patterns of matrix metalloproteinases and vascular endothelial growth factor during epiphyseal ossification. *J Bone Miner Res* **20**, 1011-1021 (2005).
164. Ortega, N., Behonick, D.J. & Werb, Z. Matrix remodeling during endochondral ossification. *Trends Cell Biol* **14**, 86-93 (2004).
165. Stickens, D., *et al.* Altered endochondral bone development in matrix metalloproteinase 13-deficient mice. *Development* **131**, 5883-5895 (2004).
166. Maes, C., *et al.* Soluble VEGF isoforms are essential for establishing epiphyseal vascularization and regulating chondrocyte development and survival. *J Clin Invest* **113**, 188-199 (2004).
167. Carmeliet, P., *et al.* Impaired myocardial angiogenesis and ischemic cardiomyopathy in mice lacking the vascular endothelial growth factor isoforms VEGF164 and VEGF188. *Nat Med* **5**, 495-502 (1999).
168. Ganey, T.M., Love, S.M. & Ogden, J.A. Development of vascularization in the chondroepiphysis of the rabbit. *J Orthop Res* **10**, 496-510 (1992).
169. Wang, G., *et al.* Genetic ablation of Rac1 in cartilage results in chondrodysplasia. *Dev Biol* **306**, 612-623 (2007).
170. Lallier, T.E. Semaphorin profiling of periodontal fibroblasts and osteoblasts. *J Dent Res* **83**, 677-682 (2004).
171. Harper, J., Gerstenfeld, L.C. & Klagsbrun, M. Neuropilin-1 expression in osteogenic cells: down-regulation during differentiation of osteoblasts into osteocytes. *J Cell Biochem* **81**, 82-92 (2001).
172. Togari, A., Mogi, M., Arai, M., Yamamoto, S. & Koshihara, Y. Expression of mRNA for axon guidance molecules, such as semaphorin-III, netrins and neurotrophins, in human osteoblasts and osteoclasts. *Brain Res* **878**, 204-209 (2000).
173. Lanyon, L.E. Control of bone architecture by functional load bearing. *J Bone Miner Res* **7 Suppl 2**, S369-375 (1992).
174. Rubin, J., Rubin, C. & Jacobs, C.R. Molecular pathways mediating mechanical signaling in bone. *Gene* **367**, 1-16 (2006).
175. Lories, R.J. & Luyten, F.P. The bone-cartilage unit in osteoarthritis. *Nat Rev Rheumatol* **7**, 43-49 (2011).
176. Heinegard, D. & Saxne, T. The role of the cartilage matrix in osteoarthritis. *Nat Rev Rheumatol* **7**, 50-56 (2011).
177. Hopwood, B., *et al.* Identification of differentially expressed genes between osteoarthritic and normal trabecular bone from the intertrochanteric region of the proximal femur using cDNA microarray analysis. *Bone* **36**, 635-644 (2005).
178. Day, J.S., *et al.* A decreased subchondral trabecular bone tissue elastic modulus is associated with pre-arthritis cartilage damage. *J Orthop Res* **19**, 914-918 (2001).
179. Goldring, M.B. & Goldring, S.R. Articular cartilage and subchondral bone in the pathogenesis of osteoarthritis. *Ann N Y Acad Sci* **1192**, 230-237 (2010).
180. Radin, E.L. & Rose, R.M. Role of subchondral bone in the initiation and progression of cartilage damage. *Clin Orthop Relat Res*, 34-40 (1986).
181. Ding, Y.B., *et al.* Association of VCAM-1 overexpression with oncogenesis, tumor angiogenesis and metastasis of gastric carcinoma. *World J Gastroenterol* **9**, 1409-1414 (2003).

182. Yamazaki, D., *et al.* WAVE2 is required for directed cell migration and cardiovascular development. *Nature* **424**, 452-456 (2003).
183. Walsh, D.A., *et al.* Angiogenesis in the synovium and at the osteochondral junction in osteoarthritis. *Osteoarthritis Cartilage* **15**, 743-751 (2007).
184. Sadaf, S., Khan, M.A. & Akhtar, M.W. Expression enhancement of bubaline somatotropin in *E. coli* through gene modifications in the 5'-end coding region. *J Biotechnol* **135**, 134-139 (2008).
185. Pecho-Vrieseling, E., Sigrist, M., Yoshida, Y., Jessell, T.M. & Arber, S. Specificity of sensory-motor connections encoded by Sema3e-Plxnd1 recognition. *Nature* **459**, 842-846 (2009).
186. Pittler, S.J. & Baehr, W. Identification of a nonsense mutation in the rod photoreceptor cGMP phosphodiesterase beta-subunit gene of the rd mouse. *Proc Natl Acad Sci U S A* **88**, 8322-8326 (1991).
187. Sidman, R.L. & Green, M.C. Retinal Degeneration in the Mouse: Location of the Rd Locus in Linkage Group Xvii. *J Hered* **56**, 23-29 (1965).
188. Connolly, S.E., Hores, T.A., Smith, L.E. & D'Amore, P.A. Characterization of vascular development in the mouse retina. *Microvasc Res* **36**, 275-290 (1988).
189. Alvarez, Y., *et al.* Selective inhibition of retinal angiogenesis by targeting PI3 kinase. *PLoS One* **4**, e7867 (2009).
190. Gerhardt, H., *et al.* VEGF guides angiogenic sprouting utilizing endothelial tip cell filopodia. *J Cell Biol* **161**, 1163-1177 (2003).
191. Lalani, S.R., *et al.* SEMA3E mutation in a patient with CHARGE syndrome. *J Med Genet* **41**, e94 (2004).
192. Hall, B.D. Choanal atresia and associated multiple anomalies. *J Pediatr* **95**, 395-398 (1979).
193. Pagon, R.A., Graham, J.M., Jr., Zonana, J. & Yong, S.L. Coloboma, congenital heart disease, and choanal atresia with multiple anomalies: CHARGE association. *J Pediatr* **99**, 223-227 (1981).
194. Gay, C.M., Zygmunt, T. & Torres-Vazquez, J. Diverse functions for the semaphorin receptor PlexinD1 in development and disease. *Dev Biol* **349**, 1-19 (2011).
195. van der Zwaag, B., *et al.* PLEXIN-D1, a novel plexin family member, is expressed in vascular endothelium and the central nervous system during mouse embryogenesis. *Dev Dyn* **225**, 336-343 (2002).
196. Kremer, H., *et al.* Localization of a gene for Mobius syndrome to chromosome 3q by linkage analysis in a Dutch family. *Hum Mol Genet* **5**, 1367-1371 (1996).
197. Michielse, C.B., *et al.* Refinement of the locus for hereditary congenital facial palsy on chromosome 3q21 in two unrelated families and screening of positional candidate genes. *Eur J Hum Genet* **14**, 1306-1312 (2006).
198. van der Zwaag, B., *et al.* Sequence analysis of the PLEXIN-D1 gene in Mobius syndrome patients. *Pediatr Neurol* **31**, 114-118 (2004).
199. Roodink, I., *et al.* Semaphorin 3E expression correlates inversely with Plexin D1 during tumor progression. *Am J Pathol* **173**, 1873-1881 (2008).
200. Roodink, I., *et al.* Plexin D1 expression is induced on tumor vasculature and tumor cells: a novel target for diagnosis and therapy? *Cancer Res* **65**, 8317-8323 (2005).
201. Roodink, I., Verrijp, K., Raats, J. & Leenders, W.P. Plexin D1 is ubiquitously expressed on tumor vessels and tumor cells in solid malignancies. *BMC Cancer* **9**, 297 (2009).

202. Casazza, A., *et al.* Sema3E-Plexin D1 signaling drives human cancer cell invasiveness and metastatic spreading in mice. *J Clin Invest* **120**, 2684-2698 (2010).
203. Barberis, D., *et al.* p190 Rho-GTPase activating protein associates with plexins and it is required for semaphorin signalling. *J Cell Sci* **118**, 4689-4700 (2005).
204. Driessens, M.H., *et al.* Plexin-B semaphorin receptors interact directly with active Rac and regulate the actin cytoskeleton by activating Rho. *Curr Biol* **11**, 339-344 (2001).
205. Rohm, B., Rahim, B., Kleiber, B., Hovatta, I. & Puschel, A.W. The semaphorin 3A receptor may directly regulate the activity of small GTPases. *FEBS Lett* **486**, 68-72 (2000).
206. Pasterkamp, R.J. R-Ras fills another GAP in semaphorin signalling. *Trends Cell Biol* **15**, 61-64 (2005).
207. Uesugi, K., Oinuma, I., Katoh, H. & Negishi, M. Different requirement for Rnd GTPases of R-Ras GAP activity of Plexin-C1 and Plexin-D1. *J Biol Chem* **284**, 6743-6751 (2009).
208. Bellon, A., *et al.* VEGFR2 (KDR/Flk1) signaling mediates axon growth in response to semaphorin 3E in the developing brain. *Neuron* **66**, 205-219 (2010).
209. Kinbara, K., Goldfinger, L.E., Hansen, M., Chou, F.L. & Ginsberg, M.H. Ras GTPases: integrins' friends or foes? *Nat Rev Mol Cell Biol* **4**, 767-776 (2003).
210. Ito, Y., Oinuma, I., Katoh, H., Kaibuchi, K. & Negishi, M. Sema4D/plexin-B1 activates GSK-3beta through R-Ras GAP activity, inducing growth cone collapse. *EMBO Rep* **7**, 704-709 (2006).
211. Turner, L.J., Nicholls, S. & Hall, A. The activity of the plexin-A1 receptor is regulated by Rac. *J Biol Chem* **279**, 33199-33205 (2004).
212. Hu, H., Marton, T.F. & Goodman, C.S. Plexin B mediates axon guidance in Drosophila by simultaneously inhibiting active Rac and enhancing RhoA signaling. *Neuron* **32**, 39-51 (2001).
213. He, H., Yang, T., Terman, J.R. & Zhang, X. Crystal structure of the plexin A3 intracellular region reveals an autoinhibited conformation through active site sequestration. *Proc Natl Acad Sci U S A* **106**, 15610-15615 (2009).
214. Cai, H. & Reed, R.R. Cloning and characterization of neuropilin-1-interacting protein: a PSD-95/Dlg/ZO-1 domain-containing protein that interacts with the cytoplasmic domain of neuropilin-1. *J Neurosci* **19**, 6519-6527 (1999).
215. Lanahan, A.A., *et al.* VEGF receptor 2 endocytic trafficking regulates arterial morphogenesis. *Dev Cell* **18**, 713-724 (2010).
216. Sakai, K., *et al.* Stage- and tissue-specific expression of a Col2a1-Cre fusion gene in transgenic mice. *Matrix Biol* **19**, 761-767 (2001).
217. Zhu, Y., *et al.* Ablation of NF1 function in neurons induces abnormal development of cerebral cortex and reactive gliosis in the brain. *Genes Dev* **15**, 859-876 (2001).
218. Martin, E. & Shapiro, J.R. Osteogenesis imperfecta: epidemiology and pathophysiology. *Curr Osteoporosis Rep* **5**, 91-97 (2007).
219. Wheeler, V.R., Cooley, N.R., Jr. & Blackburn, W.R. Cardiovascular pathology in osteogenesis imperfecta type IIA with a review of the literature. *Pediatr Pathol* **8**, 55-64 (1988).

220. Adami, S., *et al.* Effects of oral alendronate and intranasal salmon calcitonin on bone mass and biochemical markers of bone turnover in postmenopausal women with osteoporosis. *Bone* **17**, 383-390 (1995).
221. Liberman, U.A., *et al.* Effect of oral alendronate on bone mineral density and the incidence of fractures in postmenopausal osteoporosis. The Alendronate Phase III Osteoporosis Treatment Study Group. *N Engl J Med* **333**, 1437-1443 (1995).
222. Devogelaer, J.P., Malghem, J., Maldague, B. & Nagant de Deuxchaisnes, C. Radiological manifestations of bisphosphonate treatment with APD in a child suffering from osteogenesis imperfecta. *Skeletal Radiol* **16**, 360-363 (1987).
223. Hoekman, K., Papapoulos, S.E., Peters, A.C. & Bijvoet, O.L. Characteristics and bisphosphonate treatment of a patient with juvenile osteoporosis. *J Clin Endocrinol Metab* **61**, 952-956 (1985).
224. Glorieux, F.H. Experience with bisphosphonates in osteogenesis imperfecta. *Pediatrics* **119 Suppl 2**, S163-165 (2007).
225. Rao, S.H., Evans, K.D., Oberbauer, A.M. & Martin, R.B. Bisphosphonate treatment in the oim mouse model alters bone modeling during growth. *J Biomech* **41**, 3371-3376 (2008).
226. Uveges, T.E., *et al.* Alendronate treatment of the brtl osteogenesis imperfecta mouse improves femoral geometry and load response before fracture but decreases predicted material properties and has detrimental effects on osteoblasts and bone formation. *J Bone Miner Res* **24**, 849-859 (2009).
227. Letocha, A.D., *et al.* Controlled trial of pamidronate in children with types III and IV osteogenesis imperfecta confirms vertebral gains but not short-term functional improvement. *J Bone Miner Res* **20**, 977-986 (2005).
228. Plotkin, H., *et al.* Pamidronate treatment of severe osteogenesis imperfecta in children under 3 years of age. *J Clin Endocrinol Metab* **85**, 1846-1850 (2000).
229. Vyskocil, V., Pikner, R. & Kutilek, S. Effect of alendronate therapy in children with osteogenesis imperfecta. *Joint Bone Spine* **72**, 416-423 (2005).
230. DiMeglio, L.A. & Peacock, M. Two-year clinical trial of oral alendronate versus intravenous pamidronate in children with osteogenesis imperfecta. *J Bone Miner Res* **21**, 132-140 (2006).
231. Delos, D., *et al.* The effects of RANKL inhibition on fracture healing and bone strength in a mouse model of osteogenesis imperfecta. *J Orthop Res* **26**, 153-164 (2008).
232. Gerstenfeld, L.C., *et al.* Comparison of effects of the bisphosphonate alendronate versus the RANKL inhibitor denosumab on murine fracture healing. *J Bone Miner Res* **24**, 196-208 (2009).
233. Chipman, S.D., *et al.* Defective pro alpha 2(I) collagen synthesis in a recessive mutation in mice: a model of human osteogenesis imperfecta. *Proc Natl Acad Sci U S A* **90**, 1701-1705 (1993).
234. Weis, S.M., *et al.* Myocardial mechanics and collagen structure in the osteogenesis imperfecta murine (oim). *Circ Res* **87**, 663-669 (2000).
235. Kuznetsova, N.V., McBride, D.J. & Leikin, S. Changes in thermal stability and microunfolded pattern of collagen helix resulting from the loss of alpha2(I) chain in osteogenesis imperfecta murine. *J Mol Biol* **331**, 191-200 (2003).

236. Mayorga, M., Bahi, N., Ballester, M., Comella, J.X. & Sanchis, D. Bcl-2 is a key factor for cardiac fibroblast resistance to programmed cell death. *J Biol Chem* **279**, 34882-34889 (2004).
237. Eun, S.Y., *et al.* Identification of cytochrome c oxidase subunit 6A1 as a suppressor of Bax-induced cell death by yeast-based functional screening. *Biochem Biophys Res Commun* **373**, 58-63 (2008).
238. Butcher, H.L., Kennette, W.A., Collins, O., Zalups, R.K. & Koropatnick, J. Metallothionein mediates the level and activity of nuclear factor kappa B in murine fibroblasts. *J Pharmacol Exp Ther* **310**, 589-598 (2004).
239. Novitskiy, G., Potter, J.J., Rennie-Tankersley, L. & Mezey, E. Identification of a novel NF-kappaB-binding site with regulation of the murine alpha2(I) collagen promoter. *J Biol Chem* **279**, 15639-15644 (2004).
240. Okamoto, O. & Fujiwara, S. Dermatopontin, a novel player in the biology of the extracellular matrix. *Connect Tissue Res* **47**, 177-189 (2006).
241. Toyoshima, T., *et al.* Differential gene expression of 36-kDa microfibril-associated glycoprotein (MAGP-36/MFAP4) in rat organs. *Cell Tissue Res* **332**, 271-278 (2008).
242. de Simone, G. & de Divitiis, O. Extracellular matrix and left ventricular mechanics in overload hypertrophy. *Adv Clin Path* **6**, 3-10 (2002).
243. Janicki, J.S. & Brower, G.L. The role of myocardial fibrillar collagen in ventricular remodeling and function. *J Card Fail* **8**, S319-325 (2002).
244. Chen, M.M., Lam, A., Abraham, J.A., Schreiner, G.F. & Joly, A.H. CTGF expression is induced by TGF-beta in cardiac fibroblasts and cardiac myocytes: a potential role in heart fibrosis. *J Mol Cell Cardiol* **32**, 1805-1819 (2000).
245. Sibinga, N.E., *et al.* Collagen VIII is expressed by vascular smooth muscle cells in response to vascular injury. *Circ Res* **80**, 532-541 (1997).
246. Houweling, A.C., van Borren, M.M., Moorman, A.F. & Christoffels, V.M. Expression and regulation of the atrial natriuretic factor encoding gene *Nppa* during development and disease. *Cardiovasc Res* **67**, 583-593 (2005).
247. Chau, D.Y., Collighan, R.J., Verderio, E.A., Addy, V.L. & Griffin, M. The cellular response to transglutaminase-cross-linked collagen. *Biomaterials* **26**, 6518-6529 (2005).
248. Walther, T., *et al.* Accelerated mitochondrial adenosine diphosphate/adenosine triphosphate transport improves hypertension-induced heart disease. *Circulation* **115**, 333-344 (2007).
249. ten Dijke, P. & Arthur, H.M. Extracellular control of TGFbeta signalling in vascular development and disease. *Nat Rev Mol Cell Biol* **8**, 857-869 (2007).
250. Thapa, N., Lee, B.H. & Kim, I.S. TGFbeta1/betaig-h3 protein: a versatile matrix molecule induced by TGF-beta. *Int J Biochem Cell Biol* **39**, 2183-2194 (2007).
251. Van Scoyk, M., *et al.* Wnt signaling pathway and lung disease. *Transl Res* **151**, 175-180 (2008).
252. Brigstock, D.R. Regulation of angiogenesis and endothelial cell function by connective tissue growth factor (CTGF) and cysteine-rich 61 (CYR61). *Angiogenesis* **5**, 153-165 (2002).
253. Corvol, P., Lamande, N., Cruz, A., Celerier, J. & Gasc, J.M. Inhibition of angiogenesis: a new function for angiotensinogen and des(angiotensin I)angiotensinogen. *Curr Hypertens Rep* **5**, 149-154 (2003).

254. Gao, X. & Xu, Z. Mechanisms of action of angiogenin. *Acta Biochim Biophys Sin (Shanghai)* **40**, 619-624 (2008).
255. Li, M. & Ransohoff, R.M. The roles of chemokine CXCL12 in embryonic and brain tumor angiogenesis. *Semin Cancer Biol* **19**, 111-115 (2009).
256. Jiang, X.C., *et al.* Expression of plasma phospholipid transfer protein mRNA in normal and emphysematous lungs and regulation by hypoxia. *J Biol Chem* **273**, 15714-15718 (1998).
257. Lafont, J.E., Talma, S., Hopfgarten, C. & Murphy, C.L. Hypoxia promotes the differentiated human articular chondrocyte phenotype through SOX9-dependent and -independent pathways. *J Biol Chem* **283**, 4778-4786 (2008).
258. Ohradanova, A., *et al.* Hypoxia upregulates expression of human endosialin gene via hypoxia-inducible factor 2. *Br J Cancer* **99**, 1348-1356 (2008).
259. Park, S.Y., *et al.* Hypoxia increases androgen receptor activity in prostate cancer cells. *Cancer Res* **66**, 5121-5129 (2006).
260. Littler, C.M., *et al.* Protein kinase C-epsilon-null mice have decreased hypoxic pulmonary vasoconstriction. *Am J Physiol Heart Circ Physiol* **284**, H1321-1331 (2003).
261. MacBeath, J.R., Shackleton, D.R. & Hulmes, D.J. Tyrosine-rich acidic matrix protein (TRAMP) accelerates collagen fibril formation in vitro. *J Biol Chem* **268**, 19826-19832 (1993).
262. Takeda, U., *et al.* Targeted disruption of dermatopontin causes abnormal collagen fibrillogenesis. *J Invest Dermatol* **119**, 678-683 (2002).
263. Hata, R., Kurata, S. & Shinkai, H. Existence of malfunctioning pro alpha2(I) collagen genes in a patient with a pro alpha 2(I)-chain-defective variant of Ehlers-Danlos syndrome. *Eur J Biochem* **174**, 231-237 (1988).
264. Malfait, F., *et al.* Total absence of the alpha2(I) chain of collagen type I causes a rare form of Ehlers-Danlos syndrome with hypermobility and propensity to cardiac valvular problems. *J Med Genet* **43**, e36 (2006).
265. Sasaki, T., *et al.* Ehlers-Danlos syndrome. A variant characterized by the deficiency of pro alpha 2 chain of type I procollagen. *Arch Dermatol* **123**, 76-79 (1987).
266. Schwarze, U., *et al.* Rare autosomal recessive cardiac valvular form of Ehlers-Danlos syndrome results from mutations in the COL1A2 gene that activate the nonsense-mediated RNA decay pathway. *Am J Hum Genet* **74**, 917-930 (2004).
267. Ohkubo, H., *et al.* Cloning and sequence analysis of cDNA for rat angiotensinogen. *Proc Natl Acad Sci U S A* **80**, 2196-2200 (1983).
268. Sane, D.C., Kontos, J.L. & Greenberg, C.S. Roles of transglutaminases in cardiac and vascular diseases. *Front Biosci* **12**, 2530-2545 (2007).
269. Falvo, K.A., Klain, D.B., Krauss, A.N., Root, L. & Auld, P.A. Pulmonary function studies in osteogenesis imperfecta. *Am Rev Respir Dis* **108**, 1258-1260 (1973).
270. Migliaccio, S., *et al.* Impairment of diastolic function in adult patients affected by osteogenesis imperfecta clinically asymptomatic for cardiac disease: casualty or causality? *Int J Cardiol* **131**, 200-203 (2009).
271. Takken, T., *et al.* Cardiopulmonary fitness and muscle strength in patients with osteogenesis imperfecta type I. *J Pediatr* **145**, 813-818 (2004).
272. Cropp, G.J. & Myers, D.N. Physiological evidence of hypermetabolism in osteogenesis imperfecta. *Pediatrics* **49**, 375-391 (1972).

273. Fulzele, K., *et al.* Disruption of the insulin-like growth factor type 1 receptor in osteoblasts enhances insulin signaling and action. *J Biol Chem* **282**, 25649-25658 (2007).
274. Rached, M.T., *et al.* FoxO1 expression in osteoblasts regulates glucose homeostasis through regulation of osteocalcin in mice. *J Clin Invest* **120**, 357-368 (2010).
275. Rached, M.T., *et al.* FoxO1 is a positive regulator of bone formation by favoring protein synthesis and resistance to oxidative stress in osteoblasts. *Cell Metab* **11**, 147-160 (2010).
276. Rosen, C.J. Sugar and bone: a not-so sweet story. *J Bone Miner Res* **23**, 1881-1883 (2008).
277. Li, W.F., *et al.* Genetics of osteoporosis: accelerating pace in gene identification and validation. *Hum Genet* **127**, 249-285 (2010).
278. Cox, R.D. & Church, C.D. Mouse models and the interpretation of human GWAS in type 2 diabetes and obesity. *Dis Model Mech* **4**, 155-164 (2011).

IV. Publications

Frank Thiele*, Christian M. Cohrs*, Armando Flor, Thomas S. Lisse, Gerhard K.H. Przemeck, Marion Horsch, Anja Schrewe, Valerie Gailus-Durner, Boris Ivandic, Hugo A. Katus, Wolfgang Wurst, Catherine Reisenberg, Hollis Chaney, Helmut Fuchs, Wolfgang Hans, Johannes Beckers, Joan C. Marini, Martin Hrabé de Angelis

Bone-independent dysfunction of heart and lung in *Aga2* mouse mirrors findings in children with Osteogenesis imperfecta.

Submitted to PNAS

* Authors contribute equally to this work

Frank Thiele, Christian M. Cohrs, Gerhard K.H. Przemeck, Wolfgang Wurst, Helmut Fuchs, Martin Hrabé de Angelis

In vitro analysis of bone phenotypes in *Col1a1* and *Jagged1* mutant mice using a standardized osteoblast cell-culture system.

Manuscript in preparation

Christian M. Cohrs, Thomas S. Lisse, Frank Thiele, Matthias Klaften, Marion Horsch, Ingeborg Klymiuk, Helmut Fuchs, Johannes Beckers, Gerhard K.H. Przemeck, Wolfgang Hans and Martin Hrabé de Angelis

A point mutation in the murine *Plxnd1* causes osteoarthritis, chondrodysplasia and ectopic bone formation in hindlimbs.

Manuscript in preparation

Yasunari Matsuzaka, Christian M. Cohrs, Wolfgang Hans, Frank Thiele, Matthias Klaften, Sibylle Wagner, Tim Strom, Sebastian Eckl, Jack Favor, Wolfgang Wurst, Jochen Graw, Julia Calzada-Wack, Koichiro Abe, Birgit Rathkolb, Eckhard Wolf, Lore Becker, Thomas Klopstock, Ildikó Rácz, Andreas Zimmer, Jan Rozman, Martin Klingenspor, Dirk H. Busch, Markus Ollert, Helmut Fuchs, Valérie Gailus-Durner, Gerhard Przemeck, Martin Hrabé de Angelis

Nonsense mutation in mouse *Shc2* gene causes defects in bone remodelling, body metabolism, behaviour, anaemia and corneal avascularity.

Manuscript in preparation

Angelique Ale, Vladimir Ermolayev, Eva Herzog, Christian M. Cohrs, Martin Hrabé de Angelis, Vasilis Ntziachristos

Next generation Fluorescence Molecular Tomography performance using hybrid implementation with X-ray computed tomography.

Manuscript in preparation

V. Acknowledgements

Ich möchte mich bei Prof. Martin Hrabé de Angelis für die Vergabe dieses interessanten Themas und das entgegengebrachte Vertrauen bedanken. Darüber hinaus waren die ständige Diskussionsbereitschaft und die gewährte Freiheit für das Gelingen dieser Arbeit von großem Wert.

Ich möchte mich auch bei Dr. Wolfgang Hans und Dr. Gerhard Przemeck für die großartige Betreuung und Unterstützung während meiner Doktorarbeit bedanken. Die konstruktiven Ratschläge und Diskussionen waren für mich stets eine Bereicherung.

Dr. Frank Thiele danke ich für die tolle Zusammenarbeit während der gemeinsamen Zeit am Institut. Der wertvolle Ideenaustausch, die vielen langen Diskussionen und die gemeinsam geplanten Experimente trugen maßgeblich zum Gelingen dieser Arbeit bei.

Bei Bastian Hösel, Daniel Gradinger und Davide Cavanna möchte ich mich für die großartige Zusammenarbeit und die Diskussionen bedanken, die mir auch viele wichtige Einblicke in andere Themenbereiche gewährt haben.

Im möchte mich bei allen Mitarbeitern des Instituts für die angenehme Zeit und das freundliche Arbeitsklima während meiner Arbeit bedanken. Ein ganz besonderer Dank gilt Nina Schieven, Michael Schulz und Nicole Boche für die großartige Unterstützung im Labor.

Ferner möchte ich mich bei allen Beteiligten der GMC für die Durchführung des Primärscreens und die daraus resultierenden Ergebnisse und Diskussionen bedanken. Ganz speziell möchte ich mich bei Reinhard Seeliger, Susanne Wittich, Michaela Grandl, Sabrina Bothur und Anja Wohlbier für die Hilfe mit der Mausearbeit im Dysmorphologie Screen bedanken.

Prof. Joan Marini, Dr. Anja Schrewe, Dr. Marion Horsch, Helga Wehnes, Angelique Ale und Dr. Ermolayev danke ich für ihre Unterstützung und die Durchführung von Experimenten im *Aga2*-Projekt.

Abschließend möchte ich mich bei meinen Eltern und Großeltern sowie meiner Schwester und meinen Freunden bedanken. Die uneingeschränkte Unterstützung, das Vertrauen und die Geduld haben mir das alles letztendlich ermöglicht.

VI. Affirmation

Ich erkläre hiermit an Eides statt, dass ich die vorliegende Arbeit selbstständig, ohne unzulässige fremde Hilfe und ausschließlich mit den angegebenen Quellen und Hilfsmitteln angefertigt habe.

Die verwendeten Literaturquellen sind im Literaturverzeichnis (References) vollständig zitiert.

Diese Arbeit hat in dieser oder ähnlicher Form noch keiner anderen Prüfungsbehörde vorgelegen.

München, den 19.05.2011

Christian Cohrs